Institute of Fundamental Technological Research

Polish Academy of Sciences

Thermomechanical Properties of Additively Manufactured Shape Memory Epoxy for Advanced Shape-Morphing Applications

Thesis submitted in partial fulfilment of the requirements
for the degree

Doctor of Philosophy

in

Materials Engineering

by

Mana Nabavian-Kalat

under the supervision of

Prof. dr hab. inż. Zbigniew Kowalewski (Supervisor)

Prof. Andrés Díaz Lantada (Co-supervisor)

Warsaw 2025

2025

Mana Nabavian-Kalat

DECLARATION

I hereby declare that the work presented in this Thesis is the result of my own original research conducted at the Department of Experimental Mechanics, Institute of Fundamental Technological Research, Polish Academy of Sciences (IPPT PAN), Warsaw, Poland. This Thesis has not been submitted, either in whole or in part, for any other degree or qualification at any other institution. I affirm that I have complied with all standards of academic integrity and ethical conduct. No part of this work has been fabricated, falsified, or plagiarized. All sources and contributions of other researchers have been appropriately acknowledged and cited.

Mana Nabavian-Kalat

June, 2025

تقدیم به مادر و پدرم، الهه و مسعود.

Dedicated to my parents, who endured my absence for the sake of my progress.

ACKNOWLEDGEMENTS

First and foremost, I would like to express my sincere gratitude to my supervisor, Professor Zbigniew L. Kowalewski, for his invaluable guidance, support, and trust in me, even though I joined his team midway through my PhD journey. I deeply appreciate his expertise and encouragement, which were essential in bringing this work to completion.

I am equally grateful to my co-supervisor, Professor Andrés Díaz Lantada, for accepting to guide me as co-supervisor, generously sharing his invaluable knowledge and support, and hosting me at the Polytechnic University of Madrid (UPM). During my research stay, I had the privilege of learning from him and his outstanding team. I would also like to extend my thanks to everyone at the Product Development Laboratory, Department of Mechanical Engineering (UPM), for their kind support and collaboration. In particular, I wish to thank Eng. Carlos Polvorinos for providing the CAD modeling tasks and Mr. Pedro Ortego for his help with SLA 3D printing.

I am very thankful to all the professors, colleagues, and friends at IPPT PAN for their support and cooperation throughout my doctoral work. I would especially like to acknowledge Dr. Mateusz Kopeć, Dr. Yasamin Ziai, Dr. Arkadius Gradys, M.Sc. Kinga Dziedzic, M.Sc. Angelika Zaszczyńska, Mr. Leszek Urbański, Professor Elżbieta Pieczyska, Dr. Maria Staszczak, Dr. Karol Golasiński, M.Sc. Ved Dubey Prakash, Dr. Kamil Bochenek, Professor Michał Basista, and Professor Paweł Sajkiewicz. Without their help, I could not have achieved the results presented in this thesis.

I gratefully acknowledge the support provided by the 14th call of the KMM-VIN Research Fellowship Programme, which enabled our collaborative project “Investigation, Modeling, and Processing of Shape-Memory Polymers for Smart Micro-Actuators” between IPPT PAN and UPM. This fellowship also supported my research stay at UPM, which greatly enriched this work.

Finally, I would like to thank all my dear friends, whose friendship and kindness made life away from my home country much easier and more enjoyable.

TABLE OF CONTENTS

LIST OF FIGURES

LIST OF TABLES

LIST OF ABBREVIATIONS

Abbreviation	Definition
SMP	Shape memory polymer
AM	Additive manufacturing
PU-SMP	Polyurethane shape memory polymer
FDM	Fused deposition modeling
SLA	Stereolithography
SMEp	Shape memory epoxy
CAD	Computer-aided design
T_g	Glass transition temperature
T_m	Melting temperature
FFF	Fused Filament Fabrication
DLP	Digital light processing
SLS	Selective laser sinthering
PLA	Polylactic acid
IPA	Isopropyl alcohol
TPU	Thermoplastic polyurethane
UV	Ultra-violet
DSC	Differential scanning calorimetry
SEM	Scanning electron microscopy
PCA	Post curing apparatus
FTIR	Fourier transform infrared spectroscopy
ATR	Attenuated total reflectance
TGA	Thermogravimetric Analysis
TMA	Thermomechanical Analysis
CTE	Coefficient of thermal expansion
SR	Shape recovery
SF	Shape fixity

VITA

2012-2017 Bachelor of Science in Polymer Engineering, Department of polymer engineering, Islamic Azad University, Science and Research Branch, Tehran, Iran.

2017-2019 Master of Science in Polymer Engineering, Department of Chemical Engineering, Tarbiat Modares University, Tehran, Iran.

2020-2025 Doctor of Philosophy in Materials Engineering, Department of Experimental Mechanics, IPPT PAN, Warsaw, Poland.

PUBLICATIONS

- **Nabavian Kalat M.**, Ziai Y., Dziedzic K., Gradys A. D., Urbański L., Zaszczyńska A., Lantada, A.D., Kowalewski Z. L., **Experimental evaluation of build orientation effects on the microstructure, thermal, mechanical, and shape memory properties of SLA 3D-printed epoxy resin**, EUROPEAN POLYMER JOURNAL, ISSN: 0014-3057, DOI: 10.1016/j.eurpolymj.2025.113829, Vol.228, pp.113829-1-18, **2025**.
- **Nabavian Kalat M.**, Staszczak M., Urbański L., Fernandez C., Vega C., Cristea M., Ionita Lantada, A.D., Pieczyska E.A., **Investigating a shape memory epoxy resin and its application to engineering shape-morphing devices empowered through kinematic chains and compliant joints**, MATERIALS AND DESIGN, ISSN: 0264-1275, DOI: 10.1016/j.matdes.2023.112263, Vol.233, No.112263, pp.1-15, **2023**.
- Staszczak M., **Nabavian Kalat M.**, Golasiński K.M., Urbański L., Takeda K., Matsui R., Pieczyska E.A., **Characterization of Polyurethane Shape Memory Polymer and Determination of Shape Fixity and Shape Recovery in Subsequent Thermomechanical Cycles**, Polymers, ISSN: 2073-4360, DOI: 10.3390/polym14214775, Vol.14, No.4775, pp.1-19, **2022**.
- **Nabavian Kalat M.**, Razzaghi-Kashani M., **The role of reduced graphene oxide as a secondary filler in improving the performance of silica-filled styrene-butadiene rubber compounds**, POLYMER JOURNAL, ISSN: 0032-3896, DOI: 10.1038/s41428-021-00570-3, pp.1-11, **2021**.

- Raef M., Hosseini S.M., **Nabavian Kalat M.**, Razzaghi-Kashani M., **Vulcanization kinetics of styrene butadiene rubber reinforced by graphenic particles**, SPE Polymers, ISSN: 2690-3857, DOI: 10.1002/pls2.10039, pp.1-12, **2021**.

CONFERENCE ABSTRACTS

- **Nabavian Kalat M.**, Urbański L., Lantada A.D., Kowalewski Z.L., **Effect of Printing Orientation on Thermomechanical Behavior of SLA 4D-printed Shape Memory Epoxy**, DAS 2024, 40th DANUBIA-ADRIA SYMPOSIUM on Advances in Experimental Mechanics, 2024-09-24/09-27, Gdańsk (PL), pp.1-2, **2024**.
- **Nabavian Kalat M.**, Staszczak M., Urbański L., Lantada A.D., Pieczyska E., **Shape Memory Epoxy Resin for Shape-Morphing Additive Manufacturing**, DAS 2023, 39th Danubia-Adria Symposium on Advances in Experimental Mechanics, 2023-09-26/09-29, Siofok (HU), pp.46-47, **2023**.
- **Nabavian-Kalat M.**, Staszczak M., Ziai Y., Urbański L., Pieczyska E., **Effect of Shape Recovery and Cyclic Loading on the Evolution of Micro-Cracks in Shape Memory Polymers**, IUTAM Symposium, IUTAM Symposium on Enhancing Material Performance by Exploiting Instabilities and Damage Evolution, 2022-06-05/06-10, Warszawa (PL), DOI: 10.24423/iutam2022warsaw, No.P040, pp.54-54, **2022**.
  Financed by Grant No. 2017/27/B/ST8/03074
- Staszczak M., **Nabavian Kalat M.**, Urbański L., Cristea M., Pieczyska E.A., **Influence of Strain Rate and Cooling Rate on the Mechanical Behaviour Shape Memory Polyurethane with Tg = 65 °C**, ICEM, 19th International Conference on Experimental Mechanics, 2022-07-17/07-21, Kraków (PL), pp.280-281, **2022**.
  Financed by Grant No. 2017/27/B/ST8/03074
- **Nabavian Kalat M.**, Staszczak M., Ziai Y., Gradys A., Urbański L., Pieczyska E.A., **The Effect of Shape Memory Behavior on the Microstructure of the PU-SMP (Tg = 45°C)**, ICEM, 19th International Conference on Experimental Mechanics, 2022-07-17/07-21, Kraków (PL), pp.278-279, **2022**.
  Financed by Grant No. 2017/27/B/ST8/03074
- Nabavian Kalat M., Razzaghi-Kashani M., Pieczyska E., Staszczak M., **The Role of Reduced Graphene Oxide as A Secondary Filler in Reducing the Energy Dissipation**

of Silica-Filled Styrene-Butadiene Rubber Composites Under Dynamic Deformation, TTP 2021, International Conference Thermography and Thermometry in Infrared, 2021-09-28/09-30, Kazimierz Dolny - on-line (PL), pp.1-2, **2021**.

Financed by Grant No. 2017/27/B/ST8/03074

- Staszczak M., Pieczyska E., **Nabavian Kalat M.**, Matsui R., Takeda K., **Analiza energetyczna polimeru z pamięcią kształtu w procesie rozciągania**, TTP 2021, International Conference Thermography and Thermometry in Infrared, 2021-09-28/09-30, Kazimierz Dolny - on-line (PL), pp.1-2, **2021**.

  Financed by Grant No. 2017/27/B/ST8/03074

ABSTRACT

Shape memory polymers (SMPs) have attracted considerable interest as smart materials capable of undergoing programmed shape transformations in response to external stimuli, particularly heat. Their integration into additive manufacturing (AM) has enabled the realization of 4D-printed, shape-morphing structures that can respond autonomously to their environment. The convergence of responsive materials, intelligent design strategies, and high-resolution fabrication methods offers an innovative pathway for creating programmable, adaptive systems. However, a key challenge often overlooked is the in-depth thermomechanical characterization of the SMP before its application in a specific design and manufacturing context.

This research systematically investigates thermo-responsive SMPs in both thermoplastic and thermoset forms, aiming to assess their suitability for 4D printing and application in programmable shape-morphing devices. The preliminary study focused on a thermoplastic polyurethane SMP (PU-SMP), evaluating its thermal, mechanical, and microstructural behavior under tensile loading and cyclic thermomechanical conditions. A framework was established to quantify shape fixity and recovery performance. However, limitations in fused deposition modeling (FDM) printability, unstable high-temperature behavior, and material supply necessitated a shift to stereolithography (SLA) and the use of a thermoset shape memory epoxy (SMEp).

The second phase explores the influence of the build orientation on the thermomechanical behavior of SLA-printed SMEp specimens. Identical dog-bone specimens were printed from two distinct surfaces (flat and edge) to study how layer count and surface area affect thermal expansion, dimensional stability, mechanical performance, and shape memory efficiency. Edge-printed specimens (comprising more numerous and smaller layers) demonstrated 13% higher tensile strength, reduced thermal expansion, and superior shape recovery (74%) compared to flat-printed ones (66.5%). Conversely, flat-printed specimens exhibited greater elongation but lower recovery efficiency.

In the final phase, the insights gained were applied to design and 4D print monolithic smart devices with embedded compliant joints and kinematic chains. These non-assembled structures were fabricated in a single printing step directly from computer-aided design (CAD), using SMEp material alone. Two actuation strategies (S-shaped and torsional compliant joints) were implemented to enable localized thermally-triggered motion. The prototypes were trained through thermomechanical cycles using hot and cold water, achieving up to 95% shape recovery by

actuating only the embedded joint. Thermal imaging confirmed localized actuation without heating the entire device.

This study highlights the importance of comprehensive material characterization, anisotropy management, and functional design in enabling responsive 4D-printed systems. The presented framework offers a robust foundation for developing programmable, single-material, shape-morphing devices, with potential applications in soft robotics, biomedical engineering, deployable structures, and precision micro-mechanisms.

STRESZCZENIE

Polimery z pamięcią kształtu (Shape Memory Polymers) aktualnie stanowią obiekt dużego zainteresowania jako inteligentnych materiałów zdolnych do przenoszenia programowalnych transformacji kształtu w odpowiedzi na bodźce zewnętrzne, w szczególności ciepło. Ich integracja z technikami druku (Additive Manufacturing) doprowadziła do powstania cztero-wymiarowych technologii drukowania umożliwiających produkcję struktur o zmiennej formie, które mogą autonomicznie reagować na warunki środowiska zewnętrznego. Powiązanie materiałów reagujących na bodźce zewnętrzne, inteligentnych strategii projektowania oraz metod wytwarzania o wysokiej rozdzielczości oferuje innowacyjną ścieżkę do tworzenia programowalnych, adaptacyjnych systemów. Jednak kluczowym wyzwaniem, które jest często pomijane w różnych analizach, jest dogłębna charakterystyka termomechaniczna polimerów z pamięcią kształtu przed ich zastosowaniem zarówno w określonym kontekście projektowania, jak i produkcji. Ramowy program badań obejmował systematyczne testowanie termoczułych materiałów z pamięcią kształtu SMP w postaci polimerów termoplastycznych i termoutwardzalnych i jego celem była ocena ich przydatności do druku 4D i zastosowania w programowalnych urządzeniach o zmiennym kształcie. Wstępne badania przeprowadzone w rozprawie skupiały się na termoplastycznym poliuretanowym polimerze z pamięcią kształtu (PU-SMP), w celu oceny jego termicznego, mechanicznego i mikrostrukturalnego zachowania pod wpływem obciążenia rozciągającego i przy cyklicznych zmianach o charakterze termomechanicznym. Dla badanych materiałów opracowano ramowy program badań ukierunkowany na ilościowe określenie trwałości kształtu i efektywności jego odzyskiwania. Ograniczenia w możliwości zastosowania technologii druku 3D, polegającej na warstwowym nanoszeniu stopionego materiału termoplastycznego na platformę roboczą drukarki (Fused Deposition Modelling), w postaci niestabilnego zachowania badanych materiałów w wysokiej temperaturze i braku odpowiedniej ich ilości do badań, wymusiły zastosowanie w badaniach stereolitografii (SLA) i termoutwardzalnego polimeru z pamięcią kształtu o matrycy epoksydowej (SMEp).

W drugiej części programu badań oceniano wpływ orientacji druku na zachowanie termomechaniczne próbek SMEp drukowanych metodą SLA. Próbki płaskie o jednakowej geometrii zostały wydrukowane w dwóch różnych orientacjach (płaskiej i krawędziowej), aby zbadać, w jaki sposób liczba warstw i ich powierzchnia wpływają na rozszerzalność cieplną,

stabilność wymiarową, wydajność mechaniczną i efektywność pamięci kształtu. Próbki drukowane krawędziowo (obejmujące większą liczbę warstw, ale o mniejszej powierzchni) wykazały o 13% wyższą wytrzymałość na rozciąganie, zmniejszoną rozszerzalność cieplną i lepsze odzyskiwanie kształtu (74%) w porównaniu do próbek drukowanych w orientacji płaskiej (66,5%). Z kolei próbki drukowane w orientacji płaskiej wykazywały większe wydłużenie, ale niższą wydajność odzyskiwania kształtu.

W ostatniej części programu badawczego rozprawy uzyskane wyniki wykorzystano do projektowania i drukowania w technologii 4D monolitycznych inteligentnych urządzeń z wbudowanymi, podatnymi połączeniami i łańcuchami kinematycznymi. Tego typu struktury zostały wytworzone w jednym kroku drukowania bezpośrednio z CAD, przy wyłącznym użyciu SMEp. Wdrożono dwie strategie aktywacji (podatne połączenia w kształcie litery S i skrętne), aby umożliwić lokalny ruch elementów badanych konstrukcji wyzwalany termicznie. Prototypy trenowano za pomocą cykli termomechanicznych z użyciem ciepłej i zimnej wody, uzyskując do 95% odzysku pierwotnego kształtu poprzez aktywację tylko wbudowanego podatnego łącznika. Zastosowanie w badaniach termowizji potwierdziło lokalną aktywację połączenia bez konieczności podgrzewania całego urządzenia.

Opracowana rozprawa podkreśla znaczenie znajomości kompleksowej charakterystyki materiałowej, zarządzania anizotropią i funkcjonalnego projektowania dla umożliwienia drukowania odpowiedzialnych elementów z użyciem technologii 4D. Ilustruje ponadto solidne podstawy do opracowywania programowalnych, jednomateriałowych, zmieniających kształt urządzeń, z potencjalnymi zastosowaniami w robotyce miękkiej, inżynierii biomedycznej oraz rozkładalnych strukturach i precyzyjnych mikromechanizmach.

Chapter 1

Foundation of Shape-Morphing Technologies: Advancements, Research Motivation, and Thesis Framework

This chapter provides a brief overview of additive manufacturing of shape-morphing structures and their diverse applications across various sectors. It outlines a step-by-step approach for achieving structures capable of shape transformation. The chapter then presents the motivation and objectives of the thesis, followed by its organization, offering a brief overview of each chapter.

1.1 An Overview of Advanced Manufacturing of Shape-Morphing Structures

Shape-morphing structures are smart devices, designed to adjust their configuration in reaction to external stimuli, enhancing their interaction with their surrounding environment. Such shape-adaptive devices are capable of executing pre-determined shape transformations to carry out a range of functions, from the simplest to the most complex tasks, specifically designed for their applications. Owing to their sensitivity to environmental changes and their adaptability, shape-morphing structures have significantly influenced various industrial sectors, including robotics, healthcare, architecture, interior design, automotive, aviation, and aerospace technology. In soft robotics, shape-morphing capabilities enable the creation of highly flexible and adaptive robots, capable of navigating complex environments and performing delicate tasks with precision. Deployable satellite systems, adaptive furniture, climate-reactive facades, aerodynamic blades for wind turbines, aircraft wings, minimally invasive surgical instruments, scaffolds for tissue engineering, and customizable implants are among the innovations benefiting from the incorporation of shape-morphing mechanisms or adaptive components made from diverse shape memory materials in soft robotics. Figure 1 illustrates various applications of shape-morphing structures [1–8].

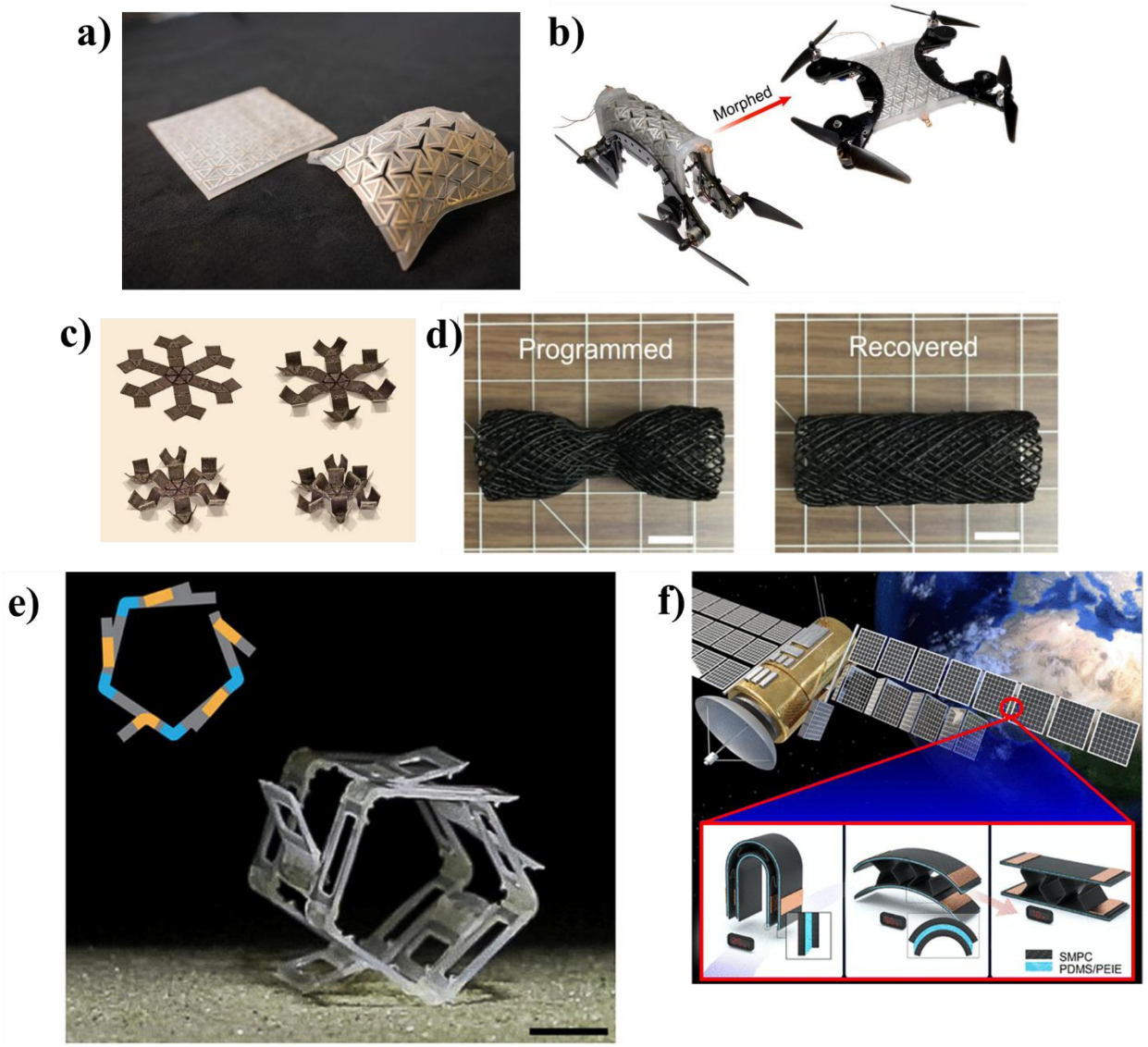

Figure 1. *Diverse applications of shape-morphing structures demonstrating transformative capabilities across different scales and functionalities : a) Flat vs. activated state of a geometrically patterned, shape-shifting structure [9]; b) A drone equipped with a shape-morphing component, demonstrated in static and morphed states [10]; c) Sequential demonstration of a shape-morphing structure, showcasing expansion upon thermal activation [11]; d) Shape-morphing composites with designed micro-architectures, highlighting its ability to recover its programmed shape [12]; e) Representation of a shape-changing architectural element, exhibiting its transformation capabilities [13]; f) A deployable structure in space engineering, illustrating its folded and unfolded states [1].*

The utilization of shape-morphing devices spans a wide array of applications, from large-scale implementations in buildings, vehicles, aircraft wings, and machinery to micro- and nano-scale manipulators for precision engineering tasks such as micro-transport systems [14], micro-grippers [15], micro-vascular devices [16], and micro-actuators [17,18].

An innovative approach for achieving precise control over movement in complex smart devices involves integrating a small-scale actuator directly within the structure. When triggered by a specific external stimulus, the micro-actuator generates a force that propagates through the device, enabling it to transform its configuration in a controlled, pre-programmed manner. This highlights the powerful potential of shape-morphing technologies in advancing soft robotics and adaptive systems [19].

To develop intelligent devices with complex shapes and shape-morphing properties that can execute predefined tasks within specific environments, several critical factors must be addressed:

a) Selecting an appropriate smart material capable of shape transformation in response to a stimulus;

b) Choosing a suitable stimulus to activate the material and device, depending on the intended application and material;

c) Investigating and understanding the material's mechanical behavior and transformability in response to the chosen stimulus;

d) Designing the devices to optimize their functionality for their intended tasks, considering their investigated properties;

e) Selecting a manufacturing process that aligns with the chosen material, design, shape complexity, and final application requirements [20].

Among the various smart materials capable of transformative shape changes, Shape Memory Polymers (SMPs) are particularly notable. These materials possess the remarkable property of "remembering" an original shape and recovering it when exposed to specific stimuli [21].

This characteristic meets the essential criteria for the creation of intelligent devices with adaptable structures. Furthermore, the advancement of additive manufacturing (AM) technology, commonly known as the 3D printing method, has revolutionized the production process, enabling precise, rapid, cost-effective, and waste-minimizing product fabrication. The latest innovation in AM is the 4D printing method. This technique employs smart materials such as SMPs to construct objects that can change their shape dynamically over time. 4D printing facilitates the creation of soft actuation devices, which could be useful in many applications, including soft robotics, deployable structures, and biomedical devices [22].

1.2 Thesis Motivation and Objectives

1.2.1 Motivation

The primary motivation of this thesis is to investigate the thermomechanical behavior of a thermo-responsive SMP and to utilize its shape memory and shape-shifting capabilities through innovative design and precision manufacturing. By integrating SMPs with AM, specifically in the context of 4D printing, this work aims to develop complex, adaptive structures capable of responding to environmental stimuli.

In this study, a shape memory epoxy is employed in stereolithography (SLA), a high-resolution 3D printing technique, to enable the one-step fabrication of monolithic, non-assembled, shape-morphing devices. These devices assure the controlled deformation and motion through the integration of compliant joints and kinematic chains within their structural design. The integration of material behavior with structural design offers a simplified yet powerful approach for creating smart systems, particularly well-suited to applications in soft robotics and microscale adaptive mechanisms.

A comprehensive investigation of the thermomechanical behavior of the shape memory polymer is essential before designing and manufacturing these devices. For instance, the extent of thermal expansion, shape recovery during the shape memory cycle, and the mechanical behavior of the material all highlight the importance of a comprehensive material characterization to optimize the design and application of shape memory materials. Conducting thermomechanical analysis and quantifying the shape memory behavior of thermo-responsive shape memory epoxy can help identifying potential challenges and confirm the suitability of the material for the intended structural design. This is crucial for assessing how these properties interact with specific designs, particularly for small-scale, fine-detailed, intricate, and delicate components.

Additionally, due to the inherent anisotropy of the SLA printing process, where structures are formed layer-by-layer, build orientation plays a critical role in determination of the final properties and functionality of printed components. Thus, this study also investigates how build orientation affects the mechanical and shape memory performance of SLA-printed SMP parts, further informing design considerations for real-world applications.

In addition, this thesis benefited from international collaboration. The author is grateful for the support provided by the 14th call of the KMM-VIN research fellowship programme. This

support enabled the collaborative project titled *"Investigation, Modeling, and Processing of Shape-Memory Polymers for Smart Micro-Actuators"* between the Institute of Fundamental Technological Research, Polish Academy of Sciences, and the Polytechnic University of Madrid (UPM). It also supported a research stay of the author at UPM, where part of the work was carried out at the Product Development Laboratory in the Mechanical Engineering Department, with contributions from colleagues in CAD design and 3D printing tasks. These collaborations not only facilitated technical progress but also enriched the international scope and context of the doctoral research.

1.2.2 Objectives

1- Preliminary investigation of the thermomechanical behavior and FDM 3D printability of thermoplastic shape memory polyurethane (PU-SMP)

- Evaluate the mechanical, thermal, and microstructural behavior under uniaxial tensile loading.
- Develop a protocol to calculate shape fixity and shape recovery in a thermomechanical cycling.
- Investigate the fused deposition modeling (FDM) 3D printability of recycled PU-SMP filament, focusing on shape memory performance and structural integrity of printed parts.

2- Comprehensive investigation of SLA 3D-printed thermoset shape memory epoxy (SMEp), focusing on the influence of build orientation on the thermomechanical behavior of printed specimens.

- Evaluate the influence of printing orientation on the surface morphology, microstructure, interlayer bonding, and thermal transitions.
- Assess anisotropic dimensional stability under water exposure and temperature cycling.
- Analyze mechanical performance and fracture behavior.
- Quantify shape fixity and shape recovery across different build orientations using thermomechanical cycling.

3- Design, fabrication, and training of monolithic SLA 4D-printed shape-morphing prototypes using SMEp

- Develop functional smart structures by integrating compliant joints and kinematic mechanisms within single-material designs.
- Employ high-resolution SLA 3D printing to fabricate monolithic, assembly-free prototypes incorporating localized actuation points.
- Validate localized shape memory activation using thermal cycling and thermal imaging techniques.
- Quantify deformation and recovery behavior using geometrical parameters in multiple prototype configurations.

1.3 Thesis Organization

This thesis begins with an introduction to the field of 4D printing for shape-morphing structures, emphasizing the importance of material behavior, structural design, and advanced manufacturing methods.

Chapter 1 outlines the motivation behind the study, defines the objectives, and provides an overview of the thesis structure.

Chapter 2 provides the background and literature review, beginning with an overview of SMPs and the characterization of their shape memory behavior. It then explores AM techniques, particularly those suited for processing SMPs, and reviews recent advancements in 4D printing of shape-adaptive structures. The chapter concludes by identifying key research challenges and gaps in the current state of the art.

Chapter 3 details the materials and methods used throughout the study. It includes preliminary investigations on thermoplastic PU-SMP and its printability, followed by a transition to SLA 3D printing using SMEp. This chapter outlines the full sequence of experimental procedures, from specimen fabrication and testing to the development and training of shape-morphing prototypes.

The experimental results and discussions are presented in three dedicated chapters.

Chapter 4 focuses on the thermomechanical behavior of PU-SMPs. A systematic protocol is developed to quantify shape fixity and shape recovery under controlled thermomechanical cycles. Mechanical, thermal, and microstructural properties are also examined in detail.

Chapter 5 addresses the transition to thermoset SMEp due to challenges with FDM 3D-printing and the thermal limitations of PU-SMP. This chapter centers on a detailed investigation of the thermomechanical performance of SMEp processed via SLA 3D printing. Specifically, two types of specimens were printed from different build surfaces, resulting in variations in the number and surface area of printed layers. This approach allowed for a systematic evaluation of how printing orientation influences thermal expansion, mechanical behavior, shape memory properties, and microstructural integrity. By comparing the two build strategies, the study reveals how anisotropy introduced during printing affects the overall performance of SLA-printed shape memory structures.

Chapter 6 discusses the design and fabrication of monolithic 4D-printed devices by integrating compliant joints into kinematic chain mechanisms. This chapter presents the 4D printing process, thermomechanical training, and evaluation of shape-morphing performance in various prototype designs.

Chapter 7 summarizes the main findings of the study as conclusion.

Thesis includes a **REFERENCES** section with cited publications throughout the thesis.

Chapter 2

Background of 4D Printing of Shape-morphing Structures: From Material to Design and Manufacturing

This chapter provides a comprehensive background and literature review on shape memory polymers, highlighting their functionality in comparison to conventional polymers. It also discusses experimental methods for quantifying shape memory parameters through thermomechanical cycling. The chapter then continues with a detailed explanation of AM steps and methods, introducing the concept of 4D printing of shape-morphing structures and their wide-ranging applications in soft robotics and shape-adaptive devices. Finally, the chapter outlines the current challenges and research gaps in 4D printing and the training of shape-morphing structures for practical applications, gaps that this thesis aims to address.

2.1 Shape Memory Polymer

SMPs are a unique class of smart stimulus-responsive materials that have attracted significant attention in material science. These polymers are known for their ability to undergo significant and reversible physical transformations, enabling them to be deformed and fixed into a temporary shape, and then recover their original shape when exposed to an external stimulus to complete a shape memory cycle. The choice of an external stimulus to activate SMPs depends on both the material's characteristics and its intended use, encompassing options such as heat, light, moisture, magnetic fields, or electric fields, each offering distinct advantages for specific applications.

The stimuli-responsive nature of SMPs has led to their application in various fields (Figure 2). In biomedical fields, they are used in devices like self-tying sutures and stents, adapting to body conditions and then transforming to fulfill a specific function [23–25]. In aerospace, SMPs are integral in developing morphing structures, such as wings, which change shape in response to environmental factors, enhancing aerodynamic performance. Their lightweight, high shape reconfiguration, recovery force, and good manufacturability make them ideal for these applications [26]. They are particularly useful in engineering fields where adaptability and responsiveness are

crucial. Additionally, in smart textiles, SMPs adjust properties like porosity in response to temperature variations. Their use in everyday consumer products, such as self-fitting and adaptive clothing, also demonstrates their versatility [27]. Another significant application is in shape-morphing technologies, where SMPs are used to create objects that can change their shape dynamically, offering innovative solutions in robotics and adaptive structures [3,28].

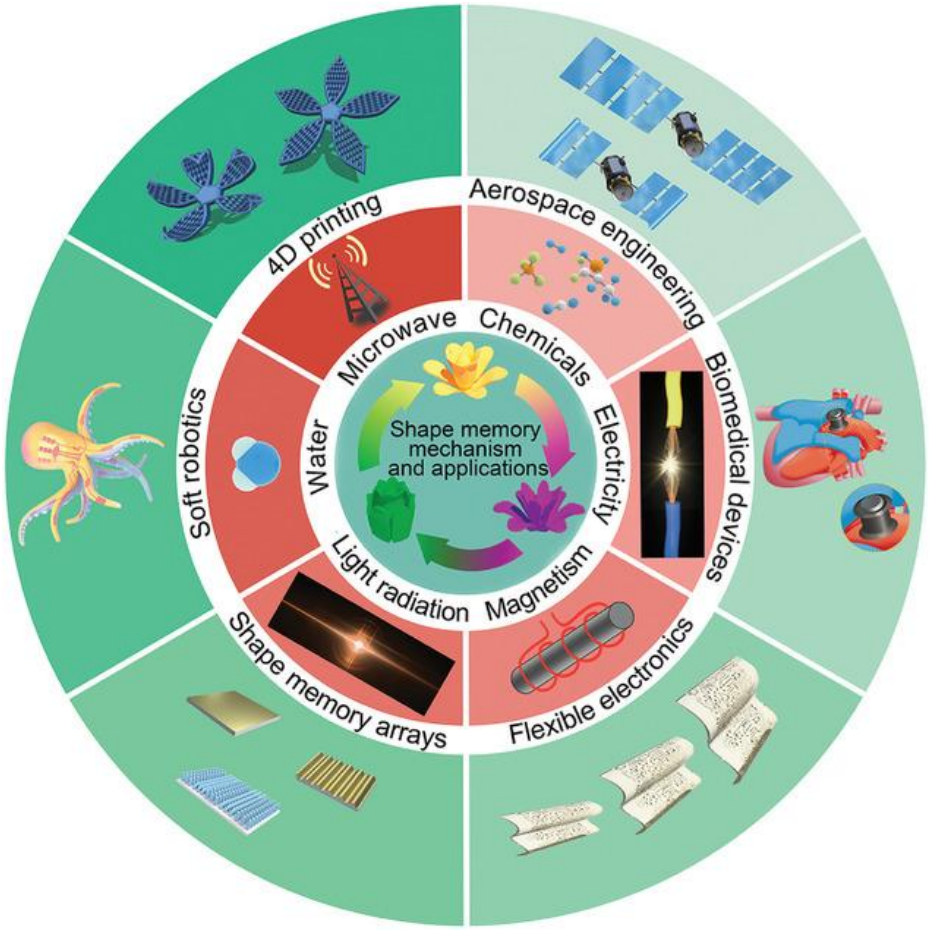

Figure 2. *Scheme of SMPs: mechanism, stimuli, and applications [29].*

Among different stimuli, the most commonly used one is heat, where the shape memory behavior is typically associated with thermal transitions, namely, glass transition temperature (T_g) of the polymer. Therefore, thermo-responsive SMPs, in particular, are designed to respond to changes in temperature. When heated to a certain threshold, SMPs soften, allowing them to be easily deformed. Upon cooling, they retain this deformed shape. When reheated, they return to their original form (Figure 3). This temperature-dependent behavior is integral to their

functionality and is utilized in various applications, from self-healing materials to deployable structures in space [21,30–33].

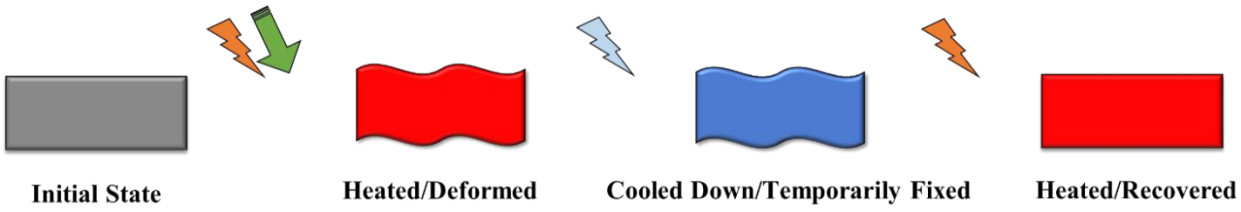

Figure 3. *Illustration of thermosensitive SMP exhibiting its shape memory behavior when subjected to changes in temperature.*

2.1.1 Shape Memory Polymers versus Conventional Polymers: Structural and Functional Differences

The shape memory effect is the ability of a SMP to return to its original shape from a deformed state when exposed to an appropriate external stimulus. Therefore, the main difference between a conventional polymer and a thermo-responsive SMP is primarily in their ability to respond to heat and recover their original shape. This phenomenon largely lies in the specific arrangement and characteristics of SMP's molecular networks.

As shown in Figure 4, for a polymer to exhibit shape memory effect, two structural elements are needed: permanent net-points and reversible switching segments. In other words, SMPs are designed with a unique molecular structure that typically involves a combination of hard and soft segments. The hard segments or net points define the permanent shape, while the soft segments are responsible for the temporary shape and can be soften, deformed, fixed and recovered by increase and decrease of temperature with respect to an activation temperature. The net points establishing the permanent shape can be either physical or chemical. Physical net points might arise from hydrogen bonding, crystallization, Van der Waals forces, chain entanglements and block copolymer structure, while chemical net points might be covalent bonds. Chemical crosslinking at net points ensures that the deformation force applied to the polymer does not result in extensive chain slippage and that the macroscopic shape alteration is reversible. In contrast, switch segments are crucial for fixing the temporary shape and recovering the original shape, when subjected to an external stimulus.

Conversely, conventional polymers may not have such a distinct phase-separated structure. They are typically either thermoplastics, which soften upon heating and harden upon cooling without a defined temporary shape, or thermosets, which are cross-linked polymers that do not soften upon reheating. These polymers lack the specific molecular architecture that enables the shape memory effect. Their structure is more uniform and does not facilitate the reversible change between a fixed and a temporary shape [34].

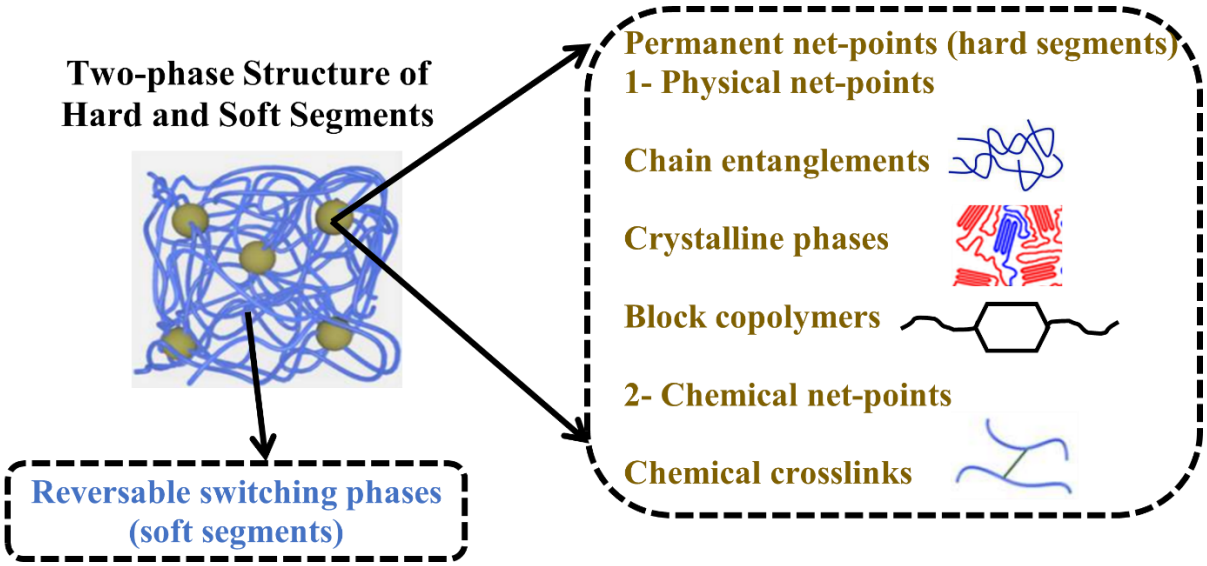

Figure 4. *Structural requirements for shape memory behavior.*

2.1.2 Thermo-responsive SMPs Behavior in a Thermomechanical Cycle

A thermo-responsive SMP can be activated thermally by raising the surrounding temperature above its transition temperature, namely T_g through direct or indirect heating. The shape memory behavior of a SMP is primarily an entropic event. Figure 5 illustrates a conceptual representation of the macroscopical (in the middle) and molecular process behind a thermally triggered SMP. In the original configuration (Figure 5a), the SMP chains are at their maximum entropic state, arranged in a random coil configuration. Upon heating these chains above their T_g (Figure 5b), chain movement is enabled, allowing them to be easily deformed into a temporary configuration, leading to a reduced entropic state (Figure 5c). To fix the polymer in this lower state of entropy, the SMP is cooled while under a fixed load below its T_g, effectively immobilizing the polymer's molecular chains (Figure 5d). Afterwards, the mechanical force is removed, and the polymer chains lack the necessary energy to revert the deformation and the temporary shape

remains fixed (Figure 5e). When the SMP is reheated above T_g, the mobility of the molecular chains is restored, causing the chains to experience entropic recovery and revert to their random coil pattern (Figure 5f).

Overall, the shape-memory characteristic is not tied to an inherent material property, indicating that the effect emerges from a mix of appropriate molecular polymer network design and a specific shaping process [21,33,35,36].

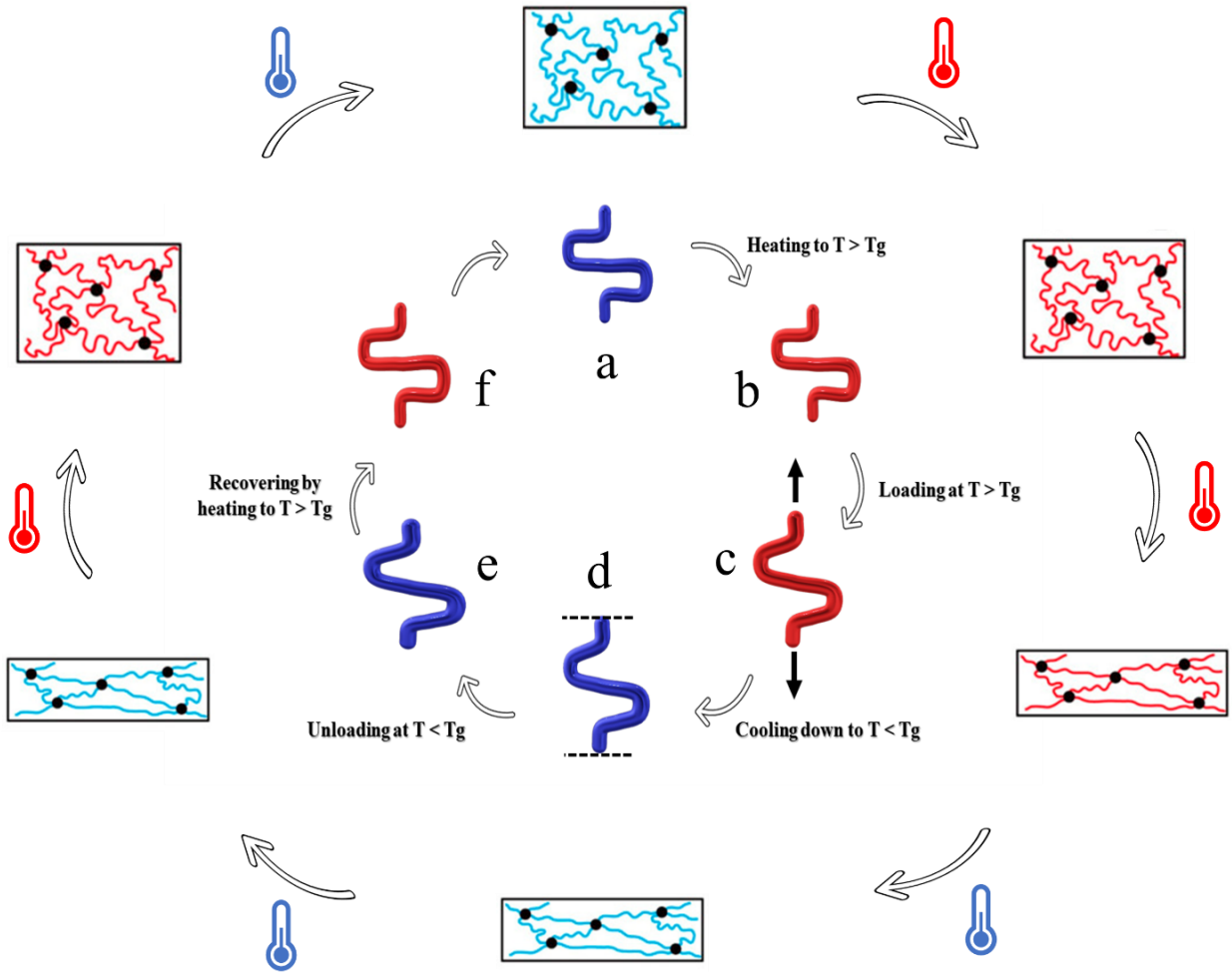

Figure 5. *Schematic of the macroscopical (in the middle) and microscopical process of shape memory behaviour of an SMP object in a shape memory cycle: a) original state of the SMP; b) SMP heated to temperature T> T_g; c) SMP loaded at T > T_g; d) SMP cooled down to T < T_g while keeping the strain; e) SMP unloaded at T < T_g; f) the thermally recovered SMP after being heated to T > T_g.*

2.1.3 Thermoset and Thermoplastic Networks of Thermo-responsive SMPs

Among thermo-responsive SMPs, thermoset and thermoplastic SMPs are particularly distinguished (Figure 6). Thermoset SMPs can be created through chemical crosslinking of linear or branched polymers. The shape memory and mechanical behavior in crosslinked thermoset SMPs is influenced by crosslink density. One type of thermoset SMP is the "amorphous" thermoset network, characterized by a distinct T_g. Above T_g, these amorphous thermoset SMPs exhibit rubbery elasticity due to the presence of covalent crosslinks.

One widely known example of an amorphous thermoset network is epoxy. Epoxies are formed by curing epoxy resins to create a densely crosslinked, amorphous polymer network that lacks a regular crystalline structure. While epoxies are valued for their robustness, rigidity, and chemical resistance, they are not inherently shape memory polymers. However, epoxies can be engineered to exhibit shape memory behavior, resulting in what is known as shape memory epoxies.

To enable shape memory functionality in epoxies, several key factors must be carefully controlled:

- *Crosslink density:* must be optimized to be moderate, sufficiently high to ensure mechanical stability but low enough to allow reversible deformation and elastic energy storage.
- T_g*:* must be tunable to define the switching temperature between the temporary and original shapes.
- *Network flexibility:* often enhanced by incorporating flexible molecular segments into the backbone to promote large, reversible strains.

The shape memory effect in SMEps is primarily driven by the T_g. Above T_g, the material enters a soft, rubbery state where it can be deformed into a temporary shape; upon cooling below T_g, this shape is fixed. Reheating above T_g allows recovery of the original configuration.

Importantly, both the mechanical performance and the degree of shape recovery in SMEps can be precisely adjusted by modifying formulation and curing conditions. This tunability makes shape memory epoxies highly attractive for applications that demand a combination of durability, high performance, and stimulus-responsive behavior [37].

Another type of thermoset SMP is the “semi-crystalline” thermoset network with a transition temperature equal to the melting temperature (T_m). the modulus of semicrystalline thermoset SMPs are dependent on crystallinity rather than their degree of crosslinking.

Thermoplastic SMPs, are notable for their reprocessability. Polyurethane shape memory polymers (PU-SMPs) as amorphous thermoplastic with $T_{transition} = T_g$ are block co-polymers composed of hard and soft segments that create their unique properties. The hard segments, formed by the reaction of diisocyanates with short-chain diols or diamines, create rigid domains that act as physical crosslinks or netpoints, defining the permanent shape through strong molecular interactions like hydrogen bonding. In contrast, soft segments are usually made of an amorphous polyol, like polyester or polyether. The length of soft segments and the content of hard segments significantly influence SMP performance. Optimal shape memory properties are achieved with 35-40 wt% hard segment content in the PU-SMP. The activation of shape-memory behavior in amorphous thermoplastic SMPs is attributed to the T_g of the soft segments [38].

Thermoplastic SMPs with $T_{transition} = T_m$ have a structure similar to those with $T_{transition} = T_g$, but the soft segment crystallizes upon elongation, making T_m the transition temperature. High crystallinity of the soft segment is essential for exhibiting shape memory behavior in crystalline thermoplastic SMPs [36].

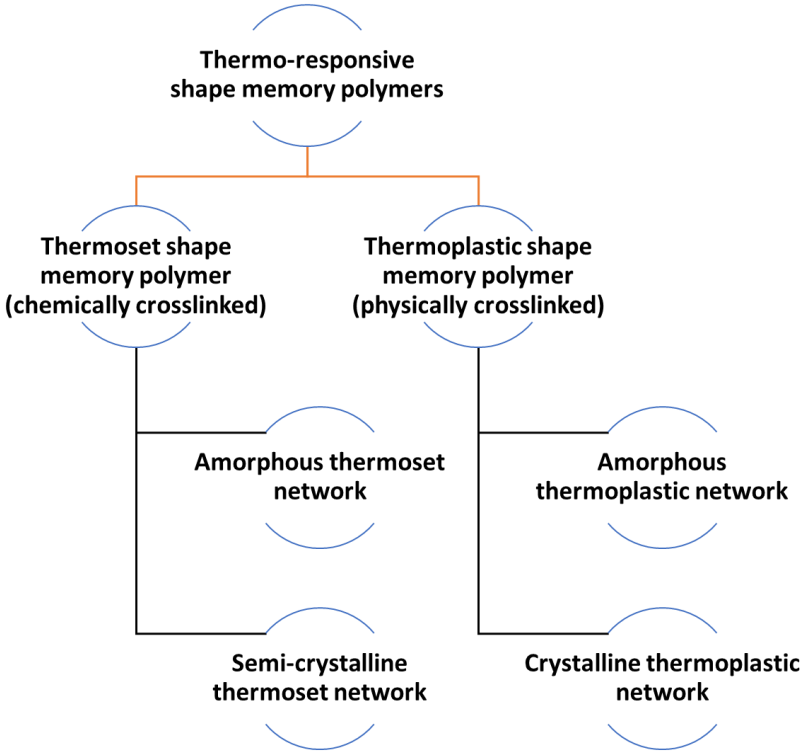

Figure 6. *Classification of thermo-responsive shape memory polymers.*

2.1.4 Quantification of Shape Memory Behavior in a Thermomechanical Cycle: Shape Fixity and Shape Recovery

Quantifying shape memory behavior within a thermomechanical cycle is crucial for predicting the performance of materials in their intended applications. This predictive capability is essential to avoid failure and select the most suitable SMP for a desired design and application. Two key parameters to quantify shape memory behavior are “shape fixity” and “shape recovery”.

Shape fixity refers to the ability of the SMP to fix a temporarily deformed shape. It quantifies the extent to which the material can retain a deformed shape upon unloading at a temperature below T_g. The temporary shape is fixed by the vitrification mechanism and storing strain energy of the polymer chains upon the fast cooling. Shape fixity measures the ability of the material to memorize a temporary shape, which is crucial for applications requiring the material to hold a specific form before activation. Shape recovery is the ability of SMP to return to its original shape upon exposure to heat. During the recovery, the stored strain energy is gradually released as the temperature approaches T_g of the SMP. Shape recovery quantifies the material’s ability to recover its original shape from the temporary shape. This property is fundamental for the functionality of shape memory materials in applications such as actuators, self-healing materials, and deployable structures. The quantification of these properties in a thermomechanical cycle involves cyclic loading and unloading tests, combined with thermal cycling. Figure 7 illustrates a schematic of the stress-strain behavior of a thermores-ponsive SMP in a strain-controlled thermomechanical program, enabling the quantification of shape fixity and shape recovery. Step 1 represents the loading of the SMP at a temperature above its T_g. In Step 2, stress increases as the SMP is cooled to a temperature below T_g while maintaining a fixed strain. Subsequently, in Step 3, the SMP is unloaded to zero force at a temperature below T_g. Finally, in Step 4, the SMP recovers its original shape upon reheating to a temperature above T_g. The shape fixity can be calculated by measuring the deformation after unloading at a low temperature below T_g (see Figure 5e) and comparing it to the initial deformation (see Figure 5a). The shape recovery is determined by measuring the deformation after heating above T_g (see Figure 5f) and comparing it to the deformation before heating (see Figure 5e).

Therefore, the extent of shape memory behavior in thermo-responsive SMP and its shape memory parameters can be quantified through experimental data derived from a comprehensive thermomechanical cycling program that includes sequential steps of heating, loading, cooling,

unloading, and recovery. However, each phase in this cycle is critical, as it establishes specific conditions for the material's shape memory performance. During the test, several parameters must be carefully controlled to achieve accurate and reproducible results, including heating temperature, recovery temperature, heating rate, thermal expansion properties of the SMP, cooling rate and strain rate. Variability in any of these factors can impact the accuracy and reliability of the measured shape memory parameters [33,39–43].

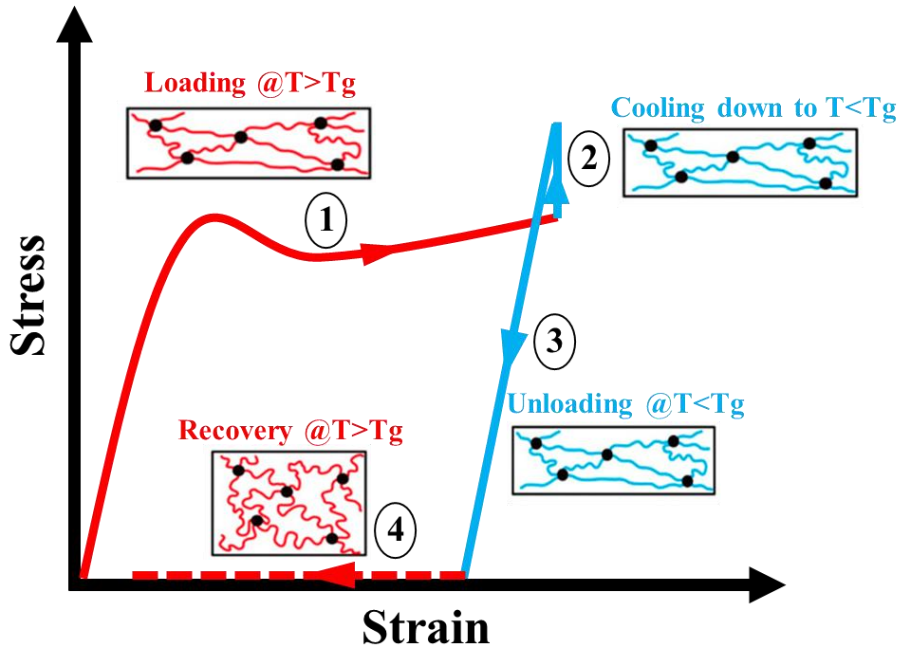

Figure 7. *A schematic of the stress-strain behavior of a thermo-responsive SMP in a strain-controlled thermomechanical program.*

2.2 Additive Manufacturing

Manufacturing complex-shaped polymeric parts using traditional methods proves to be time-intensive, often resulting in lower dimensional accuracy, and necessitates extensive post-processing and assembly efforts. However, these challenges can be significantly reduced by AM technologies, commonly known as 3D printing. The main principle that distinguishes AM from traditional manufacturing methods is that it constructs objects through a layer-by-layer 3D printing process, depositing material one layer at a time, based on a digital model. Each layer is deposited, cured, or solidified before the next layer is added directly on top, with the process repeating until

the object is fully formed. This method allows for the creation of complex geometries and structures that would be difficult or impossible to achieve with traditional manufacturing methods. The layer-by-layer approach provides a high degree of design flexibility, making it ideal for prototyping, customized manufacturing, and producing intricate components. AM technologies facilitate the direct construction of detailed designed objects with sophisticated geometries from a digital computer-aided design (CAD) file in a singular step. 3D printing offers significant potential in lowering manufacturing expenses and decreasing production timelines, particularly for objects and components with intricate designs that utilize various materials. This technology enables a decrease in the number of separate parts required, leads to lighter overall product weight, and enhances the ability to customize the final product [44–48].

2.2.1 Additive Manufacturing Steps

Figure 8 illustrates the process of 3D printing from the initial design phase to the final physical object.

1- *3D CAD File:* The process begins with a 3D model created on a CAD software. This model is typically saved in the .STL file format, which is a widely used format for 3D printing because it contains the surface geometry of the modeled object.

2- *Slicing:* The next step involves slicing the 3D model into layers. This is done using a specific software, which converts the 3D model into a series of thin layers and produces a ".GCODE" file. The ".GCODE" file format contains instructions for the 3D printer, such as the movement of the print head and the amount of required material. This slicing process is crucial as it determines the resolution and accuracy of the final printed object. The more layers there are, the higher the resolution and level of detail that can be achieved.

3- *3D Printing:* In this step, the 3D printer uses the ".GCODE" file to print the object layer by layer. The illustration shows a simplified representation of a 3D printer with the print head depositing material onto a build platform to create each layer. Over time, these layers build up to form the final object.

4- *Final Physical Object:* The last image shows the final, physical object that has been produced by the 3D printer. The object appears to be a solid pyramid, indicating that the printing process has been completed [49].

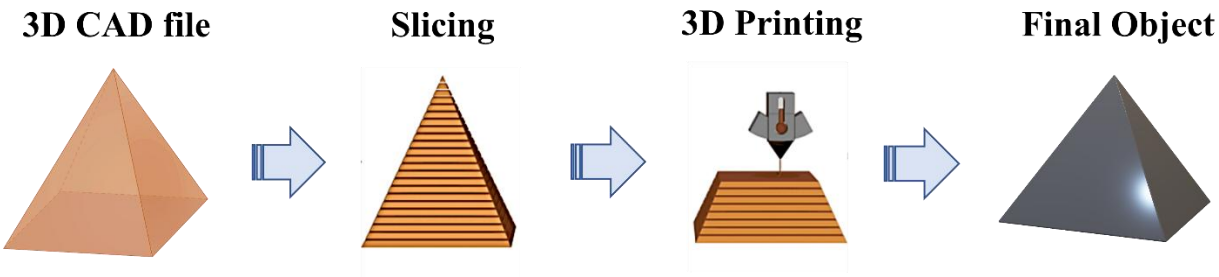

Figure 8. *Sequential workflow of the 3D printing process from design to realization* [50].

2.2.2 Different Additive Manufacturing Methods, Applications and Challenges

3D printing, encompasses a diverse range of processes, each designed to fabricate objects with specific characteristics suited to their intended geometry and applications. The selection of an appropriate AM technique depends on the functional requirements of the final product, including its mechanical properties, resolution, and aesthetic quality. This decision is further influenced by the compatibility of materials available for each method, such as polymers, composites, or ceramics, to optimize process performance and product quality. To provide a standardized framework, the ISO/ASTM 52900 standard classifies AM technologies into seven distinct process categories, based on how material is deposited and solidified layer-by-layer (Figure 9) [51]:

1. Material Extrusion
2. VAT Photopolymerization
3. Material Jetting
4. Sheet Lamination
5. Powder Bed Fusion
6. Directed Energy Deposition (DED)
7. Binder Jetting

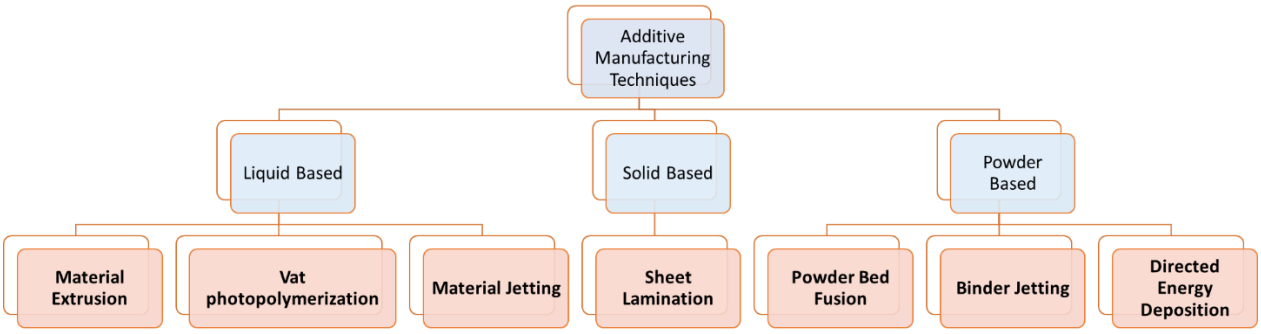

Figure 9. *Classification of additive manufacturing techniques according to ISO/ASTM 52900, grouped by material form.*

Each category comprises specific techniques and systems, with varying material compatibility, resolution, mechanical properties, and application potential. In the context of SMP fabrication and 4D printing, which will be discussed later and are the focus of this study, the most relevant categories are:

- **VAT photopolymerization**, which includes stereolithography (SLA) and digital light processing (DLP), is based on the selective curing of liquid photopolymer resins using a light source (laser or projector). This method is ideal for fabricating thermoset SMPs due to its high precision, excellent surface quality, and the ability to control crosslink density during polymerization [52].
- **Material extrusion**, particularly fused filament fabrication (FFF) or Fused Deposition Modeling (FDM), is based on the controlled deposition of molten thermoplastic filament through a heated nozzle to build parts layer by layer. This method supports thermoplastic SMPs with good repeatability, accessibility, and cost-effectiveness, making it widely used for prototyping and functional testing [53].
- **Powder bed fusion**, most notably selective laser sintering (SLS), involves the layer-by-layer sintering of powdered materials using a laser. Although less common for SMPs compared to VAT photopolymerization and extrusion-based methods, SLS has been applied to thermoplastic SMP powders to some extent, offering the advantage of producing complex geometries [54].

The following sections focus on the specific AM methods most commonly used for printing with SMPs, especially those that support shape adaptability through thermomechanical stimuli.

A) Material Extrusion, Fused Deposition Modeling (FDM)

FDM, also known as Melt Extrusion (Figure 10a), is the most accessible AM technique, favored for its affordability and versatility. The process involves the melting and precise extrusion of thermoplastic filament through a heated nozzle, layer by layer, to create the desired structure. In FDM systems, extrusion may be carried out using either a single nozzle (mono-extrusion), which deposits one type of filament at a time, or multiple nozzles (multi-extrusion), which enable the simultaneous printing of different filaments. Multi-extrusion offers greater design flexibility by allowing the combination of distinct materials, colors, or even functional phases (e.g., rigid and flexible polymers) within the same component, which is particularly advantageous in the context of 4D printing with SMPs. FDM allows for the use of various infill patterns, such as grid, honeycomb, or concentric designs (Figure 11a) and the size and spacing of these patterns (so-called fill density) significantly influence the resolution and properties of the printed part (Figure 11b). Smaller, tightly spaced patterns result in higher resolution and greater structural strength, while larger, more widely spaced patterns reduce material usage and weight but may compromise precision and durability. This flexibility makes FDM suitable for a wide range of functional and aesthetic requirements. Figure 11c illustrated an example of an FDM-printed part firstly right after 3D-printing (the left most), with a textured surface and the presence of support structures.
These supports must be carefully removed after printing, often leaving visible marks or imperfections on the surface, as seen in the center example. The rightmost part demonstrates a smoother finish achieved after support removal and additional post-processing, highlighting how the surface quality of FDM products can be enhanced with proper handling. However, FDM may not be the most suitable manufacturing method for producing intricate parts with fine details.

FDM supports a wide variety of materials, including standard polymers like polylactic acid (PLA) as well as advanced options like fiber-reinforced composites, metal-polymer blends, and ceramics.

FDM is widely applied across industries for rapid prototyping, functional part manufacturing, tooling, architectural modeling, and educational purposes. Its adaptability extends to specialized fields such as aerospace, where lightweight and durable parts are critical, and medicine, where FDM-produced components can be used for anatomical models and assistive devices [55–59].

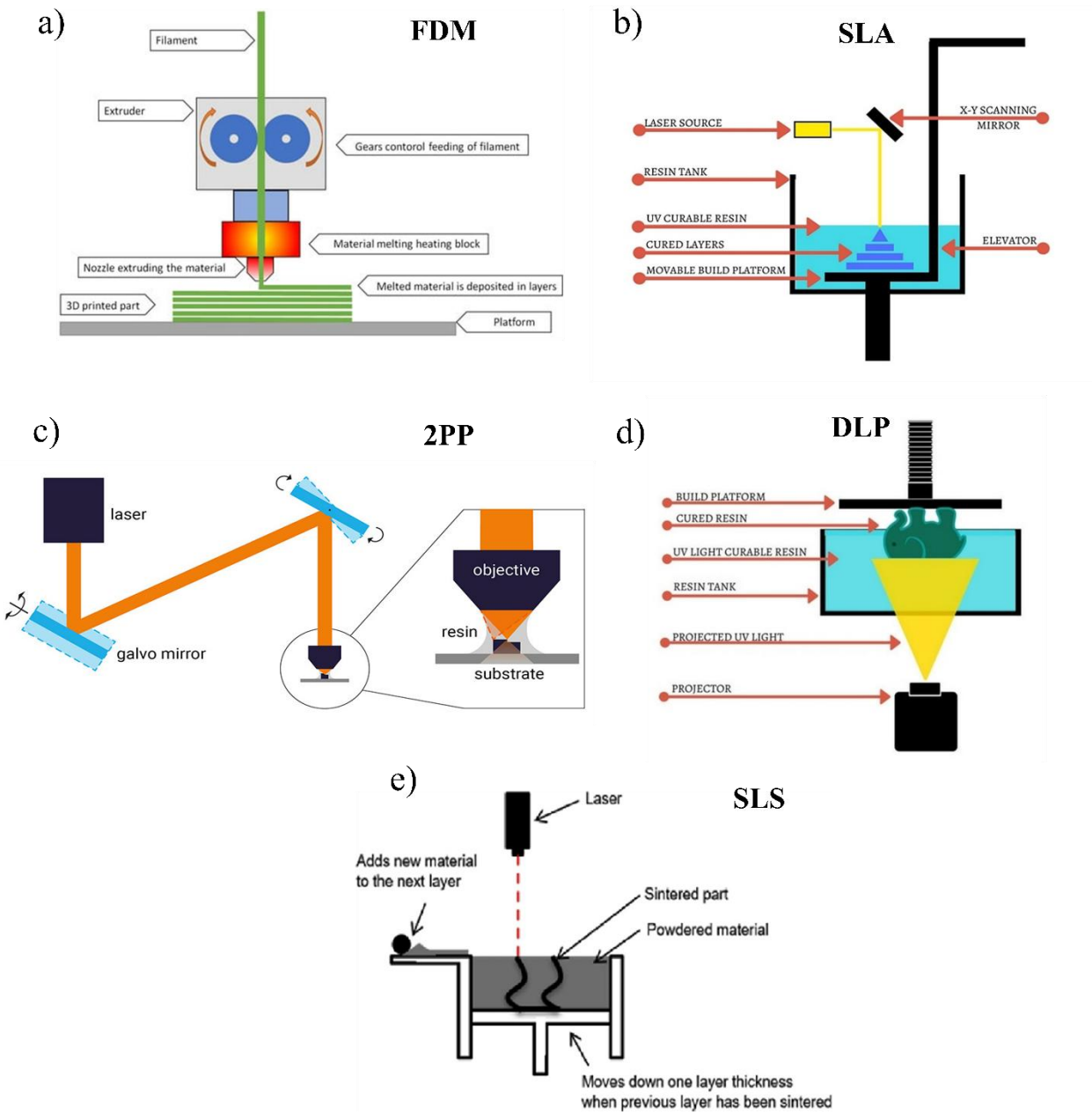

Figure 10. *Schematics of additive manufacturing methods commonly used for printing SMPs: a) FDM; b) SLA; c) 2PP; d) DLP; e) SLS* [60,61].

B) VAT Photopolymerization, Stereolithography (SLA)

SLA (Figure 10b) utilizes ultraviolet (UV) lasers to cure liquid photopolymer resins into solid structures, layer by layer, with remarkable precision. Unlike other 3D printing methods, SLA achieves its high level of detail by curing the resin point by point, following the design's exact coordinates. This process allows SLA to produce objects with intricate details, sharp edges, and

exceptionally smooth surface finishes, making it ideal for applications requiring aesthetic refinement and high resolution. SLA is particularly well-suited for creating prototypes, limited production runs, and items with complex geometries [62,63].

Recent improvements in SLA technology include enhanced precision, reduced printing times, and the availability of advanced resin formulations. For example, biocompatible resins have expanded the utility of SLA into the medical field, supporting applications such as dental aligners, surgical guides, and prosthetics. The method is also a preferred choice in industries like jewelry design and custom prototyping, where precision and surface quality are paramount. Figure 11d illustrates examples of SLA-printed products, showcasing their ability to achieve more intricate and complex geometries compared to FDM-printed prototypes [64–66].

The cured resin parts often require post-processing, such as cleaning in an isopropyl alcohol (IPA) bath and UV curing to ensure full polymerization and optimal mechanical properties. Additionally, the resins used in SLA are often more expensive than materials for other 3D printing methods, and their handling requires care due to their sensitivity to light and potential toxicity. Furthermore, SLA-printed parts are typically more brittle than those produced using FDM or SLS, which may limit their applications in functional or load-bearing scenarios. Despite these challenges, SLA remains a top choice for applications where precision and surface quality are critical.

Beyond conventional SLA, other VAT photopolymerization techniques have emerged. Micro-SLA enables the fabrication of microscale structures with exceptionally fine resolution, making it valuable for applications in microfluidics, biomedical devices, and micromechanical systems. Even more advanced, Two-Photon Polymerization (2PP) [67,68] allows true 3D structuring at the micro- and nano-scale by exploiting nonlinear light–matter interactions to induce localized polymerization. 2PP is particularly suited for creating highly detailed architectures, responsive microactuators, and nano-engineered SMP-based devices for next-generation 4D printing applications. Figure 10c shows the 2PP process, in which galvo scanners move the focal point within the focal plane at speeds of several hundred millimeters per second to enable fast and precise printing [61].

C) VAT Photopolymerization, Digital Light Processing (DLP)

DLP (Figure 10d) shares similarities with SLA in that it also uses photopolymer resins and UV light for printing. However, DLP differs in its approach to curing: instead of curing the resin

point by point as in SLA, DLP uses a digital light projector to illuminate and cure an entire layer at once. This layer-by-layer curing process allows DLP to achieve significantly faster printing speeds compared to SLA. Although DLP generally produces slightly lower resolution than SLA, it still delivers excellent surface quality, making it well-suited for applications requiring the rapid production of small to medium-sized objects (Figure 11e) [69,70].

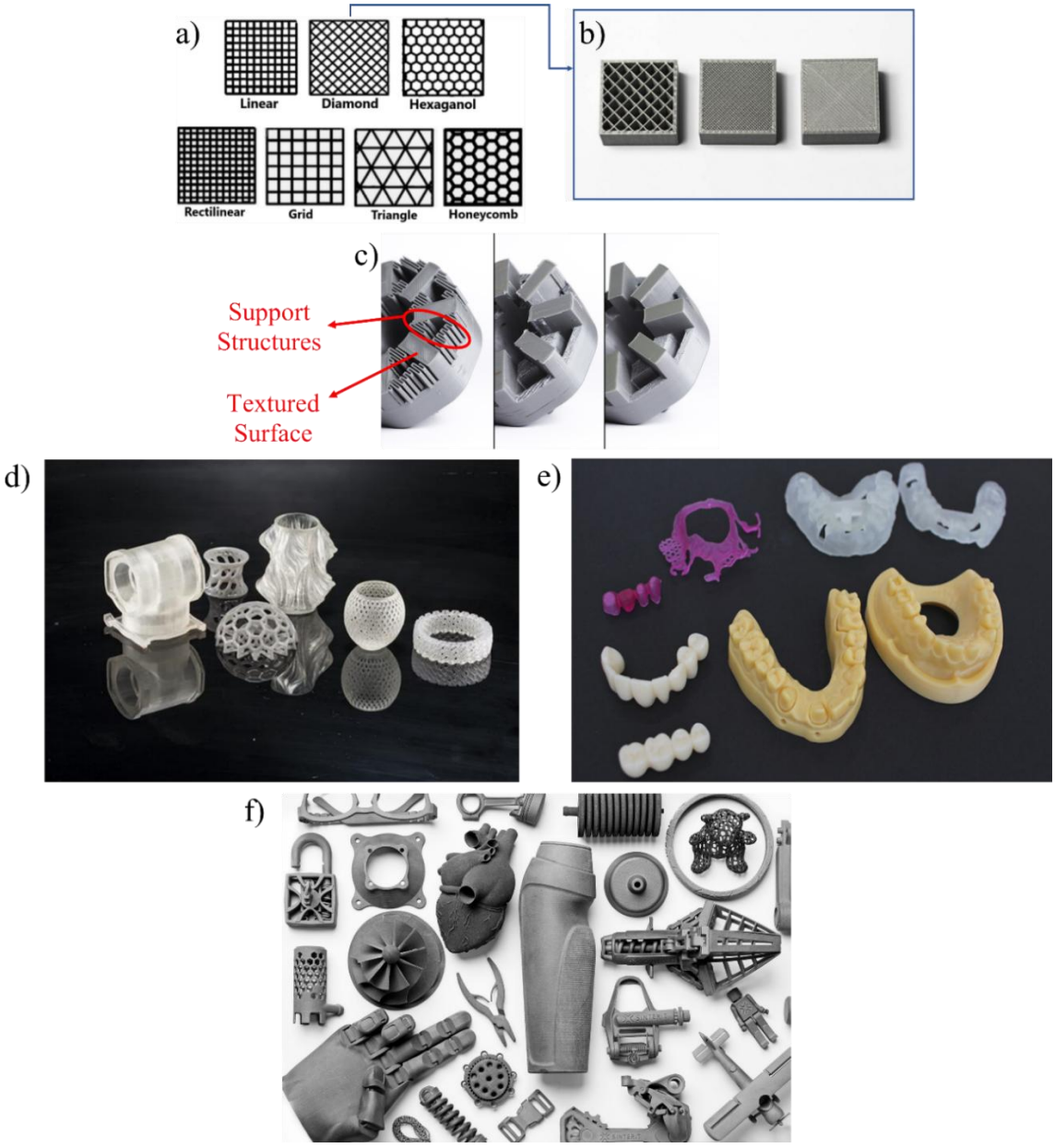

Figure 11. *a) Examples of infill patterns for FDM-printed parts; b) The internal geometry of FDM prints with different fill density; c) An example of FDM-printed part* [71]*; d) Examples of SLA-printed parts* [72]*; e) Examples of DLP-printed parts* [73]*; f) Examples of SLS- printed parts* [74].

D) Powder Bed Fusion, Selective Laser Sintering (SLS)

SLS is a highly versatile method suitable for creating complex geometries, including internal structures and interlocking components, which are challenging to achieve with other AM methods (Figure 10d). The process involves the sintering of powdered materials, such as polymers (e.g., nylon), metals, or ceramics, layer by layer using a laser. Unlike SLA and FDM, SLS does not require support structures, as unsintered powder provides inherent support during printing.

SLS accommodates a broad range of materials, enabling manufacturers to customize properties like strength, flexibility, and thermal resistance to specific needs. Although less common than VAT photopolymerization and extrusion-based approaches, SLS has also been used to process SMPs, particularly thermoplastic powders such as thermoplastic polyurethane (TPU), though its application remains limited compared to other AM techniques. Common applications of SLS include functional prototypes, end-use parts, and components for industries such as automotive, aerospace, and healthcare. While SLS generally results in a rougher surface finish than SLA or FDM, post-processing techniques can address this aspect to achieve desired aesthetics or functional characteristics. Additionally, managing and recycling the unsintered powder can add complexity and cost to the process. Furthermore, the equipment for SLS is typically more expensive than other AM methods, which may limit its accessibility for smaller-scale applications. Figure 11f represents examples of SLS-printed parts [75,76].

2.3 4D-printing of Shape-morphing Structures

2.3.1 Shape-morphing Structures

Shape-morphing structures, capable of adapting their geometry, configuration, or functionality in response to external stimuli, represent a transformative approach in modern engineering. These systems are at the forefront of innovation, addressing the growing demand for adaptable, efficient, and multifunctional devices in fields such as robotics, aerospace, and biomedical engineering. Developing such structures requires an understanding of both rigid-body and compliant mechanisms, as their integration forms the foundation of many shape-morphing designs. Rigid-body mechanisms, consisting of linkages, joints, gears, and cams, are a well-established field with standardized designs widely used in traditional manufacturing processes. Kinematic chains, a fundamental component of rigid-body mechanisms, are systems of

interconnected rigid links and joints designed to produce controlled motion with specific degrees of freedom. These chains are integral to many mechanical systems, such as robotic arms, four-bar linkages, and other systems requiring precise motion and force transmission. However, rigid-body mechanisms, including those based on kinematic chains, have notable limitations, including backlash, high assembly time and cost, frequent maintenance, wear, and added weight [77,78]. Compliant mechanisms are systems that derive their motion and force transmission from the elastic deformation of their components, eliminating the need for traditional rigid links, hinges, bearings, or sliders. By relying on strategically designed regions of flexibility, these mechanisms simplify design, reduce weight and multiple piece assembly, as well as increase reliability, enabling elastic deformation to perform specific motions or tasks [79–81]. Figure 12a and b illustrate the difference between two design approaches for achieving motion in mechanisms. On the left, the design employs rigid links connected by kinematic joints, which allow rotation at discrete points. On the right, the pin joints are replaced with compliant joints, which use the elastic flexibility of the material to enable motion without the need for discrete mechanical components. This compliant design eliminates the need for assembly of joints and reduces mechanical complexity while maintaining similar functionality through elastic deformation. Figure 12c represents a prototype of the compliant gripper in its inactive mode (left) and gripping mode (right).

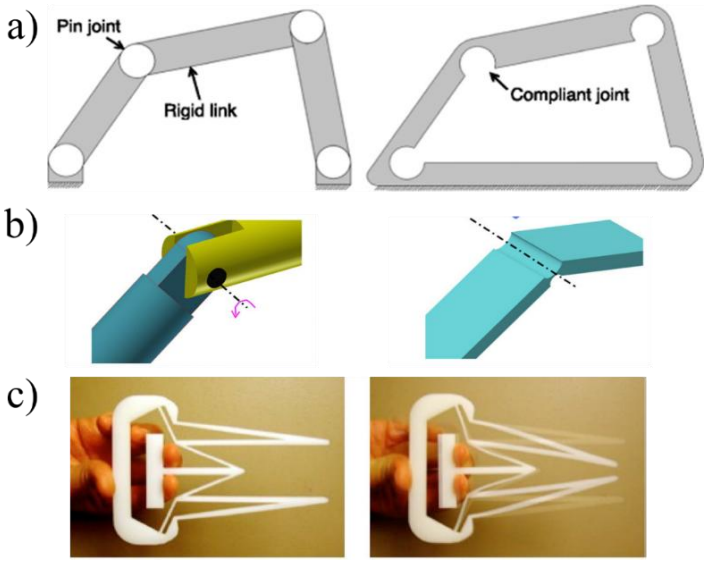

Figure 12. *a) The left design illustrates a rigid-body mechanism that achieves motion through kinematic pairs (pin joints), while the right design shows a compliant mechanism that relies on elastic deformation at the compliant joints to enable motion; b) Schematic representation of a kinematic joint (left) and a compliant joint (right); c) Prototype of a compliant gripper in its inactive mode (left) and gripping mode (right)* [82–84].

Shape-morphing structures can be based on the principles of kinematic chains and compliant mechanisms, designed to dynamically change their geometry, configuration, or shape in response to external stimuli such as temperature, light, magnetic fields, or mechanical forces. These structures combine flexibility and adaptability, allowing them to transition between configurations for specific tasks or environmental adaptability. A key subset of shape-morphing structures includes multistable structures, which can maintain stability in multiple distinct configurations without continuous external input. This multistability enables "snap" transitions between predefined shapes, enhancing functionality and efficiency in applications like deployable systems, reconfigurable robotics, and energy-efficient actuators [78,81].

Designing structures that adapt their shape in response to specific stimuli is a growing area of research with applications in robotics, aerospace, and biomedical devices. With an innovative design that combines rigid-body elements, compliant joints and mechanisms, and kinematic joints, it is possible to create a device capable of performing a predetermined deformational task. For example, Milojević *et al*. developed an adaptive compliant gripper finger with embedded actuators, allowing the gripper to morph its shape to accommodate various objects (Figure 13). This design enhances the gripper's versatility and adaptability in handling differently shaped and sized items [81].

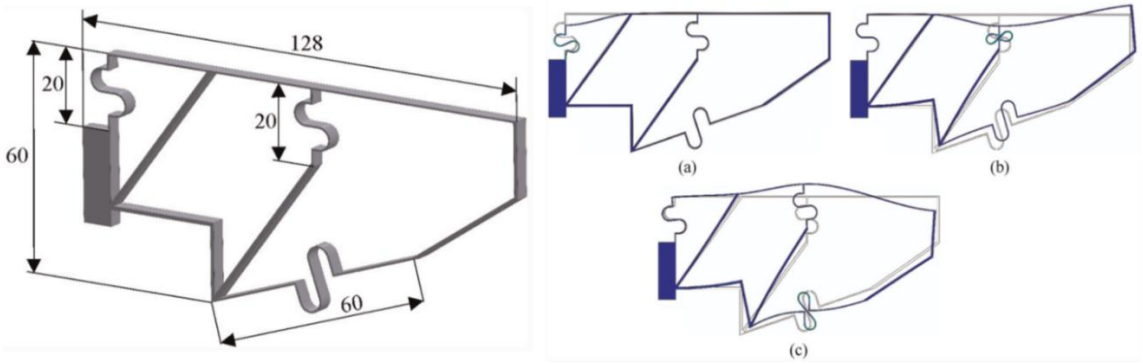

Figure 13. *Design of the adaptive shape-morphing compliant structure with embedded contracting actuators* [81].

2.3.2. Integration of Stimuli-Responsive Materials to Shape-morphing Structures

3D printing technology allows for the creation of complex geometries that were previously impossible or economically unfeasible with traditional manufacturing methods. A significant advancement in this field is the emergence of 4D printing, which extends the capabilities of 3D

printing by introducing time as the fourth dimension. This innovative approach incorporates smart shape memory materials in 3D-printing methods, leading to manufacturing complex shape-morphing devices that can change their shape or function in response to external stimuli. Unlike the static and inert objects typically produced through conventional 3D printing techniques (Figure 14a), 4D printed parts are dynamic and adaptive, capable of undergoing controlled transformations after fabrication (Figure 14b) [85–89].

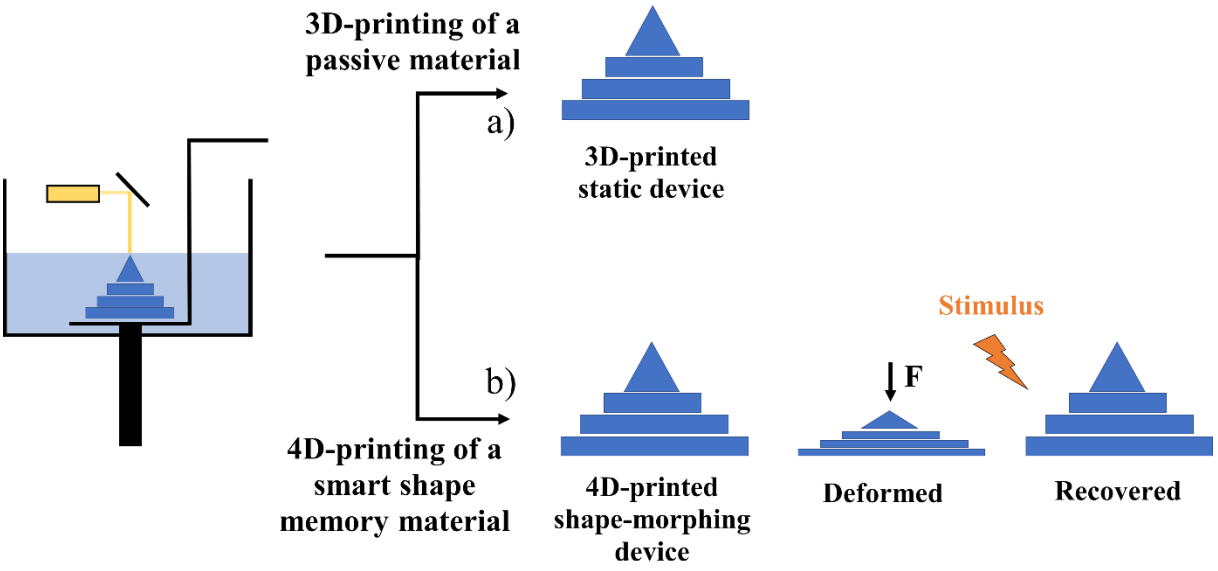

Figure 14. *Comparison between: a) 3D printing of a passive material leading to a static device; and b) 4D printing of a smart shape memory polymer resulting in a dynamic, shape-adaptive device responsive to external stimuli.*

Methods such as in situ polymerization and casting to a film have been extensively employed with shape memory polymers. However, as the complexity of shape-adaptive devices grows, the number of required manufacturing steps to finalize the device also increases. 4D printing provides an opportunity for additively manufacturing smart and complex shape-adaptive devices. The integration of smart materials into multistable structures enables more advanced functionalities and enhanced controllability in 4D printing. In fact, 4D printing of shape-morphing structures, using smart materials, has led to improvement in various technologies such as smart actuators, foldable robots, deployable structures, foldable electronics, shape-shifting antennas and biomedical devices [90–92].

The success of shape-morphing structures lies in the effective integration of advanced design techniques, smart materials, and AM technologies. By leveraging the capabilities of 4D printing, it becomes possible to create complex, shape-transformative prototypes that incorporate various motion features, such as kinematic and compliant joints, in a single manufacturing step. These self-assembling prototypes eliminate the need for post-manufacturing assembly, significantly simplifying production. However, the realization of such intricate shape-morphing objects requires exceptional precision and manufacturing accuracy. These challenges are effectively addressed by advanced additive photopolymerization techniques, particularly laser-based stereolithography, which ensures the high resolution and accuracy necessary for fabricating such innovative designs.

2.3.3 SLA 4D-printing of Complex Shapes and Adaptive Structures

SLA 3D printing method stands out for its ability to construct intricate objects with exceptional detail and precision. The process involves the selective UV polymerization of a photosensitive resin, achieved by exposing the resin's free surface to a laser beam. This laser, characterized by specific power and frequency parameters tailored to the resin's properties, scans the surface layer by layer, solidifying the liquid resin into the desired shape. During the curing process, SLA polymers undergo a viscosity increase, transforming into a gel-like resin before evolving into crosslinked polymers (see Figure 15). This crosslinking results in the formation of a strong structure that inhibits their return to a liquid state.

The key to SLA success in 4D printing lies in its compatibility with a wide range of resin materials, including those with shape memory properties. By carefully selecting a suitable SMP as the printing material, SLA can be used to create solid smart structures with shape memory properties. These materials can be deformed to a pre-defined shape by folding, bending, or twisting. This transformation is reversible, allowing the objects to return to their printed form by exposure to a pre-determined stimulus. Choong et al. [96] conducted a study on the shape adaptability of a 4D-printed, SMP-based buckyball with a complex geometry, created using the SLA method, as shown in Figure 16. They examined the thermo-sensitivity of the SMP in response to temperature variations both below and above the Tg when immersed in water. The 4D-printed buckyball transitioned from a flat plane to its original shape with great durability.

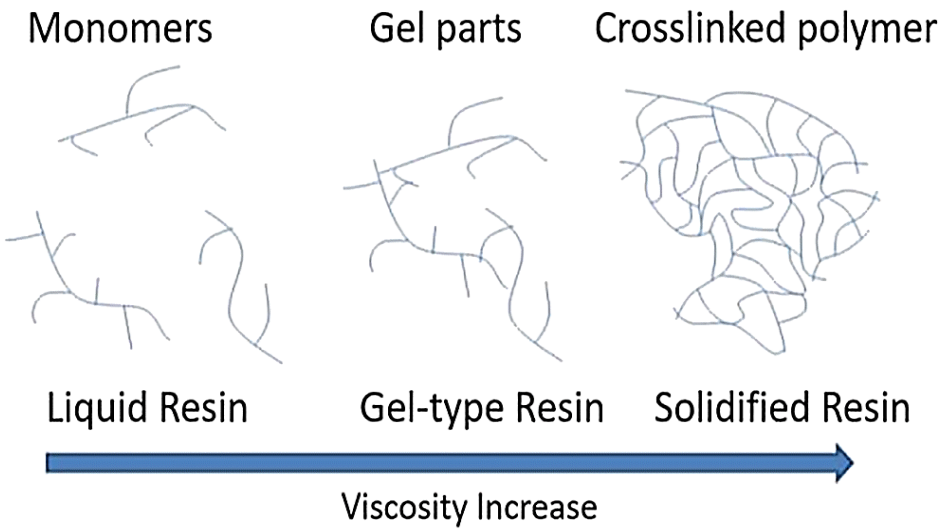

Figure 15. *Curing process in a photopolymer's structure* [93].

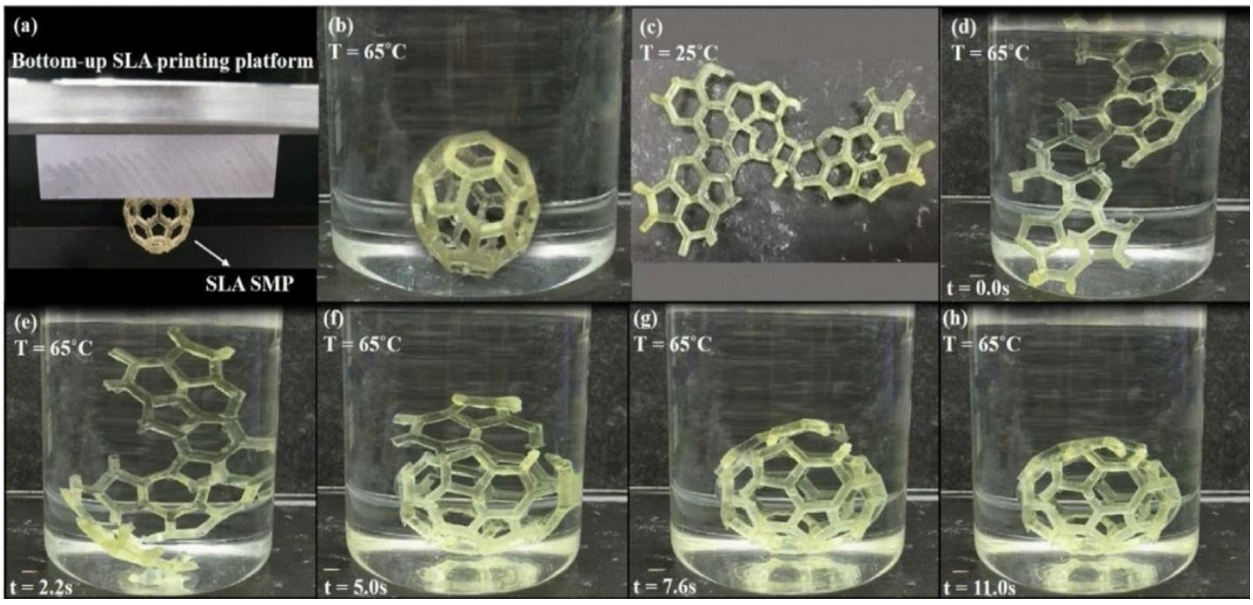

Figure 16. *a) SLA SMP C60 buckyball in printing; b-c) Unfolded after printing, and; d-h) Recovered its original buckyball shape by soaking at 65˚C of water* [94].

Ge *et al*. [95] employed a micro-SLA 3D printing technique along with photocurable methacrylate-based copolymer networks to fabricate micro grippers. These grippers demonstrated the capability to grasp and release objects, as shown in Figure 17.

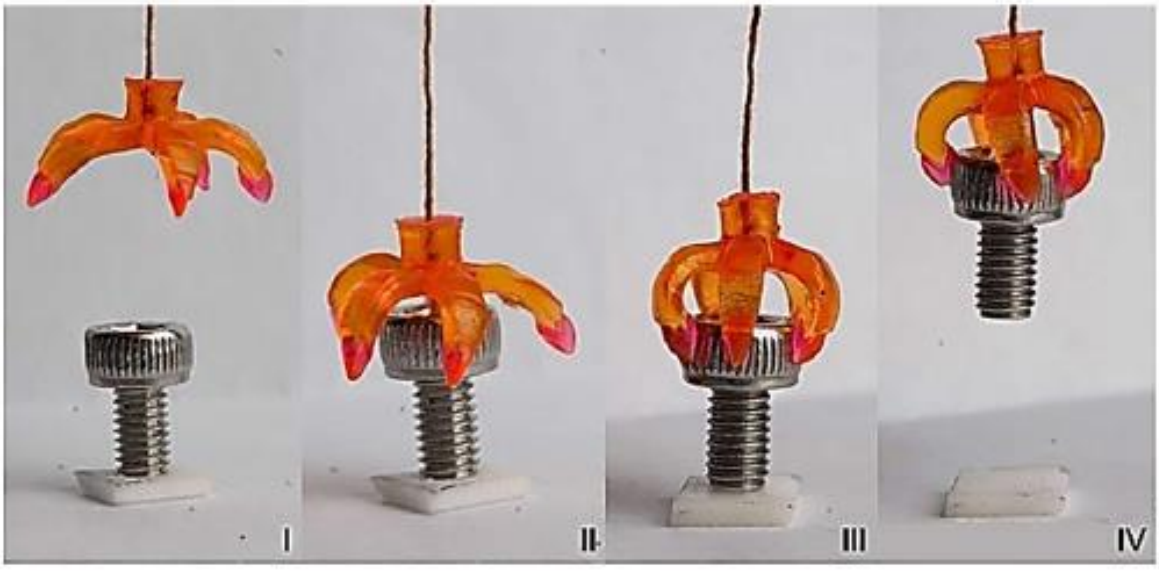

Figure 17. *4D printed SMP gripper that enables gripping and releasing of objects when thermally actuated* [95].

The most commonly used SMP resin in the SLA 3D-printing method is epoxy resin. Lantada *et al*. [16] showcased the manufacturing process of micro-vascular shape memory epoxy actuators with intricate geometrical designs. These micro-vascular devices can be designed with internal channels that resemble blood vessels, capable of transporting fluids and transforming their shape in response to the temperature of the fluid. These complex structures and 3D networks were directly designed and 4D-printed from CAD files using SLA manufacturing technology. Figure 18 demonstrates the shape memory behavior of the 4D-printed shape memory epoxy devices. The micro-claw closes, and the spring expands due to the heating effect of the injected water running through the micro-vasculatures.

Lantada *et al*. highlighted the critical role of design in 4D printing, showing that a thoughtful and precise design is as vital as the manufacturing technique, material, and stimulus for triggering. A precise and considered design is pivotal in manipulating the shape-adaptive system to demonstrate our intended pre-defined shape transformations effectively.

Balancing design and functionality is essential. For example, incorporating features like hinges, springs, grippers, spirals, hollow channels or folds can enhance the material's response to heat. These elements can move in a controlled manner, aligned with the material's phase transitions, enabling complex actions such as folding, bending, or curling. It is crucial to design the structure with an understanding of the material's properties and thermomechanical behaviors.

The thermal conductivity of polymers is generally low, making the heat-induced activation of SMPs a slow and often uneven process across the device. In their study, Lantada *et al*. avoided the need to incorporate micro or nanoparticles to facilitate induction heating. Instead, they employed a microvascular design technique to let the hot water pass through the structure, establishing direct contact between the SMP and the heat source for a more effective activation.

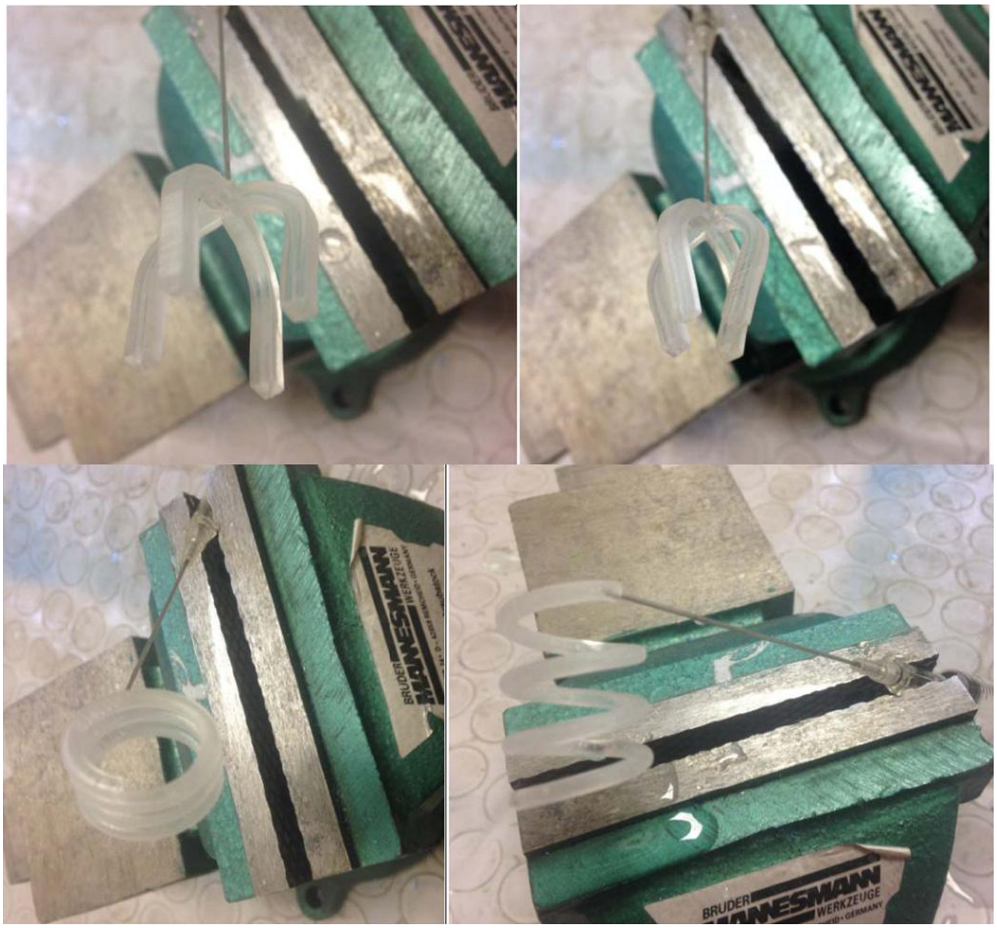

Figure 18. *Activation of shape memory effect in 4D-printed shape-adaptive structures: the micro-claw closes and the spring expands due to the injection of hot water through the micro-vasculatures* [16].

This approach demonstrates the importance of leveraging material properties and employing thoughtful design and manufacturing methods to create effective adaptive structures [16].

In another study, a stent with a complex shape was fabricated using SLA 3D-printed shape memory epoxy, directly from the CAD model in a single step. Figure 19 illustrates the CAD design and printed braided stent on the top. The stent is in its temporarily compressed form following

deformation (on the left below), which is designed to revert to its original shape upon heating (on the right below). In fact, the braided design of this stent facilitates easier opening and closing due to its flexible and sturdy lattice structure, allowing for precise deployment within the body's vessels [96].

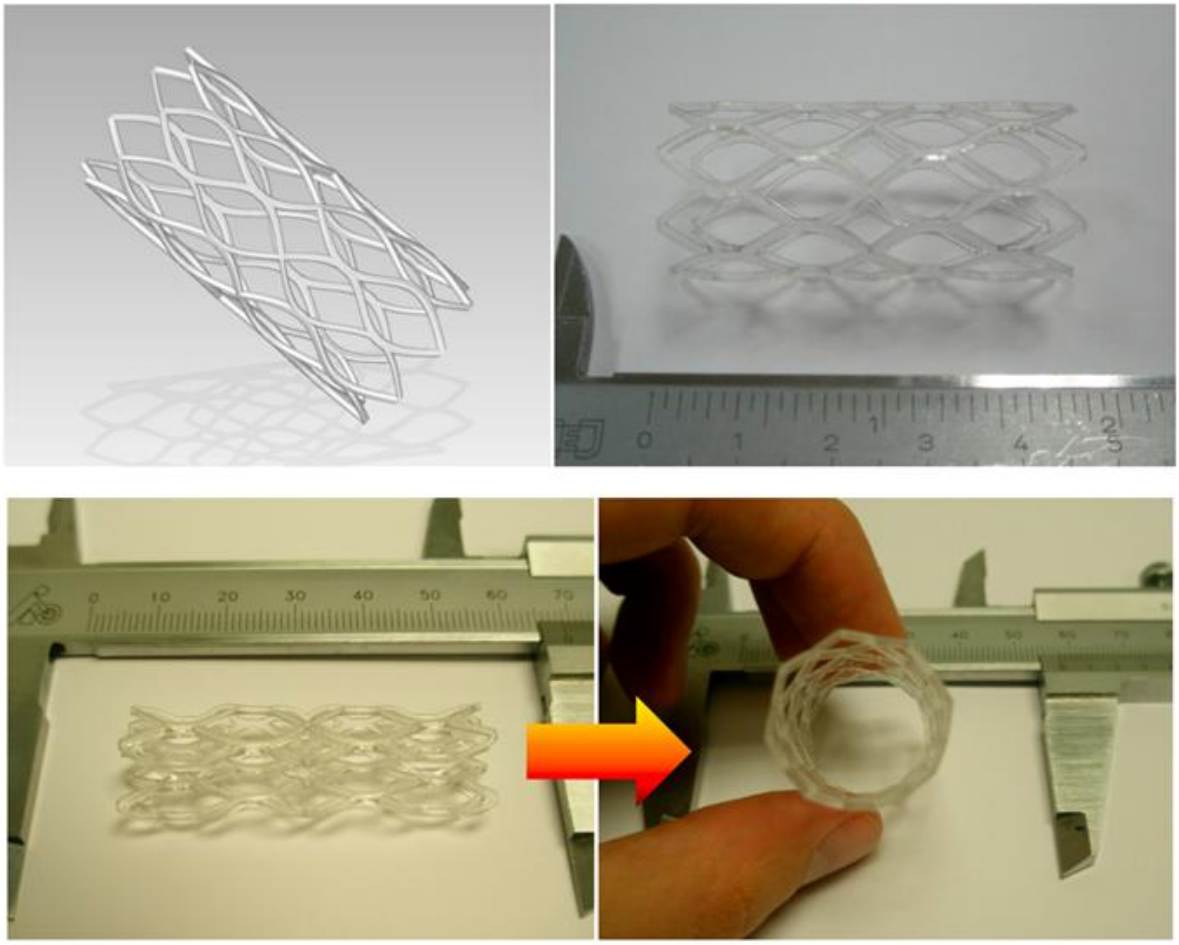

Figure 19. *From the top left: CAD modeling of an SMP-based stent's intricate structure, rapid prototyping, temporary compression, and heat-induced shape restoration* [96].

2.4 Challenges and Research Gaps

For the successful 4D printing of a shape-adaptive device to perform a pre-defined movement task, selecting a suitable material and proper additive manufacturing technique is crucial. This selection should align with the intended design and the functional requirements of the device. Understanding the chosen material's characteristics and its reaction to the activating stimulus is essential as well. This knowledge enables us to predict how the material will alter its

shape within the intended environment, allowing the precise design of the shape-morphing structure with attention to detail (Figure 20). To successfully and accurately complete this path, certain actions must be undertaken, some of which have not received sufficient attention in the literature.

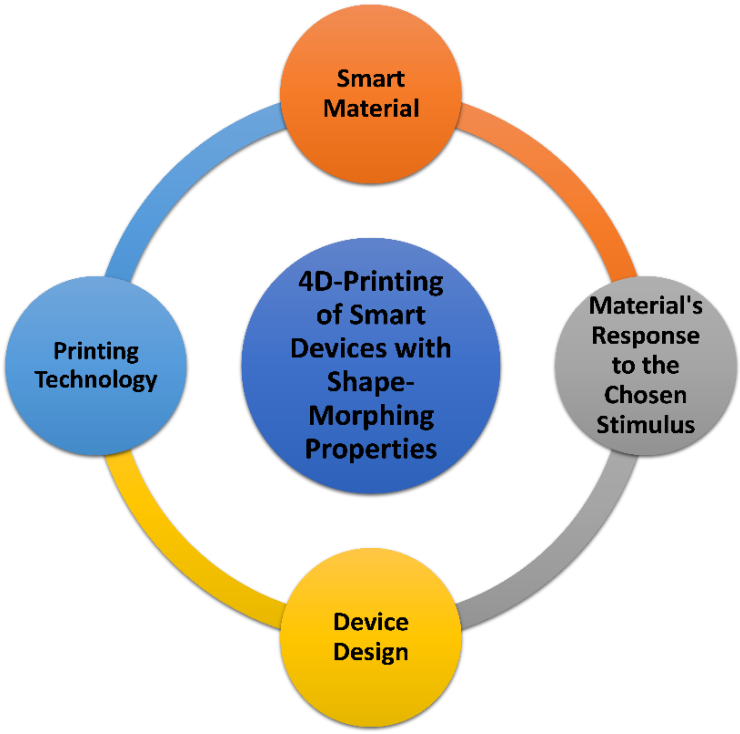

Figure 20. *Stages of 4D printing: developing shape-morphing devices through smart materials and responsive design to 3D-printing technique.*

2.4.1 Thermomechanical Investigation of 4D-printed Shape Memory Polymers

Before employing a device as a shape-adaptive mechanism, it is crucial to first examine the thermomechanical behavior and shape memory characteristics of the chosen material. To investigate the shape memory characteristics, namely shape fixity and shape recovery, of a 3D-printed specimen, it is essential to conduct the thermomechanical cycle within a carefully designed experimental framework. Investigating the thermomechanical properties of an additively manufactured SMP specimen enables the prediction of its behavior effectively and utilizing them in applications where precision and reliability are critical. This analysis helps us understand and quantify the extent to which the material can support the design of a printed device, facilitating its transformation in shape in response to heat. While the mechanical and thermomechanical characterization of thermoplastic specimens printed via FDM has been widely studied, thermoset

specimens produced by SLA 3D printing have not been as extensively and precisely examined in the literature. Therefore, complex morphing structures are often fabricated using SLA 3D printing without prior quantification of the shape memory properties [87, 89–91].

2.4.2 Anisotropy Challenges in Additive Manufacturing

Despite the numerous advantages of 3D-printing techniques, AM faces the challenge of anisotropy in manufactured devices. Anisotropy refers to the directional dependence of a material's properties, meaning that a material can exhibit different strengths, stiffness, or thermal properties in different directions.

In AM, objects are constructed layer by layer, which can result in anisotropic mechanical properties. The bonds between layers are often weaker than the material within each layer, making the mechanical performance of the printed part highly dependent on the direction of loading. The terms "printing orientation" or "build orientation" refer to the direction in which the object is printed relative to the build platform. This orientation plays a critical role in determining the strength, surface finish, and the amount of support material needed for the print. Properly selecting the build orientation can optimize the part's performance and reduce material usage.

Anisotropy in mechanical properties is a common characteristic in parts produced by AM techniques (Figure 21). Mechanical properties can vary significantly depending on the loading direction, with notable differences observed when the load is applied parallel or perpendicular to the printed layers. This variation highlights the critical role of anisotropy in influencing the performance and reliability of AM-produced components.

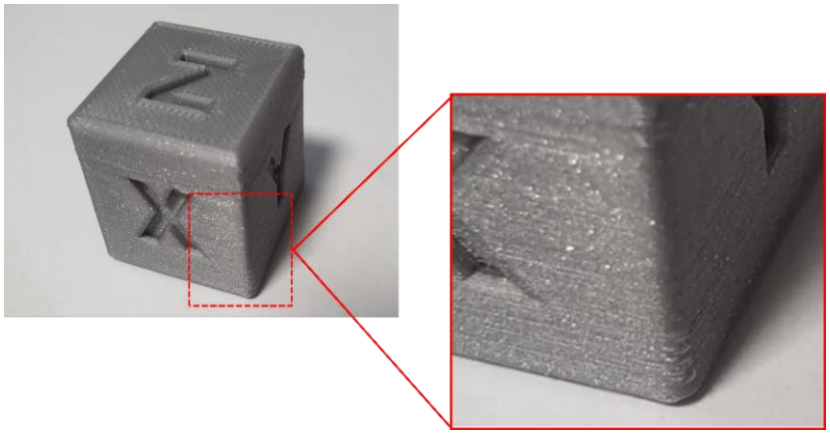

Figure 21. *Image of an FDM 3D-printed object showing the layered surface.*

Depending on the design and geometry of the item being printed, there are several possible orientations for printing successive layers relative to the print platform. Figure 22 illustrates a dog-bone specimen commonly used in tensile testing, demonstrating how the specimen's layers can be fabricated at various angles relative to the print bed, ranging from 0° to 90°, which can affect the material's mechanical properties. Consequently, selecting the most suitable printing orientation is crucial for optimizing the mechanical properties of the printed part to fulfill the specific requirements of its intended application [100,101].

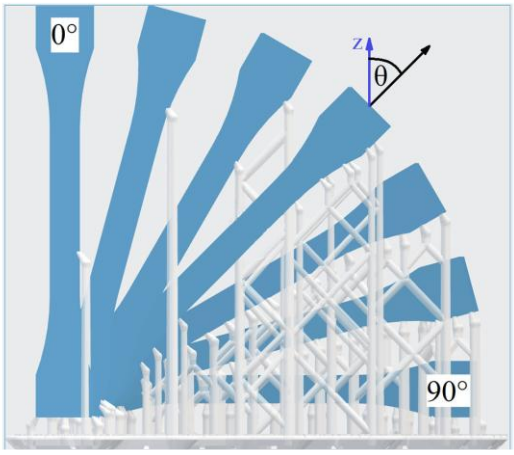

Figure 22. *A tensile testing specimen with different printing angles with respect to the 3D printing platform. The amount of support for each angle is shown in the white color* [100].

Given the widespread use of FDM as a preferred 3D-printing technique, due to its cost-effectiveness and accessibility, the impact of anisotropic characteristics on the mechanical properties of FDM-printed specimens has gained more interest, compare to other methods such as SLA [102–105].

While both SLA and FDM exhibit anisotropic properties, the extent and nature of anisotropy differ due to their unique processes. SLA tends to produce parts with more uniform properties across different directions, due to the nature of resin curing and crosslinking, whereas FDM parts often show more pronounced anisotropy due to the physical layering and cooling of thermoplastic materials. However, it is crucial not to overlook the impact of anisotropy in SLA 3D-printed devices, especially those incorporating micro-actuators or designed with microscale features. In complex and small-scale applications, where precision in mechanical behavior is critical, the effects of anisotropy can be more noticeable.

Addressing the anisotropy challenge in additively manufactured devices requires a comprehensive understanding of the underlying causes and the development of strategies to reduce its effects. Some approaches include optimizing print orientation, adjusting processing parameters to improve interlayer bonding, and post-processing treatments designed to homogenize material properties. Innovative design considerations, alongside precise application of forces and triggering, can also decrease the influence of anisotropy on structures with complex, shape-altering geometries.

2.4.3 Thermal Expansion in Shape Memory Polymers

Thermal expansion in polymers is a physical response to an increase in temperature, which results from the enhanced movement of polymer chains. As the temperature rises, the kinetic energy of the polymer chains increases, leading to greater vibrational and rotational movements within the material's structure. This increase in motion causes the polymer chains to occupy more space, manifesting as an expansion of the material's volume [106]. This phenomenon is not isolated to conventional polymers but also occurs in SMPs in response to temperature rise.

The importance of thermal expansion in the shape memory cycle cannot be overstated. Thermal expansion can cause SMP components to change size or warp, undermining the precision of the shape memory effect. When an SMP device is heated to trigger a shape change, it may overshoot or distort due to expansion. For example, in fiber-reinforced shape memory composites, researchers observed "unexpected deformation, during the heating process, particularly in the first thermomechanical cycle" [107].

If the expansion is non-uniform (e.g., due to temperature gradients or material inhomogeneity), parts of the structure may deform unevenly. Such dimensional instability means the recovered shape may not exactly match the original design, which is problematic in applications requiring tight tolerances. Residual expansion after cooling can also prevent full returning to the original dimensions, effectively introducing error in shape recovery, resulting in limitations on the application fields of SMPs where fast actuation, dimensional stability, and a low thermal expansion coefficient are crucial [108,109]. Accordingly, Bibhuti Bhusan Rath *et al*. reported that while thermal expansion can trigger useful actuation behaviors, it also poses challenges for the predictability and control of material responses [110].

Issabayeva and Shishkovsky's research on FDM-printed shape memory polylactic acid (PLA) highlights the significant impact of thermal expansion on material performance. Their

findings show that thermal expansion can compromise both dimensional stability and the material's ability to return to its original shape after deformation. This study highlights the complex relationship between thermal expansion and the functionality of SMPs, particularly in 3D printing applications [111].

In the additive manufacturing of complex, small-scale structures, thermal stresses can become trapped during the printing process. Subsequent thermal cycling may lead to stress relaxation, which can significantly increase thermal expansion. Therefore, understanding the thermal behavior of additively manufactured objects is essential for accurately designing and applying shape memory materials, ensuring their reliable performance in advanced technological and engineering applications.

Thermal Expansion in Shape Memory Polymers, Possible Mitigation Strategies

One direct way to mitigate thermal expansion is to choose or modify the polymer composition for a lower coefficient of thermal expansion. Polymers with higher crosslink density or crystallinity generally exhibit less thermal expansion. For example, using a thermoset SMP (cured network) instead of a thermoplastic can reduce expansion and improve dimensional stability over cycles [33].

Another material design approach is to create SMP composites by adding fillers or reinforcements. Fillers like silica, carbon black, nanoclay, carbon nanotubes (CNTs), or fibers have much lower CTE than the polymer, so they restrain the matrix from expanding. Incorporating these fillers can drastically lower the overall CTE of the material. For instance, carbon-based fillers (CNTs, graphite, etc.) not only reduce thermal expansion but also increase stiffness and thermal conductivity, which helps an SMP hold its programmed shape and heat uniformly [112].

Moreover, how the SMP is processed and programmed can significantly affect thermal expansion outcomes. One effective technique is "cold programming," wherein the polymer is deformed at a temperature below or just around its T_g, rather than far above it. This avoids heating the entire part to a high temperature, thus minimizing the thermal expansion that occurs during programming [108].

Another strategy is to ensure uniform and slow heating/cooling during shape change, to reduce temperature gradients that cause uneven expansion. Using temperature-controlled chambers or heating an SMP slowly can allow the whole part to expand more uniformly (reducing

internal stress). In some cases, local heating (e.g., with a focused heater or light) is used to activate only a portion of the SMP – this prevents the entire object from expanding at once, improving precision.

Additionally, annealing or pre-conditioning an SMP part after fabrication can help. By heating the part once (without constraint) to let it freely expand and then cooling it, one can relieve internal stresses from manufacturing. This means that when the part is later actuated in service, it has less "built-in" stress to cause unpredictable distortion.

Finally, applying mechanical constraints during actuation is a practical trick: for example, using fixtures or applying a counter-force can resist thermal expansion. One study found that holding a constant tensile load on a shape memory composite during heating was a reliable solution to reduce the thermal distortion and improve its geometric stability [107].

3D-printed SMPs can also be affected by the thermal expansion behavior of the material, a factor that has been relatively underexplored. The anisotropic nature of the layer-by-layer printing process can lead to directional variations in thermal expansion and contraction, which may significantly impact the final performance of printed devices. This effect is particularly critical in applications where even minor deviations from the pre-programmed deformation can propagate through the structure, leading to tolerance stack-up issues that affect overall functionality. This challenge becomes even more crucial in 4D printing, where precise control over shape-adaptive structures is necessary to ensure reliable and predictable actuation.

2.4.4 Design and Manufacturing of Shape-morphing Structures

The critical role of design in the development of shape-morphing structures cannot be overstated. The design process is pivotal in 3D-printed devices not only for defining the aesthetic and functional aspects of the final product but also for ensuring its successful manipulation and performance. The incorporation of innovative design features can facilitate or enhance the shape-shifting process.

Moreover, the selection of an appropriate 3D printing technique is equally crucial and must be carefully aligned with the specific requirements of the intended application and functionality of the device. Different additive manufacturing methods offer varied advantages in terms of material compatibility, resolution, strength, and surface finish. Each of these factors can significantly influence the efficiency and effectiveness of the shape-morphing behavior. For instance, a device

designed to undergo precise and complex transformations may benefit from the high resolution and accuracy offered by SLA. Conversely, applications requiring enhanced material strength and durability might be better served by FDM or SLS techniques, which can fabricate parts with strong mechanical properties. Therefore, selecting an appropriate design and manufacturing approach based on our specific application is crucial for the efficient development and rapid prototyping of intelligent, shape-adaptive devices.

As discussed, the 4D printing of shape-adaptive devices presents considerable promise across various fields. However, the exploration of 4D printing and smart materials for the development of shape-morphing structures with intricate geometries is still relatively new, it is anticipated that more demonstrations and prototypes will emerge in the near future. These developments will undergo thorough examination to evaluate their benefits and potential drawbacks. Obtaining a shape-shifting structure through rapid prototyping of smart materials, incorporating thoughtful design via suitable 3D printing techniques as fast and simple as possible, requires extensive investigation. SMPs currently stand out as the preferred materials for 4D printing, attributed to their enhanced functionality. Future enhancements in 4D printing material technology should aim at reducing activation temperatures, enabling multi-stimuli and remote selective activation, shortening activation times, amplifying activation forces, and facilitating multi-position actuation.

Chapter 3
Materials, Methods, and Experimental Workflow

Given the experimental nature of this thesis, this chapter thoroughly outlines the methodologies and processes used to investigate the shape memory and thermomechanical behavior of a thermo-responsive SMP. It also provides a step-by-step account of the design and 3D printing techniques employed to fabricate a smart, shape-adaptive structure from the SMP, capable of performing a predefined task.

The research begins with the detailed characterization of thermoplastic PU-SMPs, supplied in sheet form, to develop a protocol for accurately determining the shape memory parameters through thermomechanical cycling. The mechanical and thermomechanical investigations presented in this chapter (subchapters 3.2.2, 3.2.4, 3.6.8, 3.6.9) were carried out within a broader research framework developed by the research team led by Prof. Elżbieta Pieczyska. The experimental methodologies, testing protocols, and part of the data analysis were developed and conducted in collaboration with Prof. Elżbieta Pieczyska, Dr. Maria Staszczak, and Mr. Leszek Urbański. The results shown here include data obtained during joint research activities, which were subsequently extended and interpreted in the context of the present doctoral dissertation.

Furthermore, part of the doctoral research was conducted within the framework of long-standing scientific cooperation between IPPT PAN and AICHI Institute of Technology (AIT), Toyota City, Japan, established under the agreement signed in 2005 by Prof. W. K. Nowacki, Director of IPPT PAN, and Prof. Yasuyuki Goto, President of AIT. This international collaboration, coordinated on the IPPT PAN side by Prof. Elżbieta Pieczyska, provided an important scientific context for the research activities described in this chapter.

The chapter then describes the methods used for extruding PU-SMP into filaments and 3D printing the filament using FDM techniques. During these stages, specific challenges were encountered, particularly related to the behavior of the thermoplastic PU-SMP at elevated temperatures, which significantly influenced the research direction.

As a result, the focus shifts towards thermoset SMEp, selected for their superior structural integrity and functional performance in shape-morphing applications, enabled by SLA 3D printing. The chapter details the SLA 3D printing process of epoxy resin, as well as the characterization and thermomechanical investigation of the printed specimens.

Based on the findings from these experiments, designs for the final smart devices are proposed. The chapter concludes with a description of the 3D printing and prototyping phase of the designed devices, where the final shape-morphing structures are tested to ensure they meet the designated functional requirements.

The explanation of all design, fabrication, and experimental characterization steps for both SMPs is structured to reflect the sequence of actions undertaken in the project. This approach ensures a clear and logical presentation of the methods employed.

3.1 Materials

An important consideration in this study was to select a multipurpose and widely available material for additive manufacturing to ensure this research is replicable and beneficial to the broader community of 3D printer users. The polyurethane shape memory polymer, which was initially chosen and characterized for this study, is not commonly used, and its production is limited. These factors later contributed to the decision to shift the focus of the research to shape memory epoxy, which offers broader accessibility and application potential.

3.1.1 Shape Memory Polyurethane

The thermoplastic PU-SMP (MM 4520) utilized in this study was purchased from SMP Technologies, Tokyo, Japan, in the form of 0.4 mm thick sheets, due to the Grant No. 2011/01/M/ST8/07754 of the Polish National Science Centre (Harmonia), coordinated by Professor Elżbieta Pieczyska, with partner Professor Hisaaki Tobushi, AICHI Institute of Technology (AIT), Japan. The technical data sheet provided by the manufacturer indicates that the material's molecular weight ranges from 1 to 2 × 105 g/mol, and its T_g is specified at 45 °C. The chemical formula for PU-SMP MM4520 is depicted in Figure 23. The polymer is prepared through a polyaddition reaction involving diphenylmethane-4,4'-diisocyanate, adipic acid, ethylene glycol, ethylene oxide, polypropylene oxide, 1,4-butanediol, and bisphenol A. Each component contributes distinct properties: for instance, diphenylmethane-4,4'-diisocyanate imparts rigidity and thermal stability, while segments derived from ethylene oxide and polypropylene oxide enhance flexibility and confer thermoplastic characteristics. Given the thermoplastic nature and thermo-responsive shape memory properties of PU-SMP MM4520, its suitability for use in FDM 3D printing was investigated. This exploration not only assesses the material's compatibility with

FDM 3D printing but also expands the potential applications of shape memory polymers in smart device fabrication and advanced manufacturing technologies.

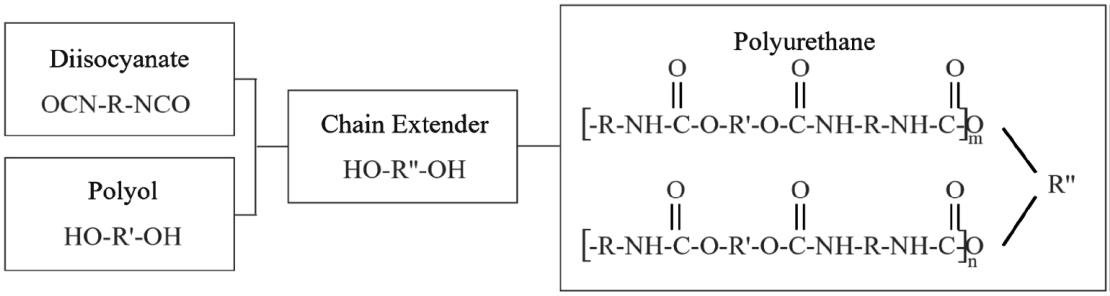

Figure 23. *Composition of hard and soft segment in PU-SMP MM4520* [108].

3.1.2 Shape Memory Epoxy

SLA 3D printing is based on VAT polymerization, which is an additive manufacturing technology that involves photopolymerization in a resin tank, often referred to as a VAT. This tank contains monomers, and photoinitiators, which are molecules that react to ultraviolet light to initiate polymerization, and additives that impart color and specific properties to the resin. The intense beam of UV laser initiates and facilitates the polymerization reaction by irradiating the photosensitive resin, leading to the polymerization and crosslinking of the resin. The photoinitiators absorb the light and generate active species. These activated species then react with the monomers, causing an increase in molecular weight and leading to the formation of polymeric chains or networks. As the resin solidifies, the polymer's molecular weight increases rapidly until the viscosity reaches a level where the material effectively becomes solid. The polymerization reaction then slows and ultimately stops as the concentration of available monomers in the exposed regions diminishes. Extending the exposure time or increasing the laser power expands both the depth and width of the crosslinked region. This photopolymerization process transforms the liquid photosensitive resin into a solid form through additive or layered techniques [113,114].

In this study, the epoxy resin SOMOS WaterShed R XC11122 (DSM Desotech BV, Slachthuisweg 30, 3151 XN Hoek van Holland, the Netherlands) was used. The composition of the resin is as follows: 45-70 wt% of epoxies, 5-20 wt% of acrylate, 10-25 wt% of oxetane, 5-15 wt% of photoinitiators, and 0-10 wt% of additives. It is a low viscosity (~260 cps @ 30 °C), colorless, liquid photopolymer, suitable for AM of highly detailed parts with high resolution,

toughness and water resistance, with the density of ~1.12 g/cm^3 @ 25 °C according to the material's data sheet and standardized tests. These parts can mimic the look and performance of thermoplastic polymers such as acrylonitrile butadiene styrene (ABS) and polybutylene terephthalate (PBT). Besides, the resin is compatible with laser stereolithography systems from the two main developers of this technology (3D Systems and Stratasys). It is worth noting that the datasheet for this material does not mention its shape memory behavior.

3.2 Characterization and Testing of PU-SMP Specimens

3.2.1 Thermal Characterization, Using Differential Scanning Calorimetry (DSC)

DSC was performed on the PU-SMP to analyze the thermal transitions of the PU-SMP material. The analysis was conducted using a calorimeter Pyris1 DSC (Perkin-Elmer, USA), and took place under a nitrogen atmosphere. The sample, weighing approximately 6.4 mg, was sealed in aluminum crucibles. The analysis initially involved a series of heating and cooling cycles with a heating rate of 10 °C/min, covering a temperature range from 0 °C to 200 °C. Figure 24 illustrates the step-wise temperature profile applied to the sample over time.

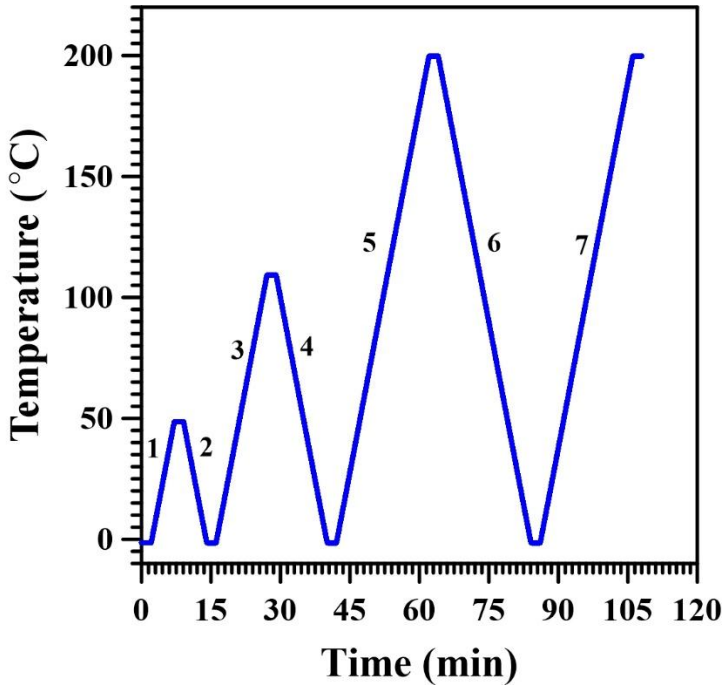

Figure 24. *Temperature profile over time during the sequential thermal cycles applied in the DSC analysis. Each numbered segment corresponds to a specific heating or cooling step.*

The second DSC analysis involved a heating-cooling-heating cycle with a heating rate of 10 °C/min, covering a temperature range from 0 °C to 200 °C.

3.2.2 Mechanical Characterization, Using Tensile Testing Machine

A) Specimen

The geometry and size of the dog-bone specimens (see Figure 25a) used for uniaxial tensile testing in mechanical studies were determined through extensive preliminary investigation by the operator on similar materials, and the specimens were cut using a special device designed and manufactured within the framework of Grant No. 2011/01/M/ST8/07754 of the Polish National Science Centre (Harmonia), coordinated by Professor Elżbieta Pieczyska with partner Professor Hisaaki Tobushi, AICHI Institute of Technology (AIT), Japan. A principal design goal was to ensure that the specimens would fracture in the center when subjected to loading until failure. These specimens were precisely cut from a PU-SMP sheet using a cutting die and press (see Figure 25b).

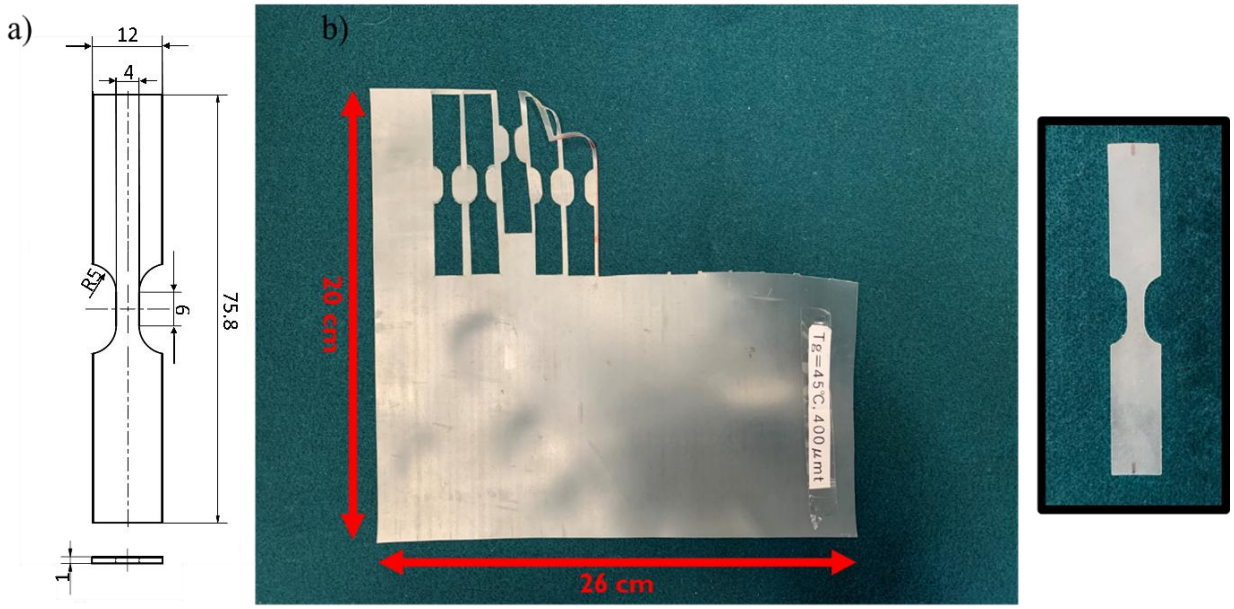

Figure 25. *a) Technical drawing of the dog-bone PU-SMP specimen used for mechanical and thermomechanical investigations; b) Image of the PU-SMP sheet along with the dog-bone specimens that were cut from it.*

B) Tensile Test to Failure

Tensile tests were conducted on the dog-bone PU-SMP specimens using an Instron 5969 testing machine (Instron, USA) (Figure 26a), purchased under Grant No. 2014/13/B/ST8/04280 of the Polish National Science Centre, coordinated by Professor Elżbieta Pieczyska. The tensile testing machine provided a maximum load capacity of 50 kN (Figure 26b) and was equipped with an environmental thermal chamber to ensure uniform temperature control around the specimen (Figure 26c). The specimens of 6 mm gauge length were mounted and subjected to elongation by the testing machine at a constant strain rate of 10^{-2} s^{-1} under isothermal conditions at 25°C (T_g - 20°C) until the specimens' fracture. This setup was designed to investigate the elastic-plastic behavior of the PU-SMP at ambient temperature, providing valuable insights for further thermomechanical investigations. Throughout the elongation, the testing machine recorded both force and displacement, which were used to plot the stress-strain curve using the following equations:

$$\sigma = \frac{F(L_0+\Delta L)}{L_0 S_0} \quad (1)$$

$$\varepsilon = \ln\left(\frac{L_0+\Delta L}{L_0}\right) \quad (2)$$

Equations 1 and 2 are used to calculate the stress and strain values, respectively. In these Equations, F represents the applied force, L_0 - the initial length of the specimen (which here is the gauge length), ΔL - the displacement corresponding to each force, and S_0 - the original cross-sectional area of the specimen.

C) Single Loading-Unloading Tensile Test

Before the tensile loading-unloading test, one specimen was preheated to 110 °C in a thermal chamber (outside of the tensile grips), and then, gradually cooled to room temperature, while the other specimen was tested without preheating. In this test, the material was elongated to 60% under a constant strain rate of 10^{-2} s^{-1}, reaching the post-yield hardening phase at room temperature, corresponding to the glassy state of the PU-SMP. Subsequently, the specimen was unloaded to zero force. This test was designed to evaluate the material's behavior during cold deformation, which involves loading-unloading below its T_g while in the glassy state.

The same tensile loading-unloading test with the same condition was conducted on PU-SMP dog-bone specimens at T_g-20°C (25°C), T_g (45°C), and T_g+20°C (65°C) to assess the effect of temperature on the mechanical response of PU-SMP.

D) Strain-Controlled Cyclic Loading-Unloading Tensile Test

To assess the endurance of PU-SMP under repeated deformation, a strain-controlled cyclic tensile loading-unloading test was conducted. A preheated (at 110 °C) and gradually cooled SMEp specimen was subjected to 9000 cycles of tensile loading at a constant strain rate of 10^{-2} s^{-1}, reaching 60% strain per cycle before being fully unloaded. Since the specimen was subjected to strain-controlled cyclic loading and unloaded to zero strain in each cycle, the minimum stress consistently returned to zero. As a result, the maximum stress before unloading directly represents the full stress range in each cycle, and was therefore used instead of stress amplitude for characterizing the evolution of mechanical response. Additionally, because the stress always cycled between zero and a positive maximum, the asymmetry coefficient (R-ratio), defined as $R = \sigma_{min}/\sigma_{max}$, remained constant at zero throughout the test, indicating fully tensile, non-reversed loading. The test was performed at ambient temperature, ensuring that the material remained in its glassy state throughout. Stress-strain data were recorded to evaluate changes in mechanical response over successive cycles, focusing on hysteresis behavior and potential material stabilization.

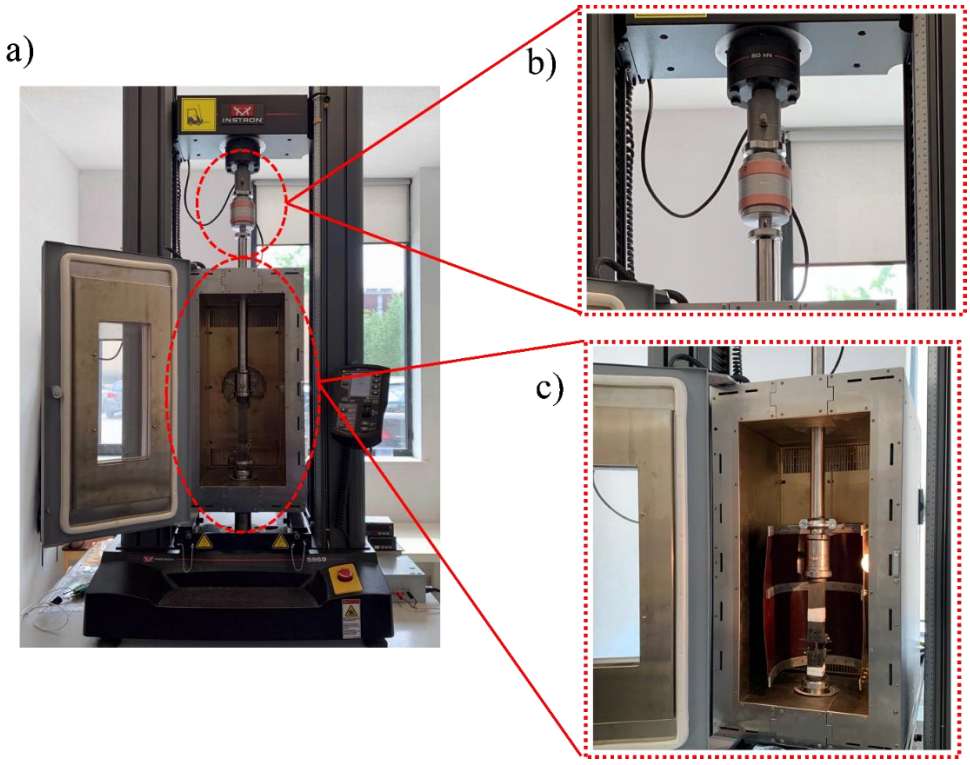

Figure 26. *a) Coupled setup of the Instron tensile testing machine inside an environmental thermal chamber; b) Maximum load capacity of 50 kN, supporting the entire setup; c) An environmental thermal chamber for controlling and maintaining uniform temperature around the tensile grips.*

3.2.3 Surface Morphology Analysis, Using Scanning Electron Microscopy (SEM)

Analysis of PU-SMP surface microstructure was performed using a JEOL JSM-6390LV microscope to observe the surface morphology and the formation of microdefects in the PU-SMP after 1, 3, 5, 8, 9000 loading-unloading tensile cycles. Additionally, SEM was used to examine the surface of the specimen after thermal recovery, allowing for an investigation into the crack healing phenomenon in the PU-SMP following plastic cold deformation. Before imaging, samples were coated for 2x2 minutes with an approximately 8 nm thick gold layer using a SC7620 Polaron mini sputter coater (Quorum Technologies Ltd, Ashford, UK).

3.2.4 Thermomechanical Characterization of PU-SMP; Shape Memory Behavior

After conducting mechanical investigations at two temperatures, below and above the T_g, it was found that the high flexibility of the dog-bone PU-SMP at 65°C makes it difficult for the testing machine to sense the force due to its high maximum load capacity (50 kN). Therefore, to investigate the thermomechanical properties of the PU-SMP, a stripe specimen with a larger cross-section (Figure 27) was used instead of a dog-bone specimen. Here, the primary objective is to design a thermomechanical cycle program to accurately quantify shape memory behavior, focusing on two parameters: shape fixity and shape recovery.

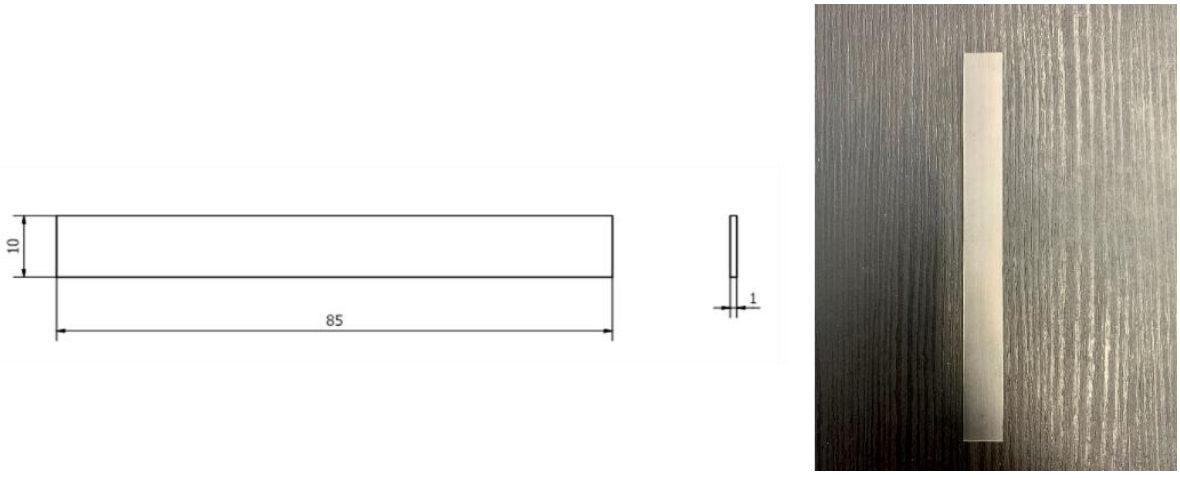

Figure 27. *Engineering drawing and picture of the stripe PU-SMP specimen.*

The shape memory behavior of the PU-SMP was examined using a thermomechanical loading program conducted inside the environmental thermal chamber (Figure 26).

- In the first step of the thermomechanical cycle, the PU-SMP specimen with a gauge length of 25 mm was placed in the grips of the tensile machine and heated to T_g+20 °C (65 °C) under a small force of 0.2 N while recording the thermal elongation of the specimen.
- Once the thermal chamber reached 65°C, the specimen was held at this temperature for 30 seconds to ensure uniform heating. It was then uniaxially loaded at a strain rate of 10^{-3} s^{-1} up to 20% strain.
- Subsequently, the deformed specimen was cooled to T_g-20°C (ambient temperature) while maintaining the maximum strain.
- Next, the cooled specimen was unloaded at a strain rate of 10^{-3} s^{-1} to zero force.
- Finally, the specimen was reheated to T_g+20 °C under a 0.2 N force to estimate the shape recovery of the PU-SMP. The force during the heating steps was set to 0.2 N instead of zero because several pre-tests on shape memory polymers indicated that a minimal fixing force is necessary and facilitates shape transformation.

The stress-strain curves of each step of this cycle were determined using Equations 1 and 2. Based on these characteristics, the shape fixity and shape recovery were calculated, which are key shape memory parameters. The calculation procedure will be explained in detail in the Chapter entitled “Results and Discussion”.

3.3 FDM 3D Printing Process of PU-SMP

To explore the practical applications of PU-SMP, an FDM 3D printing was utilized to fabricate small shape-shifting devices. FDM was chosen as it is one of the most effective additive manufacturing techniques for thermoplastic shape memory polymers. However, due to the lack of commercially available PU-SMP filament, we customized the 3D printing process by repurposing and extruding our own filament. To achieve this, the waste and discarded PU-SMP specimens from previous mechanical and thermomechanical tests were recycled. These specimens were shredded and reprocessed into a filament suitable for FDM 3D printing. The shredding process was carried out using the SHR3D-IT shredder, as shown in Figure 28.

Once shredded, the PU-SMP particles were processed using a 3devo filament extrusion system (Figure 29a). The shredded material was placed in the hopper, a funnel-shaped component that directs the raw polymer into the extruder (Figure 29b).

The control panel (Figure 29c) allowed for precise temperature regulation across multiple heating zones in the extrusion barrel. The display showed both the set and actual temperatures for each zone, labeled 4, 3, 2, and 1, which correspond to different segments along the extruder. Based on DSC analysis and the technical data sheet of the material, we determined the melting temperature of PU-SMP to be between 150 °C and 170 °C. The specific temperature settings for each heating zone are provided in Table 1.

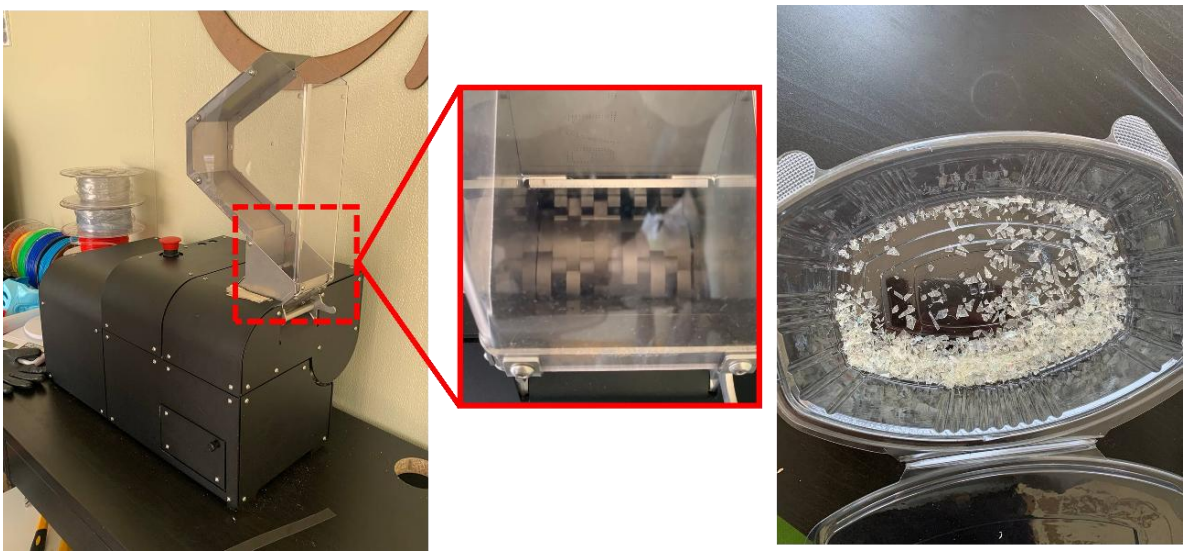

Figure 28. *Pictures of shredding process of PU-SMP.*

The filament diameter was set to 1.75 mm, corresponding to a standard size for FDM printing. The feed rate of the extrusion screw was adjusted to 3.4 RPM, controlling the speed at which the material was processed through the system.

As the molten polymer exited the extrusion nozzle (Figure 29d), it was directed through a filament cooling system to ensure dimensional stability. Cooling fans helped solidify the extruded filament, while drive rollers maintained tension and ensured a consistent filament diameter as it was wound onto the filament spool (Figure 29e). The molten polymer then exited the extruder (Figure 29d), forming the filament through the extrusion nozzle. The filament passed through a guide to ensure it was directed properly onto the spool, while cooling fans helped solidify the

filament quickly after extrusion. The drive rollers pulled the filament from the nozzle and guided it onto the spool, ensuring consistent tension and diameter. Meanwhile, the control panel continuously monitored the filament diameter and displayed it.

Finally, the filament spool collected and wound the extruded filament (Figure 29e). The red color of the final filament was due to residual pigment from previous extrusion processes remaining in the extruder (Figure 29f).

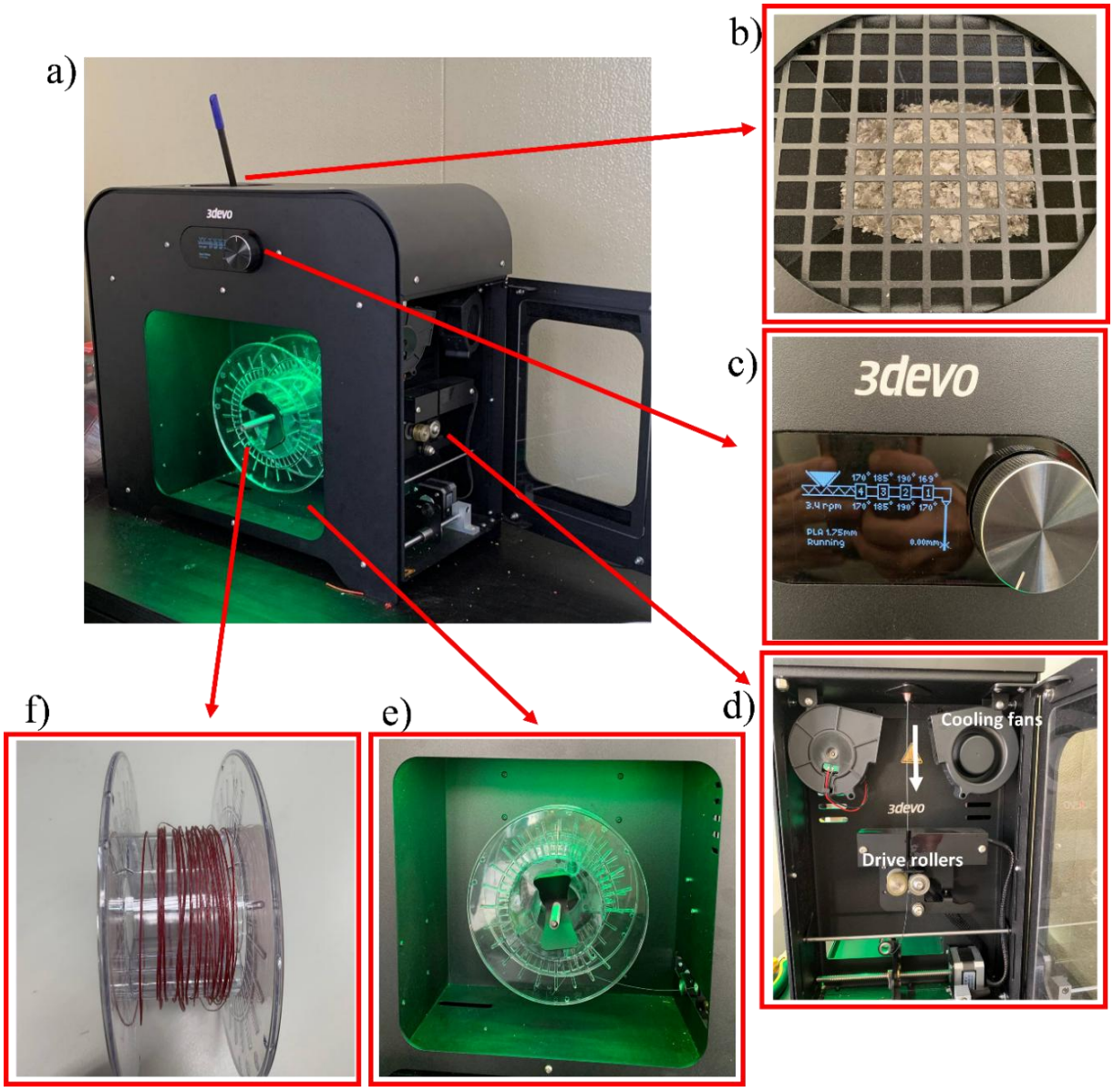

Figure 29. *a) 3devo filament extruder; b) hopper filled with shredded PU-SMP; c) control panel; d) molten, extruded PU-SMP exiting the extrusion nozzle; e) filament collected and wound on a spool; f) filament spool.*

Table 1. *Temperature settings and justifications for each extruder zone*

Zone	Temperature (°C)	Justification
Feeding Zone (4)	170	At the upper limit of the polymer's melting range. This temperature is sufficient to begin softening the polymer pellets as they enter the extruder, ensuring they start to melt without clogging the feed mechanism. It ensures the material is adequately softened for subsequent compression and melting.
Compression Zone (3)	185	Above the melting range of the polymer. This higher temperature ensures that the polymer fully melts and transitions into a homogenous molten state. It also helps eliminate any remaining solid particles, ensuring a consistent melt flow.
Metering Zone (2)	190	Still above the polymer's melting point. This temperature maintains the polymer in a fully molten state while slightly increasing to ensure thorough mixing and stabilization of the flow. This helps in maintaining consistent pressure and flow rate before the polymer reaches the nozzle.
Nozzle Zone (1)	169	Slightly below the upper limit of the polymer's melting range. This ensures that the polymer remains molten and flows smoothly through the nozzle. It also helps in achieving the right viscosity for filament extrusion, preventing clogging and ensuring uniform filament diameter.

3.3.1 Design, FDM 3D Printing of PU-SMP and Evaluation of Shape Memory Behavior

Several simple structures were designed using Autodesk Inventor. These designs were intended to function as shape-adaptive connectors, actuators, or grippers, capable of recovering their original form after deformation.

The extruded filament was then fed into an Ender 3 FDM 3D printer for printing the PU-SMP devices (Figure 30). The filament was heated to 180 °C and melted inside the nozzle beyond the polymer's glass transition temperature. The material was then deposited onto the build plate through the coordinated movement of the extrusion head and the build plate along the x, y, and z axes. To assess the shape memory behavior, the printed structures were subjected to a deformation-recovery cycle. Given the inherent flexibility of PU-SMP at room temperature, the prototypes were

manually deformed without requiring additional heating above T_g. Recovery was induced by placing the deformed structures on a heating plate set to 45 °C.

The shape recovery process was evaluated based on structural integrity, particularly observing whether the initial deformations and delaminations diminished upon heating.

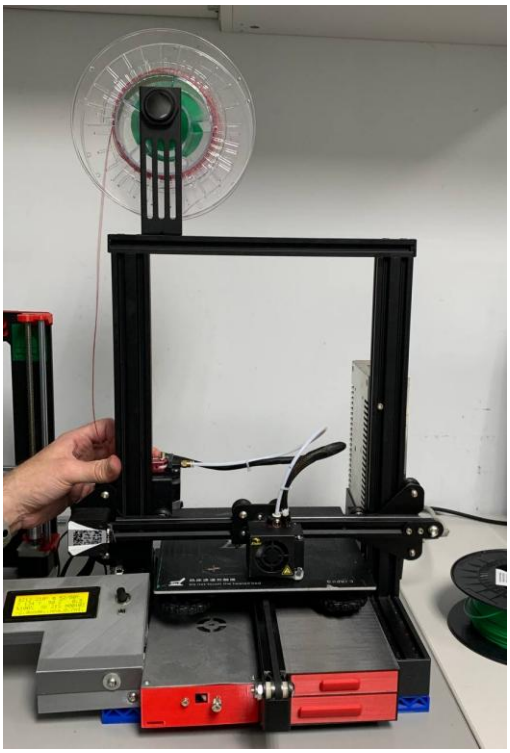

Figure 30. *Ender 3 FDM 3D printer setup with the extruded PU-SMP filament loaded on the spool.*

3.4 Transition to Shape Memory Epoxy

The initial phase of this research utilized PU-SMP, which, while effective in certain applications, presented several challenges that limited their utility in our specific context. The key issues included the material's behavior at elevated temperatures and inadequate layer adhesion during the FDM 3D printing process. It has to be mentioned here that due to material shortage issues, repeating of the testing conditions to optimize the parameters for this SMP was limited. Furthermore, FDM 3D printing of thermoplastic SMPs proved unsuitable for the complex, small, and delicate designs intended for the shape-morphing structures. The FDM process, while versatile, lacks the resolution and detail needed for such intricate geometries, leading to less-than-ideal performance and reliability in the final products.

Therefore, a transition to a different shape memory polymer and manufacturing method was necessary. Shape memory epoxy offers several advantages over PU-SMPs that are critical for our applications, such as enhanced thermal stability, improved layer adhesion, versatility in mechanical properties, better resolution and surface finish.

The following sections provide an overview of the software used for CAD design, slicing, and orientation of a dog-bone specimen for thermomechanical investigation. Next, the additive manufacturing process of a shape memory epoxy specimen is technically explained. The experimental methods and framework for characterizing and testing the 3D printed specimens, as well as the rationale behind the experiments, are then described. Subsequently, the design and optimization of the shape-morphing structures and the logic behind the design are discussed. In the final stage, the 3D printing and prototyping phase are carried out in order to verify whether the 3D-printed devices exhibit the desired shape adaptive properties [3,115].

3.5 Stereolithography Additive Manufacturing of Shape Memory Epoxy Specimens for Testing

3.5.1 Stereolithography Process Overview

Stereolithography is a 3D-printing manufacturing method that produces solid models from a liquid photopolymer resin using an intense UV laser beam (Figure 31). The process unfolds as follows:

1. Design and slicing: The desired model is designed using CAD software, and the design data is sliced into thin layers representing the cross-sections of the final object.
2. Material preparation: A liquid resin with photopolymerization properties is selected and filled in the resin tank.
3. Build setup: The sliced data is imported to the SLA machine. The build platform is positioned just below the surface of the liquid resin.
4. Layer formation: A laser generator and scanner guide a focused laser beam across the resin surface, solidifying the resin according to the pattern of the first cross-sectional layer. The laser beam triggers photopolymerization in the resin to form a solid layer.

5. Layer advancement: After the first layer is formed, the build platform is lowered to a specific depth (layer thickness), submerging the formed layer under a fresh resin layer. A sweeper moves to ensure an even coating of resin for the next layer.

6. Layer-by-layer build: The laser draws (solidifies) subsequent cross-sectional layers on top of the previously cured layers, adhering the layers together to gradually build up the entire 3D model. This process continues until the entire object is completed.

7. Post-processing: The completed part is removed from the resin tank and cleaned. It is then exposed to high-intensity UV light to ensure full polymerization.

8. Finishing: Final finishing methods such as sanding, painting, or dyeing can be applied to the completed part to achieve the desired appearance and surface texture [113].

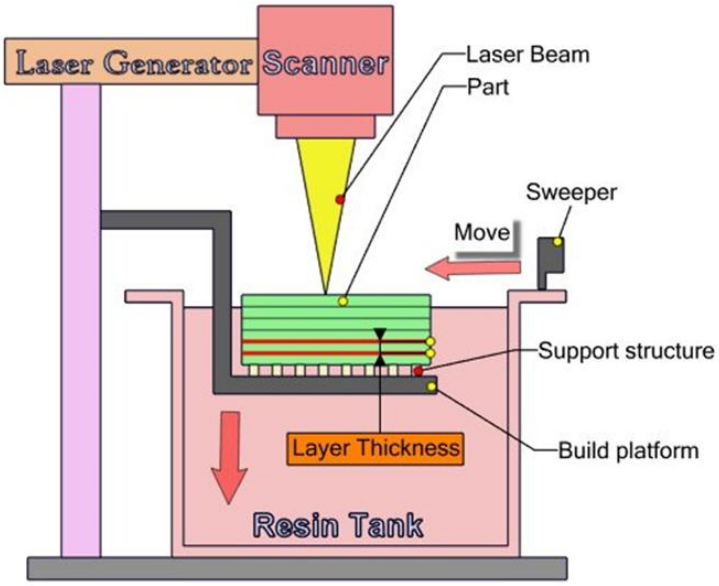

Figure 31. *Schematic of SLA 3D printing [107].*

3.5.2 Shape Memory Epoxy Specimens

To fabricate the shape memory epoxy specimens used in this study, a series of preparatory steps were carried out, including CAD design, orientation selection, slicing, and support generation. The following subsections detail the design considerations and 3D printing setup necessary to produce high-quality SLA-printed specimens suitable for thermomechanical testing [3,115].

A) CAD Preparation

SLA technology allows for the direct 3D printing of highly intricate and complex components from CAD, with one of its key advantages being the ability to enable personalized production. In this study, standard dog-bone specimens, commonly used for thermomechanical testing, were initially designed using NX-12 software (Siemens PLM Solutions, Germany). The geometry was selected based on prior experience with PU-SMP for thermomechanical analysis (see Figure 25a). This specific design promotes fracture initiation at the center of the specimen when subjected to tensile loading until failure.

B) Orientation, Slicing and Support Generation

Choosing a printing orientation (with respect to the 3D printer platform) and slicing process are crucial steps in 3D printing which involve converting the 3D model designed in CAD software into a format that the 3D printer can interpret and print layer by layer. Slicing involves dividing the 3D model into numerous horizontal layers, generating a path for the printer to follow. This process translates the geometric design into specific instructions for the printer, detailing the movements and actions required to build each layer accurately. In this study, the designed dog-bone specimen was imported into 3D Lightyear software for slicing. However, the configuration and angle relative to the 3D printer platform must be decided before slicing and 3D-printing. The three printing orientations schematically illustrated in Figure 32 are among the most commonly selected configurations for 3D printing dog-bone specimens. These orientations are typically used in layer-by-layer additive manufacturing on a standard build platform. The orientations are vertical, on the side edge (lateral), and flat. It should be noted that, due to the layer-by-layer building process in 3D printing, each orientation affects the anisotropy in the final structure, influencing the thermomechanical properties, surface finish, dimensional accuracy and print time of the printed specimen.

In this study, the vertical orientation was not selected for printing the dog-bone specimens. The primary reason is the recommendation in the SLA user's reference manual to minimize the build height, which facilitates faster 3D printing. Secondly, when the specimen is printed in a vertical orientation, the layers are stacked perpendicular to the direction of the applied tensile force, making them more susceptible to delamination under loading. Conversely, when the specimen is printed in either the on-edge or flat orientation, the layers are parallel to the tensile force during testing.

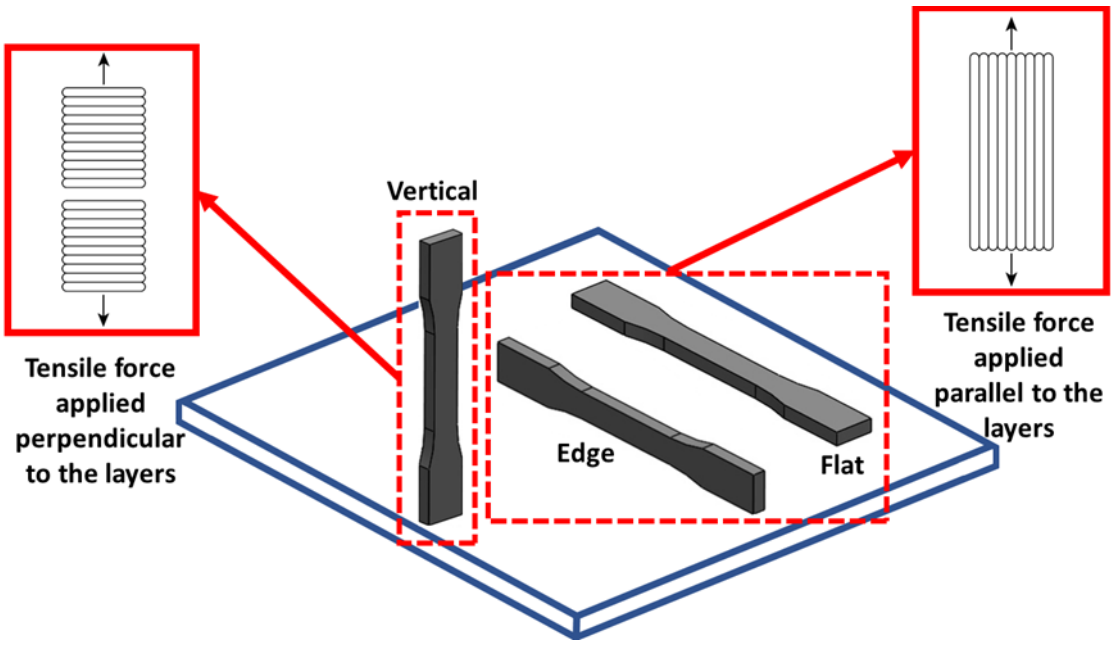

Figure 32. *Common build orientations for 3D-printing of dog-bone specimens: vertical, edge and flat.*

Taking the above into account, the lateral and flat orientations for 3D printing the specimens were selected to ensure that the angle between the printed layers and the 3D printing platform, as well as the tensile force during mechanical testing, was equal to zero. This approach led to two types of specimens with identical geometry, dimensions, and layer thickness; however, with different number of layers and the surface area of each layer (Figure 33). The variations in layers configuration between the two orientations were expected to influence the properties and performance of the specimen. In this study, the specimen printed on its side surface is referred to as SMEp1, while the specimen printed flat is designated as SMEp2 [116].

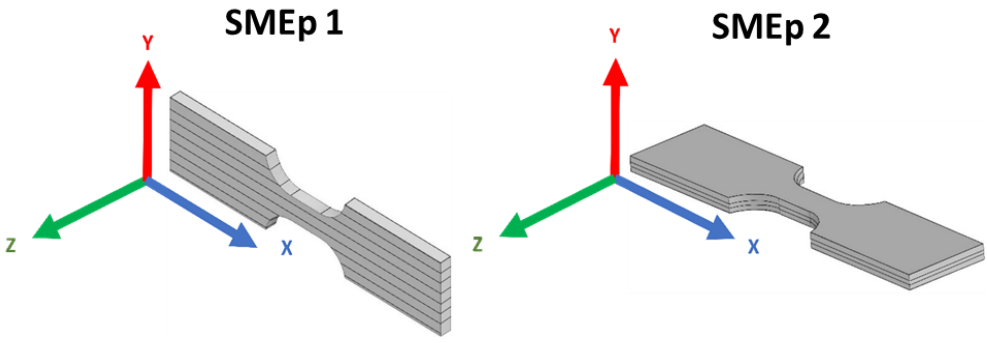

Figure 33. *Two 3D-printing configurations of the dog-bone specimen relative to the 3D printer platform: one along the Y-axis from the lateral surface (left) and the other from the flat surface (right).*

Another important issue during the SLA 3D printing is the generation of supports. In the 3D printing process, it is essential to create a small, easily removable region between the SLA build platform and the parts. Without supports, the initial layers of an object would cure directly onto the SLA platform, causing the solidified resin to adhere to the platform. This situation would make some difficulties during removing stage of the finished parts without damaging them. Therefore, the use of supports reduces the points of contact between the parts and SLA build platform. Figure 34a and b illustrate the support structures used in SMEp1 and SMEp2, respectively, which connect the specimen's printing surface to the 3D printing platform. During the 3D printing process, the supports are printed first, followed by the actual specimen.

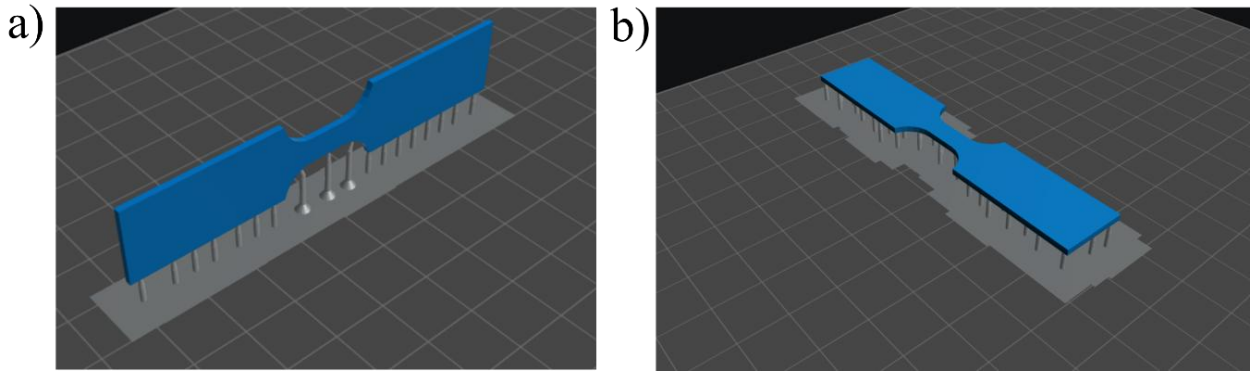

Figure 34. *3D modeling of support generation for: a) SMEp1; and b) SMEp2, showing how each specimen is oriented and anchored to the SLA printing platform.*

One of the key functions of the 3D Lightyear software is the generation and attachment of supports to STL files. This step is essential in preparing STL files for the SLA printing. After supports are generated and optimized, they are included in the preparation (slicing) process along with other objects on the 3D Lightyear build platform. These supports are then incorporated into the build files and fabricated as a part of the SLA job, ensuring that parts can be removed successfully without any damage.

3.5.3 SLA 3D printing of Shape Memory Epoxy Specimens

As described, SLA is based on the focused point-by-point polymerization of a thin layer of resin inside the VAT using a laser beam. The SLA-3500 machine, developed and commercialized by 3D Systems (Rock Hill, SC, USA), was utilized for this process at room temperature. Figure 35 demonstrates the SLA 3D printer setup and the building platform made of aluminum.

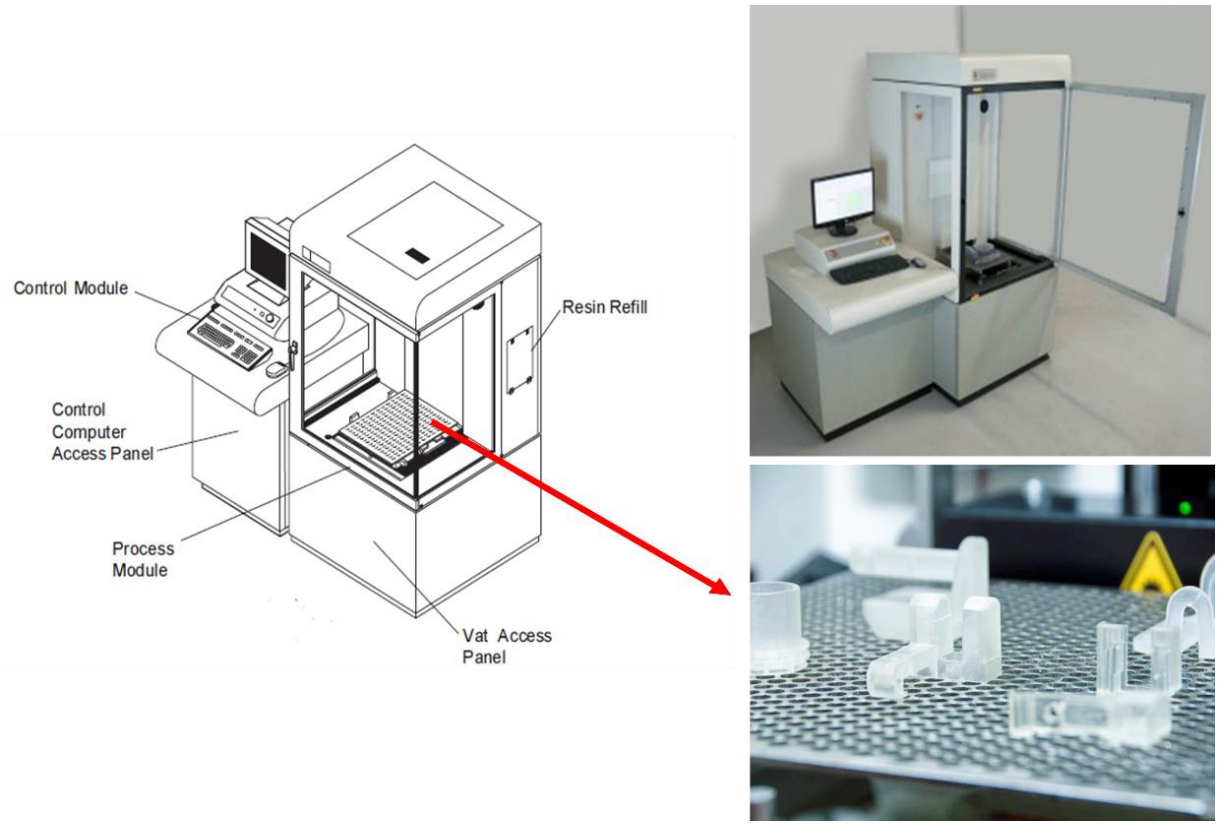

Figure 35. *Schematic representation and actual images of the SLA-3500 3D printer setup, including the aluminum 3D printing platform.*

Before the build begins, the system verifies the SOMOS WaterShed R XC11122 epoxy resin level in the VAT. If the resin volume is insufficient, additional resin must be added. Once the resin is near the correct level, an automatic leveling system performs fine adjustments to ensure optimal resin height.

The sliced design of the dog-bone structure was imported into the system to be 3D printed in two different orientations. The process started with the laser beam drawing the initial support cross-sections, which adhered to the platform. After each layer was drawn by the UV laser, the elevator dips the solidified cross-section below the resin surface, coating it with epoxy resin. After forming a few support layers, the first layer of the part was solidified. Then, the elevator placed the part approximately one-layer thickness below the resin surface, and the recoater blade (Zephyr recoating system) swept across to apply a fresh coating of resin for the next layer. Subsequently, the laser drew the next layer, which firmly became attached to the previous layer. This process was repeated until all layers had been drawn to form the three-dimensional object. The SLA-3500 printer specifications are provided in Table 2.

Table 2. *Technical specifications of the SLA-3500 3D printer.*

Laser type	Solid State Nd:YVO_4 (Neodymium-doped Yttrium Vanadate)
Laser power	160 mW
Laser wavelength	354.7 nm
Laser beam diameter	0.20 – 0.30 mm
Part drawing speed	2.54 m/sec
XY resolution	0.25 – 0.2 mm spot size
Layer thickness resolution	0.05 – 0.1 mm
Maximum vuild volume	350 x 350 x 400 mm

3.5.4 Post Processing of Shape Memory Epoxy Specimens

Post-processing of stereolithography parts involves cleaning, final curing, and finishing.

A) Cleaning

SLA 3D printing results in partially cured parts, requiring the removal of excess liquid resin before complete curing. Following the 3D printing process, excess liquid resin must be drained from the part for 5-15 min. To achieve this, the platform was tilted to remove the resin from the exterior and drain any trapped liquid. The 3D-printed dog-bone specimen was then detached from the platform, along with any supports that connect the specimen to the platform. The supports were removed. Any non-polymerized resin remaining on the surface must be washed off. To achieve this, the parts were typically submerged in a VAT containing a suitable solvent that does not cause the polymer to swell. An ultrasonic bath is often used to effectively remove the resin. The washing step may be repeated to achieve a smooth surface finish, if necessary.

B) Final Curing

Once cleaned, the specimen was placed in a Post Curing Apparatus (PCA) to solidify any uncured sections by exposing the part to UV light. For this process, the specimen was placed in a UV chamber for 10 minutes, as specified by the photoresin's guidelines and considering the small size of the manufactured parts, to achieve the desired final properties.

C) Finishing

For finishing, sandpaper was used to smooth the edges of the specimen, which were rough due to the removal of supports.

3.6 Characterization and Testing of SLA 3D-printed SMEp Specimens

3.6.1 Surface Morphology Analysis, Using Scanning Electron Microscopy (SEM)

The surfaces of SLA 3D-printed specimens, fabricated from two different surfaces (flat and edge), were analyzed, using a JEOL JSM-6390LV microscope, once after 3D printing and once following fracture due to elongation under tension, to compare the surface morphology and determine how different 3D printing configurations influence the overall surface characteristics and integrity. Before imaging the surface, samples were coated for 2x2 minutes with an approximately 8 nm thick gold layer using a SC7620 Polaron mini sputter coater (Quorum Technologies Ltd, Ashford, UK). By examining the microstructural details, one can better understand the impact of build orientation on the material properties, quality of the printed layers and failure mechanism.

3.6.2 Water Absorption Characterization

The swelling test was conducted on three specimens from each of SMEp1 and SMEp2 specimens. Initially, the dry specimens were weighed to establish a baseline. Following this, each specimen was submerged in water in separate beaker to prevent cross-contamination and ensure accurate measurement of water absorption for each sample.

The specimens were weighed at specific time intervals: after 1 h, 2 h, 3 h, 4 h, 8 h, 24 h, and 48 h. This allowed for the monitoring of water intake over time and provided a profile of the swelling behavior for both types of specimens. The weight measurements were used to calculate the swelling rate and to understand the water absorption characteristics of the different printing orientations in SLA 3D-printing method.

3.6.3 Chemical Analysis, Using Fourier Transform Infrared Spectroscopy (FTIR)

FTIR was used to characterize the functional groups of the 3D-printed SMEp specimens. The purpose of the FTIR analysis was to explore if different printing orientations affect the molecular structure and degree of cross-linking or not. The analyses were conducted in attenuated total reflectance (ATR) mode with a Bruker Vertex70 FTIR spectrometer and carried out in the wavenumber range of 400–4000 cm^{-1} with a resolution of 2 cm^{-1} and eight scans for each sample.

3.6.4 Thermal Characterization, Using Thermogravimetric Analysis (TGA)

Thermal stability of the cross-linked sample was assessed using TGA. This analysis was carried out on a Discovery TGA 5500 (TA Instruments, USA) at a heating rate of 10 °C/min. A sample of 6.2 mg was placed in a platinum crucible and heated from room temperature to 700 °C under a nitrogen flow of 25 mL/min.

The TGA experiments were carried out at the "Petru Poni" Institute of Macromolecular Chemistry (Iași, Romania) by Dr. M. Cristea and Dr. D. Loniță, within the framework of the joint Polish–Romanian scientific cooperation between the Polish Academy of Sciences and the Romanian Academy, in collaboration with Prof. Elżbieta Pieczyska's research team.

3.6.5 Thermal Characterization, Using Differential Scanning Calorimetry (DSC)

DSC was performed on the crosslinked 3D-printed SMEp specimens to assess thermal characteristics and transitions of the specimens printed from the lateral and flat surfaces. The analysis was conducted using a calorimeter Pyris1 DSC (Perkin-Elmer, USA) and took place under a nitrogen atmosphere. A sample with an approximate weight of 6 mg was sealed in aluminum crucibles. The analysis involved a heating-cooling-heating cycle with a heating rate of 10 °C/min, covering a temperature range from 0 °C to 90 °C.

3.6.6 Dimensional Stability Investigation, Using Thermomechanical Analysis (TMA)

TMA testing was carried out on 3D-printed SMEp specimens to evaluate their dimensional stability during thermal cycling, with particular attention to the effects of printing orientation and the anisotropy introduced by the layer-by-layer manufacturing process. For accurate and consistent comparison, specimens with a cross-section equal to 5 mm × 5 mm were cut from both printing orientations, SMEp1 (side-printed) and SMEp2 (flat-printed). Each specimen underwent thorough cleaning and conditioning to eliminate any surface contaminants that could influence the results.

The TMA tests were performed using a TMA450 thermomechanical analyzer, equipped with interchangeable macro and micro probes to capture dimensional changes at different scales.

The initial phase of the thermomechanical analysis focused on establishing optimal testing parameters, including probe size, holding force, and heating rate, to ensure reliable data collection for the subsequent heating-cooling-heating cycle. These preliminary trials were conducted exclusively on SMEp1 specimens, serving as a pilot study to develop a consistent testing framework for the rest of the analysis.

A) Macroexpansion Measurements

For macroexpansion analysis, the larger probe was selected to cover the majority of the sample surface, providing an overview of bulk expansion behavior across multiple printed layers (Figure 36a). A low fixed force of 0.002 N was applied to gently hold the specimen in place while allowing free thermal expansion.

Three SMEp1 specimens underwent a heating process separately under the probe in the chamber, in which the temperature was ramped from 25 °C to 85 °C at controlled heating rates of 5 °C/min, 10 °C/min, and 20 °C/min. The resulting dimensional changes and thermal expansion coefficients were continuously monitored and recorded.

B) Microexpansion Measurements

To gain deeper insight into the thermal expansion behavior at the layer level, the probe was replaced with a smaller micro probe to focus on a localized region, targeting a smaller surface area and fewer printed layers (Figure 36b). This setup provided a more detailed view of the expansion characteristics within individual layers.

The same heating rates and temperature range were applied to three individual SMEp1 specimens (from 25 °C to 85 °C at heating rates equal to 5, 10, and 20 °C/min), with the holding force initially kept at 0.002 N, matching the macroexpansion tests. However, measurement noise was observed at this scale, likely due to the lower force applied in combination with minor surface irregularities.

C) Optimization for Improved Accuracy

To improve measurement accuracy and reduce noise during the microexpansion tests, the applied force was increased to 0.02 N in a subsequent set of experiments. This adjustment provided better contact between the probe and the sample surface, enhancing data reliability.

Each adjusted test followed the same thermal profile on three individual SMEp1 (from 25 °C to 85 °C at heating rates equal to 5, 10, and 20 °C/min) to ensure comparability. All dimensional changes were recorded continuously, and the coefficient of thermal expansion (CTE) was determined by drawing a tangent to the expansion curve within the target temperature range.

Table 3 summarizes the TMA experimental conditions, including probe type, applied force, and heating rates for each test configuration.

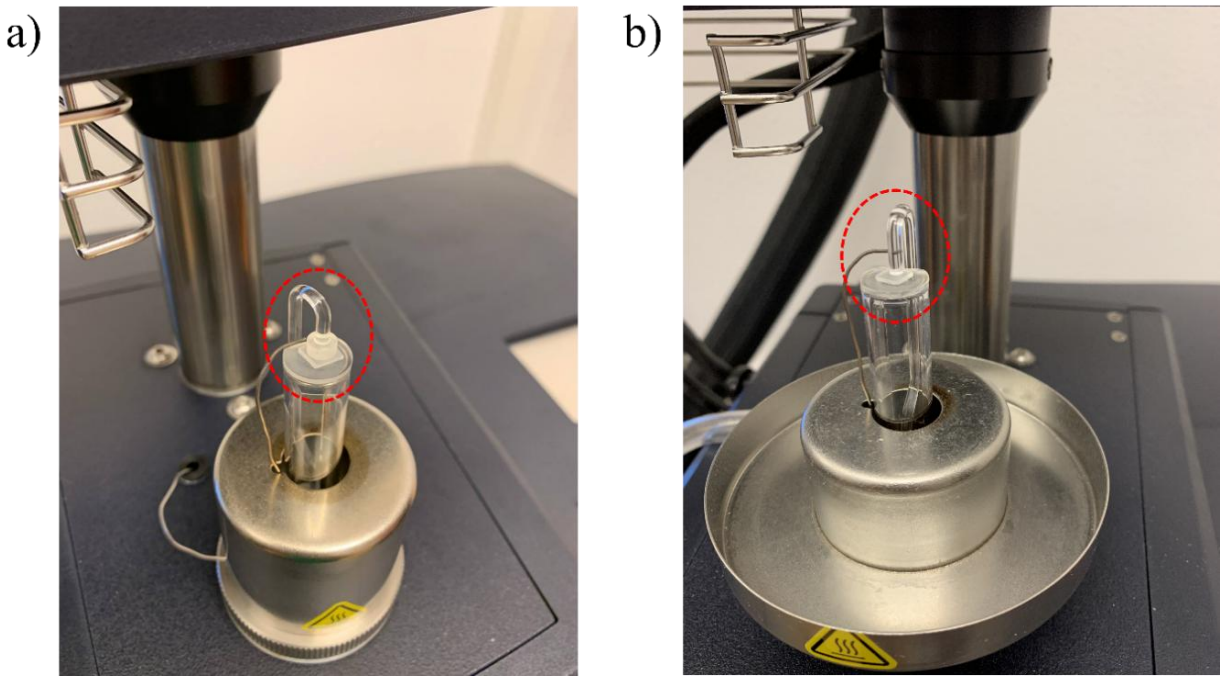

Figure 36. *a) SMEp sample positioned between the TMA macro probe and the sample holder; b) SMEp sample positioned between the TMA micro probe and the sample holder.*

Table 3. *Summary of the TMA experimental conditions.*

Experiment	Heating rate (°C/min)	Probe	Force (N)
No. 1	5, 10, 20	Macroexpansion	0.002
No. 2	5, 10, 20	Microexpansion	0.002
No. 3	5, 10, 20	Microexpansion	0.02

3.6.7 Thermal Expansion and Contraction Behavior in a Heating-Cooling-Heating Cycle

To assess the dimensional stability of the SMEp1 and SMEp2 specimens under thermal cycling, a heating-cooling-heating cycle was performed using the micro probe setup. Following preliminary trials to optimize the testing parameters, the small probe (Figure 36b) was selected to enable localized evaluation of dimensional changes in SMEp1 and SMEp2, while a holding force of 0.02 N was applied to ensure stable contact and reduce measurement noise during thermal expansion monitoring.

The thermal cycle consisted of:

- Heating from 25 °C to 85 °C

- Cooling back to room temperature
- A second heating phase up to 85 °C

All temperature changes were applied at a controlled rate of 10 °C/min during both heating and cooling.

Throughout the entire cycle, the micro probe continuously tracked expansion and contraction in the thickness direction of the specimens. To ensure the repeatability of the results, each test was repeated three times on separate specimens of both SMEp1 and SMEp2. The resulting dimensional changes were recorded as a function of temperature, providing a comprehensive view of the thermal expansion and contraction behavior of the two printing orientations.

3.6.8 Mechanical Characterization, Using Tensile Testing Machine

To evaluate the mechanical properties of SMEp1 and SMEp2 and to investigate the influence of build orientation on their elastic-plastic response, uniaxial tensile tests were performed on dog-bone specimens of both types. The tests were conducted at two temperatures, room temperature (below the T_g), representing the material's behavior in its glassy state, and 75 °C (above T_g), to capture the mechanical response in the rubbery state.

All tests were carried out using an Instron 5969 universal testing machine, equipped with a temperature-controlled environmental chamber (Figure 26), allowing precise regulation of the testing temperature. Prior to each test, the specimen was mounted between the grips (gauge length=6 mm) and conditioned inside the chamber until the target temperature was fully stabilized, ensuring uniform thermal equilibrium throughout the sample. After reaching 75 °C, the specimens were held at the set temperature for 30 to 60 seconds before initiating the test, allowing sufficient time for the material to reach thermal equilibrium within the chamber.

The specimens were loaded at a constant strain rate of 10^{-2} s^{-1} until complete failure, and the stress-strain response was continuously recorded. Each test was repeated on three separate specimens of both SMEp1 and SMEp2 at each temperature, ensuring repeatability and statistical reliability of the measured properties.

3.6.9 Thermomechanical Characterization of SMEp; Shape Memory Behavior

The shape memory behavior of SMEp1 and SMEp2 specimens was evaluated using a controlled thermomechanical loading protocol conducted inside a tensile testing machine equipped with an environmental thermal chamber. To ensure the reliability and reproducibility of the results, the test was repeated three times for each material type, using three separate specimens per group. The same experimental setup, with tensile grips mounted inside the chamber, was employed (see Figure 26). A schematic representation of the thermomechanical cycle applied to the dog-bone specimens is shown in Figure 37.

A) Standard Thermomechanical Cycle

In the first phase of the cycle, each specimen (gauge length = 6 mm) was clamped between the grips of the tensile testing machine and heated from room temperature to 75 °C (i.e., T_g+20 °C) at a controlled rate of 12 °C/min, while applying a minimal preload of 0.02 N to maintain alignment (Figure 37a–b). The specimen was held at 75 °C for 30–60 seconds to ensure thermal equilibrium. In the second phase, the specimen was subjected to uniaxial tensile loading at a constant strain rate of 10^{-2} s^{-1}until reaching 20% strain (Figure 37c). This strain value was selected based on prior mechanical testing results, confirming that neither SMEp1 nor SMEp2 fractures before this strain threshold at elevated temperature.

In the third phase, the specimen was cooled down to room temperature (below the T_g) while being held at maximum strain, effectively fixing the temporary shape through vitrification. As the temperature decreased, stress build-up due to contraction was recorded, representing the locking of internal strain energy (Figure 37d).

In the fourth phase, once the specimen reached room temperature, the tensile load was unloaded to zero while maintaining the shape in its temporary, deformed configuration. This concludes the fixing step.

Finally, in the fifth phase, the specimen was reheated to 75 °C under the same minimal preload (0.02 N), and the recovery behavior was recorded to assess the shape recovery performance of the material (Figure 37e). This complete cycle allowed the determination of both shape fixity and shape recovery for SMEp1 and SMEp2. The detailed results of this analysis are presented in the Results and Discussion section.

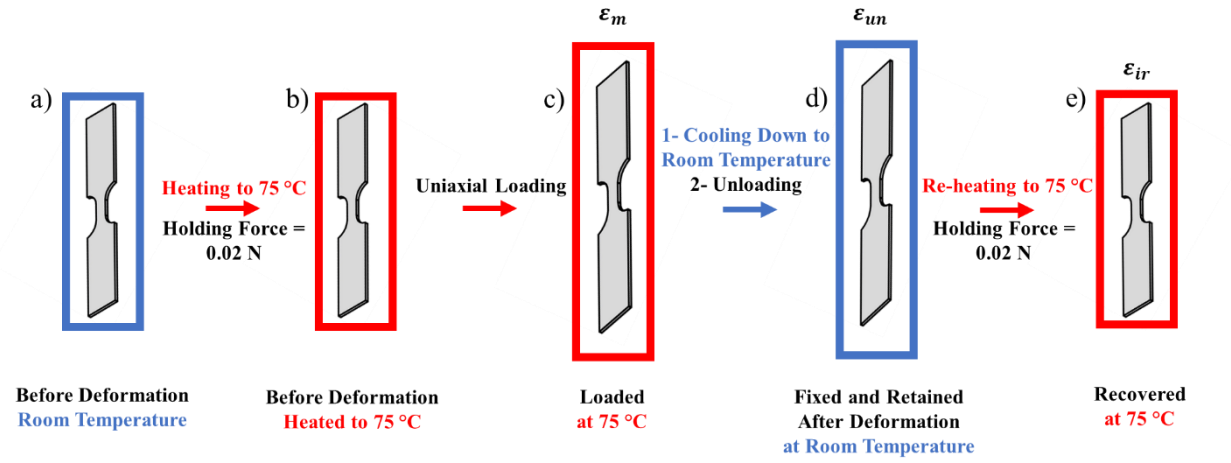

Figure 37. *Schematic representation of the thermomechanical cycle applied on the dog-bone specimen : a) Initial state of the specimen prior to heating and deformation; b) Heating to 75 °C under a minimal holding force of 0.02 N; c) Uniaxial tensile loading to a defined strain level; d) Cooling to room temperature to fix the temporary shape, followed by unloading; e) Reheating to 75 °C to evaluate shape recovery.*

B) Supplemental Thermomechanical Cycle - Thermal Expansion-Induced Deformation without Mechanical Loading

To further investigate the isolated effect of uniaxial thermal expansion on shape memory behavior, particularly its potential negative influence on shape recovery, a separate thermomechanical procedure was carried out. In this experiment, the specimens were subjected to the same thermal cycle as before, but without any mechanical loading step.

In this modified protocol, each specimen was heated from room temperature to 75 °C at a rate of 12 °C/min under the same minimal applied force of 0.02 N, solely allowing for thermal expansion (i.e., deformation caused by heating alone). The specimen was held at 75 °C for 1 minute to stabilize the thermal strain.

Instead of applying tensile loading, the thermal elongation that occurred during heating was immediately fixed by cooling the specimen to room temperature while still held in the grips. This process effectively locked the thermally induced deformation, while the contraction force was recorded as the specimen cooled and attempted to shrink.

Once fully cooled, the contraction-induced stress was released to zero. In the final step, the specimen was reheated to 75 °C under the same low preload, and the extent of strain recovery was recorded. This approach enabled the evaluation of the recoverability of SMEp1 and SMEp2, when deformed exclusively by thermal expansion without the influence of mechanically applied strain.

3.6.10 SLA-printing of Shape-morphing Prototypes

For this study, a series of complex-shaped prototypes incorporating various mechanisms and smart structural concepts were designed using NX-12. These designs aimed to harness the unique advantages of SLA 3D printing method by integrating shape-morphing actuators within functional geometries. The prototypes served as proof-of-concept structures, combining kinematic chains and compliant joints to demonstrate the potential of shape morphing in conceptual device development and to highlight the functional amplification enabled by these integrated mechanisms.

Once the designs were finalized and optimal build orientations were selected, the prototypes were fabricated using an SLA-3500 laser stereolithography system. Model slicing and support structure generation were performed using 3D Lightyear software, which programmed the laser beam trajectories necessary to selectively polymerize the photocurable resin. The printing process was conducted layer by layer, with the laser initiating polymerization to build up the intricate 3D geometries. After printing, the parts underwent a 10-minute post-curing process in a UV oven, in accordance with the resin manufacturer's specifications and adapted to the small size of the components, resulting in fully solidified and dimensionally stable structures.

3.6.11 Shape Memory Training of 4D-printed SMEp Shape-morphing Structures

The shape memory cycle was performed in line with the thermomechanical protocols previously described, to train and evaluate the shape memory behavior of the 3D-printed SMEp devices. Thanks to the moisture resistance of the SOMOS® Watershed XC 11122 resin, the printed prototypes could be directly activated using hot water, enabling them to reach temperatures above their T_g. This method significantly shortens the device's thermal response time due to the higher convective heat transfer coefficient of water compared to air heating.

Each device included a centrally placed actuator (either an S-shaped spring or a torsional joint) serving as the active region that connects and governs the motion of the entire structure. This design allowed localized training of the actuator alone, while the configuration of the full device was modified through the transmission of motion via integrated kinematic chains or compliant joints.

To activate the shape memory cycle, the actuator was locally heated to approximately 75 °C using hot water applied with a syringe, targeting only the active region to minimize heat exposure

to the surrounding structure. Once softened, the actuator was manually deformed, either by stretching the S-shaped spring or by adjusting the intersection angle in the cross-shaped device. While maintaining the deformation, the actuator was then cooled with cold water (~25 °C) to fix the temporary shape. Following the removal of external force, the recovery step was initiated by reheating the actuator to ~75 °C to restore the original configuration.

To evaluate the effectiveness of the actuation, apex angles at key joints and intersections were measured before and after recovery using ImageJ software. These angular measurements provided an estimate of the overall shape recovery achieved by triggering only the actuator.

Additionally, a FLIR A655sc thermal imaging camera (Sweden) was employed to monitor the temperature distribution across the prototypes during actuation. Each device was positioned at an optimized distance from the camera, and the thermal range was set to capture localized heating. The FLIR software was used to process the images and quantify the surface temperature distribution. Measurements were repeated to ensure the accuracy and reproducibility of the results.

Chapter 4

Results and Discussion (I): Preliminary Thermomechanical Investigation of PU-SMP

This chapter presents the design of a thermomechanical investigation protocol for SMPs, focusing on a thermoplastic polyurethane-based SMP (PU-SMP). The mechanical and thermomechanical studies (Figures 40, 41, 43a, 43b, 45–48, 50, 52, 54 and Table 8) were conducted within a broader research framework led by Prof. Elżbieta Pieczyska, in collaboration with, Dr. Maria Staszczak, and Mr. Leszek Urbański.

Part of the doctoral research was carried out within the long-standing scientific cooperation between IPPT PAN and the AICHI Institute of Technology (AIT), Toyota City, Japan, established in 2005. This international collaboration, coordinated at IPPT PAN by Prof. Elżbieta Pieczyska, provided an important scientific context for the research presented in this chapter.

A significant challenge encountered during the investigation was the material's low thickness coupled with its high deformability at elevated temperatures. This characteristic rendered the tensile testing machine ineffective, as it could not adequately detect the force exerted by the grips on the specimen at high temperatures. Consequently, a comprehensive analysis of the material's mechanical behavior at high values of temperature was not feasible.

Additionally, the limited availability of the PU-SMP material restricted the extent of our experimental exploration. Despite these limitations, the chapter lays the groundwork for the initial technical experiments conducted for investigating of the thermomechanical properties of PU-SMP. These preliminary findings set the stage for more detailed further studies, particularly focusing on epoxy-based thermoset SMP (SMEp), which will be elaborated upon in subsequent chapters.

4.1 Investigation of PU-SMP Glass Transition Temperature by Differential Scanning Calorimetry (DSC)

Understanding the thermo-responsive behavior of SMPs is crucial for their practical applications, as it directly relates to their activation temperature range, governed by the T_g. The T_g represents the boundary between two distinct states of the polymer: below T_g, the material exists

in a rigid, glassy state, whereas above T_g, it transitions into a flexible, rubbery state. The transition is critical because it defines the temperature range where the SMP can either fix a deformation in its glassy state or recover its original shape in the rubbery state.

DSC measurement was employed to analyze the thermal transitions of the thermo-responsive PU-SMP. This technique measures the heat flow associated with temperature changes in the polymer. The material was subjected to a series of heating and cooling cycles, with the T_g determined for each cycle to evaluate the thermal transitions at different temperature steps. The DSC curves for all cycles are presented collectively in Figure 38a. To ensure clarity, each cycle is displayed separately in distinct figures (Figure 38b–e), and the corresponding T_g values, along with any observed endothermic peaks, are summarized in Table 4.

The specimen was first heated from 0 °C to 50 °C and subsequently cooled back down to 0 °C (Figure 38b). In the following cycle (Figure 38c), the specimen was heated to 110 °C, and then, cooled down to 0 °C. In the subsequent cycle (Figure 38d), the specimen was heated from 0 °C to 200 °C and then cooled back to 0 °C. Finally, the specimen was heated from 0 °C to 200 °C once again (Figure 38e).

As mentioned before, polyurethane is known for its two-phase structure, consisting of hard and soft segments. The hard segments are composed of rigid, crystalline, or semi-crystalline domains derived from diisocyanates and chain extenders. These segments contribute to the mechanical strength, thermal stability, and elastic recovery of the polymer [117].

The key findings that can be identified from Figure 38 are as follows:

- During the initial heating cycle (1 in Figure 38b) from 0 °C to 50 °C, a glass transition step is at approximately 29.26 °C. This transition may correspond to the T_g of the soft segments within the PU-SMP, reflecting the thermal activation of the flexible polymer chains.

- An endothermic peak at 74.31 °C was observed during the second heating from 0 °C to 110 °C (3 in Figure 38c), suggesting the presence of a distinct low-temperature phase, likely composed of hard segments or a specific arrangement of polymer chains that melts or reorganizes at this temperature. Heating to 110 °C destroys this phase through melting or breaking specific interactions within this phase.

- The disruption of the hard phase at 74.31 °C during the second heating causes a reorganization of the polymer structure. As the hard segments melt or break down, they

potentially mix with the soft segments, leading to a higher T_g due to increased overall rigidity.

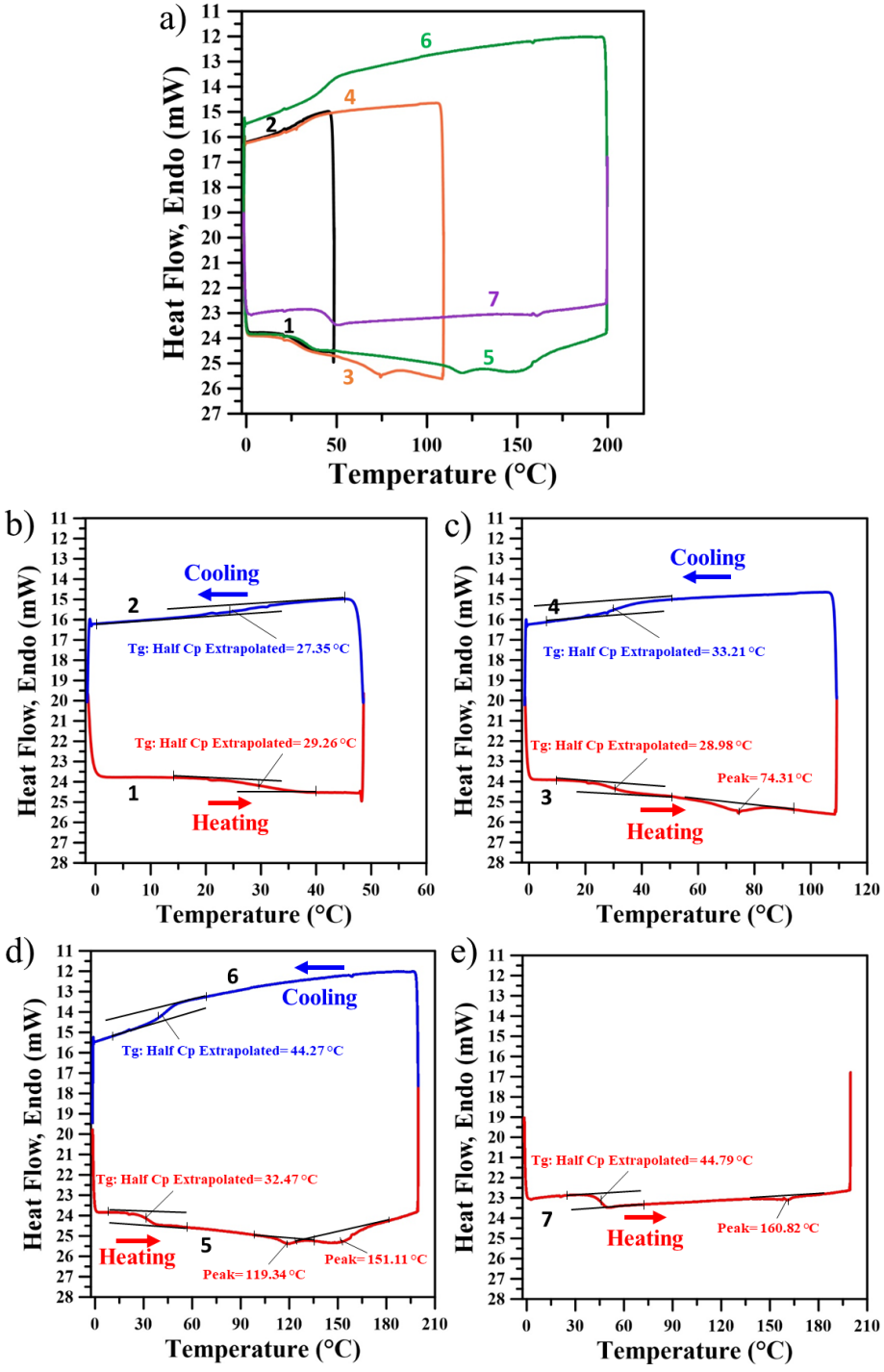

Figure 38. *DSC analysis of the PU-SMP through multiple thermal cycles: a) All DSC cycles; b–e) Individual DSC curves for separate thermal cycles: b) heating 0-50 °C followed by cooling to 0 °C; c) heating to 110 °C followed by cooling to 0 °C; d) heating to 200 °C followed by cooling to 0 °C; and e) heating to 200 °C.*

- After heating to 110 °C and subsequent cooling, the material exhibits a new T_g around 32.47 °C during the third heating (indicated as 5 in Figure 38d), reflecting a change in the soft phase due to the integration of hard segments from the destroyed low-temperature phase.
- Heating to 200 °C in the third heating further destroys additional high-temperature phases, indicated by endothermic peaks at 119 °C and 151 °C. These phases are likely more stable and require higher temperatures to break down. The breakdown releases more hard segments into the amorphous matrix, increasing the overall rigidity and shifting the T_g higher to 45 °C in the fourth last heating (indicated as 7 in Figure 38e)

The T_g of 45 °C reported in the manufacturer's data sheet may not accurately reflect the actual T_g under specific application conditions, especially when heating to relatively low temperatures (T_g+20 °C). Consequently, the T_g observed in subsequent heating cycles can vary depending on the maximum temperature to which the sample is heated. Here, the DSC results indicate that the actual T_g of the material is lower than 45 °C, if it has not been previously heated to 200 °C and cooled down. This finding also suggests that the T_g of the material is close to room temperature, necessitating caution when working with it at elevated temperatures. Therefore, the thermal history of the material significantly impacts its T_g, which should be considered when planning applications.

Table 4. *Summary of thermal cycles performed during DSC analysis, showing the T_g values and observed endothermic peaks for each cycle.*

Cycle number	Temperature (°C)	T_g (°C)	Endothermic Peak (°C)
1	0-50	29.26	-
2	50-0	27.35	-
3	0-110	28.98	74.31
4	110-0	33.21	-
5	0-200	32.47	119.34 and 151.11
6	200-0	44.27	-
7	0-200	44.79	160.82

The DSC measurement was repeated, by performing just three cycles on the PU-SMP: heating from 0 °C to 200 °C, cooling from 200 °C to 0 °C, and then reheating from 0 °C to 200 °C. This single run captured all the thermal transitions observed in the previous DSC

measurements across multiple cycles. Building on the previous DSC results (Figure 38), here the second heating curve (illustrated as the blue line in Figure 39), were used in determining the activation temperature range of the material. The onset and endpoint of the notable step change in this curve were identified at 41 °C and 48 °C, respectively. Both temperatures specify the boundaries of the PU-SMP activation range. Furthermore, T_g is derived from the midpoint of the step tangent on the DSC second heating curve, calculated to be approximately 45 °C. This temperature is pivotal as it represents the threshold above which the PU-SMP can be deformed and subsequently recovered, and below which any deformation imparted on the device remains fixed. This understanding of the temperature dependent behavior of the PU-SMP is crucial for its practical application in shape memory devices. The vicinity of T_g of the PU-SMP to ambient temperature allows for large plastic deformation, a high number of cyclic loading without failure, fast thermal actuation, as well as high values of shape recovery, in a lower temperature environment.

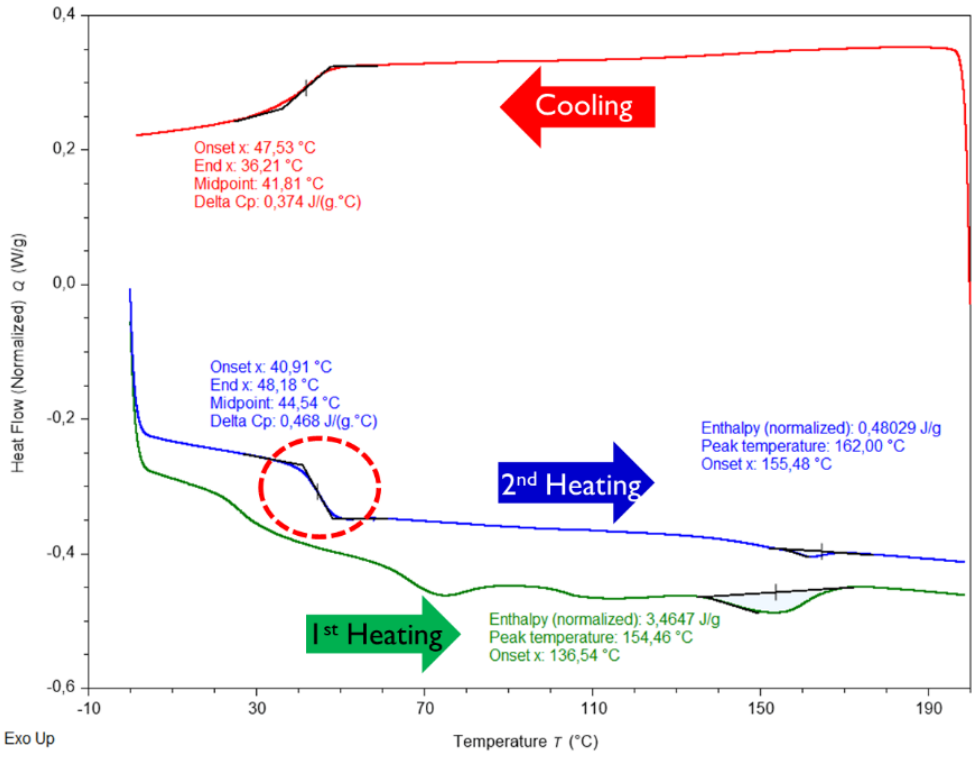

Figure 39. *DSC thermogram illustrating the thermal behavior of the material during sequential thermal cycles. The graph shows the first heating cycle (green curve), cooling cycle (red curve) and second heating cycle (blue curve).*

4.2 Investigation of PU-SMP Mechanical Properties by Tensile Testing Machine

Uniaxial tensile tests were conducted to thoroughly investigate the mechanical properties of the PU-SMP, particularly its elastic and plastic deformation behavior for subsequent thermomechanical analysis. The tests were performed on dog-bone specimens at room temperature (25 °C = T_g-20) using a constant strain rate of 10^{-2} s^{-1} until specimen failure (Figure 40).

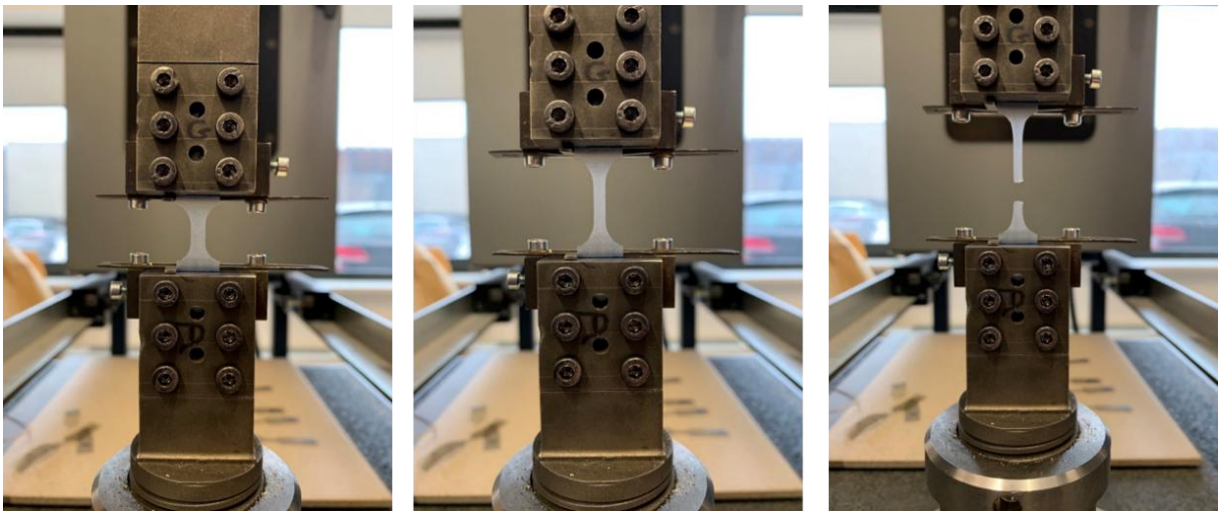

Figure 40. *Sequential images depicting the uniaxial tensile test performed on the dog-bone PU-SMP specimen at room temperature (25 °C) in the initial state (left photo), the elongation phase under a constant strain rate of 10^{-2} s^{-1} (middle photo), and the final rupture of the specimen (right photo).*

A typical stress-strain characteristic of the PU-SMP obtained from tensile tests to fracture is illustrated in Figure 41. Key mechanical properties, including the Young's modulus, yield strength, elongation at break and ultimate strength are summarized in Table 5. These parameters provide valuable insights into the material's performance under tensile stress at ambient temperature. However, due to the high flexibility of thermoplastic PU-SMP above its T_g and the substantial load capacity of the testing machine (50 kN), the testing machine was unable to register the applied force. As a result, the stress-strain behavior of PU-SMP in its rubbery state above T_g could not be determined.

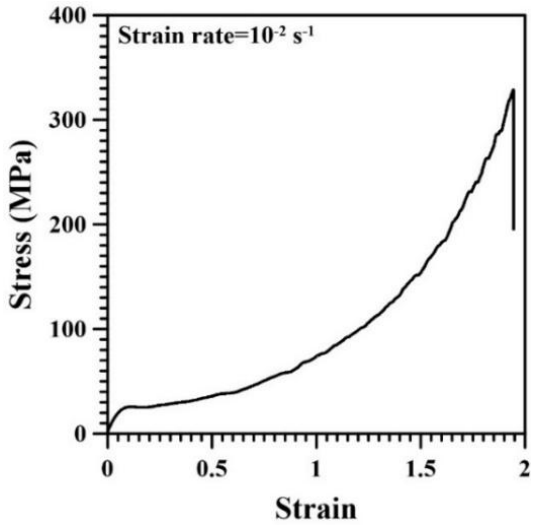

Figure 41. *Stress-strain curve of PU-SMP obtained from the uniaxial tensile test conducted at room temperature (25 °C) with a strain rate of 10^{-2} s^{-1} until fracture.*

Table 5. *Mechanical properties of PU-SMP at room temperature.*

Mechanical Properties	Values at T_g-20 = 25 °C
Young's Modulus (MPa)	391.16
Yield Strain (%)	4.29
Yield Stress (MPa)	17.98
Elongation at Break (%)	194.52
Ultimate Strength (MPa)	328.58

To further clarify the mechanical behavior of the PU-SMP, it is noteworthy to mention the exceptional deformability of the material at room temperature, as observed in the stress-strain curve in Figure 41. The curve distinctly shows strain hardening that occurs post-yielding and before fracture. Such a characteristic of SMPs indicates the potential suitability of the material for cold programming [118,119].

Traditionally, the thermomechanical cycle used to investigate the shape memory behavior of thermo-responsive shape memory polymers begins by heating the polymer above its T_g to achieve a rubbery state, where deformation is easier. It is necessary because the T_g of these polymers is significantly higher than room temperature, meaning that the polymer remains in a glassy state at room temperature. Deforming the polymer in its glassy state can result in substantial plastic deformation, which may hinder shape recovery or even lead to material failure. Therefore,

the appropriate thermomechanical cycle for these polymers typically involves sequential steps of heating, loading, cooling, unloading, and reheating to evaluate shape recovery performance. However, polymers with a T_g close to room temperature are flexible enough to exhibit plastic deformation without fracture at ambient conditions without prior heating. In cold programming, SMPs are loaded and unloaded at room temperature and then heated only for recovery, eliminating the need for initial heating and cooling steps. This simplifies the thermomechanical cycle to just three steps: loading, unloading, and heating. Shape fixity and recovery are measured as "the strain after unloading at room temperature" and "the strain after thermal recovery", respectively [120–122]. Figure 42 schematically illustrates the difference between conventional thermomechanical (hot programming) and cold programming approaches to studying shape memory behavior.

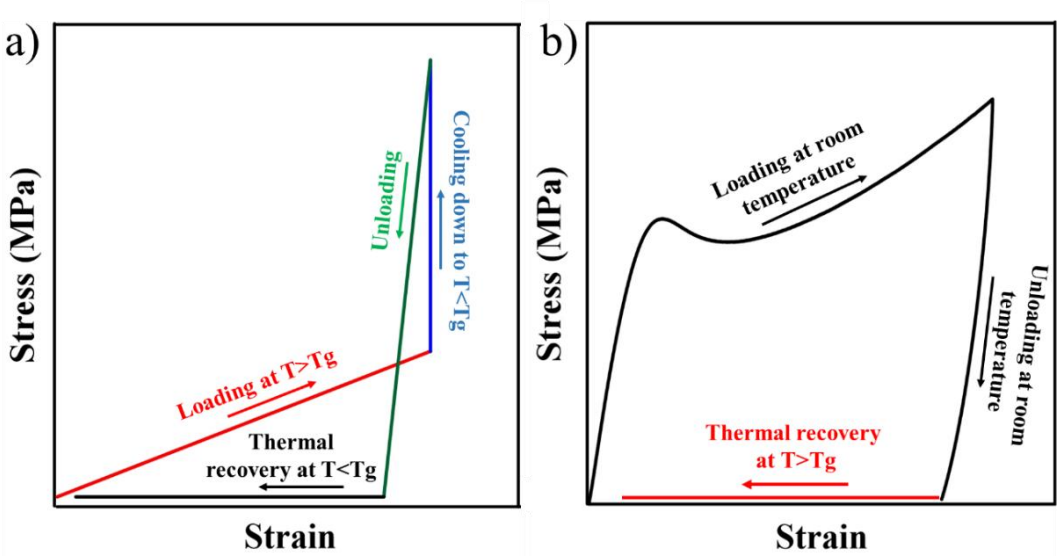

Figure 42. *Schematic of: a) conventional hot programming of SMP in a thermomechanical cycle; b) cold programming of SMP.*

The cold-programming feature is especially beneficial for polymers, where their low thermal conductivity can make reaching specific temperatures time-consuming. This approach eliminates the need for heating to induce flexibility or cooling to fix the deformation, as both processes can be efficiently performed at room temperature. Additionally, flexible SMPs with a T_g close to room temperature enable shape recovery after deformation at lower temperatures, further enhancing their practicality.

4.3 Microstructural Analysis of PU-SMP After Cold Deformation and Thermal Recovery

The temperature sensitivity of plastic deformation in polymers is a critical factor that must be considered. Below the T_g, polymers exist in a glassy state, where molecular mobility is greatly restricted. In this state, deformation often leads to brittle fracture or crazing. The formation of crazes is driven by the inability of the polymer chains to dissipate mechanical energy through molecular motion, resulting in localized stress concentrations that exceed the cohesive energy of the material. In contrast, when a polymer is deformed above T_g, in its rubbery state, the deformation mechanism shifts to involve the sliding and disentanglement of molecular chains, allowing for better energy dissipation and preventing localized failure. A thermo-responsive SMP exhibits the remarkable ability to recover from deformations that exceed both its elastic limit and yield point through the application of heat. To investigate this behavior, the effect of cold programming on the microstructure of PU-SMP was examined, where the material was loaded and unloaded at room temperature, followed by recovery induced above its T_g.

This investigation had two primary objectives: first, to compare the loading-unloading behavior of PU-SMP specimens with different thermal histories below their T_g; and second, to examine the microscopic behavior of the SMP when strained beyond its elastic and yield limits (below its T_g) and subsequently subjected to thermal recovery.

The tensile loading-unloading cycle of PU-SMP was performed under ambient conditions, as shown in Figures 43a and 43b. For the first specimen, a dog-bone PU-SMP specimen was tested without any preheating. It underwent a tensile loading-unloading cycle, during which the specimen was strained to 60% and then released at a constant strain rate of 10^{-2} s^{-1} (Figure 43a). In contrast, the second specimen was preheated to 110 °C in a thermal chamber, gradually cooled to room temperature, and then subjected to the same tensile loading-unloading cycle (Figure 43b). The 60% deformation level was specifically chosen based on prior tensile tests to rupture (Figure 41), which indicated that at this strain level, the polymer is in the strain-hardening phase. This means it has surpassed the yield point; however, it remains well below the fracture threshold, ensuring the integrity of the material throughout the cyclic loading-unloading process.

The mechanical properties of the non-preheated and preheated PU-SMP specimens are summarized in Table 6. The lower yield stress and Young's modulus observed in the non-

preheated specimen confirm the findings from the DSC analysis (Figure 39), which indicate structural changes during preheating. When the specimen is preheated to 110 °C and gradually cooled down, heating disrupts the hard phase within the polymer matrix. This disruption facilitates a reorganization of the PU-SMP structure, where the hard segments break down and mix with soft segments. This results in increased rigidity and a higher T_g, which explains the sharper yield stress and significantly higher Young's modulus in the preheated specimen. It is important to note that the values for each mechanical property are mean values obtained from repeated experiments. However, these values can vary with each test, as the material is sensitive to the environmental conditions during testing. Therefore, the comparison between the mechanical properties of the preheated and non-preheated specimens is more meaningful than the exact values themselves.

Figure 43c presents the SEM analysis of the gauge section (the stressed region) of the non-preheated PU-SMP specimen after deformation. Due to its lower T_g and reduced rigidity, the deformation primarily results in the formation of small micro-voids aligned parallel to the direction of applied force. These voids are scattered randomly across the surface and do not unify into larger defects such as crazes or cracks. This indicates that the plastic deformation of a non-preheated specimen with a T_g closer to room temperature causes minimal surface damage, likely due to its increased flexibility at ambient conditions. In contrast, Figure 43d reveals the SEM analysis of the gauge section of the preheated PU-SMP specimen post-deformation. The microstructural features highlight the formation of crazes and craze yielding, which are characteristic of deformation mechanisms in thermoplastic and amorphous polymers. Figure 43e schematically illustrates the micro-mechanism of craze formation, which occurs perpendicular to the loading direction due to plastic deformation [123,124].

The crazes are composed of elongated polymer chains (fibrils) separated by voids, with the fibrils oriented along the tensile stress direction. As the deformation progresses, the fracture of the fibrils and the expansion of voids lead to crack formation. The presence of such a deformation mechanism is evident in the SEM image of the preheated specimen (Figure 43d), where localized crazes and void formations are visible, demonstrating the larger plastic deformation of the material.

Interestingly, the yield strains of both specimens are comparable, suggesting that similar levels of deformation are required to reach the plastic zone. However, the higher T_g in the preheated specimen necessitates greater stress to exceed the yield point and induce plastic deformation, as

reflected in the stress-strain curves. This emphasizes the influence of thermal history on the mechanical response and microstructural evolution of PU-SMP under deformation.

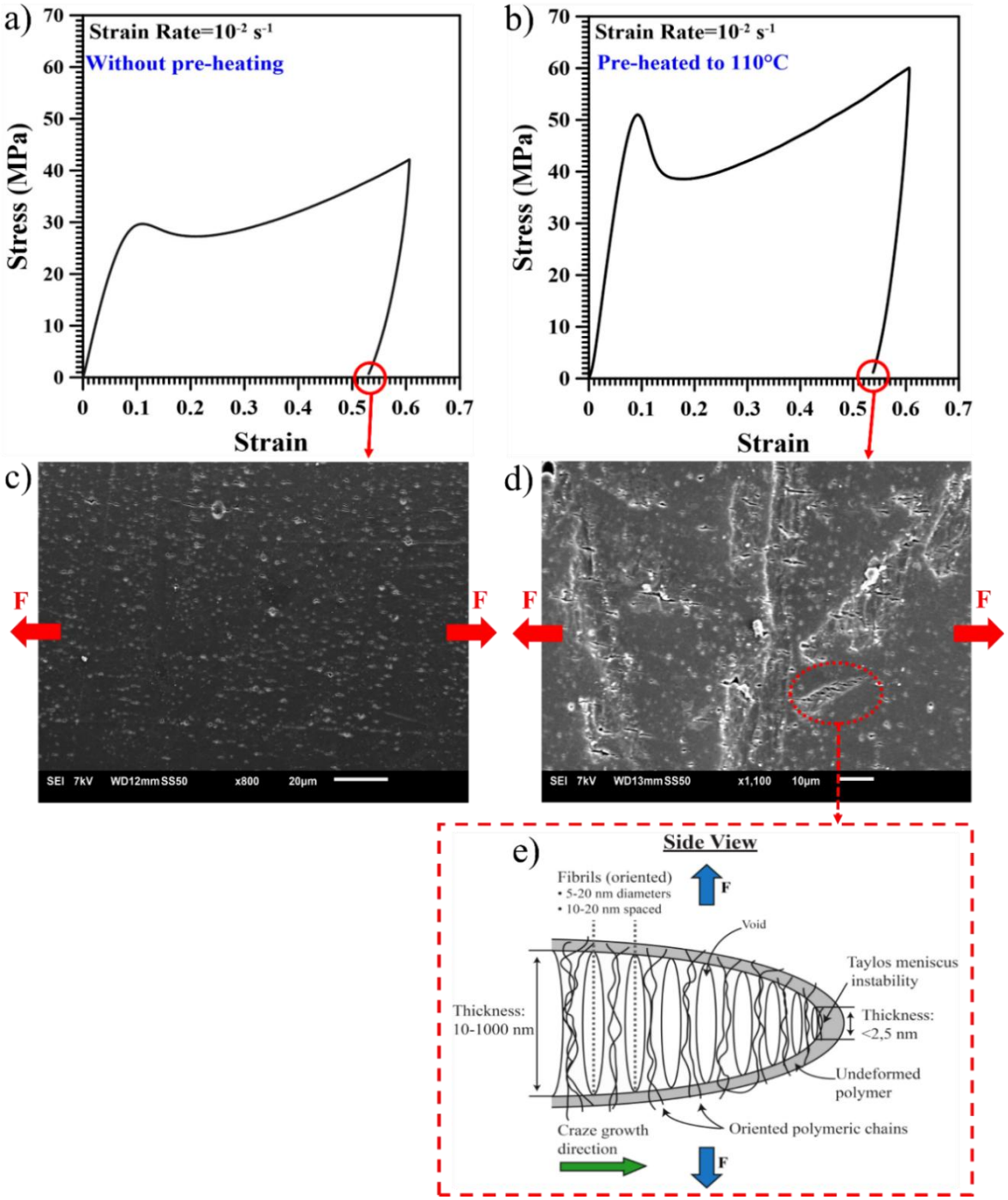

Figure 43. *a) Stress-strain curve of non-preheated PU-SMP during a single uniaxial tensile loading-unloading cycle at ambient temperatureconducted at strain rate of 10^{-2} s^{-1};b) Stress-strain curve of preheated PU-SMP under the same conditions; c) SEM image of the non-preheated specimen post-deformation, showing scattered micro-voids parallel to the loading direction (F); d) SEM image of the preheated specimen post-deformation, revealing crazes and voids perpendicular to the loading direction (F); e) Schematic of craze formation, illustrating fibrils and voids contributing to deformation* [125].

Table 6. *Comparison of mechanical properties of preheated and non-preheated PU-SMP at room temperature.*

Mechanical Properties	Values at T_g-20 = 25 °C Without Preheating	Values at T_g-20 = 25 °C Preheated to 110 °C
Young's Modulus (MPa)	384.40 ± 7.07	664.26 ± 12.13
Yield Strain (%)	6.63 ± 0.51	8.14 ± 0.62
Yield Stress (MPa)	25.39 ± 1.57	49.41 ± 3.46

Further examination involved heating and recovering of the deformed specimen in a thermal chamber to T_g+20 (65 °C), followed by re-evaluating the surface using SEM. Figure 44a shows the deformed specimen in the tensile grips (left) and the recovered specimen after being heated to 65 °C in the thermal chamber (right). Figure 44b illustrates the traces of closed voids and micro-crazes on the PU-SMP surface upon heating, demonstrating the self-healing capabilities of the SMP and its potential for durability. As a result, the material proves suitable for cold-drawing and plastic deformation at temperatures below its T_g without failure, while also exhibiting microscale shape recovery upon heating.

It is important to note that the thermal recovery of the specimens after the loading-unloading cycles was not carried out within the tensile grips. Handling the flexible material at elevated temperatures between the grips provides some technical challenges; therefore, recovery was conducted in a thermal chamber, without monitoring the stress recovery of the specimens.

Healing and closure of cracks in PU-SMP when thermally recovered above its T_g is a complex process affected by several factors, including increased molecular mobility, the intrinsic shape memory effect, stress relaxation, and the unique molecular structure of the polymer. Initially, micro-crazes or cracks form on the surface of the PU-SMP due to plastic deformation, typically caused by mechanical loading. These micro-cracks disrupt the continuity of the polymer matrix, leading to localized areas of stress concentration. When the deformed specimen is heated above its T_g, molecular mobility within the polymer increases significantly, enabling the material to undergo structural changes. The rise in temperature causes thermal shrinkage of the deformed specimen, which brings the surfaces of the cracks closer together, facilitating crack closure.

In addition to the thermal shrinkage, further heating can cause the soft segments of the polymer to enter a molten state, reducing their viscosity and allowing them to flow more freely. The molten segments are then drawn into the narrowed cracks by capillary forces, which occur due to the surface tension between the molten material and the surrounding solid polymer. As the

molten polymer flows into the cracks, it diffuses across the fractured surfaces, driven by a concentration gradient, and begins to bond the surfaces at a molecular level. Thus, the traces of healed micro-cracks observed in the PU-SMP are a result of physical healing, where the self-healing mechanisms of the material, activated by elevated temperatures, lead to the effective closure and bonding of fractured surfaces, enhancing the material's durability and longevity [126–128].

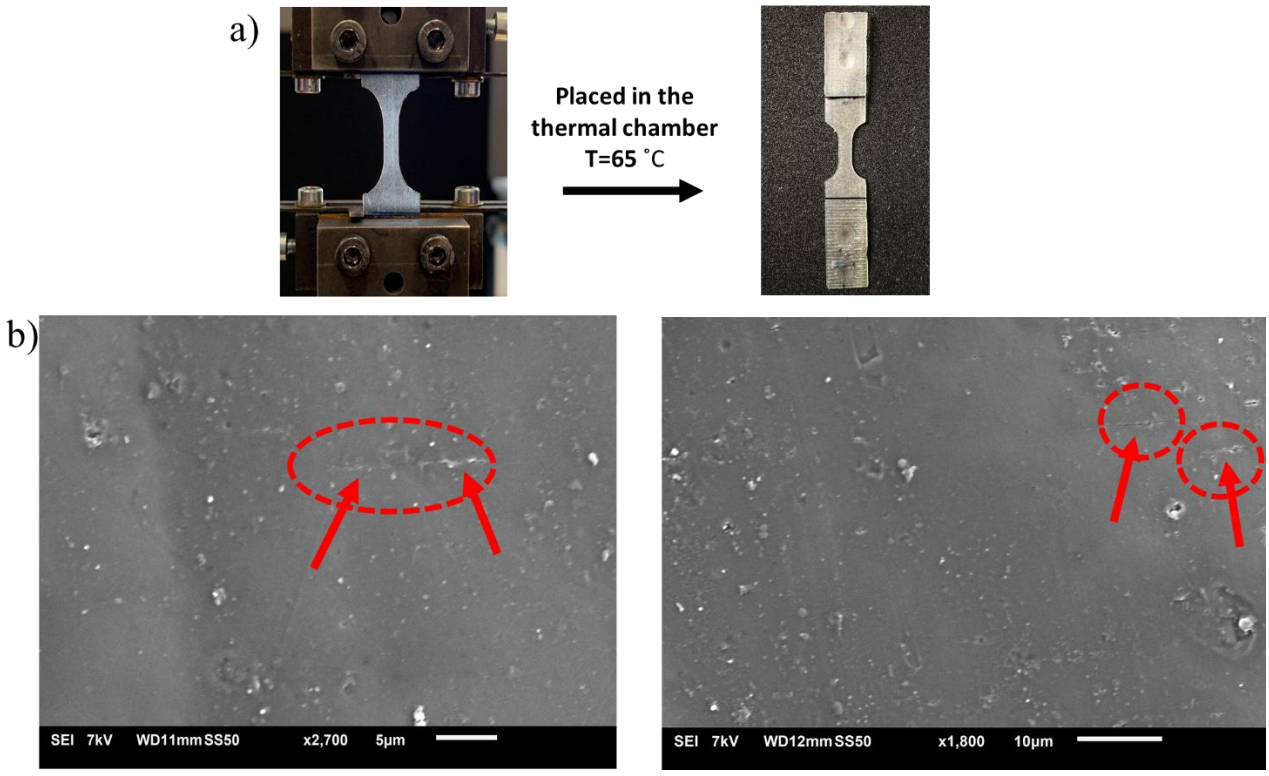

Figure 44. *a) PU-SMP specimen within the tensile grips after deformation (left) and following recovery in the thermal chamber at 65 °C (right); b) SEM images of the specimen surface after recovery at 65 °C, red circles and arrows highlight the healed micro-crazes and voids.*

It has to be emphasized that the experiments with PU-SMP faced several challenges. The high flexibility of the material, along with the high load cell capacity of the testing machine, made challenges for the instrument to accurately measure the applied force at high temperature. This limitation restricts our ability to fully evaluate the influence of high temperatures on the mechanical properties of PU-SMP. Additionally, the limited availability of PU-SMP restricted the number of experiments to be conducted in the experimental program. As a result, despite its potential for cold programming, shape memory training under cold programming conditions was not carried out.

4.4 Mechanical Behavior of PU-SMP Under Cyclic Tensile Loading-Unloading

As discussed in the previous section, PU-SMP exhibits not only high flexibility at ambient conditions but also the ability to recover micro-defects after undergoing plastic cold-drawing. This unique property motivated us to investigate its performance under repeated cyclic deformation at room temperature, a critical feature for applications requiring materials that endure cyclic mechanical loads without failure. Examples of such applications include flexible hinges in deployable structures [129], biomedical implants (e.g., stents or prosthetic components) [130,131], and fatigue-resistant components in soft robotics [132] and wearable electronics [133].

To evaluate the endurance of PU-SMP under cyclic deformation, a strain-controlled cyclic loading test was performed. A preheated SMEp dog-bone specimen was subjected to 9000 cycles of tensile loading-unloading at a constant strain rate of 10^{-2} s^{-1}, reaching 60% strain in each cycle before being unloaded to a no-load state. Remarkably, the specimen did not fracture, demonstrating the material's exceptional durability even when repeatedly deformed within its plastic zone.

Figure 45a presents the resulting stress-strain response over successive cycles. The magnified section highlights the cyclic behavior, with each cycle range color-coded to illustrate the evolution of material response during repeated loading and unloading (Figure 45b). The narrowing of hysteresis loops over time suggests a progressive stabilization of the material's deformation characteristics, reinforcing its potential for applications requiring long-term mechanical reliability.

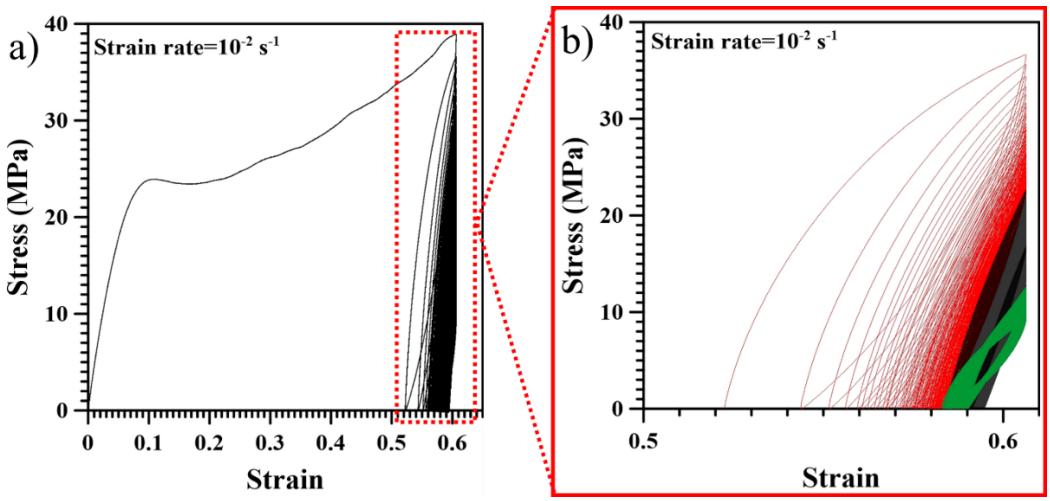

Figure 45. *a) Stress-strain curve of PU-SMP subjected to 9000 cycles of strain-controlled tensile loading-unloading at a strain rate of 10^{-2} s^{-1}, reaching 60% strain in each cycle; b) Magnified view of the cyclic loading region, highlighting the progressive stabilization of the material's response over successive cycles. The color-coded regions illustrate the evolution of hysteresis loops, demonstrating the material's endurance and plastic deformation behavior under repeated loading.*

The evolution of Young's modulus, residual strain (set), maximum stress and hysteresis loop area over repeated cycles was calculated and analyzed for each loading cycle. The trends of these features are illustrated in Figure 46, Figure 47, and Figure 48, respectively, providing insights into the mechanical response of PU-SMP under cyclic deformation.

Figure 46 shows the variation in elastic modulus across cycles, calculated from the slope of the initial linear portion of the loading phase in each cycle. The two accompanying stress-strain curves on the right illustrate how the slopes are tangent to the elastic region of the loading in the first cycle (top curve) and subsequent cycles (bottom curve) to determine the Young's modulus for each cycle. The data reveal three distinct stages in the material's response:

- Rapid increase (Red region): During the initial cycles, the elastic modulus rises abruptly from its baseline value, reflecting a cyclic hardening phenomenon. This is primarily driven by the alignment and reorientation of polymer chains as the material adapts to the repeated tensile loading. The initial loading cycles help to "reorient" the microstructure, producing strain-hardened regions that withstand deformation more effectively, thus leading to a steep increase in modulus.

- Plateau region (Black region): After the polymer chains have adjusted to the repeated loading, the elastic modulus stabilizes around 1400 MPa. At this plateau, minimal microstructural changes occur, indicating that the chain entanglement and orientation

reached in the red region are sufficiently maintained to preserve mechanical integrity. The material sustains approximately 5000 cycles with only minor fluctuations in modulus, highlighting its fatigue resistance over this span.

- Degradation phase (Green region): Beyond 5000 cycles, the modulus declines markedly, falling to about 800 MPa, signaling the onset of mechanical deterioration. This degradation is likely caused by microstructural fatigue, where repeated cyclic loading leads to the breakdown of entanglements, accumulation of microvoids, and polymer chain reorganization. These damage mechanisms progressively reduce the stiffness of the material, demonstrating that, despite its earlier resilience, the PU-SMP eventually experiences significant fatigue-induced weakening at higher cycle numbers.

This analysis highlights the initial strengthening of PU-SMP, extended stability, and eventual degradation, showing its potential for applications requiring cyclic durability, while also identifying its long-term mechanical limitations [134,135].

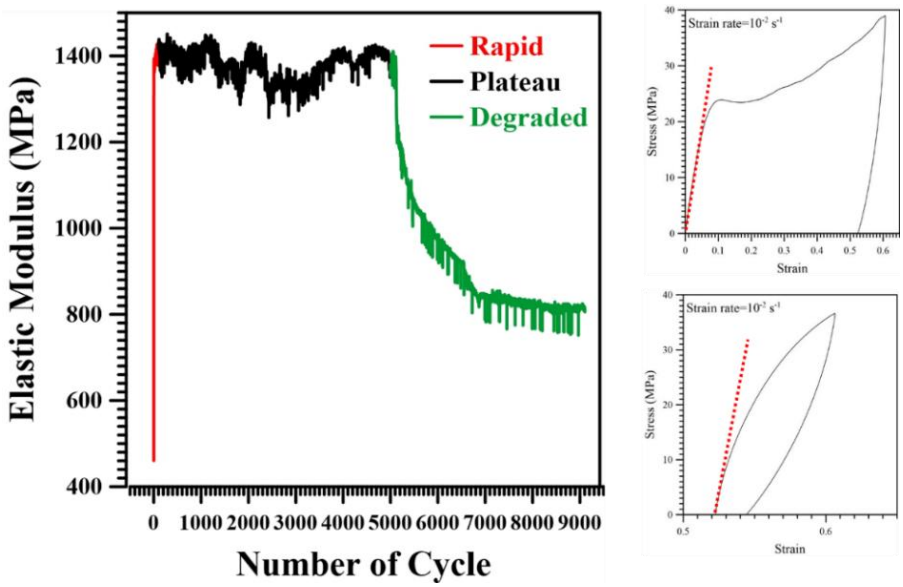

Figure 46. *Evolution of the elastic modulus in PU-SMP over 9000 strain-controlled tensile loading-unloading cycles. The rapid increase (red) indicates strain hardening, followed by a plateau (black) and eventual degradation (green). The stress-strain curves on the right compare the elastic modulus measurement in early (top diagram) and later (bottom diagram) cycles.*

Permanent set or residual set is the irreversible deformation that remains after a material has been loaded and subsequently unloaded. It quantifies the polymer's inability to fully recover

its original shape after deformation or, alternatively, its ability to retain deformation after unloading.

Here, set is defined as the unloading strain after each cycle, measured relative to the initial strain in the first cycle, which is zero.

Figure 47 illustrates the evolution of the set over 9000 cycles. The stress-strain curves on the right side visually demonstrate the measurement of the set in different cycles. The top curve represents the first cycle, and the bottom one corresponds to a later cycle. Figure 47 exhibits a characteristic three-phase behavior, similar to the trends observed for the elastic modulus (Figure 46):

- Rapid increase (red region): In the first few cycles, permanent set rises sharply, indicating that the polymer chains within the PU-SMP begin to reorganize and settle into new configurations upon repeated loading and unloading. During these early cycles, the material experiences strain-induced alignment and partial plastic flow, leading to the greater residual deformation after unloading.

- Plateau region (black region): in the plateau phase, the polymer chain network stabilizes, and microstructural changes occur at a much slower rate. The material retains a relatively constant residual deformation across thousands of cycles, suggesting that large-scale chain slippage or additional rearrangement is minimal. In other words, the polymer appears to find a steady-state deformation regime where the incremental damage (or plastic rearrangement) per cycle is negligible.

Degradation phase (green region): Beyond approximately 5000 cycles, the permanent set begins to fluctuate and slightly decrease. This can be attributed to fatigue-induced microdamage, in which chain scission, voids, or crazes disrupt the organized entanglement network. Here, a minor drop in permanent set occurs, due to the decrease of the material's capacity to hold onto the same permanently deformed configuration, allowing partial relaxation between cycles and the decrease of the residual strain. Over an extended number of cycles, these microstructural degradations lead to a new equilibrium where the residual strain, while still significant, settles to a lower level than during the plateau [136].

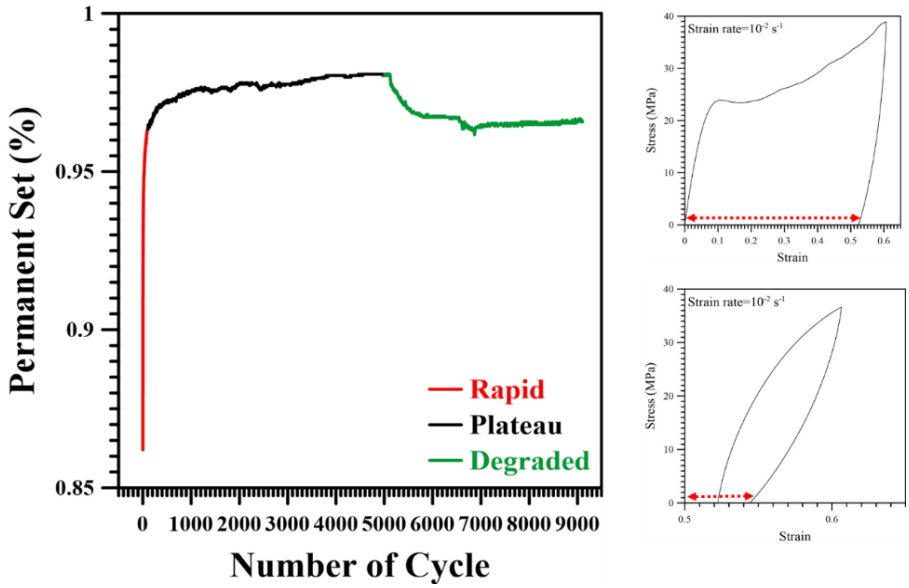

Figure 47. *Evolution of the permanent set in PU-SMP over 9000 strain-controlled tensile loading-unloading cycles, showing an initial rapid increase (red), a plateau phase (black), and eventual degradation (green). The stress-strain curves on the right compare the permanent set measurement in early (top diagram) and later (bottom diagram) cycles.*

Figure 48 presents the evolution of maximum stress before unloading over 9000 cycles. The stress-strain curve on the right illustrates the maximum stress after the first and second loading in their respective cycles, measured at the peak of the loading curve just before unloading begins. The maximum stress values for all subsequent cycles are measured in the same manner. Notably, the stress required to reach 60% strain gradually decreases with increasing cycles, following three distinct phases:

- Rapid decrease (red region): In the first few cycles, the maximum stress drops sharply from approximately 40 MPa to around 20 MPa within the first few cycles. This stress softening is characteristic for the Mullins effect, commonly observed in filled and unfilled rubbers as well as two-phase structure polymers like polyurethane. The Mullins effect is attributed to microstructural evolution, where the effective volume fraction of the soft phase increases as the material adapts to deformation, irreversible damage in the hard segments, or a combination of both mechanisms. In this region, the soft phase undergoes partial disentanglement and strain-induced molecular alignment, while the hard domains experience plastic adaptation or partial detachment, leading to the rapid decrease in maximum stress before unloading. Additionally, when polymers are loaded and unloaded

below their T_g (cold deformation), irreversible plastic deformation in the glassy state can further contribute to softening [136–138].

- Plateau region (black region): After the initial adaptation, the stress stabilizes around 15–18 MPa for nearly 5000 cycles. This indicates that the material has reached a mechanically stable state, where the polymer network is sufficiently aligned, and further entanglement rearrangement is minimal. In this region, the hard and soft phases reach an equilibrium, sustaining repeated deformation without further significant softening. The prolonged plateau suggests that the two-phase structure of PU-SMP provides good fatigue resistance, at least up to this point.

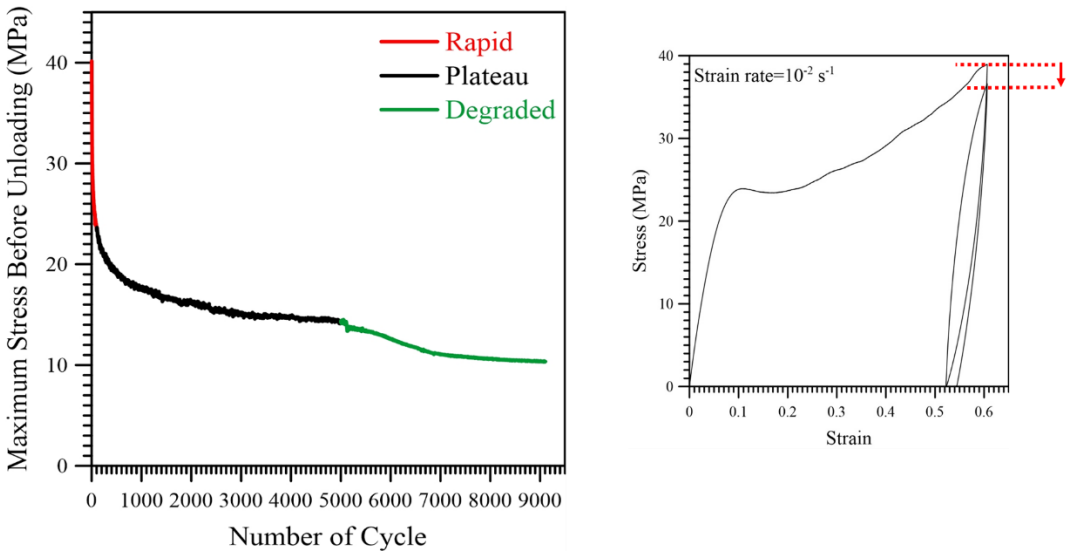

Figure 48. *Evolution of the maximum stress before unloading in PU-SMP over 9000 strain-controlled tensile loading-unloading cycles, showing an initial rapid decrease (red), a plateau phase (black), and eventual degradation (green) . The stress-strain curves on the right illustrate the maximum stress after the first and subsequent loading cycles.*

Degradation phase (green region): Beyond 5000 cycles, maximum stress starts to gradually decline, reaching about 10 MPa. This phase indicates the onset of fatigue-induced damage and progressive softening, likely due to, breakdown of entanglements in the soft phase, microvoid formation or crazing in the hard phase and phase separation or internal fracture, reducing load-bearing capacity. This behavior suggests that long-term cyclic loading leads to material deterioration, limiting its application in high-cycle fatigue environments.

At first glance, the simultaneous increase in the Young's modulus and decrease in maximum stress before unloading seem to be contradictory. However, the trends reflect distinct mechanical responses within different regions of the stress-strain curve. The Young's modulus is derived from the initial linear elastic region, where small deformations are governed by molecular interactions. In the early cycles of loading, polymer chain alignment and entanglement tightening enhance resistance to small strains, leading to an increase in modulus. This means the material becomes stiffer, but not necessarily stronger in terms of load-bearing capacity. In contrast, the maximum stress before unloading represents the polymer's ability to sustain applied strain before releasing the load. With repeated loading, chain disentanglement, phase reorganization, and energy dissipation in the plastic zone reduce internal resistance to deformation. As a result, the stress required to reach 60% strain gradually decreases, even as the material stiffens in the elastic region.

In summary, an increase in the Young's modulus indicates structural adaptation and stiffening in the elastic region, while a decrease in maximum stress before unloading suggests that the material is softening at higher strains, adapting to deformation with reduced resistance.

As the next key parameter, the hysteresis loop area of each cycle was measured, which quantifies the energy dissipation per unit volume (J/m^3) during each loading-unloading cycle. Unlike rubbers, which exhibit highly elastic behavior, thermoplastic polymers do not fully return to their original shape upon unloading, especially when deformed beyond their yield point to the plastic region. In fact, a portion of the applied mechanical energy is stored elastically during loading, enabling partial recovery during unloading. However, a significant fraction is dissipated due to molecular friction, chain sliding, and permanent deformation within the polymer matrix. As unloading begins, the stored elastic energy is released, but the material does not follow the same loading path. Instead, a hysteresis loop forms between the loading and unloading curves, representing the mechanical energy lost due to viscoelasticity, molecular rearrangement, and plastic deformation.

Figure 49a presents a schematic stress-strain curve for the first loading-unloading cycle, where the shaded area represents the hysteresis loop area. This large loop in the first cycle confirms maximum energy dissipation, primarily due to initial molecular rearrangement and plastic adaptation. In Figure 49b, subsequent loops exhibit a reduced area, indicating cyclic stabilization as polymer chains realign, entanglements tighten, and internal friction decreases over successive cycles.

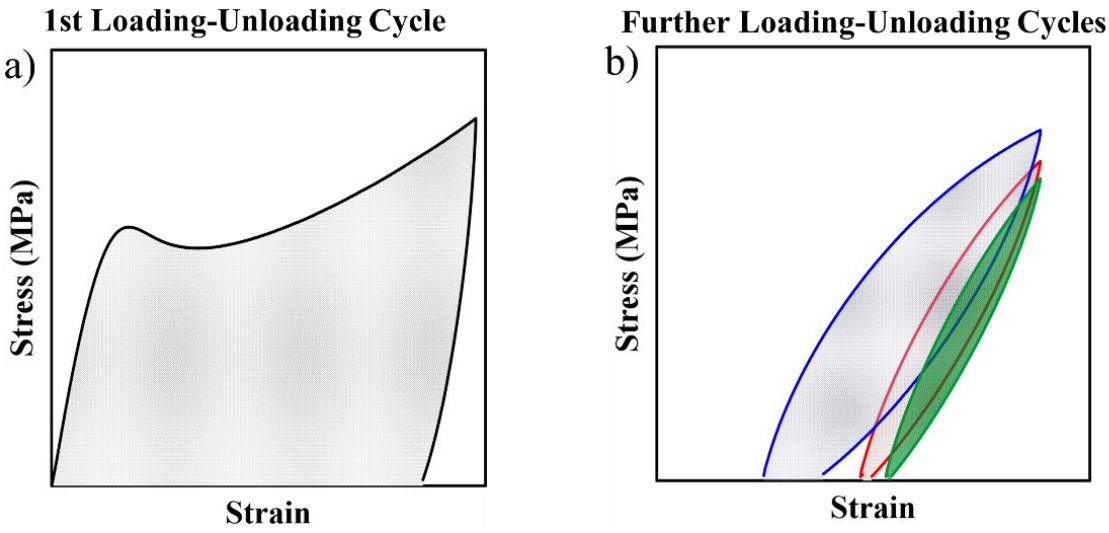

Figure 49. *Schematic representation of the hysteresis loop in the stress–strain curve: a) during the first loading–unloading cycle; and b) during subsequent loading–unloading cycles.*

Figure 50 presents the evolution of the hysteresis loop area over 9000 cycles of strain-controlled tensile loading-unloading. The hysteresis loop area is measured as the energy dissipation per unit volume (J/m^3), corresponding to the enclosed area within each cycle's stress-strain curve. This trend, consistent with previous mechanical behavior observations, follows three distinct regions:

- Rapid decrease (red region): The first cycle exhibits the largest hysteresis loop area, as clearly seen in Figure 45a and Figure 49a. During the initial cycle, polymer chains undergo irreversible rearrangement, and entanglements partially break, leading to significant energy dissipation. Additionally, microplasticity in the hard domains and internal friction within the soft phase contribute to the large hysteresis.

- Plateau region (black region): From the second cycle, the hysteresis loop area decreases and stabilizes into a plateau for approximately 5000 cycles. This reduction is due to the progressive alignment of polymer chains and the stabilization of internal structural rearrangements. In fact, the hard and soft domains adapt to cyclic deformation, leading to lower internal friction and energy dissipation per cycle. Therefore, once the material reaches this stable phase, cyclic hysteresis remains nearly constant, indicating fatigue resistance within this range.

- Degradation phase (green region): Beyond 5000 cycles, the hysteresis loop area increases again, marking the onset of mechanical degradation in the material. This increase is likely caused by microstructural fatigue, leading to progressive damage accumulation in the hard phase, such as microvoid formation, crazing and microcrack propagation. The zoomed-in view in Figure 50b highlights this increase more clearly, showing that hysteresis energy grows in the degraded region due to higher energy dissipation from emerging defects [139,140].

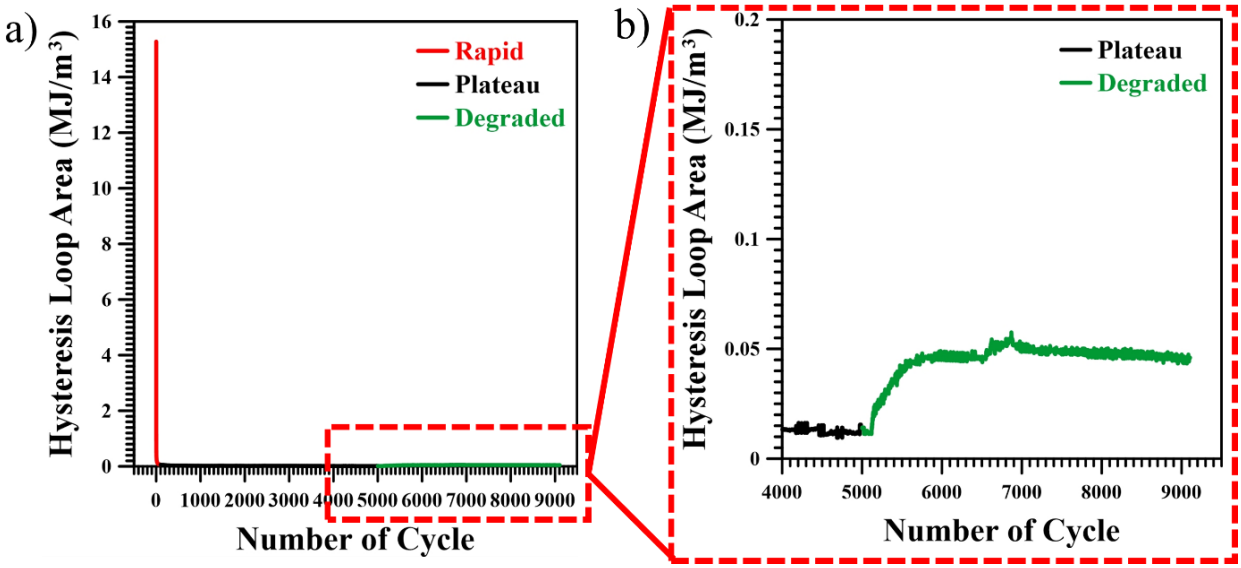

Figure 50. *a) Evolution of the hysteresis loop area in PU-SMP over 9000 strain-controlled tensile loading-unloading cycles, highlighting an initial rapid decrease (red), a stable plateau phase (black), and a subsequent increase in the degradation phase (green); b) Zoomed-in view of the degraded region, illustrating the progressive rise in hysteresis energy beyond 5000 cycles.*

4.5 Microstructural Behavior of PU-SMP after Cyclic Tensile Loading-Unloading

To investigate the microstructural changes occurring on the surface of PU-SMP specimens subjected to cyclic tensile loading-unloading, the gauge section of the specimens (the region under stress) was examined after 1, 3, 5, 8, and 9000 cycles. The cyclic tests were performed under a constant strain rate of 10^{-2} s^{-1} at room temperature, with the material being loaded to attain 60%

strain in each cycle before being fully unloaded. All specimens were preheated to 110°C and slowly cooled to room temperature before testing to ensure a uniform thermal history.

Figure 51a displays the PU-SMP surface before any deformation, showing a smooth morphology with no visible defects. Figure 51b represents the PU-SMP surface after a single loading-unloading cycle, depicting the formation of microvoids (2–10 μm) aligned parallel to the loading direction. It confirms stress-induced microvoid initiation, likely due to the localized plastic deformation and strain-induced phase separation in the polymer matrix. This image corresponds to the early-stage Mullins effect, where soft-segment mobility increases, and the hard-segment domains start adapting to strain. The surface in Figure 51b corresponds to that presented in Figure 43d, however, it shows a different area of the gauge section of the same specimen. Figure 51c shows the PU-SMP surface after 3 loading-unloading cycles, where defect traces appear more aligned with the loading direction, but no distinct microvoids are visible anymore. It can be attributed to the alignment of the polymer chains along the loading direction after a few cycles improving their ability to stretch and slide rather than fracture and improving their ability to stretch and slide rather than fracture and discrete void formation. Figure 51d depicts a rougher surface after 5 loading-unloading cycles, indicating the progression of surface damage. Interestingly, there is no significant craze or void formation at this stage, which could be again attributed to strain-hardening effects that delay the major defect growth. The increase in roughness may stem from slip deformation at the molecular level.

Figure 51e illustrates coalescence of microvoids into larger defects after 8 cycles, marking the transition toward crack initiation. The defects begin to propagate perpendicularly to the loading direction, indicating the onset of fatigue damage. This stage suggests that cyclic energy dissipation and accumulated plastic strain exceed the ability of the material to recover. Figure 51f shows widened cracks propagating perpendicular to the loading direction after 9000 cycles, signaling severe material degradation and fatigue failure. At this stage, the polymer matrix exhibits microstructural fatigue, with cracks expanding along stress concentration zones and leading to mechanical failure.

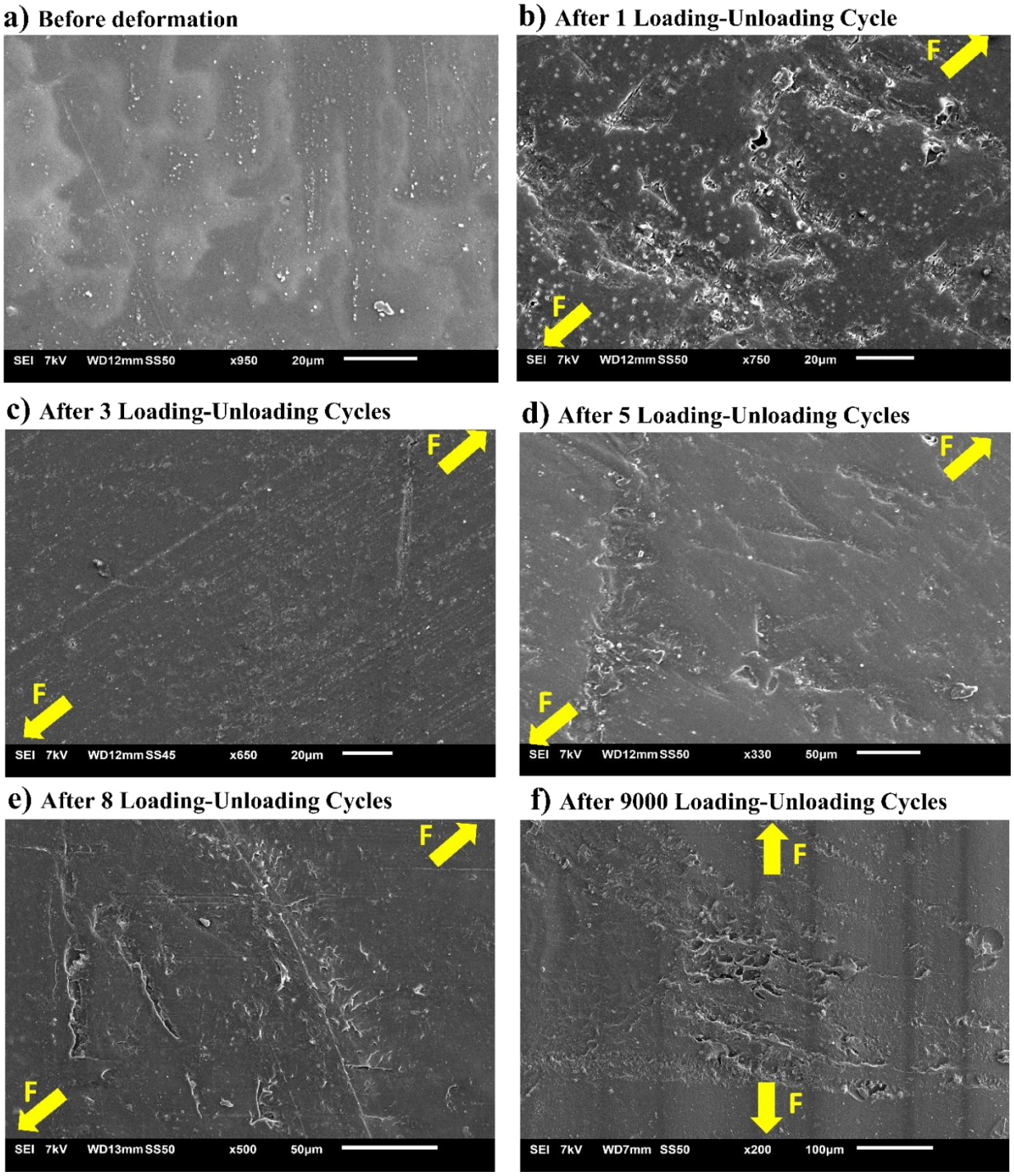

Figure 51. *SEM images of the PU-SMP surface a) before deformation; b) after 1 loading-unloading cycle; c) after 3 cycle; d) after 5 cycle; e) after 8 cycle; f) after 9000 cycle at ambient temperature.*

In fact, this observation showed that the merging of microvoids into larger defects after eight cycles indicates the start of damage accumulation; however, it does not necessarily mean immediate material failure. The viscoelastic nature of PU-SMP allows stress redistribution, slowing down crack propagation and preventing premature rupture. Additionally, strain-induced molecular reorganization enhances toughness. Over time, polymer chain entanglements strengthen, forming a secondary network that hinders rapid defect expansion. Given the relatively low applied stress per cycle, damage accumulates gradually, allowing the material to endure 9000 cycles without catastrophic failure. The stable hysteresis behavior further confirms controlled energy dissipation, indicating that while fatigue progresses, the material retains sufficient structural integrity to sustain prolonged cyclic loading.

4.6 Effect of Temperature on the Mechanical and Microstructural Response of PU-SMP in a Loading-Unloading Cycle

The effect of temperature on the mechanical behavior and surface microstructure of PU-SMP is studied in this section. A single loading-unloading cycle was performed at the constant strain rate of 10^{-2} s^{-1} on preheated PU-SMP specimens at T_g = 45 °C and T_g+20 = 65 °C, as well as on a specimen tested at room temperature (T_g-20 = 25 °C). In all cases, the specimen was loaded to attain 60% of strain before being fully unloaded.

The results in Figure 52 and Table 7 highlight the influence of temperature on the mechanical behavior of PU-SMP.

At 25 °C, the material exhibits the highest Young's modulus and stiffness as well as maximum stress before unloading, with a pronounced yield strength and strain hardening effect, reflecting its dominant glassy-state deformation. This is because the material resists deformation more effectively at lower temperatures. As the temperature reaches T_g and rises above it, the modulus decreases, since polymer chains gain mobility above T_g (45 °C), leading to a more compliant response.

The hysteresis loop area and set in a single loading-unloading cycle decrease significantly as the temperature approaches and exceeds T_g. As mentioned, in polymers, "set" refers to the permanent deformation or strain that remains in a material after it has been subjected to loading and subsequently unloaded. Hysteresis and set reduction are attributed to the transition from the glassy state (at 25 °C), where molecular mobility is restricted, to the rubbery state (at 65 °C), where

segmental motion is more active, allowing better elastic recovery and less internal friction. The residual strain at 25 °C is 86.2%, meaning that most of the applied strain remains as permanent deformation due to plasticity in the glassy state.

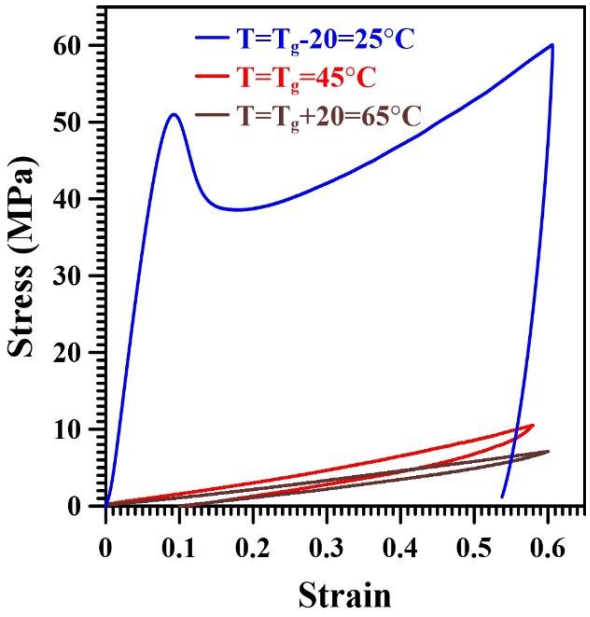

Figure 52. *Stress-strain curves of preheated PU-SMP during a single uniaxial tensile loading-unloading cycle at 25 °C, 45 °C, and 65 °C, conducted at a strain rate of 10^{-2} s^{-1}.*

Figure 53 presents SEM images of the gauge section of preheated PU-SMP specimens after a single uniaxial tensile loading-unloading cycle at 25 °C, 45 °C, and 65 °C, performed at a strain rate of 10^{-2} s^{-1}. These images highlight the effect of temperature on the microstructural evolution of PU-SMP post-deformation.

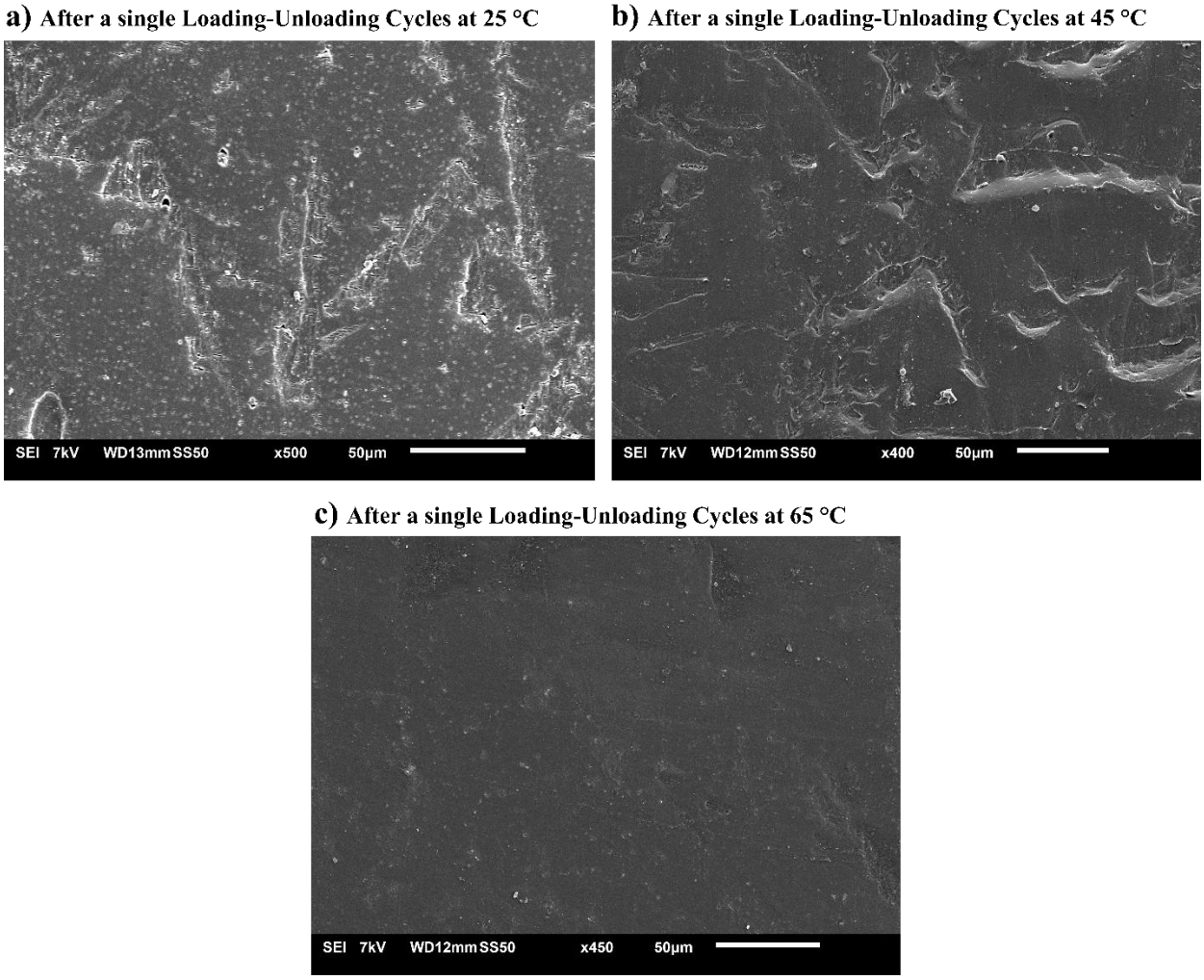

Figure 53. *SEM images of the PU-SMP surface after a single uniaxial tensile loading-unloading cycle at: a) 25 °C; b) 45 °C; and c) 65 °C.*

The surface in Figure 53a exhibits distributed microvoids across the specimen, suggesting that below T_g, the material undergoes plastic deformation with crazing and microvoid formation, characteristic of amorphous polymers in their glassy state. The high stiffness at room temperature (T_g-20 °C) restricts chain mobility, leading to stress-induced microvoid nucleation. In Figure 53b, no visible microvoids are observed on the surface; however, increased roughness and larger defects are present, indicating a more ductile deformation mechanism compared to the brittle-like behavior seen in Figure 53a. The surface in Figure 53c is significantly smoother than at lower temperatures. The polymer is in its rubbery state above T_g, where molecular motion facilitates deformation without significant microstructural damage. The material primarily undergoes viscoelastic deformation, preventing crazing or microvoid formation. Instead, the applied stress dissipates

through chain disentanglement and molecular reconfiguration, leading to a negligible residual damage.

Table 7. *Mechanical properties of PU-SMP during a single tensile loading-unloading cycle at 25 °C, 45 °C, and 65 °C.*

Temperature (°C)	Young's Modulus (MPa)	Hysteresis Loop Area (MJ/m^3)	Set (%)	Maximum Stress Before Unloading (MPa)
25	460.57	142.25	86.20	40.15
45	16.11	1.14	11.65	10.19
65	9.08	0.51	10.00	6.90

4.7 Shape Memory Behavior of Thermo-Responsive PU-SMPs: An Analysis of Shape Fixity and Recovery

Thermo-responsive SMPs exhibit a unique ability to retain a deformed shape below their T_g and to recover their original form above T_g. This dual behavior, fundamental to SMPs, can be characterized by shape fixity and shape recovery. Both parameters, originally conceptualized by H. Tobushi and S. Hayashi and subsequently explored by others, are crucial for applications where precise shape alteration is required [39,141].

A thermomechanical cycle involving five stages of heating, loading, cooling, unloading, and shape recovery - is necessary to accurately determine the shape fixity and recovery. Our initial objective was to identify the challenges associated with testing this process. However, some difficulties with the standard dog-bone thermoplastic PU-SMP specimen were encountered. When heated to 65 °C and loaded to 60% strain, the test could not proceed to the next step of the cycle. This was due to the small volume of the specimen between the tensile grips and its high flexibility at elevated temperatures, which prevented stable force detection and test continuation. As a result, the testing machine was unable to detect sufficient force, causing premature test termination during the switching steps of the thermomechanical cycle.

To overcome such situations, it was decided to apply the strip specimens with larger cross-sections instead of dog-bone specimens, facilitating force detection by the testing apparatus. Additionally, the deformation at high temperatures was limited to no more than 20% and a lower

strain rate of 10^{-3} s^{-1} was applied. The test was conducted three times on three distinct PU-SMP specimens. Figure 54 illustrates the results of thermomechanical cycles applied; specifically, diagrams in Figure 54a, b, and c present the stress-time, strain-time, and stress-strain curves for Specimen 1, respectively. Figure 54d, e, and f display the corresponding plots for Specimen 2, and Figure 54g, h, and i show the same relationships for Specimen 3. Each step in each figure is color-coded for clarity:

1. The first step (red line) starts with heating the specimen to T_g+20 °C (65 °C) in an environmental thermal chamber while located between grips under a small force of 0.2 N. During the heating, the material experienced thermal expansion, a common characteristic in polymers. Unlike other studies, the thermal elongation alongside the mechanical deformation was accounted in the subsequent step when calculating the PU-SMP shape recovery. This is because the initial thermal elongation is also a part of the deformation, and it is important to determine whether the material can recover it later or not.

2. Subsequently, the specimen was elongated by 20% at 65 °C in the environmental thermal chamber (purple line).

3. Next (blue line), the material was cooled down to room temperature while maintaining the strain, recording the material's inherent contraction stress during cooling.

4. After cooling the specimen down to room temperature, it was then unloaded to zero force (green line).

5. In the final step (black line), the specimen was reheated to T_g+20 °C under a force of 0.2 N, allowing us to observe and record the strain recovery process. It was noted that the SMP recovers its original shape up to a certain point before starting to expand. This observation was critical, indicating the need to terminate the test before the onset of this expansion.

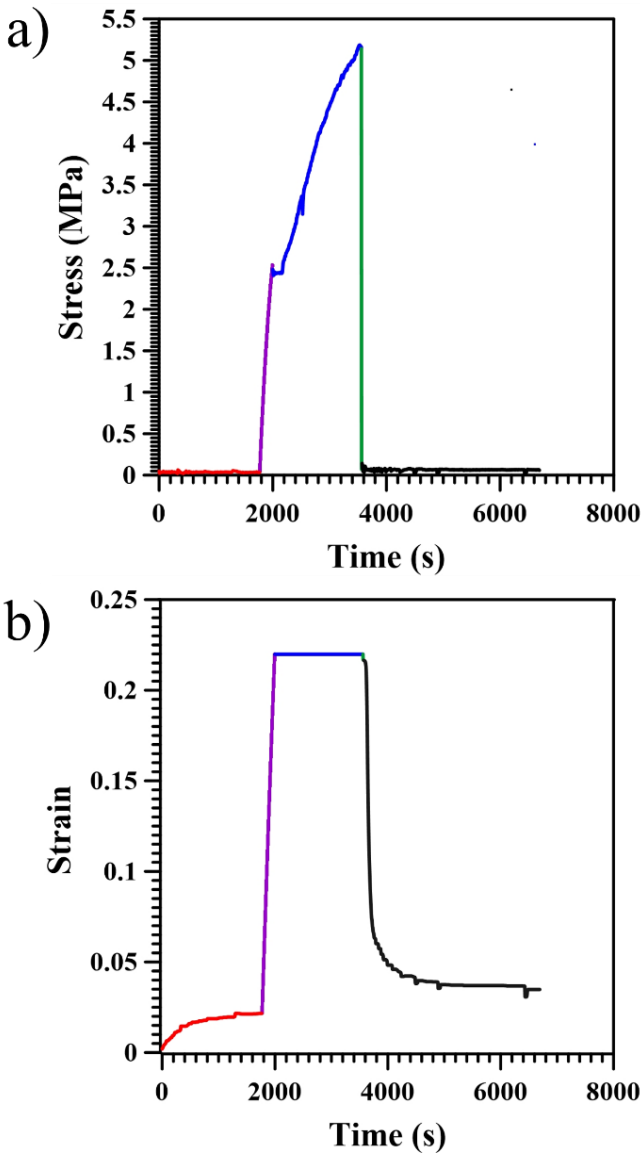
a)
Stress (MPa)
Time (s)
b)
Strain
Time (s)

Specimen 1

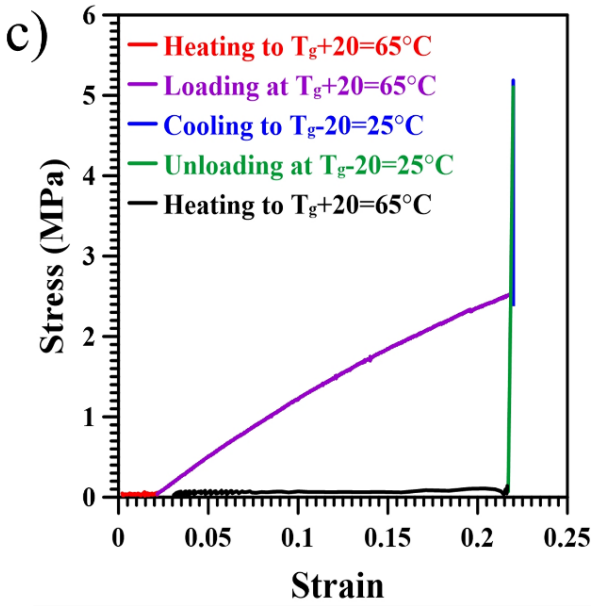
c)
Heating to Tg+20=65°C
Loading at Tg+20=65°C
Cooling to Tg-20=25°C
Unloading at Tg-20=25°C
Heating to Tg+20=65°C
Stress (MPa)
Strain

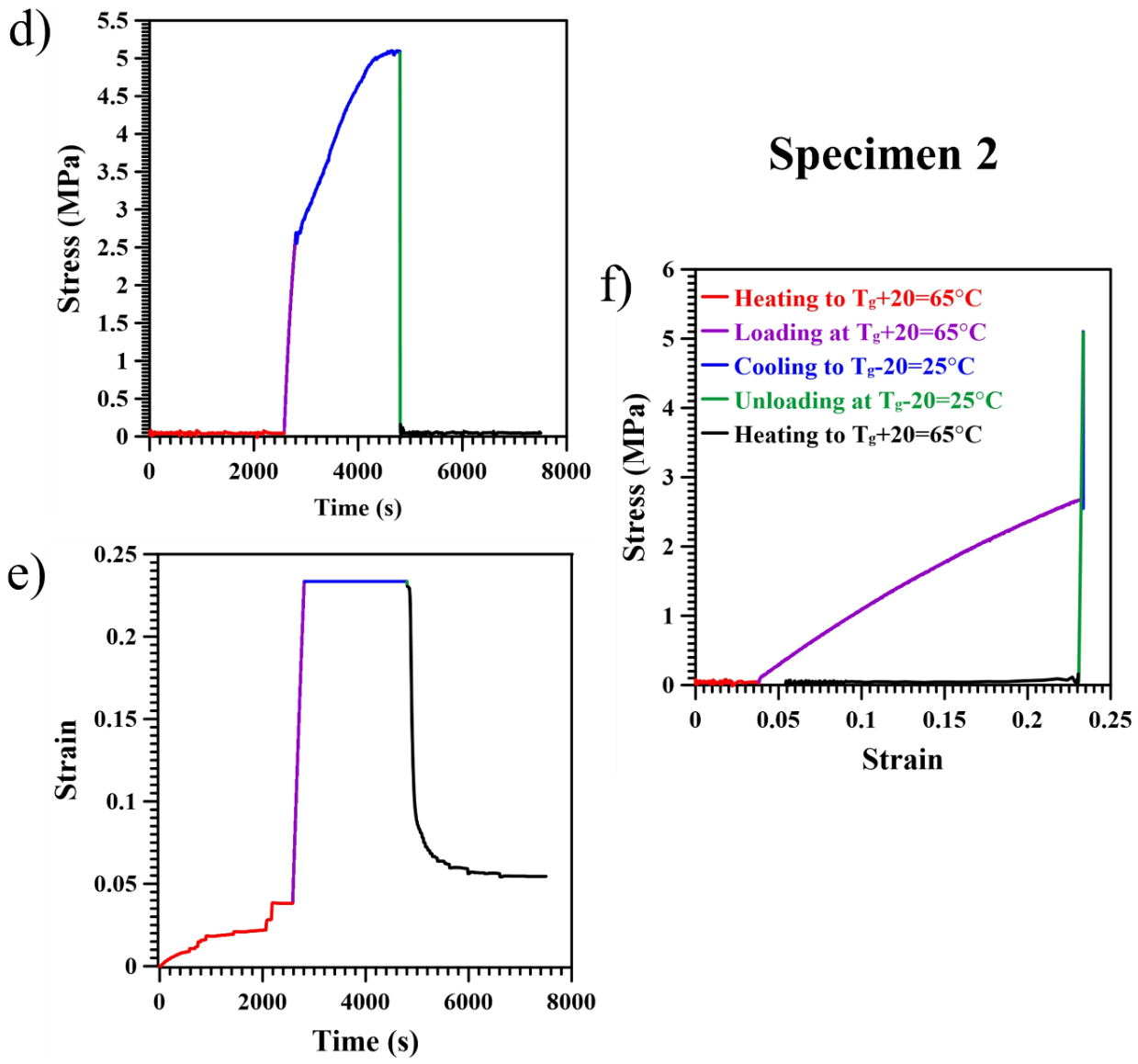
d)
Stress (MPa)
Time (s)
e)
Strain
Time (s)
Specimen 2
f)
Heating to Tg+20=65°C
Loading at Tg+20=65°C
Cooling to Tg-20=25°C
Unloading at Tg-20=25°C
Heating to Tg+20=65°C
Stress (MPa)
Strain

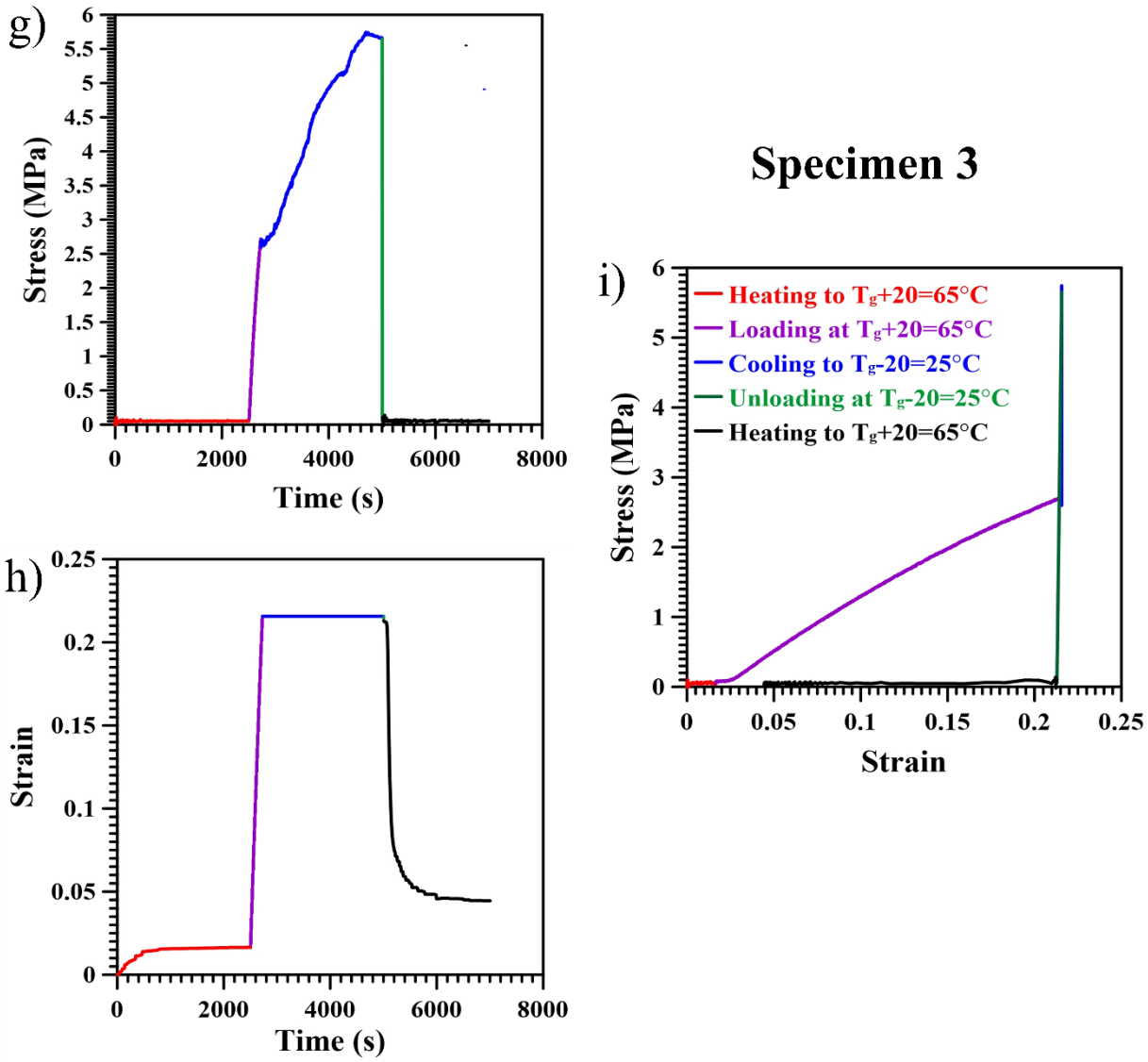

Figure 54. *Mechanical response of PU-SMP during the thermomechanical cycle for three specimens : a–c) stress-time, strain-time, and stress-strain curves for Specimen 1; d–f) corresponding curves for Specimen 2; and g–i) corresponding curves for Specimen 3.*

The shape fixity (SF) and shape recovery (SR) of PU-SMP were determined based on experimental data obtained from the thermomechanical cycle (Figure 54c, f, and i) and calculated using the following Equations (3) and (4) proposed by H. Tobushi and S. Hayashi [39]:

$$SF = \frac{\varepsilon_{un}}{\varepsilon_{max}} \times 100\% \quad (3)$$

$$SR = \frac{\varepsilon_{max} - \varepsilon_{ir}}{\varepsilon_{max}} \times 100\% \quad (4)$$

where, ε_{max} denotes the maximum strain value after mechanical loading (20%) and thermal elongation (following step 2), and ε_{un} - the strain value after unloading (following step 4) and ε_{ir} - the irrecoverable strain remaining after recovery (following step 5). Thermal elongation, shape fixity and shape recovery values are provided in Table 8 for specimens 1, 2 and 3.

Table 8. *Shape memory parameters results for PU-SMP.*

	Specimen 1	**Specimen 2**	**Specimen 3**
Thermal elongation (%)	2.16	3.82	1.70
Shape fixity (%)	98.56	98.84	98.75
Shape recovery (%)	84.16	76.65	79.36

The results indicate that thermal elongation may influence shape recovery, whereas shape fixity remains relatively stable across all specimens, suggesting that the material effectively maintains its deformed shape regardless of variations in thermal elongation. Therefore, the discrepancy in shape recovery values may be partially attributed to differences in thermal elongation among the specimens, highlighting the role of temperature-induced expansion in shape memory performance.

The thermomechanical cycle performed on the strip samples of PU-SMP to obtain the shape memory parameters served as the foundation for subsequent thermomechanical investigations, highlighting key factors that must be carefully considered to ensure accurate and reproducible results:

- Thermal expansion consideration: The thermal expansion observed during the initial heating phase is substantial enough to be considered as part of the overall deformation. Consequently, when calculating shape recovery, it is crucial not to disregard this expansion, as it provides insight into whether the SMP can recover both thermal expansion and mechanical deformation.
- Consistency in heating rate: To achieve reliable and comparable results across multiple specimens, maintaining a consistent heating rate is essential. This ensures uniform thermal elongation and minimizes variability in the thermomechanical response of the material.
- Correlation between thermal elongation and shape recovery: The relationship between the thermal expansion occurring in the first heating step and the final shape recovery must be

taken into consideration. Understanding this correlation is crucial to accurately assess the ability of the material to retain its programmed shape.

- Optimal thermal recovery duration: Prolonged heating during the final recovery step may lead to additional thermal expansion beyond the intended recovery, affecting the final shape retention. Therefore, it is critical to determine the optimal duration for the thermal recovery step to prevent undesired expansion and ensure accurate shape memory characterization.

4.8 Design, Fabrication, and Shape Memory Performance of FDM 3D-Printed PU-SMP Structures

An FDM 3D printer was used to fabricate small-scale shape-morphing actuators and connectors to explore the practical functionality of PU-SMP in real-world applications. The FDM 3D printing was selected due to material limitations and because it is the most effective additive manufacturing method for thermoplastic polymers.

Several compact and simple connector designs were created, as shown in Figure 55. These structures were chosen for their potential use as adaptive connectors or grippers, capable of recovering their original shape after deformation. If integrated into larger mechanical systems, these shape-adaptive components could enhance flexibility, adaptability, and reconfigurability, making them suitable for soft robotics, deployable structures applications.

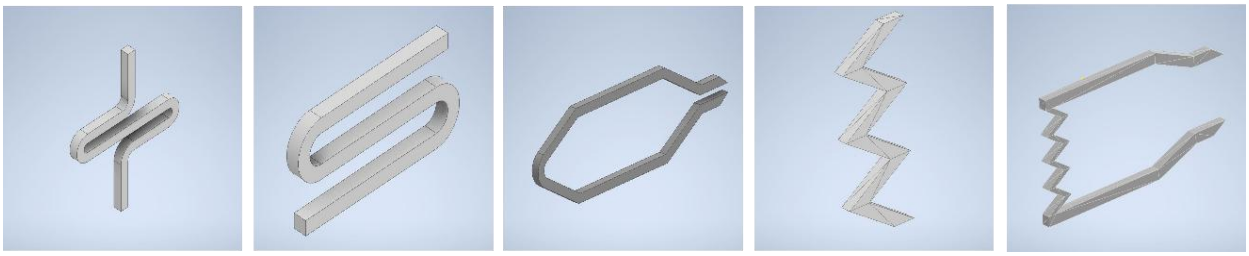

Figure 55. *Design of simple structures for FDM 3D printing using extruded PU-SMP filament.*

For the fabrication of the PU-SMP-based 3D-printed shape-morphing prototypes, the recycled material from previously tested specimens (from mechanical and thermomechanical investigations) was used. The specimens were shredded and extruded into filament for use in FDM 3D printing, as the standard PU-SMP filament was unavailable. However, some challenges arose

during the extrusion process. The filament diameter was inconsistent, with some sections being significantly thinner than others, leading to an overall diameter below the standard 1.75 mm required for FDM printing. This inconsistency was likely due to an insufficient material feed rate during extrusion, preventing uniform filament formation. Consequently, feeding issues occurred during the printing process, as the filament failed to engage properly with the extruder drive gears, resulting in difficulty in printing most of the designed prototypes.

Despite these limitations, two designs were successfully printed, as shown in Figure 56. To evaluate their shape memory performance, the 3D-printed PU-SMP prototypes were subjected to a shape memory cycle. Figures 56a and 56d depict the initial printed structures. Figures 56b and 56e show the deformed state at room temperature. Due to the low T_g of PU-SMP, precise temperature control was challenging. The specimens exhibited high flexibility even at room temperature, eliminating the need for heating before deformation. However, delamination at layer interfaces was observed (circled in red in Figure 56b and 56e), indicating insufficient interlayer adhesion during printing, possibly due to suboptimal extrusion conditions or inadequate printing temperature.

After thermal recovery at 45 °C on a heating plate, Figure 56c and 56f show that the delaminated layers reconnected, demonstrating the self-healing ability of PU-SMP. Unfortunately, due to material constraints, further investigations into the 3D printability and shape memory performance of PU-SMP could not be conducted. Optimization of printing parameters, extrusion settings, and filament preparation would be necessary to improve layer adhesion, mechanical integrity, and overall shape memory performance in future studies.

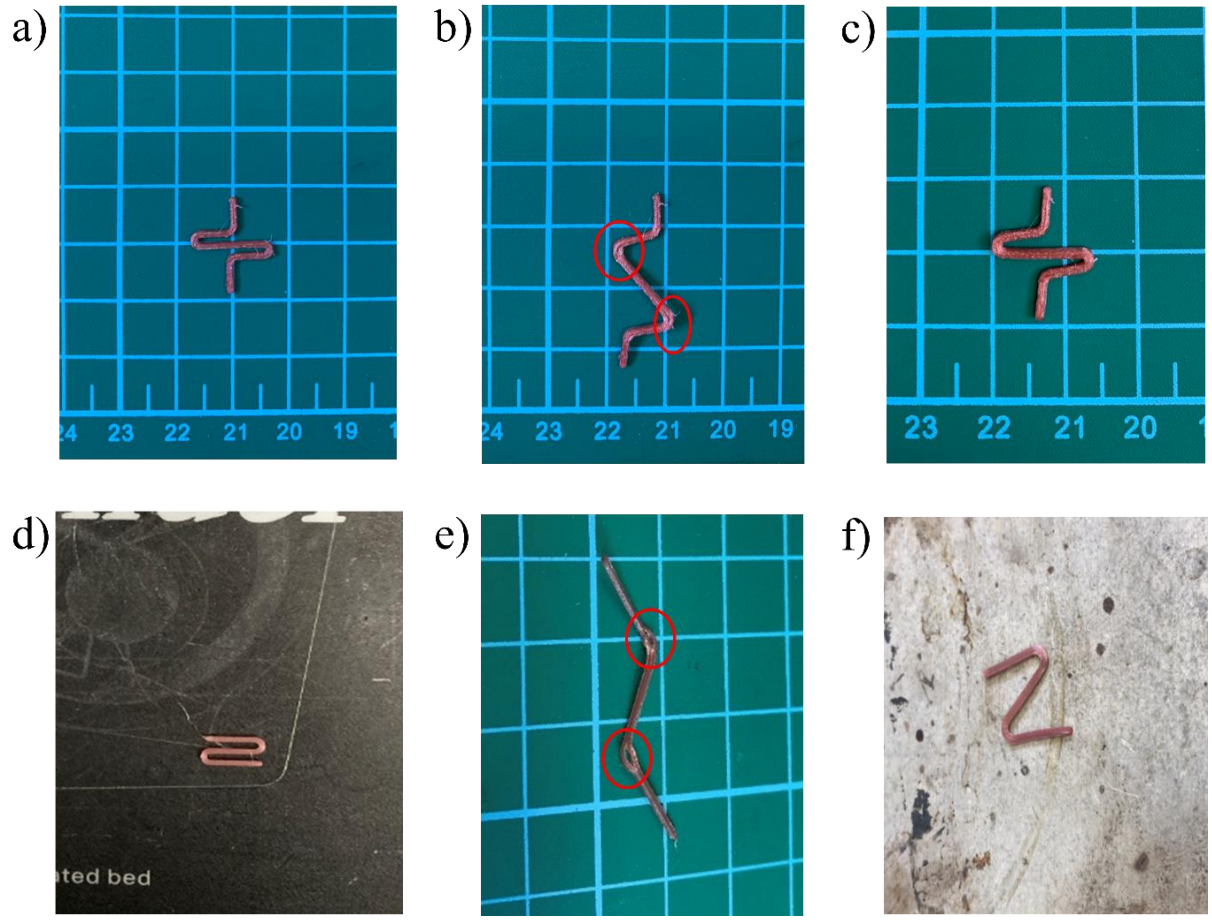

Figure 56. *Shape memory behavior of FDM 3D-printed PU-SMP prototypes . (a, d) Initial printed structures. (b, e) Deformed state at room temperature, with delaminations highlighted in red. (c, f) Shape recovery after thermal activation at 45°C, showing the disappearance of delaminations and restored structural integrity.*

Chapter 5

Results and Discussion (II): Comprehensive Investigation of SLA 3D-Printed SMEp

This chapter presents a pivotal shift in the research focus, from thermoplastic PU-SMP to thermoset SMEp, motivated by the limitations encountered with FDM printing and the thermal behavior of PU-SMP. Two different build orientations, which result in geometrically identical specimens (SMEp1 and SMEp2), are thoroughly investigated to evaluate how differences in surface area and the number of printed layers influence the properties of SLA 3D-printed parts.

The analysis includes a comprehensive evaluation of the thermomechanical behavior, mechanical performance, dimensional stability, microstructural characteristics, and fracture mechanisms of the specimens. Additionally, the shape memory properties of specimens produced from each orientation, specifically shape fixity and shape recovery, are quantified and compared.

This in-depth characterization of standard 3D-printed specimens is a critical step prior to implementing the material in functional designs. It provides essential insight for selecting suitable material formulations, design geometries, and build orientations for reliable performance in real-world, application-specific environments.

5.1 SLA 3D Printing of Shape Memory Epoxy Specimens

The dog-bone-shaped shape memory epoxy specimens (SMEp1 and SMEp2) were fabricated using SLA technology at Polytechnic University of Madrid (UPM), where the 3D printing tasks were carried out with the support of Mr. Pedro Ortego. The AM process yielded two samples with identical geometries and dimensions but differing in build orientations.

The first specimen, SMEp1, was printed with its main surface positioned laterally, meaning the layers were stacked along the narrow edge of the specimen (Figure 57a). In contrast, SMEp2 was oriented with its main surface lying flat on the build platform, so the layers were stacked parallel to the largest surface area (Figure 57b).

Figure 57 also displays post-processed images of both specimens. Due to layer-by-layer fabrication method of SLA, subtle ridges, often referred to as layer lines or layer artifacts, were left by each cured layer. These layer lines are detectable upon touch and contribute to the surface

texture of the specimen. In the case of SMEp1, the surface aligned with the X-Y plane shows these layer lines prominently, giving it a slight textured feel. Meanwhile, in SMEp2, the layer lines are noticeable on the lateral surface, aligned with the Y-Z plane.

Additionally, surfaces that were in direct contact with the support structures connected to the SLA platform exhibit increased roughness, due to the support removal process. Such roughness is predominantly found on one of the lateral surfaces for SMEp1, while for SMEp2, it appears on the largest surface. This observation highlights how build orientation not only affects the location of layer artifacts, but also influences the areas where roughness from supports may persist post-processing [115].

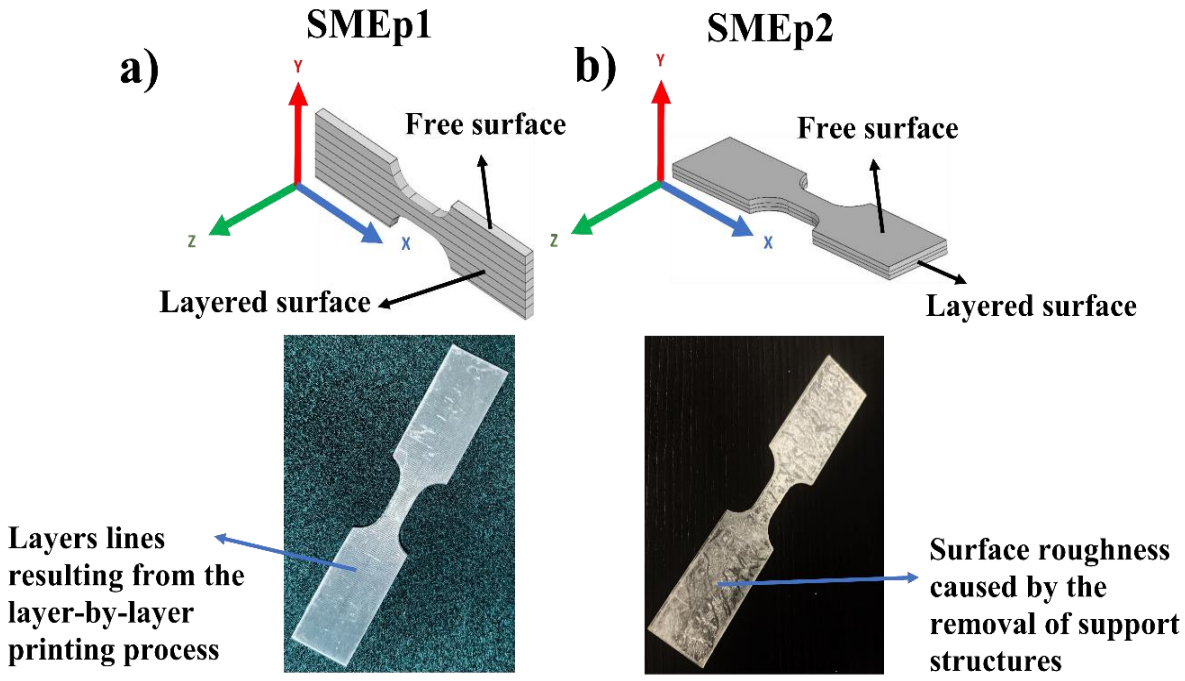

Figure 57. *Two 3D-printing configurations of the dog-bone specimen with respect to the SLA 3D-printer platform: SMEp1 printed along the Y-axis from the lateral surface and SMEp2 from the flat surface.*

5.2 Microstructural Analysis of SMEps After SLA 3D Printing

As previously discussed, the SLA 3D printing process builds objects layer by layer, using a UV laser to selectively cure resin for each layer before adding the next. This stepwise curing process is crucial, as strong interlayer bonding is necessary for the final part to maintain structural

integrity. Ensuring that each newly applied layer firmly bonds with the previous one contributes to the overall mechanical strength of the printed component.

Figure 58 presents a schematic representation of two consecutive layers in SLA printing. One important aspect here is the "cure depth," which defines the extent to which the UV light penetrates and cures the resin. For optimal adhesion between layers, the cure depth should exceed the thickness of each individual layer being applied. This approach allows the UV light to cure the new layer while also penetrating slightly into the underlying layer, thus creating a fused, reinforced bond. The extra cured depth beyond the single layer thickness is termed the "overcured amount". This intentional overlap enhances the bonding between layers by integrating each layer with the one below. However, controlling the overcure is essential; excessive overcure can introduce residual stresses into the structure, potentially leading to issues such as warping or deformation in the final printed part.

Examination of the specimens through SEM imaging (Figure 59) enabled to observe that the layer thickness in both SMEp1 and SMEp2 is approximately 100 μm. However, distinct differences arise in the visibility and characteristics of the overcured regions (or interlayer connections) within the bulk of each specimen. In SMEp2 (Figure 59b), the overcured regions of interlayers are less visible within the core material, suggesting a different internal structure compared to SMEp1 (Figure 59a). Notably, some areas of surface separation in the interlayer connections are visible in certain regions, highlighted in yellow in Figure 59b. Approaching to the edges of SMEp2, the interlayer regions appear more pronounced and bulging (highlighted in black in Figure 59b), possibly due to uneven resin flow and curing dynamics at the edges of the specimen. The edge effects could result from the fact that resin behaves differently near open boundaries, where it might receive slightly different UV exposure or experience altered flow and curing dynamics during the printing process.

In contrast, the overcured interlayers in SMEp1 (Figure 59a) appear thicker, smoother, and more consistent throughout the specimen. The difference can be attributed to the lateral build orientation of SMEp1, which requires a larger number of layers compared to the flat orientation of SMEp2. The previously cured regions undergo repeated UV exposure when new layers are applied across a narrower cross-section. This repeated UV exposure intensifies the curing effect in SMEp1, particularly on the previously cured layers, causing further polymerization and strengthening of the interlayer bonds.

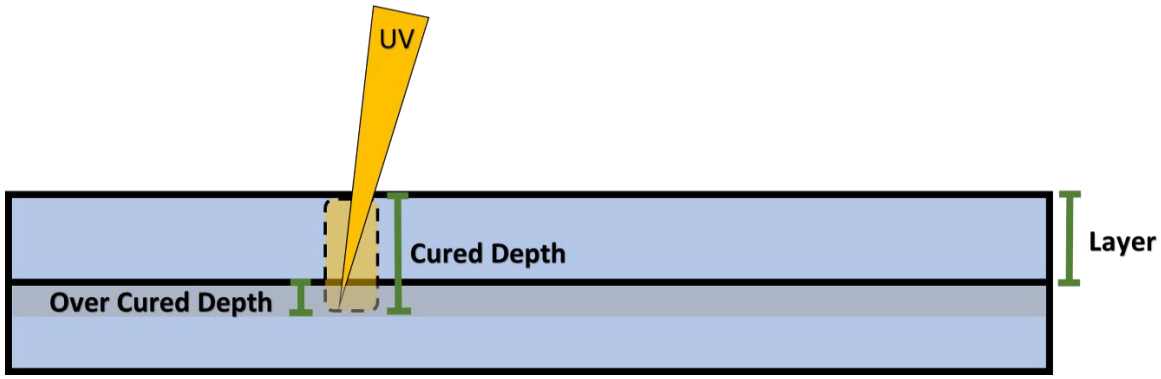

Figure 58. *Schematic representation of the curing process in SLA 3D printing, illustrating the cured depth and over cured depth of successive layers.*

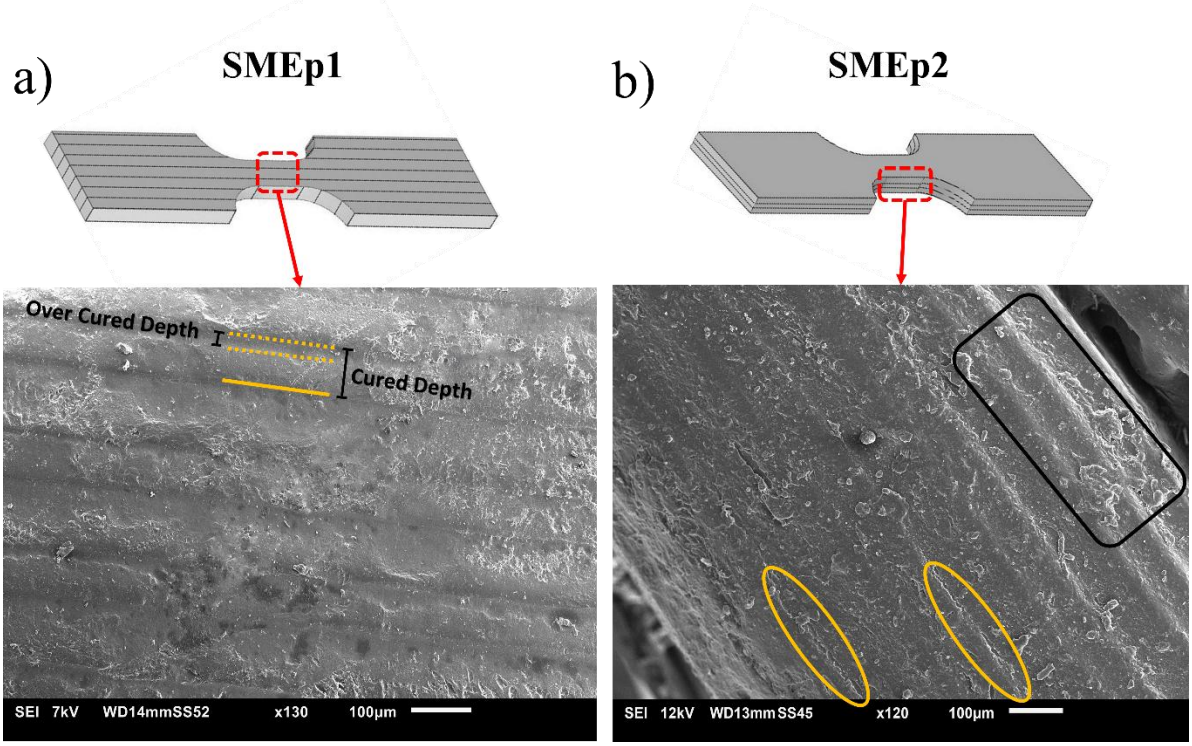

Figure 59. *SEM images of the surfaces of: a) SMEp1; and b) SMEp2 specimens after 3D-printing.*

As a result, the interlayer connections in SMEp1 are more thoroughly cured, thicker, and better integrated, leading to improved adhesion and overall strength within the specimen. Conversely, the flat orientation of SMEp2 necessitates fewer layers for the same geometry, reducing the cumulative UV exposure that each layer receives during printing. Consequently, each layer in SMEp2 undergoes less repeated curing, resulting in thinner and potentially weaker interlayer connections. This diminished exposure may lead to less robust bonding between layers,

contributing to the less distinct and less cohesive appearance of the overcured regions within the bulk of the SMEp2.

The findings emphasize the impact of build orientation in SLA printing on both surface quality and microstructural integrity. The lateral orientation of SMEp1 benefits from repeated curing, improving interlayer adhesion, while the flat orientation of SMEp2, with reduced exposure, leads to weaker bonding. Such distinction highlights the importance of build orientation selection in SLA printing for applications requiring high mechanical strength and durability [134].

5.3 Swelling Behavior and Water Absorption Analysis of SMEps

A swelling test on SLA 3D-printed thermoset specimens fabricated in two different orientations relative to the printing platform allows for an assessment of the material's swelling ratio and water resistance properties. Comparing the swelling behavior of the two configurations provides valuable insights into the porosity and water absorption characteristics of their interlayer connections.

The weight changes of three samples, cut from each of the SMEp1 and SMEp2 specimens, over time are shown in Figure 60a. The weight change results of the three samples indicate that the water absorption of the SLA 3D-printed specimens remains relatively constant throughout the 48-hour immersion period.

In order to better understand the mechanism of water absorption of both types of specimens, the mean swelling rates for each specimen were calculated using Equation (5) [142]:

$$\text{Swelling rate (\%)} = \frac{weight\ at\ time - initial\ weight}{initial\ weight} \quad (5)$$

Figure 60b shows the mean value of swelling rate versus time for SMEp1 and SMEp2 specimens. The swelling rate in both specimens is initially high during the first hour, then decreases, and subsequently increases again.

The surface of the specimens quickly absorbs the solvent at the initial stage, leading to a rapid increase in swelling, as the outer layers of the material swell quickly. It can be observed that initial rapid surface absorption is higher in SMEp2 compared to SMEp1, likely due to porosity on a bigger surface of the SMEp2, which was connected to the supports during 3D printing. It was

noticed that the surface of SMEp2 connected to the supports became rough following their removal (see Figure 60b), while the opposite free surface, which was not in contact with supports, stayed smooth. The surface roughness likely contributes to the increased porosity and absorption rate observed in SMEp2 during the initial swelling phase.

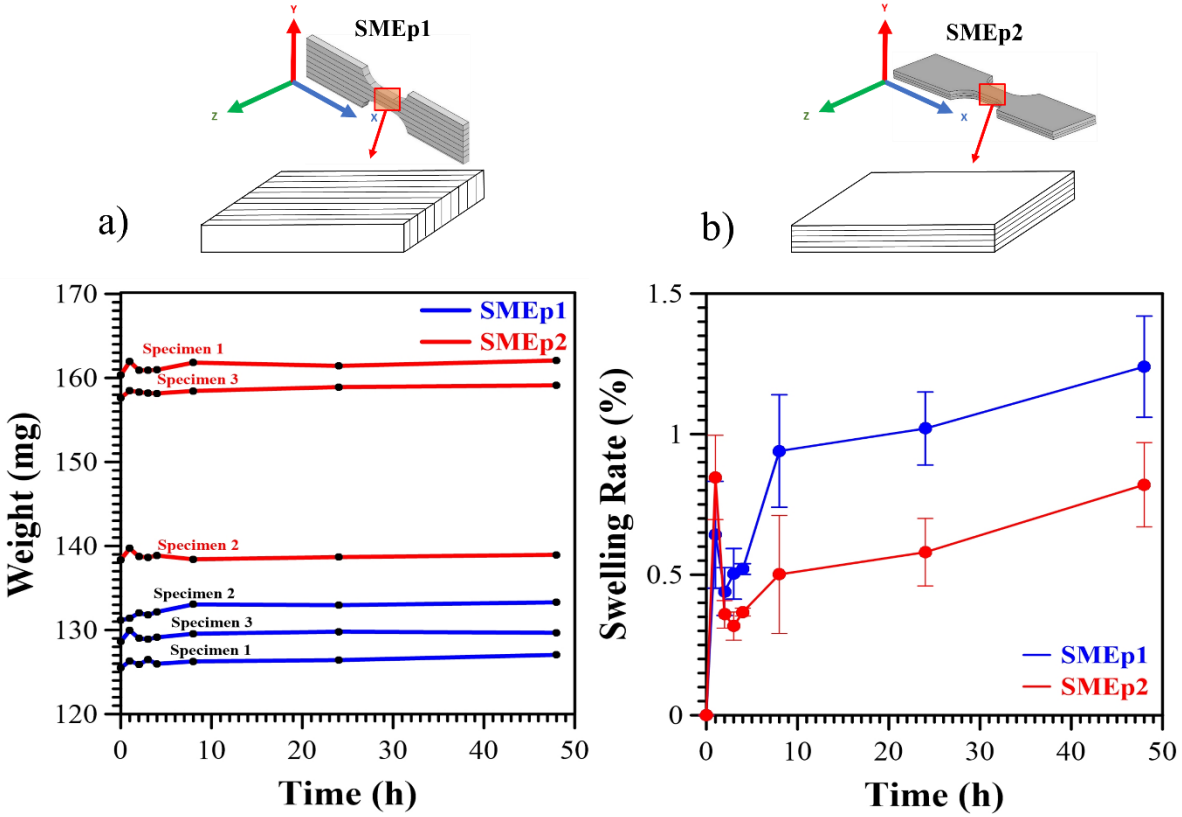

Figure 60. *Diagrams showing: a) weight variation; and b) swelling rate of SMEp1 and SMEp2 in water as a function of time.*

As a result, removing supports from the surface may cause roughness and defects, contributing to a higher initial rate of water absorption.

Following the initial fast water intake, the outer layers of the samples start to reach saturation, leading to a decrease in the pace of solvent penetration. This slowdown takes place as the permeation shifts from the surface toward the bulk of the material, where the solvent slowly infiltrates the internal network and interlayer bonds.

Interestingly, in comparison to SMEp1, SMEp2 exhibits a slower water absorption rate after the initial phase. This may be due to SMEp2 having fewer interlayer connections directly

exposed to water, resulting in reduced overall absorption. Such behavior indicates that, even with SLA 3D printing of water-resistant thermoset and crosslinked polymers, the interlayer bonds remain susceptible to environmental factors. The interlayers can contribute to swelling and volume expansion when exposed to moisture, revealing a potential weakness in the long-term durability of 3D-printed components in humid conditions. This highlights the importance of optimizing build orientation during the design and manufacturing process to minimize such effects, depending on the application.

5.4 FTIR Spectroscopy Analysis of SMEps

FTIR analysis was utilized to investigate and compare the molecular compositions of SMEp1 and SMEp2 samples. The FTIR spectra provide insight into molecular vibrations within the material (Figure 61a), which are linked to specific functional groups. Table 9 lists the various chemical bonds identified in the FTIR spectra for both SMEp1 and SMEp2, along with their corresponding wavelengths.

Characteristic changes in the spectra should be detected in order to evaluate the extent of crosslinking. Among them, one can indicate the appearance or disappearance of peaks associated with the formation of a 3D network, which is typical for cured epoxy systems. Crosslinking generally leads to the consumption of certain functional groups and the emergence of new ones. In epoxy materials, the reaction between epoxide rings (C-O-C) and the curing agent triggers the ring-opening process, ultimately resulting in a densely crosslinked structure. The process is commonly tracked by observing the weakening or complete disappearance of the absorption band corresponding to the epoxide functionality.

A signal in the range of approximately 810-950 cm^{-1} is typically attributed to the stretching vibration of the oxirane (epoxide) ring, where an oxygen atom is bonded to two carbon atoms. In the spectra for both samples, this peak is almost completely suppressed, as shown in Figure 61a, confirming that the epoxide rings were successfully opened and reacted during curing, forming a crosslinked network. Additionally, the transformation of epoxide rings into ether linkages (C-O) during curing enhances the intensity of the band within the range of 1300-1000 cm^{-1}. Consequently, a rise in the C-O peak alongside a decline in the C-O-C peak can serve as an indicator of the degree of crosslinking in epoxy resins.

Table 9. *Overview of the bonds identified in the FTIR spectra of SMEp1 and SMEp2, along with their respective wavelength ranges.*

Bond	Wavelength (cm^{-1})	Description
O-H	3400	Existence of hydroxyl groups.
C-H	2850 and 2925	Presence of methylene (-CH2-) and methyl (-CH3) groups, typically found in the main chain of epoxy polymers.
C=C	1650	Signal associated with aromatic structures, likely originating from the curing agent or the epoxy resin itself.
C=O	1723	Carbonyl functionality, present in the original molecular structure of the epoxy.
C-O	1000-1300	Ether bonds, which are essential structural elements in epoxy systems.
C-O-C	810-950	Oxirane ring (epoxide group) stretching vibration.

The data presented in Figure 61a show that both SMEp1 and SMEp2 samples display identical characteristic peaks at the same wavenumbers, confirming their chemical resemblance and indicating that both materials possess the same basic chemical framework. However, a notable difference lies in all peak intensities, with SMEp1 consistently exhibiting lower intensities than SMEp2. This disparity points to potential differences in the quantity or concentration of specific functional groups. Table 10 offers a quantitative analysis comparing the areas beneath selected FTIR peaks, specifically those associated with ether bonds (C–O), carbonyl groups (C=O), and methylene/methyl groups (C–H) for both SMEp1 and SMEp2, alongside the total area of the FTIR spectrum for each sample.

Table 10. *Quantitative comparison of peak areas in the FTIR spectra of SMEp1 and SMEp2*

Bond	Wavelength (cm^{-1})	Area under the peak SMEp1 (cm^{-1})	Area under the peak SMEp2 (cm^{-1})
C-O	**1000-1300**	10.19	33.57
C=O	**1723**	3.71	7.47
C-H	**2850-2950**	8.91	22.948
Total area under the FTIR spectrum		53.928	130.21

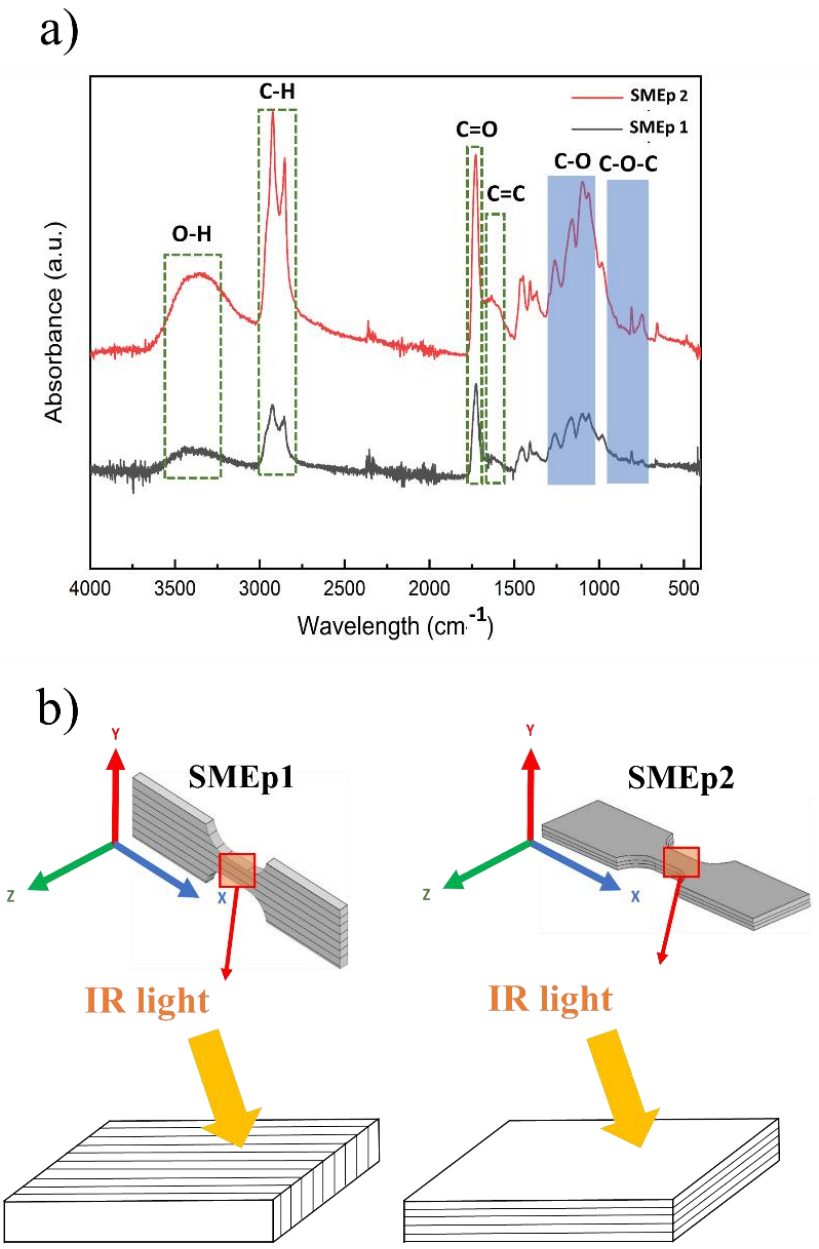

Figure 61. *a) FTIR spectra of SMEp1 and SMEp2, b) Schematic illustrating how IR light interacts with the printed layers of SMEp1 and SMEp2 during FTIR analysis.*

Because the samples were placed on the FTIR sample holder with their largest surface facing the infrared beam, the IR light passed through the material from the side marked by the yellow arrows in Figure 61b. The reduced intensity observed for SMEp1 indicates structural non-uniformity within the thickness region exposed to the IR beam. It can be attributed to the orientation of layers in SMEp1 during printing, since it was fabricated with its side surface, the

specimen contains a larger number of individual layers and interlayers boundaries. These interfaces act as scattering sites, lowering the effectiveness of IR absorption.

In contrast, SMEp2, printed flat (parallel to its widest surface), contains fewer layers and fewer interlayer boundaries. This reduces scattering and allows for more efficient IR absorption. Consequently, the structural arrangement linked to the different printing orientations gives SMEp2 the appearance of having a higher concentration of functional groups, based solely on FTIR signal intensity.

However, it is important to note that the FTIR measurements do not directly reveal which specimen exhibits a higher degree of crosslinking. Instead, the results emphasize how internal inhomogeneities within additively manufactured specimens, built layer-by-layer, affect both IR scattering and absorption efficiency [143,144].

5.5 TGA Analysis of SMEp

TGA was conducted to assess the thermal degradation behavior of the SLA 3D-printed SMEp specimen. As shown in Figure 62, the weight percentage versus temperature curve (blue line) indicates that SMEp1 begins to lose 5% of its weight at approximately 292°C, which corresponds to the onset of thermal decomposition. The derivative weight curve (DTG) (red line) highlights the maximum decomposition rate, which occurs at approximately 400°C, indicating the major thermal degradation event. This thermal stability is consistent with expectations for cured epoxy-based thermosets and confirms the suitability of the material for applications requiring elevated thermal resistance.

It is worth mentioning that, in this study, TGA analysis was conducted only for SMEp1, and this result is considered representative for both build orientations (SMEp1 and SMEp2). Such a decision is justified by the fact that both specimens were fabricated from the same photopolymer resin, using identical layer thickness, exposure settings, and post-curing processes. The only controlled difference between SMEp1 and SMEp2 is the build orientation, which influences properties such as interlayer bonding, mechanical performance, and dimensional stability. However, build orientation does not alter the fundamental chemical composition of the resin itself, meaning the bulk thermal degradation behavior, as measured by TGA, would be expected to be essentially the same for both orientations.

Since TGA primarily evaluates the thermal decomposition behavior of the polymer matrix, rather than the structural anisotropy or microstructural differences introduced by build orientation, performing TGA on SMEp1 alone is sufficient to represent the thermal stability of both specimens. This is further supported by the FTIR results, which confirm that SMEp1 and SMEp2 share the same chemical structure.

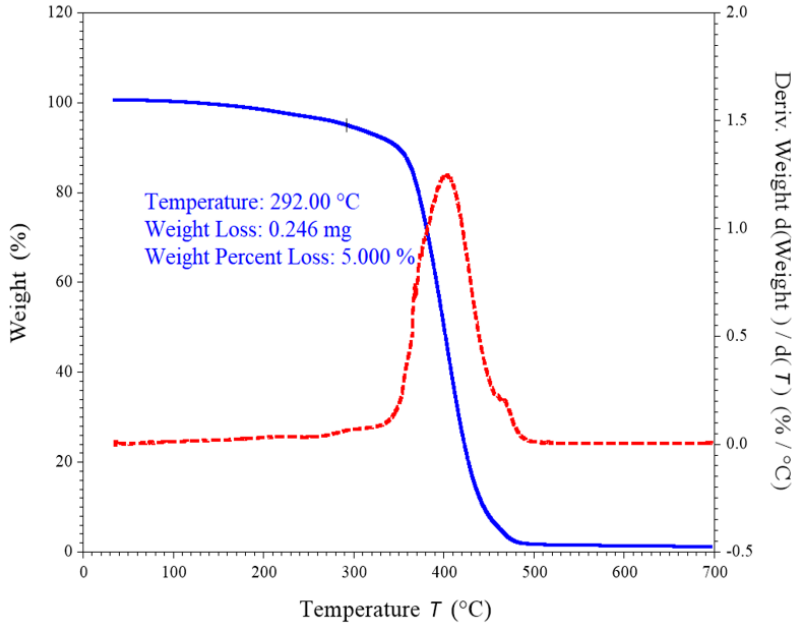

Figure 62. *TGA results of cross-linked SMEp, indicating its thermal stability* [3] *(TGA measurements were performed by Dr. M. Cristea and Dr. D. Loniță at the "Petru Poni" Institute of Macromolecular Chemistry, Iași, Romania in collaboration with professor Pieczyska's team.).*

5.6 DSC Analysis of SMEps

DSC is a technique for measuring the amount of energy absorbed or released by a specimen as it is heated or cooled, by investigating heat flow versus temperature. DSC measurement provides information about the thermal transitions such as glass transition and melting temperature as well as crystallization temperature, change in heat capacity (ΔC_p) and enthalpy (ΔH).

The peak of T_g is not a sharp single-point transition in DSC, but rather occurs as a step over a temperature range at which the polymer transitions from a hard, glassy material to a soft, rubbery material. Determining the T_g is essential for shape memory polymers, as it marks the critical temperature threshold, below which the material retains its deformed shape, and above which shape recovery is triggered.

Heat capacity or C_p is crucial for understanding how materials respond to temperature changes. C_p is a physical property of a material that measures the amount of heat energy required to raise the temperature of a given quantity of the material by a certain temperature interval. It is an indicator of the thermal inertia of the material, which is a measure of how far the material resists changing temperature when it absorbs or releases heat. In the context of materials like polymers, the heat capacity can give insights into the molecular structure and bonding. Therefore, ΔC_p value represents the change in heat capacity at T_g, indicating the change in molecular mobility within the material.

ΔH refers to the total heat flow associated with the transition process, which can include glass transition, melting, or crystallization. ΔH, calculated from the area under a heat flow vs. temperature graph, quantifies the energy involved in transitions like T_g, melting, or crystallization. In polymers, ΔH can reveal the energy required to transition from a brittle state to a more flexible one, which is directly related to the strength of the intermolecular forces within the crystalline lattice.

Figure 63 and Table 11 present the DSC results for SMEp1 and SMEp2, obtained from a heating-cooling-heating cycle. During the initial heating phase, SMEp1 (Figure 63a) exhibits a slightly elevated T_g compared to SMEp2 (Figure 63b). The higher T_g is likely influenced by a combination of factors, including crosslink density and secondary effects that hinder molecular chain movement, such as the printing orientation, residual internal stresses, interlayer adhesion, structural uniformity, and thermal history. The larger number of individual layers and interfacial regions within SMEp1 may contribute to elevated residual stresses, along with thicker and more robust interlayer bonds (which were identified as over-cured regions in Figure 58). These factors restrict molecular chain flexibility and possibly increase crosslink density, ultimately requiring greater thermal energy to initiate the glass transition.

Moreover, SMEp1 in Figure 63a displays slightly lower ΔC_p and ΔH compared to SMEp2 in Figure 63b, during the first heating run. The reduced ΔC_p in SMEp1 indicates a smaller shift in heat capacity and limited molecular mobility at T_g (due to crosslinking, internal stress, interlayer connections, etc.), while the lower ΔH suggests that the glass transition in SMEp1 involves less thermal energy and occurs more gradually, without a sharp transition. Additionally, the peak temperatures observed during the first heating cycle differ, with SMEp1 reaching a peak at 60.22

°C, whereas SMEp2 peaks at 58.05 °C. The slightly higher peak temperature for SMEp1 could be indicative of a higher degree of cure or other factors contributing to reduced chain mobility.

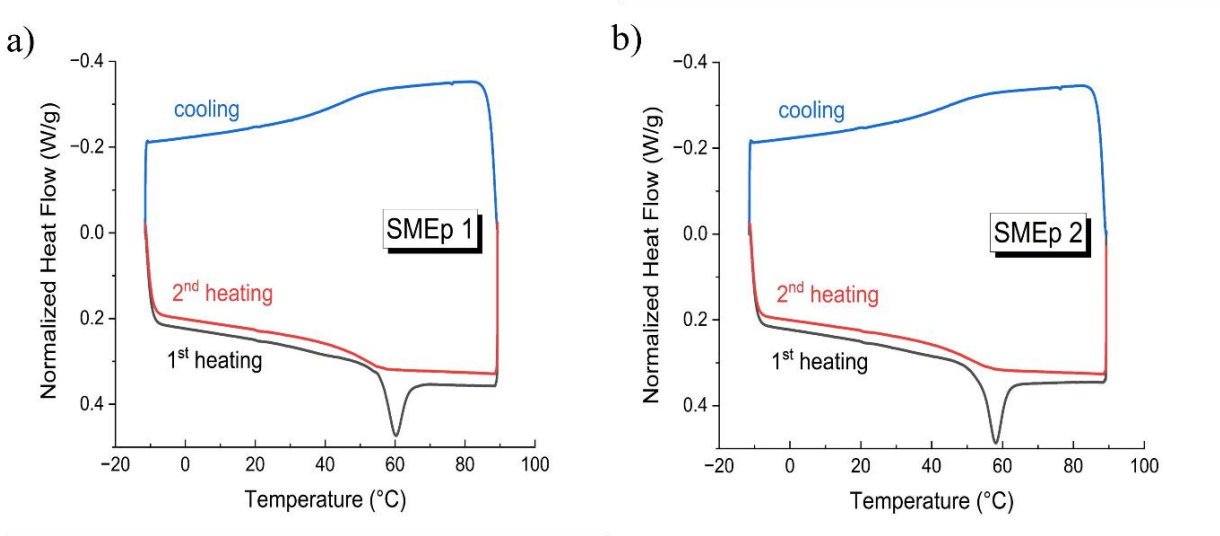

Figure 63. *DSC results for a) SMEp1; and b) SMEp2 specimens.*

Table 11. *Thermal properties of SMEp1 and SMEp2 from DSC measurement.*

First Heating	**SMEp 1**	**SMEp 2**
T_g **(°C)**	53.55	51.18
ΔC_p **(J/g°C)**	0.34	0.36
ΔH **(J/g)**	3.23	3.41
Peak (°C)	60.22	58.05
Second Heating	**SMEp 1**	**SMEp 2**
T_g **(°C)**	49.73	49.69
ΔC_p **(J/g°C)**	0.31	0.31

In the second heating step, the transition, which initially appeared as a peak, evolves into a step-like change, with T_g and ΔC_p values for both SMEp1 and SMEp2 becoming more closely aligned. This shift is likely due to the release of residual stress, completion of the curing process, or the removal of moisture from the samples during the initial heating.

The slight differences in thermal response between SMEp1 and SMEp2 can be traced back to their distinct print orientations. The surface on which each specimen was built influences the way layers are deposited and fused, potentially leading to differences in thermal properties such

as T_g and enthalpy. The bonding between adjacent layers may be stronger in one orientation than the other, affecting the overall thermal behavior. Based on the results, the side-printed SMEp1 demonstrates slightly improved thermal stability and a less pronounced thermal transition compared to SMEp2, which was printed flat. This highlights that the build direction affects thermal stability and transition characteristics of 3D-printed materials [145,146].

5.7 TMA Method Optimization and Thermal Expansion Analysis of SMEp

TMA analysis was performed to thoroughly investigate the thermal expansion behavior of SLA 3D-printed photopolymer specimens under different conditions, using both macro and micro probes. The macro probe was used to assess macro-expansion, capturing dimensional changes across a larger surface area, providing an overall view of bulk expansion behavior across multiple printed layers. In contrast, the micro probe was employed to focus on localized expansion, targeting a smaller area involving fewer printed layers, which allowed for a more detailed understanding of how individual layers respond to thermal cycling.

In this study, the Coefficient of Thermal Expansion (CTE) was selected as a key parameter to evaluate the dimensional stability of the specimens. CTE quantifies how much a material expands or contracts per unit length for each degree of temperature change. The CTE values were determined by tracking the dimensional changes during a controlled thermal cycle and calculating the slope of the expansion curve within the specified temperature range. Understanding the CTE provides valuable insight into the material's response to thermal variations, which is crucial for applications requiring precise dimensional stability.

To establish a baseline understanding of the overall thermal expansion behavior of SLA 3D-printed specimens, TMA was first conducted on SMEp1 using the macro probe (Figure 64a). Three SMEp1 specimens were heated from 25 °C to 85 °C in the chamber, each subjected to a different controlled heating rate: 5 °C/min, 10 °C/min, and 20 °C/min. Throughout the test, a constant low force of 0.002 N was applied to the specimen by the macro probe to ensure consistent contact without restricting thermal expansion. The results presented in Figure 64b show the thermal expansion as a function of temperature for each heating rate, with a summary of the calculated CTE values provided in Table 12. In all cases, the thermal expansion exhibited a nearly linear trend, with the total expansion reaching approximately 3% over the temperature range, without a noticeable change in slope at the T_g. It suggests that the macro probe, applying a small

force of 0.002 N on the sample, lacked the sensitivity required to detect the glass transition and the associated slope change, which typically occurs at higher temperatures when the material enters the rubbery state [147].

The average CTE values, determined by fitting a tangent line to estimate the mean slope at different heating rates, were nearly identical, meaning that, the heating rate had only a minor effect on the macro-expansion behavior of SMEp1 specimens, and the macro probe, under the applied force of 0.002 N, was unable to capture any distinct change in CTE across the T_g.

Expansivity parameter was also calculated in order to achieve a more precise understanding of the thermal response of the SMEp1 material. Expansivity represents the instantaneous thermal expansion rate at each temperature point, defining the localized slope of the thermal expansion curve. Formally, it can be defined in the following way:

$$Expansivity = \frac{1}{L_0}\frac{dL}{dT} \tag{6}$$

Where, L_0 is the initial length of the sample (in our case, the initial thickness under the probe, 1 mm), $\frac{dL}{dT}$ is the local rate of dimensional change with respect to temperature (i.e., the slope of the dimension change curve at each point).

The expansivity parameter expressed in units of 1/°C describes the strain rate increase per degree of temperature rise, normalized by the initial sample length. It helps to identify subtle thermal events, such as the glass transition, and allows direct comparison between materials with different dimensions and properties. Calculating expansivity enables gaining deeper insight into phase transitions, thermal stability, and structural changes within the polymer matrix. Materials exhibiting stable and nearly constant expansivity increase predictably with temperature. This predictable behavior is essential for designing components subjected to thermal cycling, especially in high-precision applications such as electronic devices, aerospace structures, and polymeric seals. For SMPs, distinct deviations or peaks in expansivity can indicate thermal events such as the T_g, crystalline melting, or stress relaxation, all critical for understanding thermomechanical programming and recovery behavior. Figure 64c shows the calculated expansivity for each heating rate. The curves are noisy across the temperature range, with no clear signal marking the glass transition.

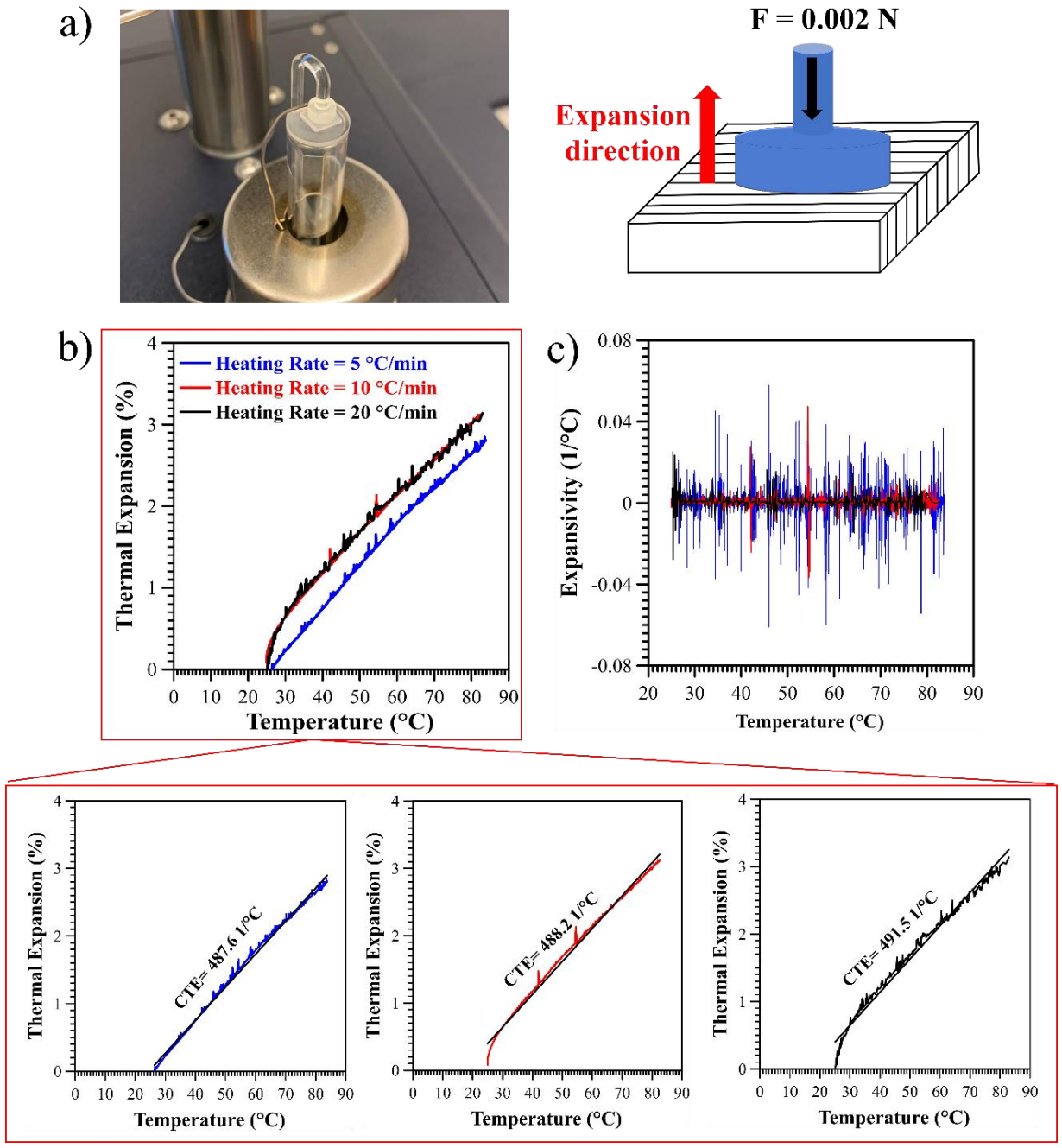

Figure 64. *Thermal expansion of SMEp1 specimens at different heating rates using the macro probe (0.002 N): a) the TMA setup with the sample positioned under the macro probe, along with the schematic, illustrating the interaction between the macro probe and the printed layers; b) thermal expansion (%) vs. temperature (it shows a nearly linear trend); c) expansivity (1/°C) vs. temperature, revealing high noise and no clear thermal events. (The three lower plots show the same thermal expansion curves from diagram (b), separated for each heating rate, with linear fits used to determine the average CTE.)*

This is consistent with the average CTEs (Figure 64b), which remained almost constant across heating rates, confirming that heating rate had a minor effect on the macro-scale expansion.

The same thermal procedure was repeated to assess micro-expansion, however, using a micro probe to capture thermal expansion across a smaller localized area, corresponding to fewer printed layers in the vertical direction (Figure 65a). The test was performed under the same minimal applied force of 0.002 N, using controlled heating rates of 5 °C/min, 10 °C/min, and 20 °C/min, consistent with the macro-expansion tests. The results are summarized in Table 12.

The resulting plots of thermal expansion versus temperature for each heating rate are presented in Figure 65b. These curves display significant noise, which made it difficult to reliably evaluate and compare thermal expansion across different heating rates. The cause of this noise is presumably the very low applied force (0.002 N), which exerted only minimal contact pressure on the specimen surface. This may have allowed slight slippage or micro-movements of the probe, particularly when interacting with surface roughness or irregularities. Additionally, the specimen could gradually relax itself at every temperature step, leading to continuous dimensional fluctuations rather than a sharp, distinct peak at T_g. Such gradual relaxation spreads the thermal response across the whole temperature range, masking the characteristic transition signal typically seen at the glass transition.

Despite the challenges mentioned above, one clear observation is that the thermal expansion measured using the micro probe was consistently lower than that recorded with the macro probe, with the expansion reaching approximately 1% over the temperature range, regardless of the measurement noise.

This discrepancy highlights the scale effect, as the macro probe measures bulk behavior across a larger area, while the micro probe focuses on a much smaller zone, capturing the local response of a limited number of layers.

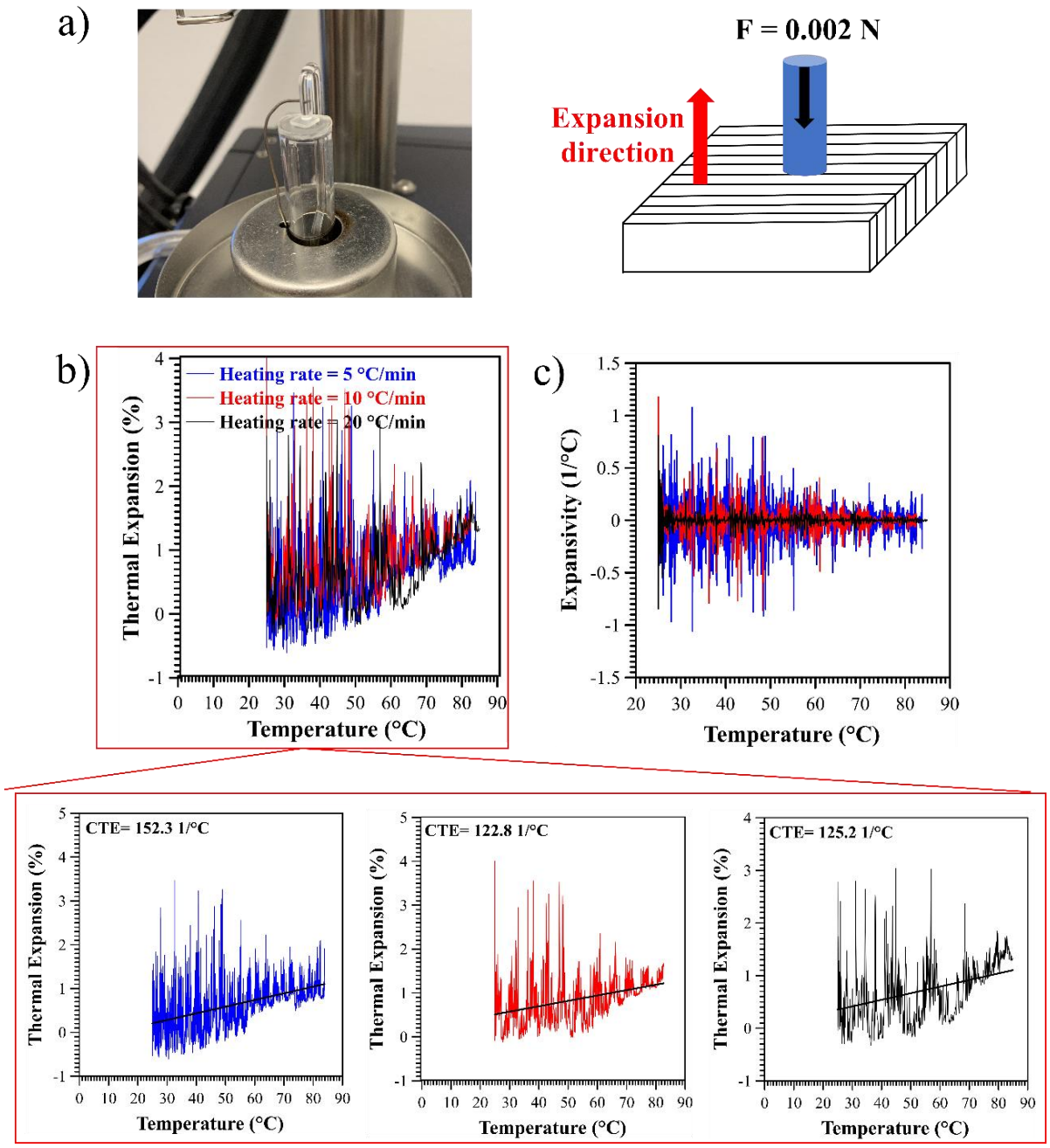

Figure 65. *Thermal expansion of SMEp1 specimens at different heating rates using the micro probe (0.002 N) : a) TMA setup with the sample positioned under the micro probe, alongside a schematic illustrating its interaction with the printed layers; b) Thermal expansion of SMEp1 (%) vs. temperature, showing significant noise; c) Expansivity (1/°C) of SMEp1 vs. temperature, exhibiting high noise with no distinct thermal events.*
(The three lower plots display the same thermal expansion curves from diagram (b), separated by heating rate, with linear fits used to determine the average CTE).

Additionally, the reduced measurement area covered by the micro probe increases local sensitivity, but also amplifies local irregularities, further contributing to measurement noise. Interestingly, a reduction in noise was observed in the temperature range near 60 °C, corresponding to the expected T_g of the material, which can be explained by the temperature-dependent mobility of polymer chains:

- Below T_g, the polymer chains remain in a glassy state, where they are rigid and constrained. It leads to higher residual stresses between layers and within the material, which can cause minor, irregular micro-movements as the layers resist thermal expansion.
- Above T_g, the polymer softens into a rubbery state, allowing the polymer chains to relax and move more freely, which promotes smoother, more uniform thermal expansion and reduces measurement noise.

Moreover, the inherently higher thermal expansion coefficient of polymers in the rubbery state produces larger, more detectable dimensional changes, which tend to overshadow minor fluctuations caused by local surface or interlayer imperfections. The shift to smoother expansion behavior, combined with larger overall expansion, helps stabilizing the measurement signal at elevated temperatures. Figure 65c shows the calculated expansivity profile for each heating rate, revealing considerable noise throughout the temperature range, with no distinct feature indicating the glass transition. However, the noise intensity gradually decreases as the temperature increases, similar to the trend presented in Figure 65b.

The holding force applied to the specimen surface in the next experiment was increased to 0.02 N by the micro probe (Figure 66a) to address the noise issues observed in the initial micro-expansion measurements. Thermal expansion was then measured for three individual SMEp specimens, each tested at a different controlled heating rate of 5 °C/min, 10 °C/min, and 20 °C/min. The results are summarized in Table 12.

The data shown in Figures 66b and 66c emphasize the critical role of the applied compression force during thermal expansion testing. Importantly, the fixed force does not restrict the ability of the material to expand. Instead, it ensures stable contact between the probe and the specimen, minimizing the risk of slippage, probe movement and dimensional fluctuations. When insufficient force was applied, the probe could fail to maintain consistent contact, leading to noise and allowing gradual relaxation at each temperature step. As a consequence, some key thermal events could be masked, including the glass transition peak. Therefore, applying an optimal

holding force seems to be essential for accurately detecting subtle thermal transitions during heating.

A distinct peak was detected at each heating rate in both the thermal expansion and expansivity curves (Figures 66b and c), which most probably represents a stress relaxation peak, that becomes more pronounced and shifts to higher temperatures as the heating rate increases. This sudden expansion corresponds to the T_g of the material, which aligns with the T_g identified in the DSC analysis during the first heating cycle.

In fact, the stress relaxation peak, which corresponds to T_g, becomes more pronounced with an increase in the heating rate. This is likely due to the insufficient time for gradual stress redistribution, leading to a sudden and more intense relaxation event. Moreover, the T_g peak shift to higher temperatures at faster heating rates can be attributed to kinetic effects. When the heating rate is higher, polymer chains have less time to rearrange and relax, which delays the onset of the glass transition. Additionally, a plateau is visible in the thermal expansion curves just before the T_g peak, and it extends further as the heating rate increases. The pre-T_g plateau reflects molecular rearrangement processes, which postpone the transition into the rubbery state. At higher heating rates, the material requires more time at elevated temperatures to mobilize its polymer chains, leading to this delay.

As shown in Figure 66b, the CTE values recorded before T_g are noticeably lower than those measured after T_g, exhibiting a typical behavior for polymers. The CTE values before and after the transition are provided in Table 12. Once the material passes through T_g and enters the rubbery state, the increased molecular mobility allows for greater dimensional changes, explaining the higher post-T_g CTE.

Interestingly, the thermal expansion observed at lower heating rates is greater, and the CTE values both before and after T_g are also higher when the specimen is heated more slowly, meaning that the material expands efficiently under slower heating condition. Thermal energy penetrates deeper into the specimen at slower heating rates, allowing the entire material volume to expand, resulting in higher measured expansion.

The thermal expansion observed with the micro-expansion probe indicates that anisotropy, caused by the layer-by-layer manufacturing process, significantly influences the thermal behavior and dimensional stability of the specimens. This underscores the importance of accounting for layer anisotropy when designing and analyzing 3D-printed materials [106,148–151].

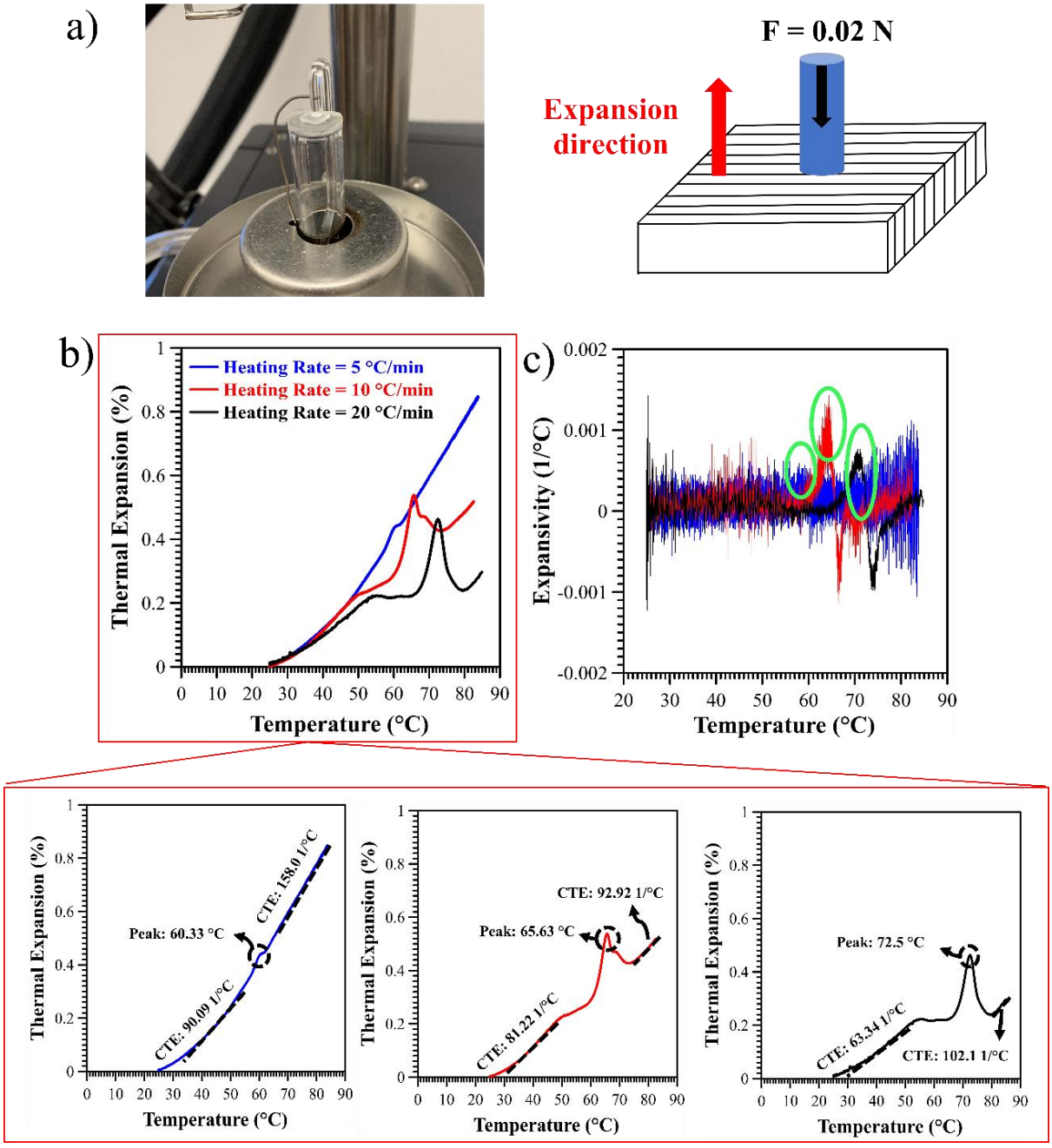

Figure 66. *Thermal expansion of SMEp1 specimens at different heating rates using the micro probe (0.02 N) : a) TMA setup with the sample positioned under the micro probe, alongside a schematic illustrating its interaction with the printed layers; b) Thermal expansion of SMEp1 (%) vs. temperature; c) Expansivity (1/°C) of SMEp1 vs. temperature, with the transition peaks at each heating rate highlighted by circles. (The three lower plots display the same thermal expansion curves from diagram (b), separated by heating rate, with linear fits used to determine the average CTE).*

Table 12. *CTE values for SMEp1 at different heating rates, measured using macro-expansion (F=0.002 N) and micro-expansion (F=0.002 and 0.02 N) probes.*

Heating rate (°C/min)	CTE (µm/m.°C) *(Macroexpansion F=0.002 N)*	CTE (µm/m.°C) *(Microexpansion F=0.002 N)*	CTE (µm/m.°C) *(Microexpansion F=0.02 N)*		
			Before T_g	Peak (T_g)	After T_g
5	487.6	152.3	90.1	60.3	158.0
10	488.2	122.8	81.2	65.6	92.9
20	491.5	125.2	63.3	72.5	102.1

This section emphasized that TMA testing parameters must be carefully selected and optimized to ensure reliable thermal expansion data for SLA-printed materials, particularly since the dimensional stability of crosslinked resins is often overlooked. Without proper contact force and probe selection, critical thermal events like T_g can be missed, and the anisotropic behavior induced by the layer-by-layer printing process may be poorly characterized. The methodological insight just presented is essential when studying thermomechanical performance of 4D-printed SMPs, where accurate thermal expansion and transitions directly influence the understanding of shape fixity and shape recovery.

The analysis performed in the framework of this research goes beyond the simple determination of CTE values and it ensures that the testing method itself does not introduce artifacts or obscure critical thermal behaviors. In practical terms, this means that future studies on SLA-printed SMPs (or other anisotropic materials) should always document and optimize TMA conditions to ensure their results are accurate, reproducible, and physically meaningful.

5.8 Thermal Expansion and Contraction Analysis of SMEps in a Heating-Cooling-Heating Cycle

The section compares the dimensional stability of SLA 3D-printed SMEp1 and SMEp2. Both specimens were subjected to a heating-cooling-heating thermal cycle under the optimized conditions established in the previous section (holding force = 0.02 N and heating rate = 10 °C/min). Thermal expansion was tracked using the micro probe, which measures thermal expansion along the thickness of the specimen. The experiment was repeated three times for each

specimen. Figure 67 presents the dimensional change versus temperature for one representative test from each sample type, while Table 5 summarizes the average values across all repetitions.

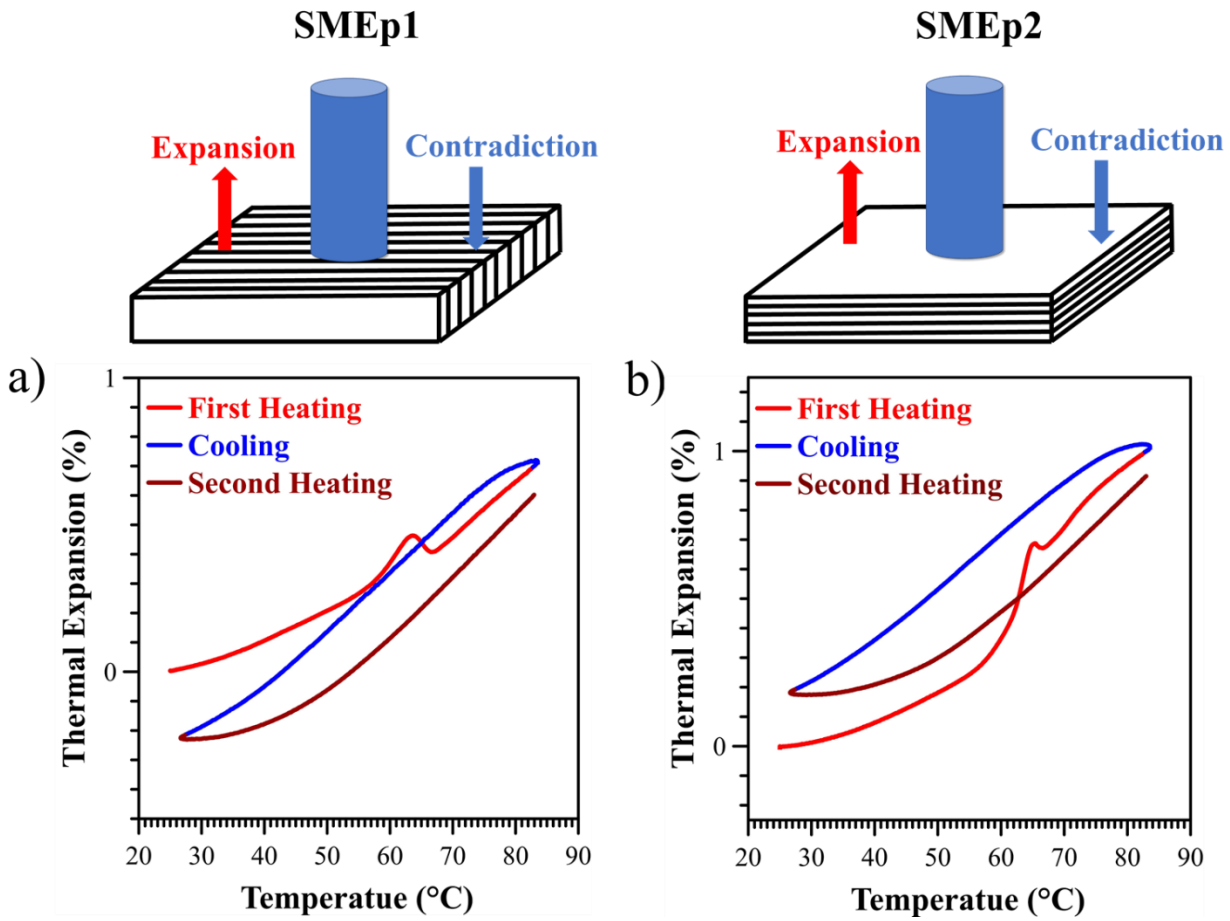

Figure 67. *Dimensional changes during the heating-cooling-heating thermal cycle for: a) SMEp1; and b) SMEp2 in response to temperature variations, using a micro-expansion probe.*

A) First Heating Phase

During the first heating, both SMEp1 (Figure 67a) and SMEp2 (Figure 67b) initially exhibited a gradual linear expansion up to about 65 °C, followed by a distinct transition peak, and subsequently, more pronounced expansion as the temperature approaches 85 °C.

The CTE values before T_g are similar for both specimens (Table 13), indicating comparable behavior in the glassy state. However, after T_g, SMEp2 underwent significantly greater thermal expansion than SMEp1, which can be attributed to two combined factors: the orientation of printed layers playing a major role, and the larger surface area of the printed layers in SMEp2.

For the specimen printed from the side surface (SMEp1), the probe measured the expansion through the thickness, oriented perpendicular to the layers, meaning the expansion crosses interlayer interfaces, as shown in Figure 67. These interfaces act as structural discontinuities that can constrain expansion, particularly if the interlayer bonding is imperfect or if the residual stresses remain trapped at the interfaces.

In the case of SMEp2 (printed flat), the probe measured expansion through the thickness and parallel to the printed layers, allowing each individual layer to expand within its own plane, where the polymer chains have greater freedom of movement and experience less interfacial constraint, leading to higher thermal expansion in the thickness direction for SMEp2.

The second contributing factor could be the larger surface area of the printed layers in SMEp2, providing more space for layer relaxation and expansion, especially if the polymer chains near the surface have lower constraint compared to the interior layers. While this surface area effect is not the primary driver in the thickness direction (since expansion was measured normal to the SMEp2 layers), it could still influence local stresses and chain relaxation, contributing indirectly to the greater expansion seen in SMEp2.

Notably, the CTE values after T_g exhibit relatively high variability within each specimen type (Table 13), leading to large standard deviations. This variability likely reflects differences in residual stresses and localized printing defects that develop during the additive manufacturing process, which were not perfectly uniform between specimens. However, despite this variability, SMEp2 consistently exhibited higher post-T_g expansion than SMEp1. The total expansion during the first heating was almost double for SMEp2 (1%) compared to SMEp1 (0.5%).

B) Cooling Phase

SMEp1 underwent greater contraction during the cooling phase than its previous expansion (0.95% contraction vs. 0.55% expansion), while SMEp2 was less contracted (0.82% contraction vs. 1% expansion). This behavior could be attributed to the internal stresses within SMEp2, which hinder its ability to fully return to its original dimensions. As a consequence, the phenomenon known as thermal hysteresis appeared, where the material does not completely recover its initial shape after a full thermal cycle. The presence of the thermal hysteresis was further supported by the lower CTE observed for SMEp2 during cooling compared to heating, indicating that residual stresses remained trapped within the structure.

C) Second Heating Phase

The dimensional changes followed a similar trend to the first heating during the second heating phase; however, no distinct transition peak was observed, indicating more stable thermal behavior after the initial thermal cycle in both SMEp1 and SMEp2. The CTE values during this phase also show greater consistency across the samples, likely due to the release of thermal history during the first heating.

Notably, SMEp1 exhibited greater dimensional expansion and higher CTE values than SMEp2 during the second heating. This suggests that SMEp1, which initially had shown less expansion and higher contraction, responded more uniformly to thermal changes in the second heating phase, likely as a result of reduced residual stresses and a more homogenized internal structure.

It is also important to note that the CTE values show less variation among the individual specimens of each type after the first heating and cooling cycle. This indicates that all specimens of the same type after the initial thermal processing behaved more consistently, highlighting the stabilizing effect of the first thermal cycle on the printed materials.

Table 13. *CTE and thermal expansion of SMEp1 and SMEp2 specimens during thermal cycles.*

Thermal Properties	SMEp1	SMEp2
First Heating		
CTE (25-50 °C) (1/°C)	68.98 ± 5.06	61.22 ± 3.35
CTE (68-85 °C) (1/°C)	136.60 ± 18.8	189.60 ± 19.85
Thermal Expansion (%)	0.55 ± 0.1	1 ± 0.05
Cooling Down		
CTE (75-40 °C) (1/°C)	174.70 ± 7.72	159 ± 2.77
Thermal Contraction (%)	0.95 ± 0.05	0.82 ± 0.20
Second Heating		
CTE (25-50 °C) (1/°C)	60.24 ± 4.30	47.03 ± 0.87
CTE (68-85 °C) (1/°C)	180.9 ± 4.17	168.93 ± 1.24
Thermal Expansion (%)	0.84 ± 0.021	0.74 ± 0.01

In summary, these findings address the impact of layer structure on the thermal stability of 3D-printed materials, highlighting the importance of controlling layers' configurations for

applications where precise dimensional consistency is critical. The variations in the thermal responses between SMEp1 and SMEp2 can be attributed to their distinct printing orientations and different internal stresses, both of which significantly affect expansion and contraction behavior under changing temperatures. Following a complete thermal cycle, SMEp1, which initially demonstrated a more stable structure, became more responsive to subsequent heating phases. In contrast, SMEp2 showed an increased potential to dimensional instability, a likely consequence of the higher initial internal stresses embedded within its structure.

5.9 Mechanical Properties and Post-Failure Microstructural Analysis of SMEps

The mechanical properties of SMEp1 and SMEp2 were evaluated at room temperature (below T_g) and at 75 °C (above T_g) to assess how temperature and printing orientation influence their elastic-plastic response. The tests were carried out using dog-bone specimens, which were subjected to uniaxial tensile loading to failure, using a tensile testing machine equipped with an environmental chamber to precisely control temperature. In both SMEp1 and SMEp2, the tensile force was applied parallel to the printed layers, but the loading configuration differs between the two orientations. In SMEp1, the force was distributed across a large number of thin layers, each with a relatively small surface area. In contrast, in SMEp2, the force acted on fewer layers, each with a larger surface area, as shown schematically in Figure 68a. Three specimens of each type (SMEp1 and SMEp2) were tested at each temperature to ensure reliability. The specimens of each kind showed similar behavior, and the stress-strain curves presented in Figures 68b and 68c represent the mean values for each sample set. Key mechanical properties, including the Young's modulus, ultimate strength, and elongation at break are summarized in Table 14, both obtained below and above T_g.

To evaluate the high-temperature mechanical performance of the specimens, they were heated while clamped in the tensile testing machine grips. A minimal holding force of 0.02 N was applied during heating, informed by TMA results, which demonstrated that heating without sufficient contact force could cause specimen shifting and introduce measurement noise. Applying this small holding force ensured that the specimens remained securely positioned within the grips throughout heating, enabling accurate capture of thermal elongation in addition to mechanical deformation.

Since polymers have inherently low thermal conductivity, heating them results in gradual temperature equilibration and often undesirable thermal gradients across the specimen. These temperature gradients can lead to non-uniform expansion, making it necessary to hold the specimen at the target temperature for a sufficient duration to allow for uniform heating and for internal stress relaxation to occur. This relaxation process is accompanied by thermal expansion, as the polymer chains gain mobility with increasing temperature.

In this study, thermal expansion was deliberately incorporated as part of the total measured deformation, providing a more realistic evaluation of the material's response under combined thermal and mechanical loads. This approach is particularly relevant for practical applications where dimensional precision at elevated temperatures is critical, such as in thermomechanical devices or functional components exposed to varying thermal environments. As shown in Table 14, at both temperatures, SMEp1 and SMEp2 displayed similar Young's modulus values, indicating that printing orientation does not significantly influence the elastic stiffness of the material. Such orientation insensitivity in elastic modulus has also been observed in previous work by Li *et al*. [152]. However, the post-yield behavior of the two specimens diverged significantly, as follows:

- Both printing orientations exhibited brittle mechanical behavior, attributed to the inherently brittle nature of the crosslinked epoxy. However, SMEp1 demonstrated a more pronounced brittle response, fracturing immediately after yielding, without notable strain hardening, plastic plateau, or necking.
- In contrast, SMEp2 demonstrated greater ductility, undergoing substantial plastic deformation after the yield point, accompanied by noticeable necking.
- SMEp2 also showed a higher elongation at break, indicating enhanced toughness, while SMEp1 exhibited a higher ultimate strength, meaning it required a greater applied force to initiate failure, possibly due to its greater number of printed layers, contributing to overall structural reinforcement.

The divergence in plastic behavior is likely influenced by the differences in the interlayer bonding between the two printing orientations. Post-printing SEM images (Figure 59 in section 5.2) revealed that SMEp1 has thicker and more prominent interlayer connections than SMEp2. It suggests that the failure behavior of SMEp1 is heavily influenced by the strength and stiffness of the interlayer bonds. Therefore, once they break, catastrophic failure follows, resulting in brittle

fracture. On the other hand, SMEp2 with thinner and less pronounced interlayer bonds, had more freedom for interlayer sliding and deformation, contributing to ductile failure.

Differences in free volume between the specimens could be another important factor. SMEp2, having fewer printed layers, was exposed to the UV laser fewer times during printing. As a result, portions of the resin may not have fully cured, potentially leading to increased free volume within the structure. A higher free volume allowed more space for polymer chains to move, making SMEp2 more compliant under stress, which would explain both its lower yield stress and its greater elongation at break. Additionally, a greater free volume resulted in a more homogeneous stress distribution, reducing localized strain concentrations and delaying strain softening, factors that contribute to smoother post-yield behavior of SMEp2 [153].

As mentioned, our goal was to incorporate thermal elongation caused by heating as a part of the overall deformation measured during the test. The thermal elongation reflected the expansion of the printed layers along the length of both SMEp1 and SMEp2. This expansion was captured directly by the movement of the tensile grips as the specimens were heated under a minimal holding force of 0.02 N. Interestingly, the greater uniaxial thermal expansion observed in SMEp2 at 75 °C aligns with the TMA results, which also demonstrated greater thermal expansion through thickness for SMEp2 during the first heating cycle (Table 14). This behavior can be linked to the larger surface area of each printed layer in SMEp2, which offered more space for dimensional relaxation and thermal expansion along the length of the specimen as the temperature rises. Moreover, the flat printing configuration of SMEp2 may promote easier layer separation and expansion in response to heat. This structural configuration, coupled with higher free volume, enhanced the ability of SMEp2 to expand under both thermal and mechanical loads.

Notably, the results also revealed that the thermal expansion along the length of specimens was substantially greater than the thermal expansion through the thickness. Specifically, the thickness expansion, recorded via TMA, reached a maximum of about 1%, while the lengthwise thermal expansion recorded during the tensile test ranged from approximately 6% to 12%, depending on the specimen type and test conditions. This discrepancy highlights the anisotropic nature of the printed specimens. Expansion occurred within the plane of the printed layers along the length, where polymer chains had greater freedom to reorient and extend.

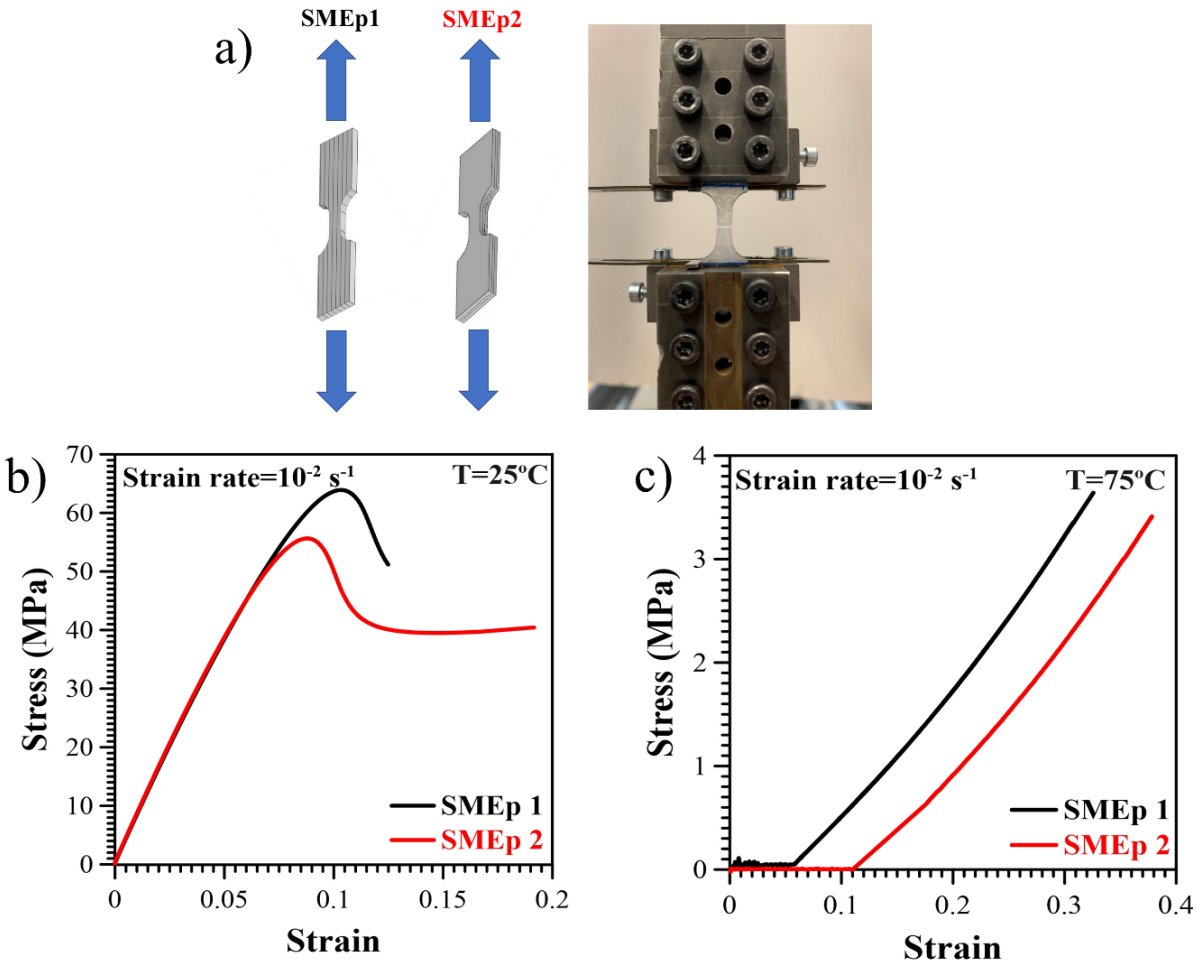

Figure 68. *a) Schematic diagram showing the tensile loading direction relative to the printed layers in SMEp2, along with an image of the dog-bone specimen mounted in the grips of the tensile testing machine ; b) stress-strain curves for SMEp1 and SMEp2 tested at room temperature (25 °C); c) stress-strain curves for SMEp1 and SMEp2 tested at 75 °C, above the material's T_g (Data for SMEp1 obtained in collaboration with Prof. Elżbieta Pieczyska, Dr. Maria Staszczak, and Mr. Leszek Urbański).*

Table 14. *Mechanical properties obtained from tensile tests to failure on SMEp1 and SMEp2 specimens, (tests carried out at room temperature and 75 °C).*

Mechanical properties	**SMEp1**		**SMEp2**	
	room temperature	*75 °C*	*room temperature*	*75 °C*
Young's Modulus (MPa)	770 ± 13.14	10.89 ± 0.491	774 ± 9.36	11.08 ± 1.50
Elongation at Break (%)	13.05 ± 0.45	32.25 ± 1.70	19.05 ± 2.02	37.98 ± 1.60
Ultimate Strength (MPa)	63.93 ± 0.435	3.63 ± 0.127	55.71 ± 0.67	3.41 ± 0.17
Uniaxial Thermal Expansion (%)	-	5.9 ± 0.35	-	11.87 ± 1.33

In contrast, through-thickness expansion was constrained by interlayer bonding, where interfaces between layers acted as structural barriers that resist thermal movement.

The mechanical properties summarized in Table 14 further emphasize the observed trends observed. At both temperatures, the Young's modulus was nearly identical between SMEp1 and SMEp2, but:

- The elongation at break of SMEp2 was approximately 46% higher at room temperature and 18% higher at 75 °C, compared to SMEp1.
- Conversely, SMEp1 exhibited a higher ultimate strength than SMEp2, by approximately 13% at room temperature and 6% at 75 °C.
- Finally, the thermal elongation at 75 °C for SMEp2 was roughly 101% greater than for SMEp1, reinforcing the previously observed greater thermal expansion capacity of SMEp2.

The mechanical results indicate that this material is not suitable for cold programming, primarily due to its inherently brittle behavior.

The effect of printing orientation on the failure mechanisms was investigated on the SLA 3D-printed specimens. Fracture surfaces of both SMEp1 and SMEp2 were carefully examined using SEM after tensile fracture at room temperature. Observations were made perpendicular to the printed layers, meaning the flat surface was examined for SMEp1, while the side surface was inspected for SMEp2. The locations of the observed fracture surfaces are marked with black circles in the schematics of specimens shown in Figure 69.

Post-fracture analysis for SMEp1 revealed that the interlayer bonds appeared brighter compared to their pre-deformation state (compare Figure 59a and Figure 69a). This lightened appearance is likely due to stress whitening and changes in electron scattering caused by local damage, which alters the way of the material interaction with the electron beam in SEM imaging. This scattering effect can make the damaged zones look visibly lighter than undamaged areas. Additionally, several closed microcracks, aligned perpendicular to both layers and the loading direction, were detected across the gauge section of the fractured SMEp1 dog-bone specimen (shown in Figure 69a and magnified in Figure 69b).

Surface examination further indicated that the long, closed cracks (ranging from approximately 5 μm to 70 μm) were formed without the presence of voids, fibrils, or crazes representing typical ductile failure markers. Therefore, it can be concluded that SMEp1 failed

through a brittle fracture mechanism, consistent with its brittle mechanical behavior observed during tensile testing at room temperature [154].

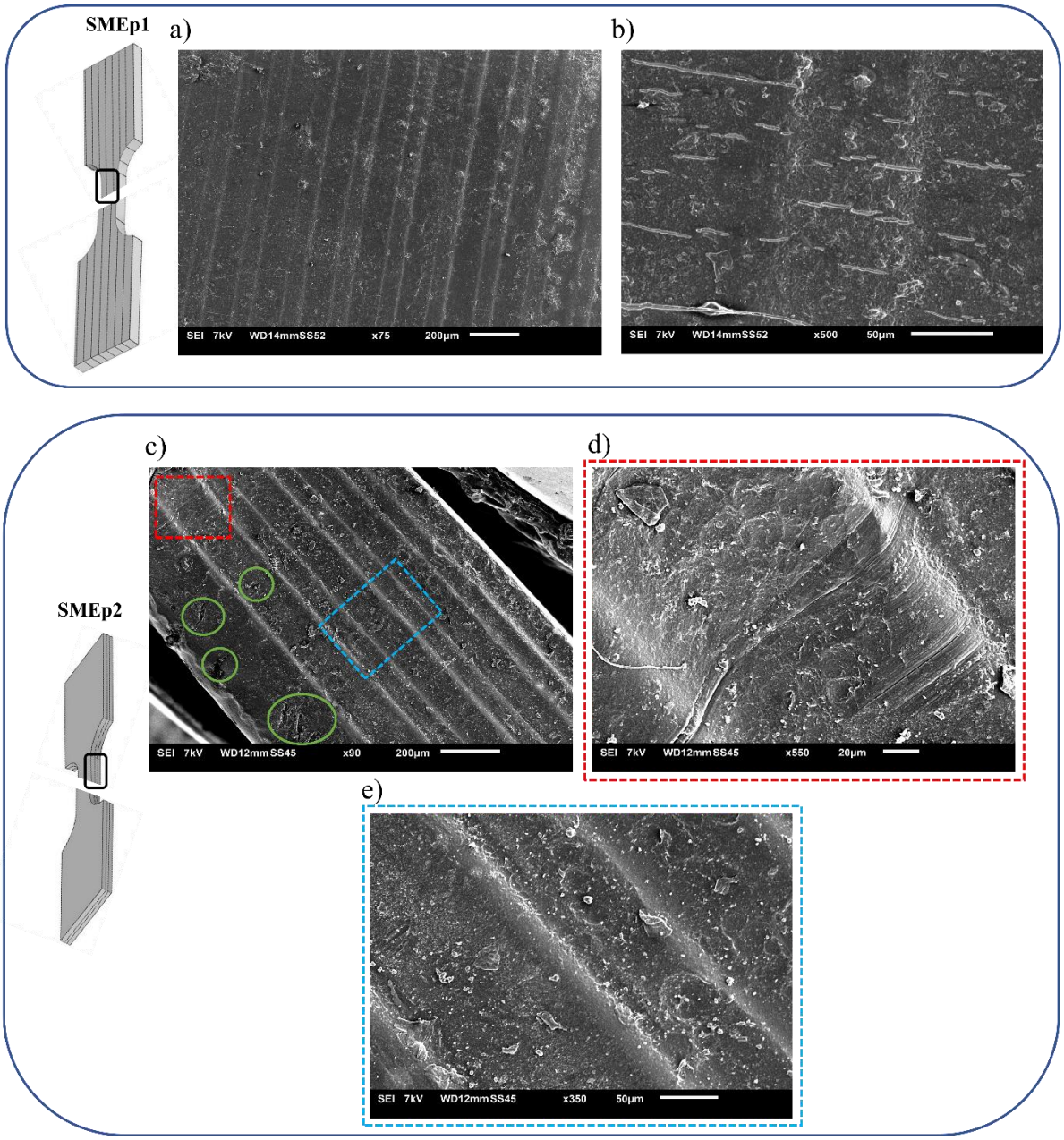

Figure 69. *SEM images of the gauge section of dog-bone specimens after tensile failure at 25 °C (observed perpendicular to the printed layers, as highlighted by black circles in the specimen schematics) : a) Fracture surface of SMEp1; b) Higher magnification view of SMEp1 showing microcracks oriented perpendicular to the layer direction; c) Fracture surface of SMEp2, with the red rectangle indicating shear-induced layer separation, the blue rectangle highlighting the absence of closed microcracks, and the green circle marking wide open cracks near the specimen edge; d) Close-up view of the shear-induced layer separation in SMEp2 near the fracture site, and; e) Detailed view of surface of SMEp2, confirming the absence of microcracks.*

In contrast, the fracture surface analysis of SMEp2 revealed a different failure mode. As shown in the schematic of SMEp2 specimen in Figure 69 (area near the fractured region), the specimen fractured in a way that indicates shear-induced separation between layers. This type of failure is more clearly presented in Figure 69d at higher magnification, which is characterized by the sliding of layers relative to each other under stress. No closed microcracks were detected on the SMEp2 fracture surface (Figure 69e), thus, further supporting conclusion that its failure process was dominated by shear-induced delamination rather than brittle fracture.

Such a type of failure generally reflects insufficient interlayer bonding strength, meaning that the bonded interfaces between layers were not strong enough to resist the applied tensile load. This interpretation aligns with the SEM images of the printed parts before mechanical testing (Figure 59b), where the interlayer bonds in SMEp2 appeared thinner and often exhibited signs of partial delamination. The weak interlayer connections allow shear deformation to occur more easily, causing the layers to slip past each other instead of undergoing uniform plastic deformation. In contrast, the SEM image shown in Figure 59a for SMEp1, exhibits thicker interlayer bonding regions (referred to as over-cured areas), which provide stronger interlayer adhesion. The stronger bonding combined with smaller individual layer surface areas, limit the potential for interlayer sliding and instead promotes uniform crack propagation across the structure, resulting in the brittle, perpendicular cracking observed in SMEp1.

Additionally, the presence of wide-open cracks and delaminated areas near the edges of the fractured SMEp2 specimen, almost perpendicular to both the layers and the loading direction (highlighted in green in Figure 69c), further supports that SMEp2 underwent more ductile failure than SMEp1. The ductile character is consistent with weaker interlayer adhesion and greater freedom for layer separation in SMEp2 [143,155].

The fractured cross-sections of specimens tested at both 25 °C and 75 °C were examined using SEM, in order to further investigate the failure mechanisms of SMEp1 and SMEp2. Figure 70a shows the fracture surface of SMEp1, printed from the lateral surface, after fracture at room temperature (below its T_g). The fracture path appears highly uneven and jagged, suggesting a brittle fracture, which is consistent with the mechanical behavior shown in Figure 68b. Typically, brittle fractures in polymers are associated with smooth and shiny fracture surfaces. However, the non-smooth fracture surface in SMEp1 could be attributed to the layered architecture of SLA printing. Since SMEp1 has a greater number of thinner layers due to its printing orientation, the failure

involves the successive fracture of many closely packed interfaces. This multi-layered failure pathway may result in a jagged and rough morphology, despite being brittle in nature.

Figure 70b presents the fracture surface of SMEp2, printed from the flat surface, after fracture at 25 °C. Here, the fracture surface is comparatively smooth and flat, which aligns with the ductile behavior observed in the stress-strain curve, Figure 68b. While ductile fractures typically produce rougher surfaces due to plastic deformation and necking, the layered structure of SMEp2 complicates this expectation. Since SMEp2 consists of fewer, thicker layers, the failure occurs across a smaller number of interlayer connections. This may lead to a cleaner break across the thicker layers, resulting in a smoother appearance despite ductile failure. Thus, the visual morphology of the fracture is influenced not only by the failure mode but also by the number and size of printed layers involved in the fracture.

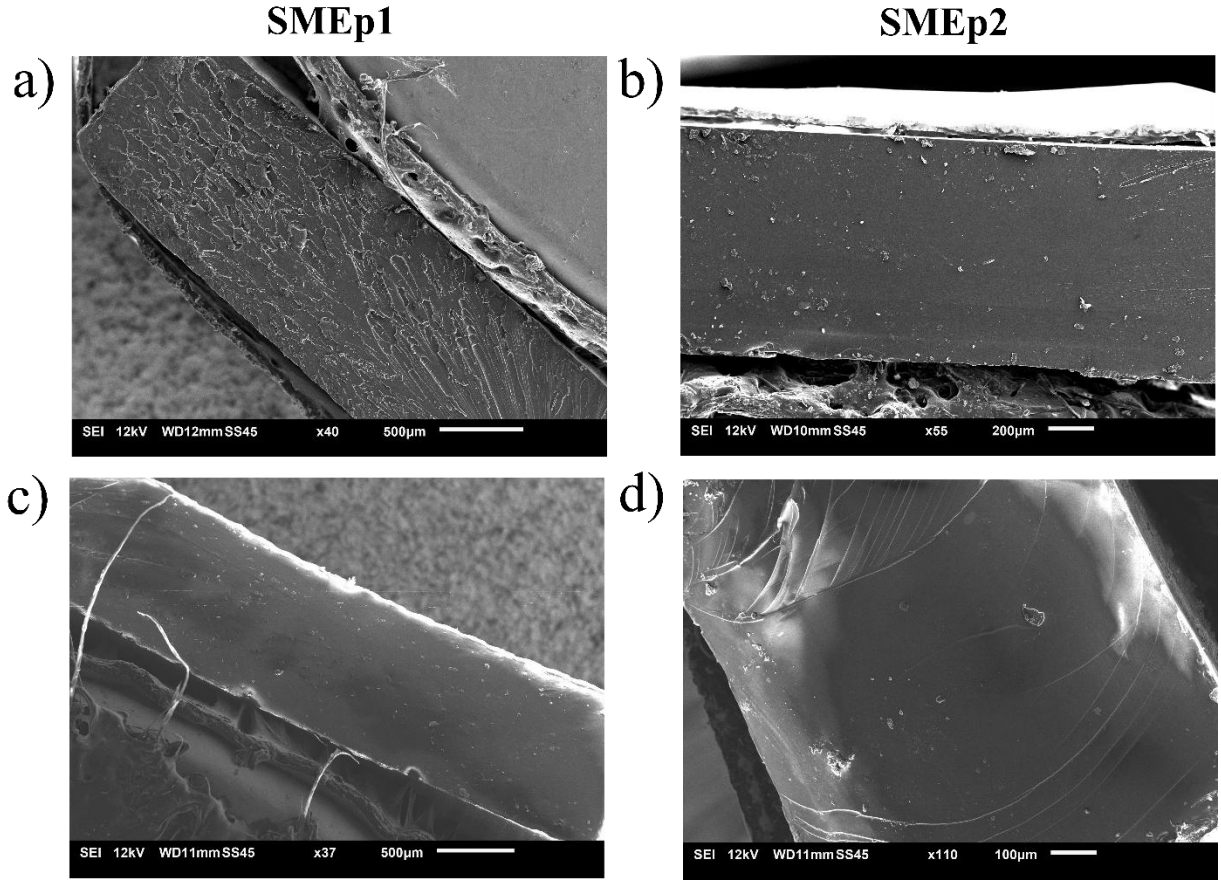

Figure 70. *SEM images of the fractured cross-sections of: a) SMEp1 at 25 °C; b) SMEp2 at 25 °C; c) SMEp1 at 75 °C; d) SMEp2 at 75 °C.*

Figures 70c and 70d show the fracture surfaces of SMEp1 and SMEp2, respectively, after testing at 75 °C, above the T_g. Both fractured cross-sections appear smoother and less irregular, which is consistent with the ductile nature of polymer behavior in the rubbery state, Figure 68c. Polymer chains gain mobility above T_g, allowing energy dissipation through plastic deformation rather than catastrophic crack propagation. The increased chain mobility also helps relax internal stresses during deformation, leading to more uniform and smooth fracture surfaces in both build orientations.

This analysis highlights how failure morphology in SLA-printed parts cannot be interpreted using traditional expectations alone. The layer-by-layer architecture of printed specimens introduces additional factors, such as layer thickness and interfacial bonding, that modify how brittle or ductile fractures manifest visually. The rough appearance of the brittle fracture in SMEp1 is likely due to the disruption of numerous thin layers. In contrast, SMEp2, with fewer but thicker layers, showed smoother fracture planes, even under ductile failure modes [152,156].

5.10 Shape Memory Evaluation of SMEps through Thermomechanical Cycle Testing

The shape memory performance of SMPs manufactured through 3D printing can be notably affected by the orientation in which the specimens are built relative to the platform. The layer-by-layer fabrication inherent to 3D printing introduces anisotropy in the thermomechanical properties of thermally sensitive 4D-printed structures, resulting in directional variations in performance and stability. Given SMPs rely on precise thermal and mechanical responses to recover their original shape, understanding how print orientation impacts shape memory performance (shape fixity, shape recovery, and actuation behavior) is vital. For instance, Zhao *et al*. [157] confirmed that the layer-wise fabrication induces significant directional differences in shape memory behavior, their experiments showed clear anisotropy in both the shape fixity ratio and the shape recovery ratio of printed thermo-responsive polymers. Liu *et al*. [158] found out that, beyond how much shape is recovered, the rate at which an SMP recovers (i.e. how fast the shape change occurs upon stimulus) also shows orientation-dependent behavior in FDM 3D printing and recovery kinetics can be faster or slower based on how the object was printed. This indicates that certain print orientations can impede the recovery rate, likely because of how the

internal stresses release and how the material softens along different orientation, whereas some orientations can enhance the actuation speed [142].

A detailed thermomechanical cycle was performed for each build orientation to comprehensively analyze and compare the shape memory behavior of SMEp1 and SMEp2. Thermomechanical cycling enables the evaluation of key properties such as shape fixity and shape recovery, which are essential indicators of the ability of an SMP to retain and recover programmed deformations. Therefore, three dog-bone specimens were tested for each orientation, SMEp1 and SMEp2 (Figure 71a, b). The results are summarized in Table 15. A thermomechanical cycle for a representative single sample of each type is shown in Figure 71c, d.

The thermomechanical cycle included the following steps:

1. *Heating*: Each sample was heated to 75 °C at a controlled rate of 12 °C/min within an environmental chamber. The specimens were clamped in tensile grips, and a minimal force of 0.02 N was applied based on TMA findings to ensure the thermal expansion was recorded with minimal noise. The uniaxial thermal expansion is recorded in this phase, which is reflected by the red line in Figure 71c, d representing the elongation.
2. *Loading*: Tensile force was applied to each specimen at 75 °C, until a 20% strain (excluding thermal deformation) was achieved at the constant strain rate of 10^{-2} s^{-1} (purple line in Figure 71c, d). The level of strain was selected based on prior mechanical testing to ensure that neither SMEp1 nor SMEp2 would fail before attaining the assumed strain level.
3. *Cooling*: The specimens, with maintained deformation, were cooled to room temperature. The stress increased during the cooling, thus preserving the deformation attained in the loading phase (blue line in Figure 71c, d).
4. *Unloading*: Each specimen was then unloaded to zero force at the same strain rate, effectively locking in the deformation established during the previous steps. This fixed deformation represents the shape that the specimen “fixes” upon cooling (green line in Figure 71c, d).
5. *Reheating*: Finally, the specimens were reheated to 75 °C with minimal applied force (0.02 N) to allow the material to recover its original shape (black line in Figure 71c, d).

Thermal elongation represents a major challenge in the hot programming of polymers, which is an unavoidable consequence of heating, which can cause the material to deform beyond the pre-

programmed strain, leading to dimensional inaccuracies in applications that require tight tolerances.

Excessive thermal expansion can also interfere with shape memory performance. If the expansion is too large, the material may fail to fully recover its intended shape, as a portion of the pre-programmed strain may be offset by the thermal expansion strain. This can reduce the shape recovery ratio, ultimately compromising the material's ability to return to its original configuration. For example, Sedat *et al*. [109] reported that thermal expansion can interfere with the shape recovery process of deformed SMPs, potentially preventing shrinkage and thereby limiting the material's performance. Expansion-related distortions can be particularly problematic in complex or multi-step shape recovery sequences, where precise control over deformation and recovery is crucial.

As it was previously established, thermal expansion in 3D-printed structures is highly dependent on build orientation. In 4D-printed SMPs, the inherent layer-wise anisotropy results in directional differences in thermal expansion between the print (in-plane) and build (through-thickness) directions. The anisotropic expansion introduces an additional layer of complexity in predicting shape recovery, as varying thermal expansion rates can lead to non-uniform deformation during heating and affect the final recovered shape.

Assessing the shape fixity (SF) and shape recovery (SR) properties is fundamental for evaluating the reliability and effectiveness of SMPs in practical applications. Shape fixity reflects the ability of the material to retain a deformed shape upon cooling, while shape recovery defines the extent to which the SMP can revert to its original configuration upon reheating. These parameters are critical in applications such as biomedical devices, aerospace components, and smart textiles, where precise control over shape change is essential under varying thermal conditions. Quantifying these properties ensures that the SMP will perform predictably and maintain structural integrity in real-world scenarios [39,122,159].

In this study, in order to precisely determine the shape fixity and recovery characteristics of SMEp specimens, the uniaxial thermal expansion was accounted during the initial heating phase along with the mechanical elongation in the loading phase. Both testing techniques mentioned above well reflect the relevant aspects of global deformation. This dual approach allows to evaluate the capacity of the material to fix and recover deformations resulting from both thermal and mechanical effects.

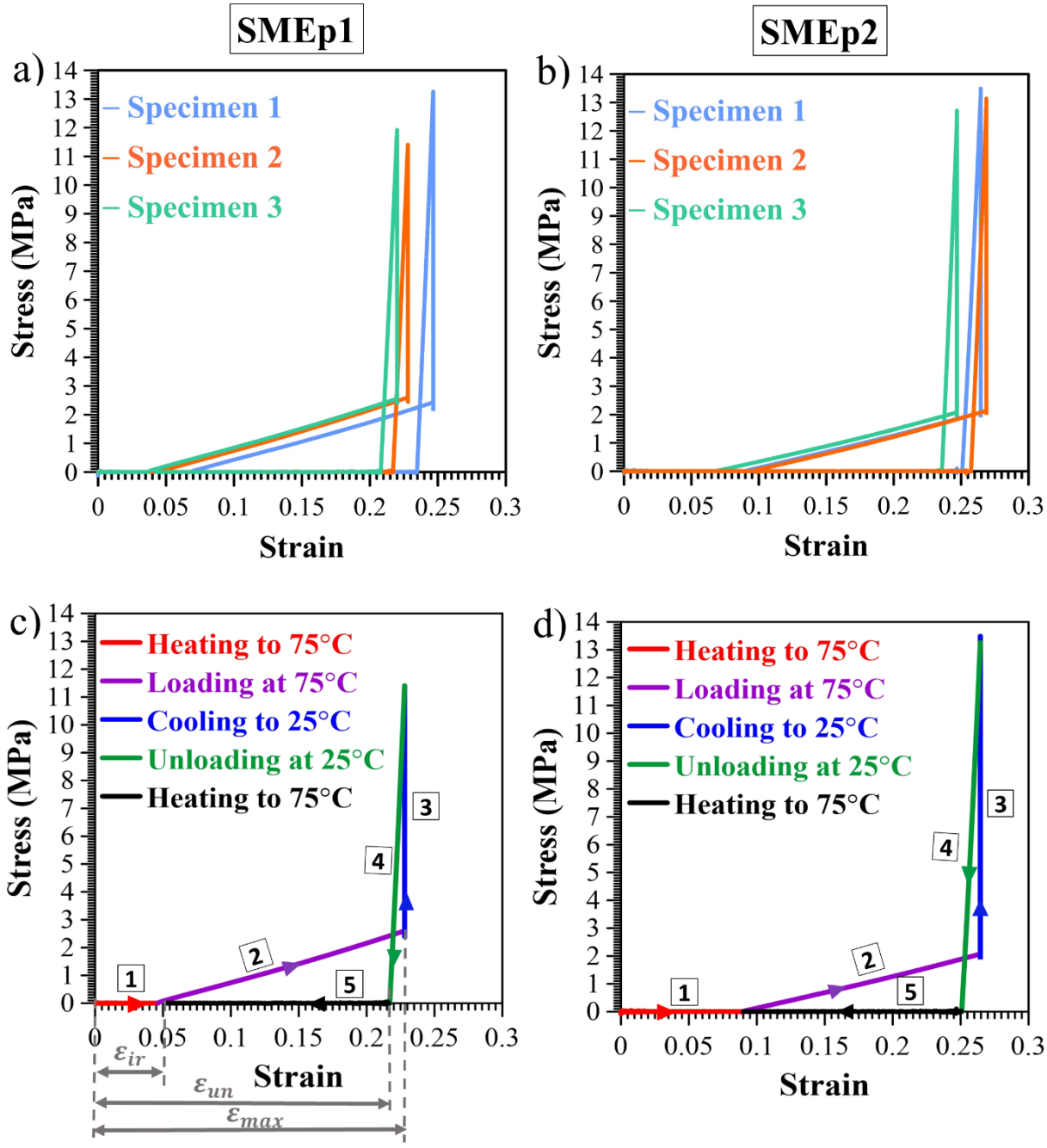

Figure 71. *Stress–strain responses obtained from the thermomechanical programming cycle: a) Three SMEp1 specimens; b) Three SMEp2 specimens; c) Representative thermomechanical cycle of SMEp1, showing the five stages: heating, loading, cooling, unloading, and reheating; d) Representative thermomechanical cycle of SMEp2, showing the same five stages* [3,115]. *(Data for SMEp1 obtained in collaboration with Prof. Elżbieta Pieczyska, Dr. Maria Staszczak, and Mr. Leszek Urbański)*

The shape fixity (SF) and shape recovery (SR) percentages were calculated based on the experimental data from the thermomechanical cycles illustrated in Figures 71c and d using Equations 3 and 4 presented in section 4.7.

In order to better understand characteristics presented in Figure 71, the diagram in Figure 71c identifies the strain components appearing during the test, i.e.: ε_{max} - maximum deformation at which the specimen was held in place during the cooling phase (step 3), ε_{un} is the recorded strain after unloading at room temperature (step 4), and ε_{ir} - irrecoverable strain observed after reheating to 75 °C (step 5).

Table 15 presents a summary of the thermomechanical properties, including uniaxial thermal elongation, shape fixity, shape recovery, shape recovery rate, and irrecoverable strain, for three specimens of each orientation (SMEp1 and SMEp2) along with their average values and standard deviations.

5.10.1 Comparison of Thermomechanical Parameters of SMEps

The results of tests showed that SMEp2 consistently exhibited greater uniaxial thermal elongation than SMEp1 across all tested specimens, despite all specimens were heated under the same conditions. This suggests that SMEp2, underwent more pronounced uniaxial expansion upon heating accompanied by greater transverse expansion due to its larger surface area and potentially weaker interlayer bonds, as indicated by TMA data. Additionally, it is evident that the amount of uniaxial elongation varied within the same type of SMEp. This might be due to the slight inconsistencies in layer bonding, residual stresses introduced during the printing process, or minor differences in curing and post-processing conditions, which could all influence the thermal response of each specimen. The variation in thermal elongation during the initial heating phase within a given specimen type may subsequently influence shape memory performance, leading to differences in the extent to which SMEp1 and SMEp2 recover their shape. This variability can affect the results repeatability and reproducibility of the final object.

Two key aspects must be considered: (1) the comparison of thermomechanical parameters between SMEp1 and SMEp2 and (2) the effect of thermal expansion on each property. Figure 72 illustrates the correlation between shape fixity, shape recovery, and shape recovery rate in both SMEp1 and SMEp2 as a function of uniaxial thermal expansion. The exact quantitative values are detailed in Table 15.

Data presented in Table 15 and Figure 72a indicate that the shape fixity values for both SMEp1 and SMEp2 are nearly identical, consistently around 95%, regardless of build orientation (lateral or flat) or uniaxial thermal expansion. It suggests that variations in thermal elongation and

build orientation have minimal impact on the ability of SMPs to retain their deformed shapes upon cooling. This behavior can be attributed to the glassy state of the polymer during the fixing phase, where molecular mobility is highly restricted, effectively locking the deformed shape in place and minimizing the influence of structural differences such as build orientation or thermal expansion.

However, SMEp1 exhibited higher shape recovery than SMEp2, with SMEp2 also demonstrating a lower shape recovery rate. This difference indicates that SMEp2 experiences greater irrecoverable strain, making it less able to fully return to its original shape after heating.

Furthermore, Figure 72b and Figure 72c show the effect of uniaxial thermal expansion on shape recovery in SMEp1 and SMEp2, respectively. The results indicate that greater uniaxial thermal expansion leads to lower shape recovery in both build orientations, suggesting that excessive expansion during heating causes stress relaxation, larger deformation and a reduction in recoverable strain.

Figure 72d and Figure 72e highlight in a similar way the relationship between uniaxial thermal expansion and shape recovery rate, showing that greater thermal expansion in the first heating step results in a slower shape recovery rate in the final step. This suggests that the extent of thermal elongation influences not only the amount of shape recovery but also the kinetics of the recovery process.

The lower shape recovery and shape recovery rate in SMEp2 compared to SMEp1 can be attributed to multiple factors related to interlayer bonding, thermal expansion, stress relaxation, and plastic deformation.

One of the primary reasons can be a weaker interlayer bonding in SMEp2, as seen in SEM results in Figure 59b, which reduces structural integrity and limits the effective transfer of stored elastic energy during recovery. The weaker adhesion between layers could lead to micro-slippage or delamination, causing some of the stored strain energy to dissipate instead of being recovered. Additionally, interfacial defects can create stress relaxation zones, further preventing the polymer from fully returning to its original shape. This contrasts with SMEp1, where stronger interlayer bonding allows for better energy transfer and a more forceful recovery.

The greater thermal expansion in SMEp2 serves as another key factor for both uniaxial and transverse directions, due to its larger surface area per layer. Higher thermal expansion in SMEp2 allowed for more stress relaxation before recovery was triggered, meaning less internal stress

remained to drive shape restoration. In contrast, SMEp1, with a more confined structure, retained a more internal stress energy, leading to a stronger recovery [160].

Additionally, the negative effect of uniaxial thermal expansion during the first heating step on shape recovery and shape recovery rate in both SMEp1 and SMEp2 is evident. An excessive thermal elongation during the initial heating phase leads to stress relaxation, redistributing internal stresses and reducing the stored elastic energy available for recovery. As a result, the material loses part of the driving force required for efficient shape recovery, leading to a slower response and a lower overall recovery percentage.

Moreover, the higher thermal elongation in SMEp2 delayed the activation of shape recovery, as the material needed time to stabilize before transitioning back to its original shape. Higher ductility of SMEp2 also led to greater plastic deformation, increasing irrecoverable strain, which reduced the amount of deformation that could be recovered.

Table 15. *Thermomechanical properties of SMEp1 and SMEp2. (Data for SMEp1 obtained in collaboration with Prof. Elżbieta Pieczyska, Dr. Maria Staszczak, and Mr. Leszek Urbański.)*

Thermomechanical properties	SMEp1				SMEp2			
	1st specimen	2nd specimen	3rd specimen	Mean	1st specimen	2nd specimen	3rd specimen	Mean
Uniaxial thermal expansion (%)	6.9	4.6	3.7	5.1 ± 1.35	9	9.5	7	8.5 ± 1.08
Shape fixity (%)	95.2	95	94.5	94.9 ± 0.29	94.8	95.8	95.4	95.3 ± 0.41
Shape recovery (%)	64.5	77	80.6	74.0 ± 6.89	65.6	63.5	70.2	66.4 ± 2.79
Shape recovery rate (s^{-1})	0.12	0.23	0.29	0.2 ± 0.07	0.11	0.10	0.12	0.1 ± 0.008
Irrecoverable strain (%)	35.5	23	19.4	25.9 ± 6.89	34.4	36.5	29.8	33.5 ± 2.79

Interestingly, the influence of the uniaxial thermal expansion on the shape recovery rate was more pronounced in SMEp1 than in SMEp2, because SMEp1 had stronger interlayer bonding, lower stress relaxation, and less ductility, making its recovery rate more sensitive to expansion-induced internal stresses. In contrast, SMEp2 exhibited greater stress relaxation and higher

ductility, allowing more strain dissipation before recovery, which reduced the impact of uniaxial expansion on its recovery rate. As a result, SMEp1 showed a steeper decline in shape recovery rate with increasing thermal expansion, while the recovery rate in SMEp2 remained more stable despite higher expansion levels.

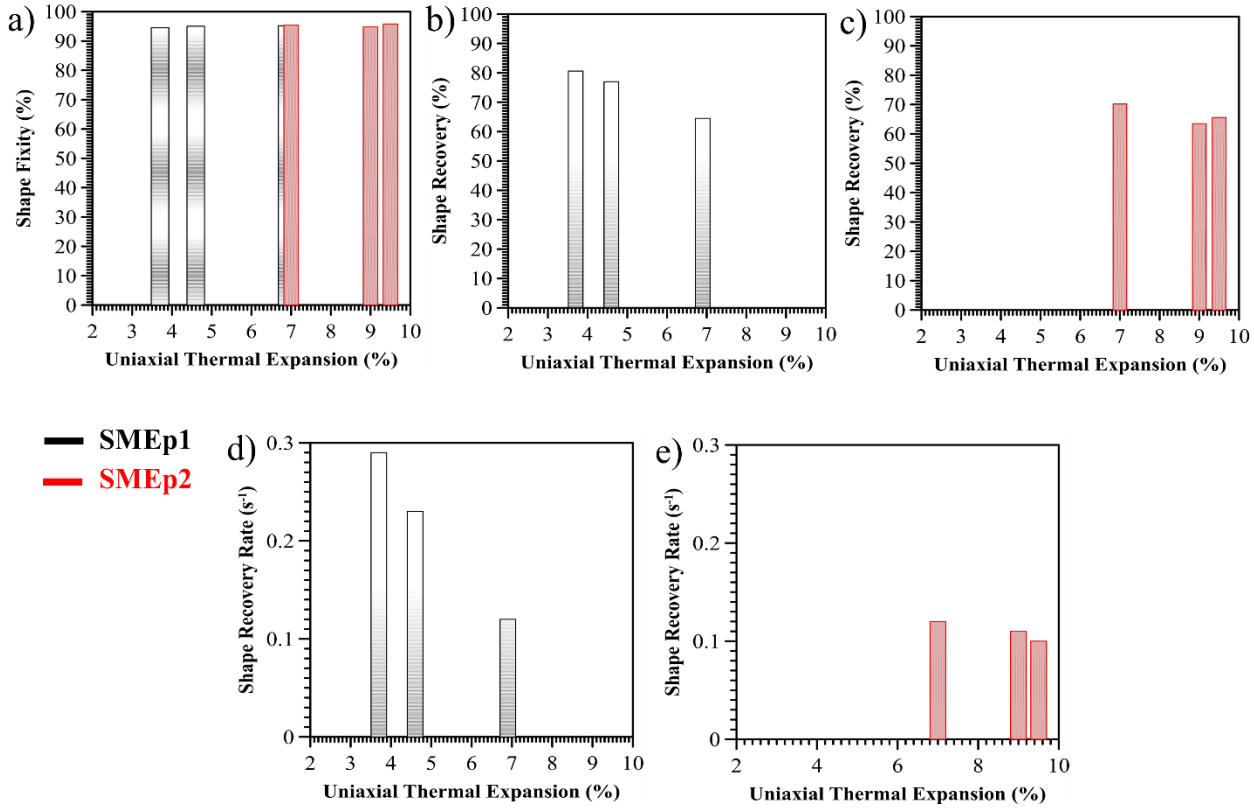

Figure 72. *Correlation between thermomechanical properties and uniaxial thermal expansion : a) Shape fixity in SMEp1 (grey) and SMEp2 (red), b) Shape recovery in SMEp1, c) Shape recovery in SMEp2, d) Shape recovery rate in SMEp1, e) Shape recovery rate in SMEp2 - all plotted as functions of uniaxial thermal expansion (%).*

The thermomechanical results obtained in this study highlight the notable impact of build orientation on the shape memory performance of SLA 3D-printed SMPs. The primary difference between the two specimens lies in the number and size of the printed layers, which significantly affected their dimensional stability and overall behavior. Specifically, SMEp2, which had a larger layer surface area, had the tendency to form weaker interlayer bonds and underwent greater thermal elongation. Both these factors negatively influenced the recovery speed and shape memory efficiency. Conversely, SMEp1 consisted of smaller, more frequent layers, resulting in stronger interlayer adhesion and improved shape recovery capabilities.

This behavior can be explained by several factors. Polymerization typically causes slight volumetric shrinkage during the SLA printing and curing process of epoxy-based resin. Here, the larger layers, like those in SMEp2, were more susceptible to uneven shrinkage, because of the broader area that needed uniform curing, potentially introducing internal stresses and reducing interlayer cohesion. Additionally, in the SLA process, the build platform was lowered slightly into the resin VAT after each layer was cured to allow fresh resin to cover the surface. For wide layers such as in SMEp2, ensuring even resin distribution across the entire surface becomes more challenging. This can cause inconsistencies in layer thickness and resin coverage, further diminishing bond strength between layers. SEM imaging in Figure 59 supports these findings, revealing that SMEp1 has more distinct and thicker over-cured layers, which contribute to the stronger interlayer bonding observed in that specimen.

5.10.2 Impact of Thermal Deformation on Shape Fixity and Recovery in SMPs

As evident, thermal elongation before loading caused a deviation in deformation (ε_m) from the pre-specified value. This means that the first negative effect of thermal expansion was related to an increase in deformation beyond the intended level. In SMP applications requiring tight tolerances, where uncontrolled deformation can impact connected components, exceeding the pre-defined deformation can be problematic.

Moreover, as discussed earlier, thermal elongation may also negatively affect the shape recovery of the SMP, likely by altering internal stress distribution and reducing the efficiency of strain recovery.

To demonstrate the negative impact of thermal elongation on the shape memory behavior of the printed SMEp specimens, shape fixity and recovery parameters were evaluated using a thermomechanical cycle framework, in which SMEp1 and SMEp2 were elongated solely by heating, without any applied mechanical loading. The stress-strain behaviors of SMEp1 and SMEp2 are illustrated in Figure 73a and Figure 73b, respectively.

To this end, the thermomechanical cycle was conducted as follows:

1- *Heating:* The specimen was positioned between the grips of a tensile testing machine inside an environmental thermal chamber and heated from room temperature to 75 °C at a rate of 12 °C/min with a minimal applied force of 0.02 N. After reaching 75 °C, the specimens were held at this temperature for 1 minute. During this step, the specimens underwent

uniaxial thermal expansion, which was recorded by the grips of the testing machine (red line in Figures 73a and b).

2- *Cooling*: The thermally elongated specimens were then cooled to room temperature while still being held in the grips, ensuring that the thermal elongation remained constant. This cooling process caused the specimens to contract, leading to an increase in stress recorded by the tensile grips due to the restorative force exerted by the polymer during contraction (blue line in Figures 73a and b).

3- *Stress Release:* Once cooled, the contraction-induced stress was released to zero, allowing the specimen to relax (green line in Figures 73a and b).

4- *Reheating for Shape Recovery:* To calculate strain recovery, the thermally deformed specimens were reheated to 75 °C while still being held in the tensile grips, allowing the recovery process to be observed (black line in Figures 73a and b).

The shape fixity (SF_T) and shape recovery (SR_T) of the thermally deformed specimens were then calculated by modifying Equations 3 and 4 into Equations 7 and 8, respectively, and the values are provided in Table 16.

$$SF_T = \frac{\varepsilon_{un}}{\varepsilon_T} \times 100 \quad (7)$$

$$SR_T = \frac{\varepsilon_T - \varepsilon_{ir}}{\varepsilon_T} \times 100 \quad (8)$$

In Equations 7 and 8 the following notations are introduced:

- ε_T represents the thermal elongation strain, which occurs when the specimen is heated from room temperature to 75 °C (above T_g) under minimal load conditions.
- ε_{un} corresponds to the strain measured after unloading the contraction stress at room temperature (below T_g).
- ε_{ir} denotes the irrecoverable strain remaining after reheating the specimen to 75 °C under minimal load conditions.

Table 16. *Uniaxial thermal elongation along with shape memory parameters of SMEp1 and SMEp2 specimens, measured under conditions of purely thermal deformation (without mechanical loading). (Data for SMEp1 obtained in collaboration with Prof. Elżbieta Pieczyska, Dr. Maria Staszczak, and Mr. Leszek Urbański)*

Thermomechanical properties	**SMEp1**	**SMEp2**
Uniaxial thermal expansion (%)	5.91	9.30
Shape fixity (%)	84.74	84.94
Shape recovery (%)	20.33	18.28

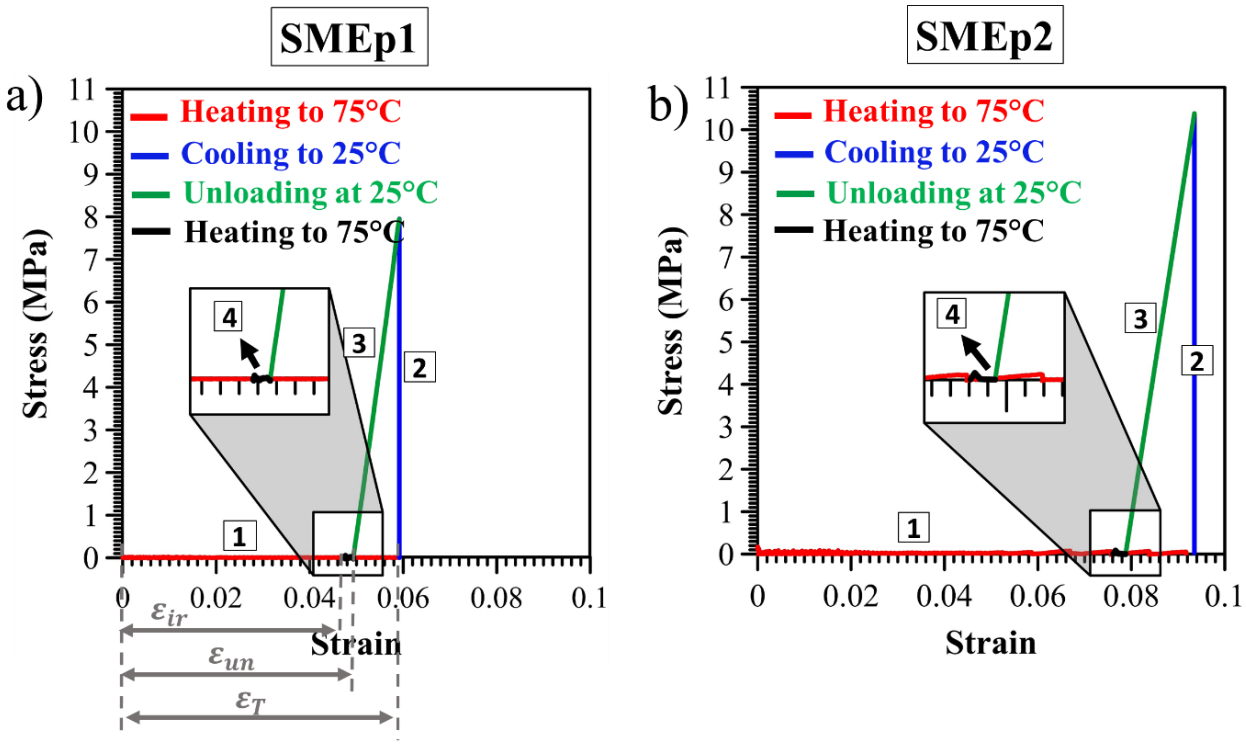

Figure 73. *Stress–strain curves from the thermomechanical cycle performed on a) SMEp1; and b) SMEp2 specimens, subjected solely to thermal expansion without applied mechanical loading. The colored curves represent different stages of the cycle: heating, cooling, unloading, and reheating* [3]. *(Data for SMEp1 obtained in collaboration with Prof. Elżbieta Pieczyska, Dr. Maria Staszczak, and Mr. Leszek Urbański)*

It has to be emphasized that based on the data presented in Table 16, the shape fixity values of both SMEp1 (84.74%) and SMEp2 (84.94%) appear lower than typically expected when specimens are programmed through mechanical deformation, which can be attributed to the fact that, the specimens experienced only thermal expansion without any applied mechanical loading. Mechanical deformation below or around the T_g in a thermomechanical shape memory programming helps to orient and freeze the polymer chains in a deformed state. However, when deformation arises solely from thermal expansion by heating to a temperature above T_g, the polymer chains have high mobility without being aligned by any mechanical force to lock the structure into a temporary shape. As a result, the material cannot fully fix the thermally induced deformation upon cooling, which leads to lower shape fixity.

The shape recovery values in Table 16 (20.33% for SMEp1 and 18.28% for SMEp2), further emphasize that both materials are largely unable to recover their original shapes after undergoing pure thermal elongation. The poor recovery is due to the relaxation of internal stresses

that occurs during heating. When polymers are heated above T_g, the increased chain mobility facilitates stress relaxation, and if the deformation is not mechanically constrained or quickly frozen, much of the strain becomes irreversible. As noted by Lendlein *et al*., such a relaxation leads to irreversible deformation, meaning that thermal deformation alone cannot effectively be recovered, resulting in high irrecoverable strain [21].

Furthermore, the higher uniaxial thermal expansion observed in SMEp2 (9.30%) compared to SMEp1 (5.91%) likely contributes to slightly lower shape recovery, as greater free expansion provides more opportunity for stress relaxation and plastic-like flow during the heating phase.

These findings highlight the importance of minimizing unnecessary thermal elongation in shape memory programming. In practical applications, especially in shape-morphing devices where tight dimensional control and repeatability are required, designs should aim to reduce heating time and avoid extended exposure above T_g. This helps to prevent thermal expansion and induced relaxation and ensures faster actuation with minimal shape loss or performance degradation.

5.11 Real-World Applications

The outcomes of this study have meaningful implications for applications in precision micro-mechanical systems, particularly in fields such as aerospace and biomedical engineering, where the behavior of 3D-printed materials under specific functional conditions is critical. Printing orientation should not only be seen as the angle between the printing platform and the printed object, but as a fundamental factor in determining the most suitable surface for fabrication to meet specific performance requirements. The chosen surface directly influences the layer count, layer surface area, interfacial bonding quality, and internal stress distribution, which in turn affect the mechanical, thermal, and shape memory responses of parts printed from different orientations. These effects are especially important in applications where fine-tuned motion control or accuracy is required, such as actuators or micro-scale mechanical assemblies. Careful consideration and optimization of printing orientation during both the design and manufacturing stages are therefore crucial for successful application.

This study emphasizes the often-overlooked anisotropic behavior of SLA-printed materials, which can significantly affect essential functions like thermal expansion, deformation

mode, and shape recovery. Neglecting anisotropy may lead to inefficient or unstable designs, while strategically managing or decreasing them can refine performance for specific use cases.

Furthermore, this study provides a practical and reproducible experimental framework for evaluating the thermomechanical performance of 4D-printed SMPs. This includes a controlled thermal cycle that allows accurate calculation of shape fixity and shape recovery, two essential metrics for assessing the reliability of shape-changing materials. These findings are particularly relevant to fields such as aerospace and biomedical engineering, where predictable actuation is essential. In addition, improvements in object performance can be achieved by tuning SLA printing parameters such as layer orientation, exposure time, post-curing, and cooling rate, helping to tailor the final material properties for specific applications [161].

Aerospace Applications:

In aerospace engineering, SLA-printed components are widely used for their lightweight structures, geometric complexity, and suitability for actuation systems in extreme environments. This study reinforces the impact of printing orientation on final part behavior. Printing from a smaller surface area per layer and higher layer counts tends to result in improved shape recovery, better thermal stability, and greater structural precision, making it ideal for deployable or adaptive mechanisms. On the other hand, printing from larger surfaces, which produces fewer and broader layers, may benefit applications that require more flexibility, such as vibration dampening or energy absorption. The proposed experimental method helps aerospace engineers to evaluate material properties and align it with mission-specific needs.

Biomedical Engineering Applications:

In the biomedical sector, SLA 3D-printed materials are widely applied in the development of implants, prosthetics, and drug delivery systems. Findings from this study suggest that components printed from a smaller surface area exhibit enhanced interlayer bonding and improved dimensional stability, making them well-suited for applications such as long-term implants or load-bearing devices. In contrast, objects printed from larger surface areas with fewer layers may offer increased flexibility, making them more appropriate for soft tissue scaffolds or devices that require greater deformability without structural failure. The experimental procedure introduced in this work enables robust characterization of such materials, facilitating the design of safer and more effective biomedical components. Furthermore, the framework for evaluating how the build surface affects material behavior could be extended to other areas like bioprinting, where layer-

by-layer fabrication plays a central role. Understanding the impact of printing orientation and surface selection could help optimize scaffold strength, mechanical integrity, and dimensional precision in tissue engineering applications [162].

Precision Micro-Mechanisms:

For small-scale mechanical systems in electronics, robotics, or optics, printing orientation becomes a crucial factor in ensuring reliable function. Aligning the printed layers with the direction of applied force can enhance the shape memory response and improve the consistency of deformation and recovery. As shown in this work, printing from a smaller surface increases interlayer bonding strength, which improves the durability and mechanical fidelity of active elements such as micro-actuators or switches. The outlined testing procedures can guide the optimization of layer orientation and support the design of robust microscale actuation systems with high repeatability.

Chapter 6

Results and Discussion (II): Design, 3D Printing and Training of SMEp Prototypes

Building upon the foundational material characterization presented earlier, this chapter focuses on applying those insights into the practical design and fabrication of shape-morphing prototypes using SMEp. By integrating the mechanical, thermal, and shape memory behaviors of the material into the design rationale, a series of monolithic, 4D-printed devices were developed to demonstrate localized, reversible actuation without the need for assembly or external stimuli beyond heat. The following sections detail the key design considerations derived from experimental findings, the implementation of compliant mechanisms and kinematic chains, and the successful demonstration of programmable shape transformation through high-resolution stereolithography. These prototypes represent a crucial step toward functional, stimulus-responsive systems tailored for real-world applications.

6.1 Design Rationale Derived from Material Characterization of SMEp

The true value of the experimental investigations lies in the practical insights they provide, offering guidance for both material selection and structural design in real-world applications. Understanding the mechanical and thermomechanical behavior of SMEp, along with the challenges encountered during testing, enables informed decisions that maximize the advantages of the material while minimizing its limitations in functional, shape-morphing prototypes.

The following outlines the key behaviors and challenges observed in SMEp, along with the corresponding design considerations derived from these findings:

1- Optimize layer orientation for enhanced shape memory performance:

Printing from the smaller surface, where the printed layers are aligned with the primary loading direction, resulted in:

- Better structural integrity,
- Stronger interlayer adhesion,
- Higher shape recovery percentage and rate,
- Reduced thermal expansion.

Therefore, regions of the structure intended for shape transformation should be designed with thinner cross-sections (smaller surface area per layer) and printed in an orientation aligned with the direction of the intended actuation force. This maximizes recovery performance and stability.

2- Unsuitability for cold programming:

Tensile-to-fracture tests conducted at both room temperature and 75 °C confirmed that SMEp behaves as a brittle material at room temperature. As a result, cold programming (deformation below T_g) is not recommended for SMEp and all deformation and actuation processes should occur above T_g, after heating the material sufficiently to induce flexibility.

3- Avoid uniform heating: design for localized thermal actuation

Challenges such as temperature gradients, prolonged heating times, and uncontrolled thermal expansion emerged during experiments.

To address these:

- Avoid designing systems that require heating the entire structure for activation. Instead, local heating zones can enable precise actuation and enhance system efficiency.
- A central micro-actuator or control module could be designed to coordinate the actuation of the entire device.

4- Thermal activation guidelines based on DSC and TMA results:

- The initial thermal activation requires heating the material above 60 °C, as indicated by the first DSC peak.
- For subsequent activations, the T_g shifts lower (to around 50 °C), enabling shape change at reduced temperatures.
- According to TMA results, faster heating results in less overall thermal expansion, although it induces a more pronounced stress relaxation peak.
- To reduce dimensional instability from thermal relaxation, it is recommended to pre-condition the polymer by heating it to at least 20 °C above its T_g, then cooling it. This process effectively resets the material's thermal history, resulting in more consistent behavior and minimizing unwanted expansion in future thermal cycles.

5- Potential for Direct Liquid-Based Actuation:

Swelling tests revealed that SMEp has a very low and slow water absorption rate, indicating good environmental stability. This opens the possibility for using hot or cold water immersion as a means of direct thermal actuation. Heating and cooling via liquid contact can significantly accelerate response times during programming, fixing, and recovery steps, especially in constrained environments where heating by convection is inefficient.

6.2 Design Strategy Combining Compliant Joints with Kinematic Chains

The work presented in this section was carried out in collaboration with colleagues from Polytechnic University of Madrid (UPM), with Eng. Carlos Polvorinos providing support in CAD modeling tasks and Mr. Pedro Ortego assisting with SLA 3D printing. Their contributions were instrumental in the successful design and fabrication of the prototypes and are gratefully acknowledged here.

Compliant mechanisms are systems that achieve motion and force transmission through the elastic deformation of their structural elements, eliminating the need for traditional rigid components like hinges, bearings, or sliders. By incorporating strategically designed flexible regions, these mechanisms reduce weight, simplify multi-part assembly, and enhance reliability while maintaining precise and predictable movement. In such systems, traditional pin joints can be replaced with compliant joints that utilize the inherent flexibility of the material to enable motion, eliminating the need for discrete mechanical connectors and reducing overall complexity.

In parallel, rigid links connected by kinematic joints provide the geometric structure and controlled motion pathways necessary for executing specific tasks. When combined, compliant mechanisms and kinematic chains can work together to deliver both structural rigidity and adaptive flexibility. Here, our approach to the design is to use rigid links connected by kinematic joints to define the overall structure and motion path, while integrating a compliant joint at a strategic location to control and trigger the motion. This compliant joint serves as the actuation point, enabling shape transformation through elastic deformation, while the surrounding rigid-body elements guide the motion in a controlled and repeatable manner. A combination of the precision of kinematic mechanisms with the adaptability of compliant elements leads to a design that offers a simple, compact, and assembly-free solution for achieving targeted shape morphing behavior.

Such a design is ideally suited for 4D printing, where additive manufacturing enables the creation of complex, functional geometries in a single fabrication step. This eliminates the need for post-processing or manual assembly while addressing both mechanical and morphological complexity.

Figure 74a presents the 2D projections of the corresponding 3D models shown below, along with the indicated direction of the applied mechanical force used to deform each device. Figure 74b shows the 3D model of a hybrid compliant-kinematic structure, developed for thermally or mechanically induced shape transformation. The structure consists of a symmetric frame composed of interconnected rigid lattice links. The lattice architecture reduces material consumption and overall weight while preserving structural rigidity. The rigid links are connected by pin-joint-inspired revolute connections, which enable articulated rotational motion across the structure. Each joint comprises:

- A circular hub located at the end of each link,
- A central cylindrical axle that passes through both connecting members,
- Sufficient clearance to allow relative rotation between adjoining parts.

The S-shaped localized element is between two rigid segments at the center of the structure. This compliant joint, designed to be thinner than the surrounding geometry (350 μm vs. 800 μm overall thickness), serves as the primary actuation region. Upon heating or mechanical input, this element undergoes elastic deformation, triggering motion throughout the entire structure. Figure 74c illustrates the 3D model of a variation of the same concept with a more compact configuration. The joint angles and link lengths have been adjusted to enable more symmetrical and balanced folding during actuation, prioritizing spatial efficiency. Figure 74d shows a 3D design that incorporates a fully enclosed rectangular frame surrounding the central mechanism. This rigid boundary introduces greater geometric constraint and symmetry, potentially enhancing stability; however, limiting the mobility of the upper arms compared to the more open configurations presented in Figure 74a and b. While all three designs in Figure 74a, b, and c operate under the same fundamental mechanism (motion driven by deformation of the central S-shaped compliant joint), the differences in the surrounding link geometry and joint placement may influence the degree of symmetry and range of deformation exhibited by the arms during actuation. Figure 74e illustrates 3D model of a cross-shaped mechanical structure composed of lattice-style rigid arms connected at the center through a compliant torsional spring element, which is highlighted in the

zoomed-in view on the right. In fact, the compliant torsional spring between the intersecting arms enables the arms to rotate relative to each other via elastic twisting of the spring.

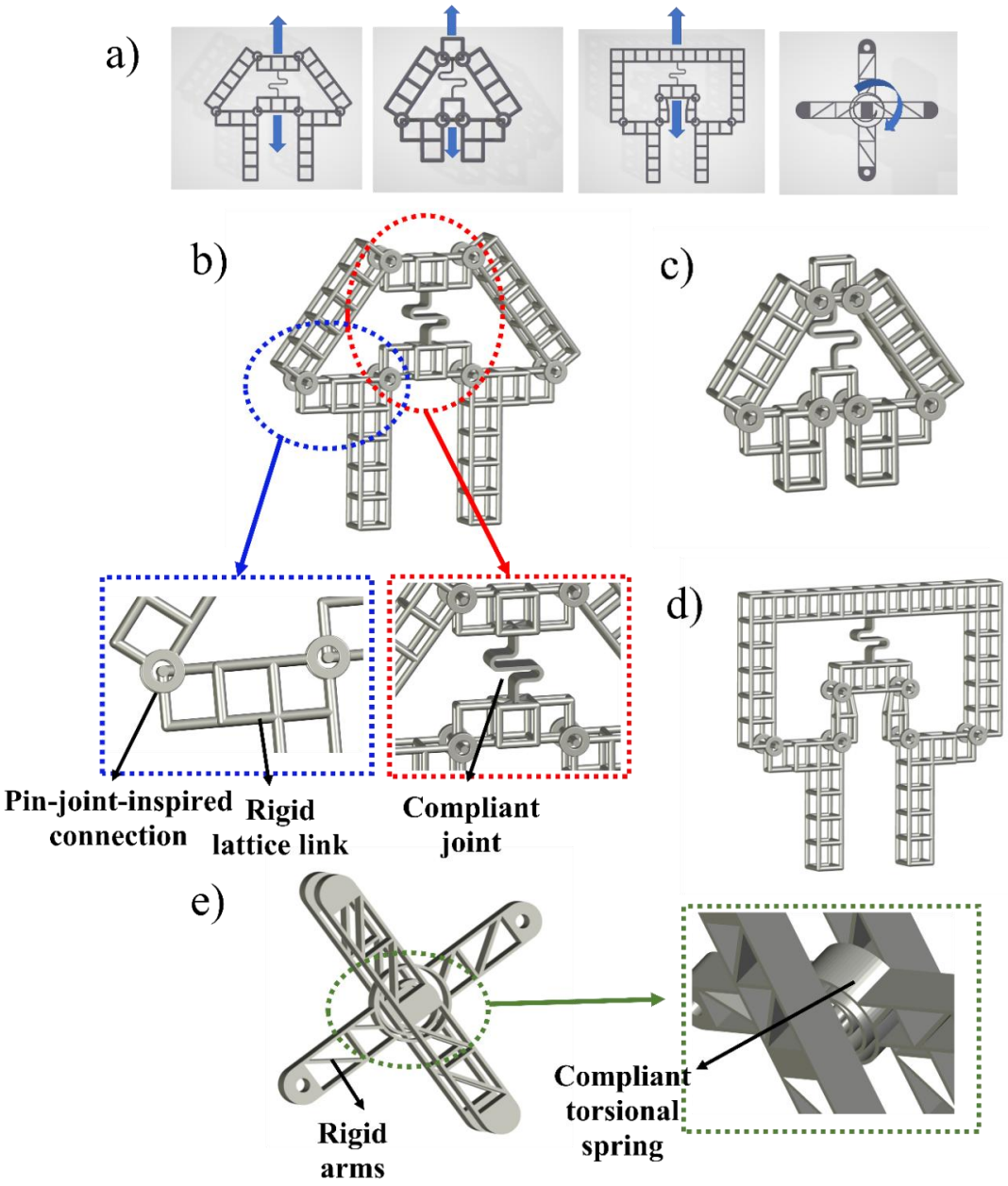

Figure 74. *Overview of the designed shape-morphing devices and their key structural features, along with the indicated direction of the applied mechanical force used to deform each device: a) 2D projections of the 3D models used in the design process; b) Full view of the hybrid compliant–kinematic structure composed of rigid lattice links, pin-joint-inspired revolute connections, and a central S-shaped compliant actuator. Zoomed-in insets highlight the revolute joint (blue box) and the compliant S-shaped element (red box), which serves as the deformation and actuation point; c) Compact variation of the mechanism with modified joint angles and link lengths for improved symmetry and folding behavior; d) Design incorporating a rigid rectangular outer frame to introduce geometric constraint and improve structural stability; e) Cross-shaped mechanism with four rigid arms connected by a compliant torsional spring at the center. The zoomed-in inset (green box) shows the integrated torsional spring, enabling elastic rotation between the arms.*

The spring is designed to store and release elastic energy during angular displacement. It facilitates controlled rotational motion of the arms with passive return capability, i.e., the structure can return to its original state after deformation. The use of a compliant spring eliminates the need for discrete hinges or pins, enabling one-piece 3D printing of the entire mechanism.

Holes at the outer ends of the arms suggest potential fixation or integration into a larger mechanism or boundary.

The entire device of each design can be fabricated in a single step using SLA 3D printing, eliminating the need for post-processing or assembly. In fact, our goal was to create fully functional devices using a single material, fabricated in one step via 3D printing, without the need to embed or integrate additional smart materials. Rather than relying on material heterogeneity, the focus was on geometry-based functionality by incorporating compliant joints directly into the design. Such an approach simplifies the fabrication process while enabling responsiveness to external stimuli through localized elastic deformation, making the final device both monolithic and functionally adaptive.

Regarding build orientation, all prototypes were designed and positioned on the printing platform such that the compliant joint (serving as the actuator) is printed on its edge. This orientation ensures higher resolution and improved mechanical performance in the actuator region. More importantly, printing the compliant joint on its edge results in layer alignment along the direction of the mechanical force that the joint is intended to experience during actuation.

In the designs featuring S-shaped actuators, this orientation aligns the layers with the expected tensile loading direction, enhancing strength and reducing the risk of interlayer failure. Similarly, in the cross-shaped design with a torsional compliant spring, the layers are aligned to withstand torsional stress, improving reliability and functionality.

As shown in Figure 75, the prototypes are arranged on the build platform accordingly, with the yellow structures representing the support material required during the SLA 3D printing process.

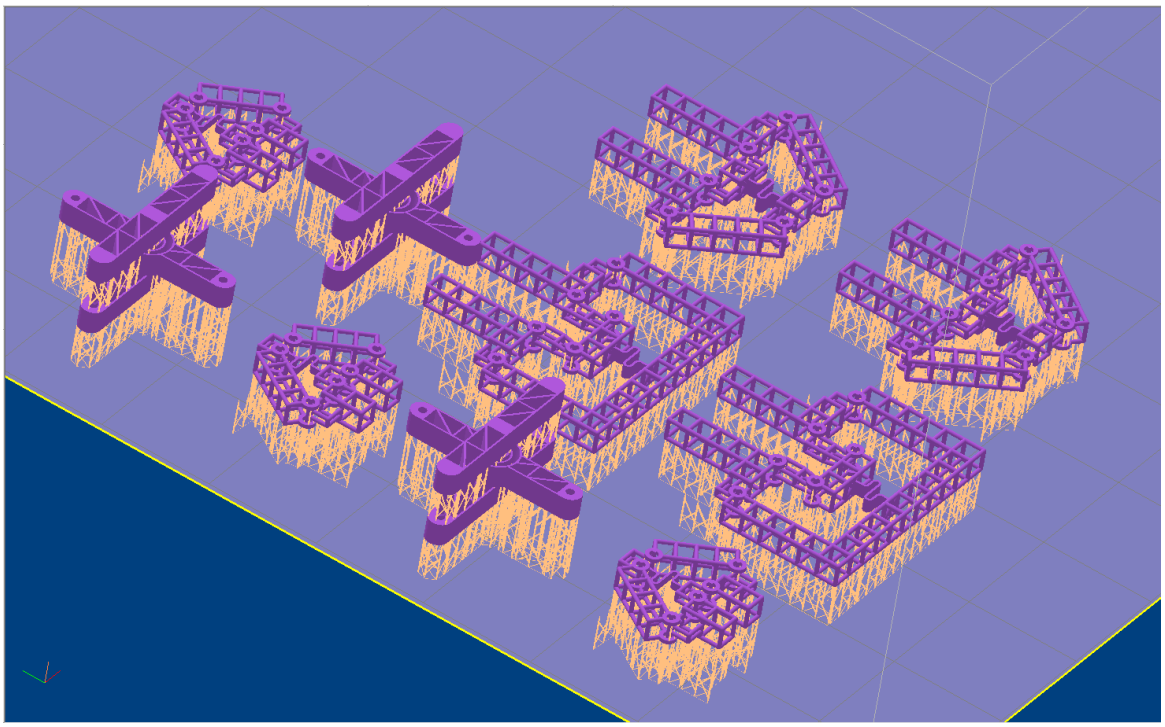

Figure 75. *Arrangement of the designed prototypes on the SLA 3D printer's build platform, with yellow structures indicating the automatically generated support material. All models are oriented to ensure optimal resolution and mechanical performance of the compliant joints, aligning printed layers with the expected actuation forces* [3].

6.3 4D-printed Shape-morphing Prototypes

A series of smart mechanical prototypes processed through high-resolution laser stereolithography were designed and fabricated using SMEp material in order to take advantage of the shape memory behavior of thermo-responsive SMPs in functional 4D-printed applications. SLA additive manufacturing technique offers significant benefits, including the ability to personalize designs, embed functional features through geometric complexity, and fabricate high-quality, stimulus-responsive components. SLA was the first additive manufacturing technology to gain widespread industrial relevance, and it continues to offer excellent performance with a well-balanced compromise between resolution, surface quality, mechanical integrity, and printable size, making it especially well-suited for the production of precise shape memory structures.

Thermo-responsive SMPs are particularly well-suited for applications such as soft robotics, deployable aerospace systems, biomedical devices, and precision micro-actuators, systems that benefit from programmable, reversible shape changes. Their ability to undergo controlled phase

transitions during thermomechanical cycles enables deformation, fixation, and recovery to be precisely managed through temperature stimuli.

Our objective was to create fully functional devices through a single-step fabrication process, without the need for assembly or integration of external actuators, by embedding compliant joints within a monolithic structure. These localized flexible regions serve as internal actuation points, enabling controlled shape transformation using only one material throughout the entire device. As shown in Figure 76, four distinct monolithic designs were developed, each integrating an active region, either the S-shaped compliant spring or torsional compliant joint, at the center of the structure. The printed prototypes closely replicate the intended designs, showcasing the precision of additive manufacturing in creating complex, integrated kinematic chains without requiring assembly. The process allows for the seamless integration of active regions and structural supports, highlighting the synergy between design and fabrication.

The compliant joints are printed thinner than the surrounding rigid lattice elements, making them more responsive to thermal stimuli while maintaining the overall structural integrity of the device. The thin geometry allows them to deform easily upon heating and return upon cooling, enabling localized and reversible actuation.

In the first three prototypes (left to right in Figure 76a), the S-shaped actuator connects the central segments of the kinematic structure, locking the device in its initial configuration when in a rigid state. During shape memory cycling (heating, deformation, cooling, reheating), the actuator softens and permits motion, unlocking a predefined path and enabling a coordinated, symmetric deformation. This behavior is further supported by the build orientation: as shown in Figure 76b, the print layers are aligned with the direction of the applied force (blue arrows) in the actuator, improving both durability and integrity of the element.

The fourth prototype incorporates a cross-shaped configuration with a torsional compliant spring as its central active element. Like the S-shaped actuator, the torsional spring is printed with a thinner cross-section to enable localized deformation under thermal stimulus, resulting in controlled rotational motion of the arms.

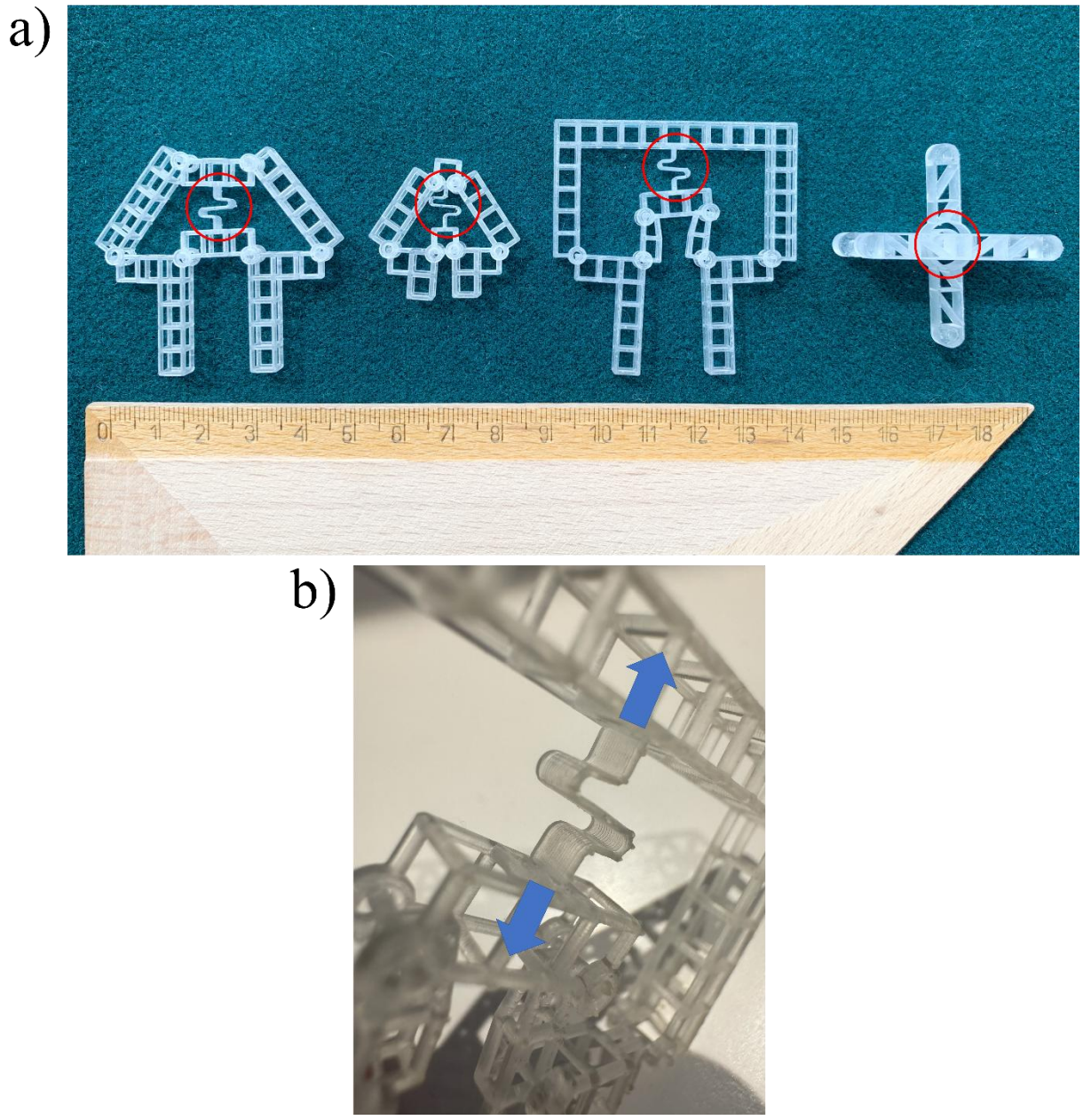

Figure 76. *a) 3D-printed monolithic SMEp prototypes featuring integrated compliant actuators for shape-morphing behavior. The first three designs (from left) incorporate an S-shaped actuator, while the fourth uses a torsional spring* [3]. *b) Close-up of the S-shaped element, with visible printed layers. Blue arrows indicate the intended direction of actuation force, which is aligned with the orientation of the printed layers.*

The importance of the actuators becomes clear when comparing functional and non-functional configurations as illustrated in Figure 77. For demonstration, the first three designs from Figure 77a were reprinted without the central S-shaped element. The presence of the S-shaped actuators in the top row effectively connects and constrains the motion of the structure, keeping

the device in a locked configuration until activation. In contrast, the bottom row shows identical geometries without the actuators, resulting in unconstrained, free movement. Without the S-shaped element, the structure behaves purely as a passive kinematic chain, allowing random motion without any controlled deformation. This comparison highlights the critical role of the S-shaped actuator and its strategic placement in transforming an otherwise passive assembly into a responsive, shape-morphing system.

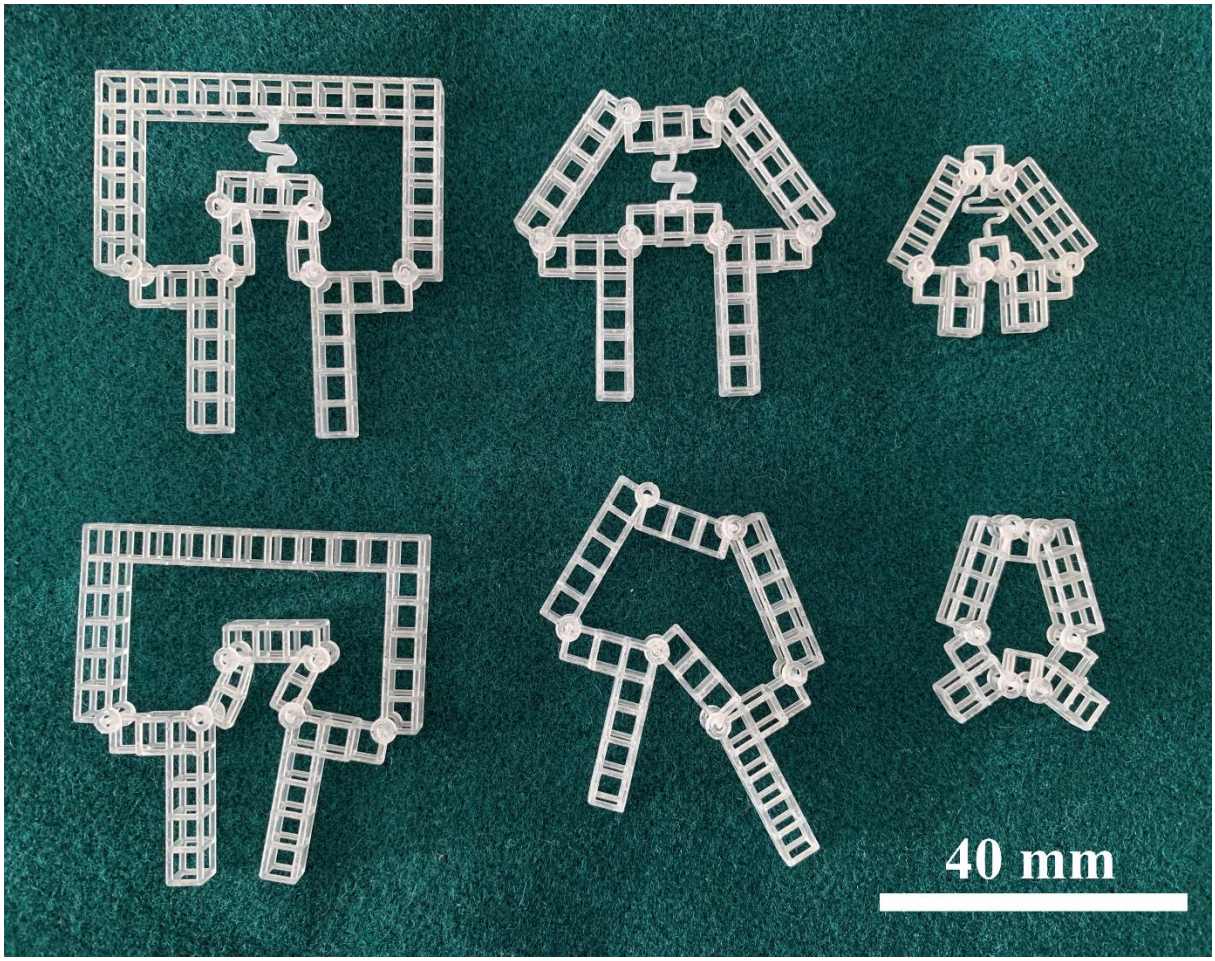

Figure 77. *3D-printed SMEp prototypes containing S-shaped elements, where the structure is over-constrained in the rigid (unactivated) state of the actuator. Bottom row: Identical prototypes printed without the S-shaped element, resulting in under-constrained configurations with unrestricted movement* [3].

By isolating actuation to a small region, the thermal load on the entire device was reduced, lowering energy consumption, shortening actuation time, and minimizing undesired thermal expansion. Moreover, thanks to SMEp's low water absorption (proved in section 5.3), these

prototypes can be thermally cycled via direct contact with hot and cold water, making them especially promising for compact, remote, or underwater shape-morphing applications.

6.4 Shape Memory Activation in Monolithic 4D-Printed Prototypes

The shape memory behavior of the 4D-printed SMEp-based prototypes was demonstrated through localized activation of their compliant actuators. Figure 78 and Figure 79 illustrate the thermomechanical cycle applied to two representative designs, first, incorporating an S-shaped linear actuator, and the second, utilizing a torsional spring mechanism.

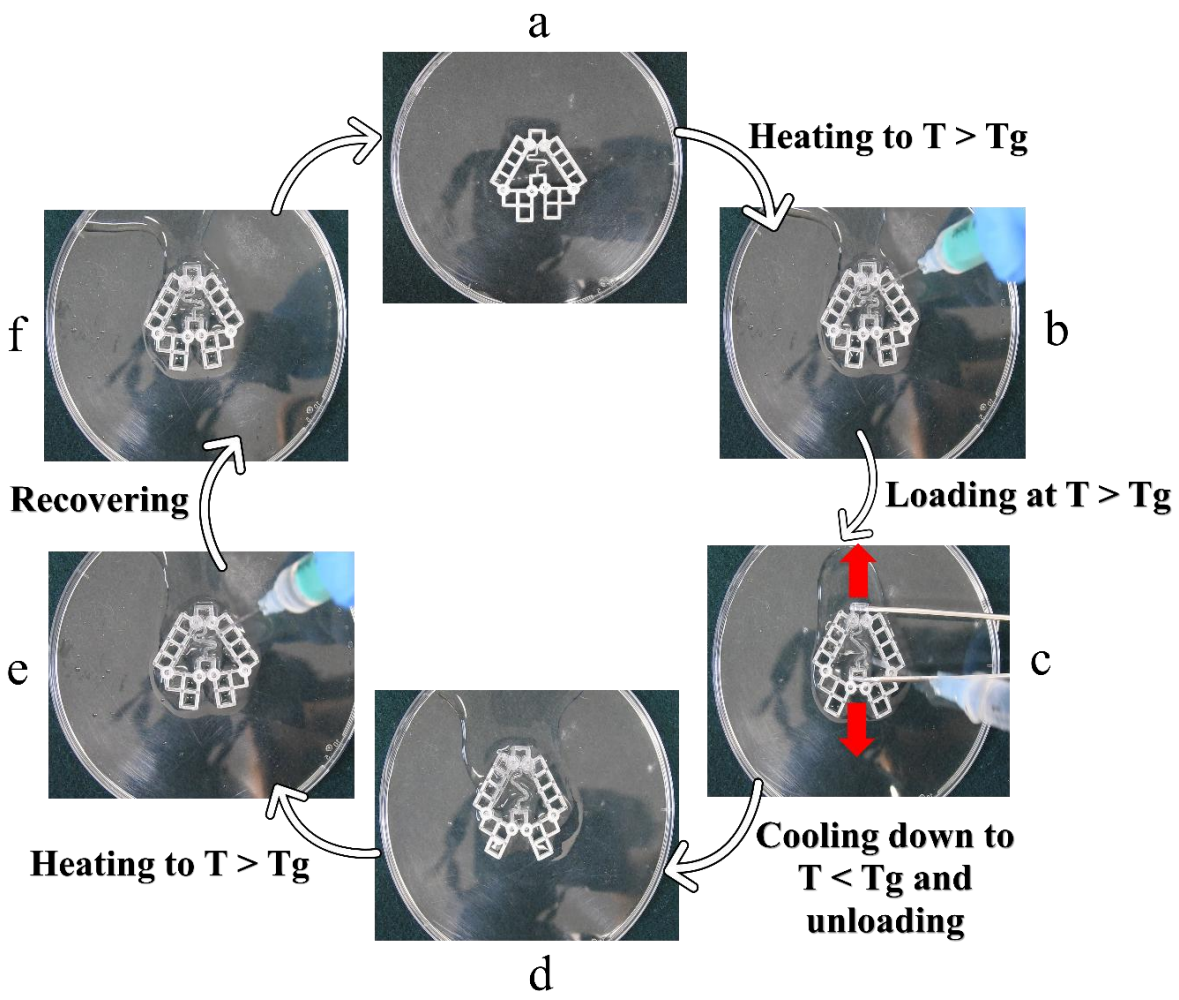

Figure 78. *Shape memory activation trial (thermomechanical cycle) conducted on a 3D-printed complex-shaped SMEp prototype featuring the S-shaped actuator : a) Original undeformed state of the prototype; b) Local heating of the actuator with hot water; c) Deformation of the softened actuator followed by local cooling with cold water (25 °C) while maintaining the deformation; d) Temporary shape fixed after removing the applied force; e) Reheating the actuator locally with hot water (75 °C); f) Recovery of the prototype to its original shape* [3].

Figure 78 showcases the shape memory activation cycle in a device with the S-shaped compliant actuator, showing the following subsequent stages:

- In its original configuration (Figure 78a), the actuator is rigid, keeping the structure locked.
- The shape memory cycle begins by locally applying hot water (~75 °C) to the S-shaped element (Figure 78b), softening it while leaving the rest of the structure unheated.
- While the actuator is softened, it is manually deformed (Figure 78c), and then fixed into the deformed configuration by applying cold water (~25 °C) to the same region while holding the deformation (Figure 78d).
- The temporary shape is fixed after unloading.
- Finally, reheating the actuator with hot water restores its original shape, resulting in full recovery of the global configuration (Figure 78e–f).

This process confirms that the actuation can be triggered exclusively through the localized deformation of the S-shaped compliant element, without requiring full-body heating or deformation. This localized approach ensures energy efficiency and minimizes thermal expansion or delays in actuation.

Figure 79 demonstrates the same cycle performed on the cross-shaped prototype with a torsional compliant spring at its center. The stages of the cycle are as follows:

- The initial configuration (Figure 79a) maintains a 90° angle between arms.
- Torsional actuator is locally heated with hot water (75 °C) (Figure 79b), then the arms are rotated manually to a nearly closed position (~10°) (Figure 79c).
- Cooling the spring with cold water (25 °C) under constrained conditions fixes the new shape (Figure 79d).
- Upon reheating (Figure 79e), the arms autonomously return to their original angle (Figure 79f).

Collectively, these demonstrations validate the design strategy: incorporating thinner compliant actuators and utilizing localized triggering and deformation enables programmable shape-shifting in fully monolithic 4D-printed devices fabricated from a single smart material.

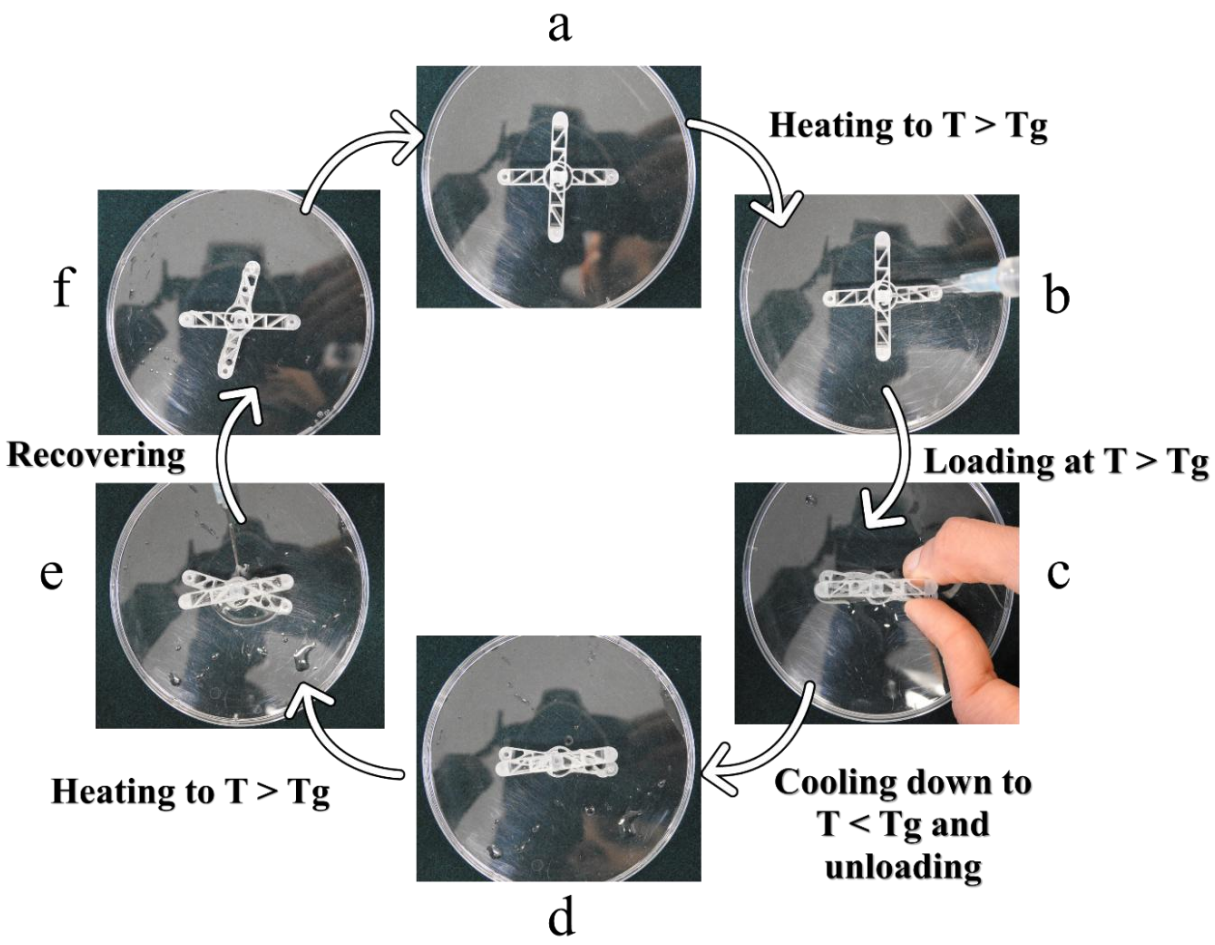

Figure 79. *Shape memory activation trial (thermomechanical cycle) conducted on a 3D-printed complex-shaped SMEp cross-shaped prototype featuring a compliant torsional spring : a) Original undeformed state of the prototype; b) Local heating of the actuator with hot water; c) Deformation of the softened actuator followed by local cooling with cold water (25 °C) while maintaining the deformation; d) Temporary shape fixed after removing the applied force; e) Reheating the actuator locally with hot water (75 °C); f) Recovery of the prototype to its original shape* [3].

In each prototype, the recovery of the deformed actuator in response to hot water generates sufficient force to drive the motion of the entire structure, resulting in full shape recovery. During thermomechanical training, the actuator responds to thermal stimuli (triggering, fixation, or recovery) within a maximum of 10 seconds, without requiring the entire device to be heated or cooled. This approach, which combines a localized active region capable of amplifying motion through embedded kinematic chains with a suitable smart material and high-resolution fabrication, enables rapid actuation and effective shape morphing performance.

6.5 Thermal Imaging of Shape Memory Activation in Monolithic 4D-Printed Prototypes

Thermal imaging was carried out to monitor temperature distribution during the shape memory trial and to further enhance the precision and insight into the shape memory behavior of the 4D-printed SMEp prototypes. Figure 80 presents a series of thermal camera snapshots showing the temperature profile of a prototype featuring the S-shaped actuator across key stages of the thermomechanical cycle.

This visualization demonstrates the effectiveness of localized actuation: although the S-shaped element undergoes thermal activation, the surrounding regions of the device remain at relatively low and stable temperatures. It confirms that shape programming and recovery are achieved through targeted heating and cooling of the actuator alone, eliminating the need for conducting a thermal cycle on the entire device.

Figure 80a shows the initial heating of the S-shaped actuator with hot water (~75 °C), where the temperature gradient is clearly concentrated in the central region. Figure 80b depicts the fully heated actuator immediately before deformation, with the rest of the structure still cool. Figure 80c captures the cooling process using cold water (~25 °C), which solidifies the temporarily deformed shape. Figure 80d shows the device in its fixed, temporarily deformed state. Figure 80e illustrates the reheating of the actuator for shape recovery. Figure 80f confirms full recovery of the device, with thermal activation again localized around the actuator.

The images in Figure 80 validate the design strategy: by integrating a thinner, thermally responsive compliant joint into the monolithic structure, the global actuation can be achieved through localized heating, enabling faster, more energy-efficient, and spatially controlled shape morphing.

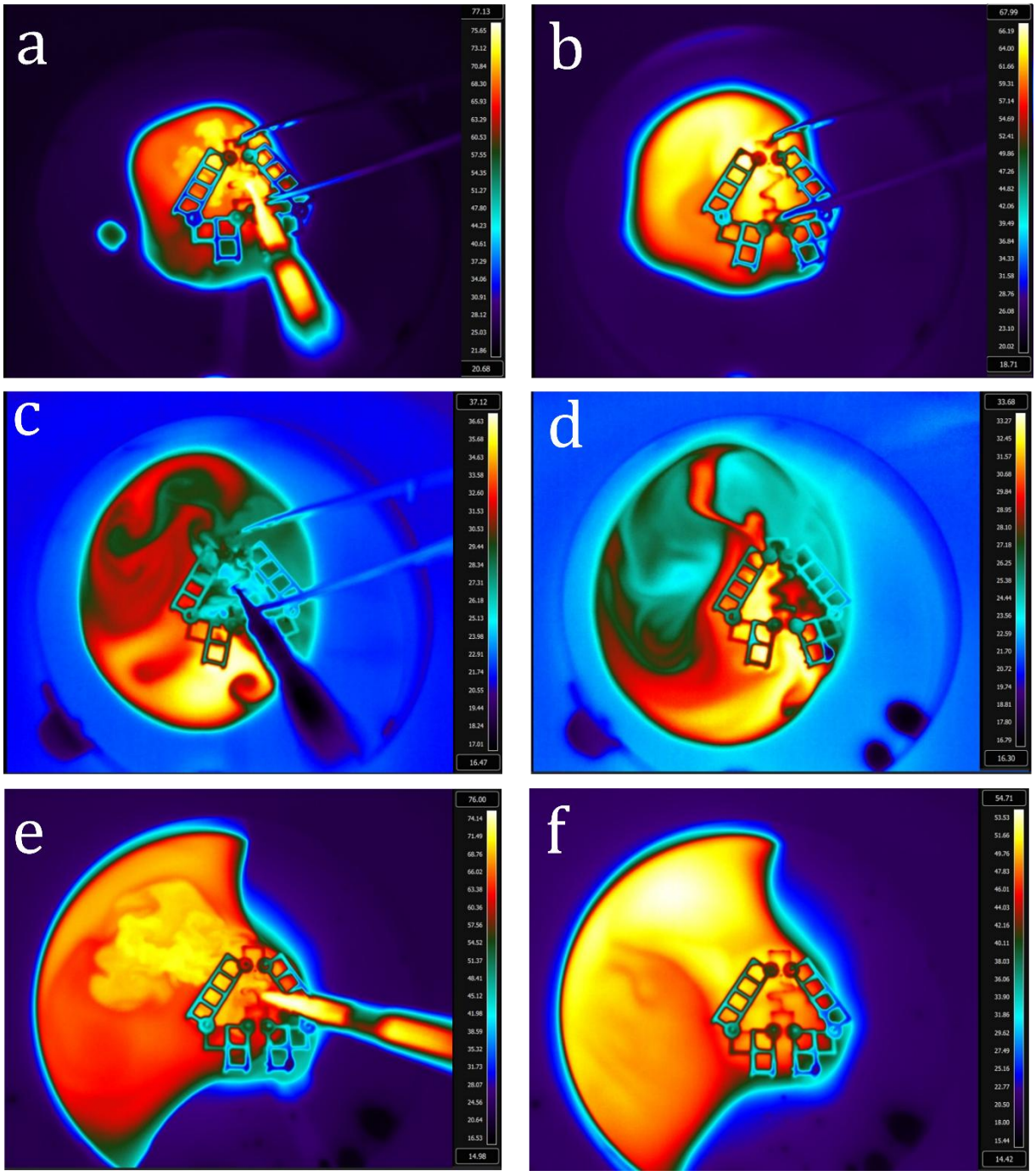

Figure 80. *Infrared thermal images showing the temperature distribution of the 3D-printed complex-shaped SMEp prototype during key stages of the thermomechanical shape memory cycle : a) Localized heating of the S-shaped actuator using hot water (~75 °C); b) Mechanical deformation of the heated actuator; c) Localized cooling of the deformed actuator using cold water (~25 °C) while maintaining the applied deformation; d) Temporary shape fixity after unloading the actuator; e) Reheating of the actuator to ~75 °C to trigger recovery; f) Complete recovery of the prototype to its original configuration* [3].

6.6 Quantitative Evaluation of Shape Recovery in Complex 4D-Printed SMEp Prototypes

Deformation and recovery behavior of four distinct monolithic devices featuring compliant actuators were analyzed to quantitatively assess the shape morphing performance of the 3D-printed SMEp prototypes. As shown in Figure 81, images (a), (b), and (c) correspond to the original, deformed, and recovered configurations of each prototype, respectively, following the thermomechanical cycle previously demonstrated in Figure 78. For the first three designs (with S-shaped actuators), the left and right apex angles (highlighted in red) were used as key geometrical parameters to evaluate deformation and shape recovery. In the fourth prototype (cross-shaped design with a torsional spring), the intersection angle between the arms served the same purpose. These angle measurements provide a straightforward and effective means to estimate the degree of actuation and recovery in response to thermal stimuli.

The shape deformation percentage (S_d) and shape recovery percentage ($S_{r\theta}$) were calculated using the following equations 9 and 10:

$$S_d = \frac{\theta_m - \theta_0}{\theta_0} \times 100\% \quad (9)$$

$$S_{rd} = \frac{\theta_m - \theta_{ir}}{\theta_m} \times 100\% \quad (10)$$

where:

θ_0 is the initial apex or intersection angle (before deformation, Figure 81a),

θ_m is the angle after deformation and cooling to room temperature (Figure 81b),

θ_{ir} is the irrecoverable angle after reheating the actuator to 75 °C under zero load (Figure 81c).

Each angle was measured multiple times using ImageJ software on two independent samples of each prototype to ensure accuracy and repeatability. The shape fixity was observed across all prototypes, to be near 100%, as minimal angle changes occurred during the cooling and unloading stages, indicating excellent temporary shape retention.

The results presented in Table 17 demonstrate that all prototypes exhibit notable shape recovery following thermomechanical cycling. Among them, the cross-shaped design with a torsional spring achieved the highest deformation (97.2%) while still recovering 93.5% of its original shape, highlighting the efficiency and robustness of the torsional actuator. The remaining prototypes, each incorporating the S-shaped actuators, also exhibited high recovery values despite

differences in geometry and deformation levels. These outcomes reflect the effectiveness of the compliant joint designs in enabling reliable shape morphing across varied structural configurations.

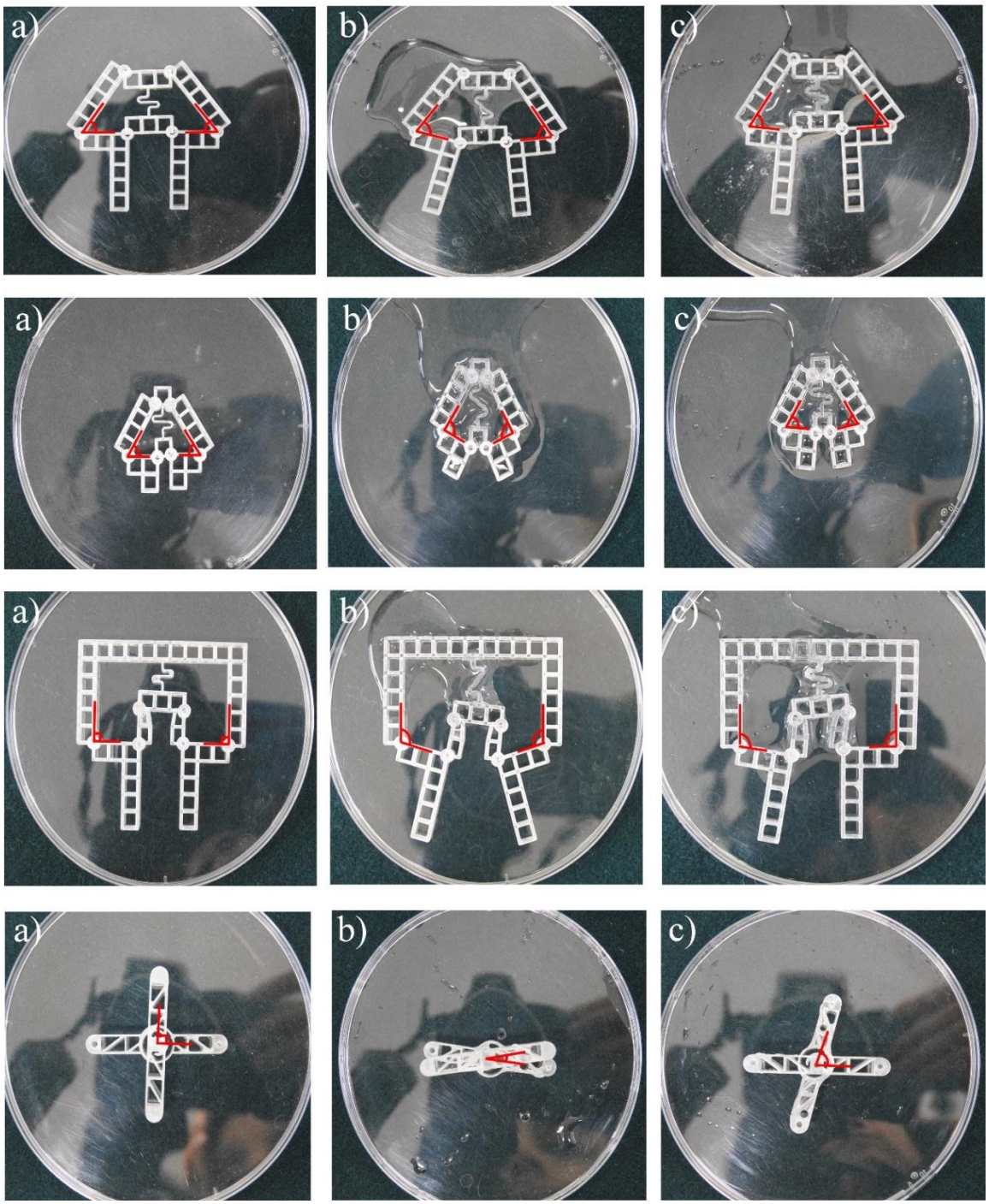

Figure 81. *a) Original, b) deformed and c) recovered shape of the 4D-printed shape-morphing SMEp prototypes, programmed in a thermomechanical trial* [3].

Table 17. *Mean values of the shape deformation and shape recovery in the 4D-printed shape-morphing SMEp prototypes.*

Prototypes	S_d (%)	$S_{r\theta}$ (%)
	34.16 ± 5	92.83 ± 3.5
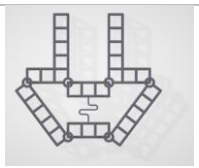	28.51 ± 2.2	95.28 ± 2.1
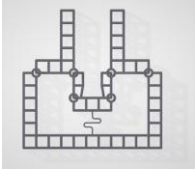	17.82 ± 3.4	95.77 ± 1.0
	97.17 ± 0.5	93.46± 2.0

6.7 Immersion-Based Actuation of 4D-Printed SMEp Prototypes

The selected SMEp material's resistance to water absorption enabled the actuation cycle to be performed not only via localized water application, but also by full immersion in hot and cold water. All designs were shown to fully recover their original shapes under immersion-based actuation. This approach simplifies the actuation process while enabling uniform heating and cooling, which is especially advantageous for practical, real-world applications.

Figure 82 demonstrates the full-cycle shape memory behavior of the cross-shaped prototype with a torsional compliant spring. In Figure 82a the deformed prototype is immersed in cold water to fix the temporary shape. Figure 82b shows the cross-shaped prototype fixing the deformation, after immersion in cold water. The prototype is then transferred to hot water (75 °C), where recovery is initiated. Finally, Figure 82c shows the prototype returning to its original cross configuration, confirming successful shape recovery through immersion-triggered actuation.

Figure 83 illustrates the same process for a design featuring the S-shaped compliant actuator. In Figure 83a, the prototype was manually deformed while immersed in hot water, thus leading to softening of the S-shaped element. Figure 83b shows the prototype being transferred to cold water to fix the deformed configuration. Upon reheating, the actuator recovered its original geometry, triggering coordinated movement of the entire structure and restoring the initial shape of the prototype, Figure 83c.

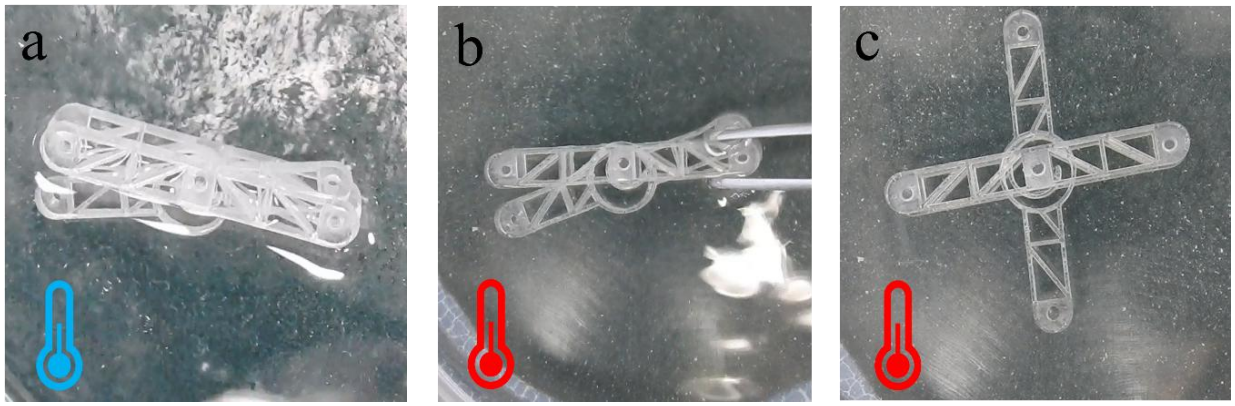

Figure 82. *Shape memory activation of the cross-shaped SMEp prototype through full immersion in water: a) Deformed prototype fixed in cold water (~25 °C); b) Immersion in hot water (~75 °C) to trigger actuation; c) Full recovery of the original shape via thermal activation of the compliant torsional spring.*

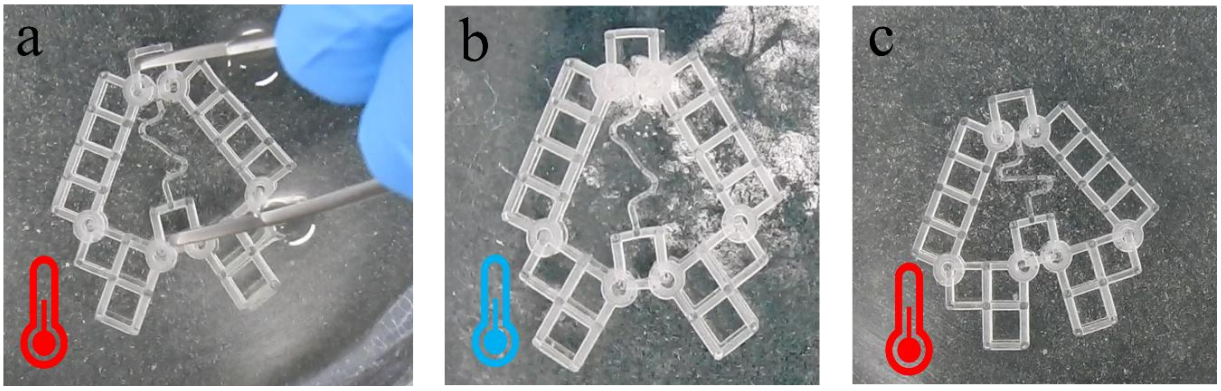

Figure 83. *Shape memory cycle of the SMEp prototype with the S-shaped actuator under full water immersion : a) Actuator deformation in hot water (~75 °C); b) Fixation of the deformed shape by immersion in cold water (~25 °C); c) Recovery of the original configuration upon reheating in hot water (~75 °C).*

The presented findings demonstrate the effectiveness of shape recovery, confirm the suitability of SMEp for aqueous environments, and emphasize the impact of structural design in

amplifying motion through thermally triggered compliant joints. Together, they offer a compelling foundation for the design of next-generation adaptive devices capable of programmable, reversible, and efficient shape transformation, entirely produced through single-material, single-step 3D printing.

6.8 Potential Applications and Conceptual Relevance

This chapter focused on the shape memory behavior of additively manufactured epoxy-based photoresin and explored design strategies for enhancing shape-morphing capabilities through the use of kinematic mechanisms and compliant joints. The 4D-printed prototypes developed in this study serve as proof-of-concept demonstrations of how monolithic structures, fabricated entirely from a single shape memory polymer (SMEp), can integrate both passive structural elements and active actuation regions within a unified design. The devices explore the feasibility of achieving programmable, localized motion directly through geometric design, without relying on external actuators, sensors, or multi-material assemblies, rather than representing finalized or market-ready products.

Although these designs are conceptual, the core design principles show strong potential for real-world applications that require compact size, independent operation, and remote activation. By integrating compliant joints and taking advantage of the shape memory behavior of SMEp, the printed mechanisms are capable of reversible and repeatable shape transformation in response to thermal stimuli. This approach enables the development of self-actuating systems that adapt their configuration to a self-determined shape, with no need for complex control hardware.
Potential application areas include:

- **Soft Robotics**: The prototypes can be employed in robotic systems requiring adaptable motion for gripping, crawling, or locomotion, where shape change and flexibility are essential.
- **Deployable Structures**: Particularly relevant for aerospace applications, such as satellite components or stowable antennas, where compact transport and on-demand deployment are critical.

- **Biomedical Devices**: Their responsiveness to heat makes them promising candidates for shape-adaptive implants or minimally invasive surgical tools that activate within the human body.
- **Energy-Efficient Actuation**: Systems using shape memory behavior and compliant mechanisms can achieve programmable multistability, enabling mechanical responses with minimal energy input during operation.

The demonstrations not only validate the mechanical and functional integration of compliant joints and smart materials but also advance the understanding of design strategies in 4D printing. Similar to early innovations in origami-inspired engineering, this work explored the design logic, mechanics, and actuation behavior that will inform future generations of fully functional smart material-based devices.

Overall, the combination of single-material manufacturing, thermally activated deformation, and structurally integrated functionality represents a versatile and scalable approach for developing adaptive, multifunctional systems across various fields of modern engineering.

6.9 Limitations of the Study and Future Research Potentials

While the results of this study are promising, several limitations remain, and further investigations are needed to extend the findings toward more advanced, high-performance, and application-ready systems.

Deeper Characterization and Multi-Cycle Behavior:

Most studies involving SMPs, particularly those aimed at high-performance actuation, often do not perform comprehensive thermomechanical characterization before designing complex shapes and employing these smart materials in additive manufacturing. This oversight can lead to suboptimal performance in the final applications. However, for instance, Slavković *et al*. [163] highlight that the thermomechanical behavior of 3D-printed SMPs, such as PLA, is highly dependent on factors like strain rate and temperature, underscoring the need for detailed characterization prior to application. Neglecting such comprehensive evaluations can result in devices that fail to meet performance expectations, particularly in applications requiring precise and repeatable actuation. Although this work has addressed critical properties such as shape fixity, shape recovery, and thermal expansion, future studies should also consider the effects of

accumulated actuation cycles (training) and the presence of opposing or residual mechanical loads. These factors can significantly influence long-term shape memory performance and are especially important for load-bearing or cyclically actuated systems [89,164].

Design-Integrated Thermal Expansion Control:

Thermal expansion was identified as both a challenge and an opportunity in this study. Our results show that localized actuation (via S-shaped or torsional joints) and the use of compliant kinematic chains can limit unwanted thermal deformation in the bulk structure, leading to faster and more precise actuation. However, further work is needed to develop systematic mitigation strategies for thermal expansion in more complex designs. Potential directions include:

- Using SMPs with a T_g near room temperature, enabling cold programming and reducing the need for full thermal activation.
- Incorporating nanoparticles to modulate thermal expansion, mechanical properties, and heat distribution. This approach requires in-depth characterization of composite SMPs to assess long-term behavior.
- Embedding mechanical metamaterials, such as auxetic or origami-based structures, into the design to absorb, guide, or redirect expansion without compromising structural integrity.

Toward Multi-Stimuli Responsiveness and Temperature-Programmed Morphing:

Looking ahead, one of the most exciting directions involves developing multi-stimuli-responsive systems. By integrating various polymers into hybrid or multi-material designs, future 4D-printed devices could be engineered to respond not only to temperature, but also to light, humidity, pressure, magnetic, or electric fields. Such systems will expand the functional range of smart devices across fields such as robotics, wearable technology, aerospace, and biomedical engineering.

Another promising strategy lies in the temperature-programmed sequential activation of different shape memory actuators within a single device. This could be achieved by designing several actuators within a complex structure, each actuator with a different crosslinking density, which in turn produce different T_g, and thus, distinct actuation thresholds. As the ambient temperature gradually increases, each actuator would activate at its own T_g, undergoing a specific, pre-programmed deformation. This would allow the creation of multi-phase shape transformations within the same structure, enabling it to adapt its geometry stepwise in response to its thermal

environment. Such designs could yield programmable, environment-sensitive systems for adaptive surfaces, soft robotic limbs, or deployable aerospace components.

Indeed, designing such complex systems requires a comprehensive thermomechanical characterization of the SMPs involved. Understanding key material behaviors, such as thermal expansion, shape fixity, shape recovery, and stress relaxation, is essential for identifying potential limitations and adjusting the structural design accordingly. Only by accounting for these parameters in advance, it would be possible to ensure that the resulting structure performs reliably and predictably throughout its actuation cycles.

This approach opens the door to programmable, environment-adaptive morphing structures, with immense potential in deployable aerospace systems, soft robotic devices, and temperature-responsive biomedical tools.

Integrating Material Behavior into Design Workflow

Finally, this study highlights the critical importance of integrating the material behavior of SMPs into the design process, especially for complex, shape-morphing structures. Properties such as thermal expansion, glass transition range, and interlayer adhesion (strongly influenced by printing orientation and surface area per layer) should be systematically considered early in the design phase. Doing so will improve the reliability, efficiency, and predictability of next-generation 4D-printed devices.

Chapter 7
Conclusions

In this study, the thermomechanical behavior and additive manufacturability of SMPs were systematically investigated, starting with thermoplastic PU-SMP and progressing to thermoset SMEp processed via SLA. The key findings are summarized below:

- **Thermomechanical behavior of PU-SMP**
    - DSC revealed **a shift in T_g from ~29 °C to ~45 °C after thermal cycling**, indicating the influence of thermal history and the reorganization of hard and soft segments on thermal transitions.
    - Mechanical characterization at room temperature showed **high ductility** (elongation at break ≈ 195%) and **notable strain hardening**, with **permanent deformation occurring well below T_g**. This confirmed the feasibility of **cold programming**, as plastic deformation could be induced at ambient conditions without heating.
    - Specimens **preheated** before deformation exhibited **increased stiffness, higher modulus, and distinct yield behavior**, while **non-preheated** samples showed **smoother stress–strain curves with not a very distinct yield point**.
    - The influence of thermal pre-treatment on microstructural behavior was further supported by SEM, which revealed **extensive crazing in preheated specimens**, as opposed to surface whitening and minor damage in cold-programmed samples. Notably, SEM after recovery suggested self-healing of craze networks, confirming reversible damage in PU-SMP.
- **Cyclic durability of PU-SMP**
    - Strain-controlled **cyclic tensile tests** were conducted up to 9000 cycles to assess durability. The mechanical response evolved in three phases:
      (1) strain hardening and modulus increase in early cycles
      (2) a relatively stable performance plateau within the range from 100 to 5000 cycles
      (3) a softening phase beyond 5000 cycles, characterized by modulus reduction and increased hysteresis.

- Despite progressive damage, **no catastrophic failure** was observed, and SEM images confirmed gradual coalescence of microvoids rather than abrupt cracking.

- **Effect of testing temperature**
  - The effect of **testing temperature** on **mechanical performance** was explored by conducting loading–unloading cycles at 25 °C, 45 °C, and 65 °C.
  - At higher temperatures: **softer response, reduced stress, more stable cycles**.
  - At lower temperatures: **more pronounced crazing, larger hysteresis loops, and less elastic recovery**.
  - Operational temperature strongly influences stress recovery and deformation mode.
- **Shape memory performance of PU-SMP**
  - Finally, a full thermomechanical cycle was conducted to quantify the shape memory performance.
  - **Shape fixity exceeded 98%, while shape recovery reached up to 84%**, confirming the material's ability to store and recover deformation effectively
  - **Losses in recovery** were mainly due to **thermal elongation**, highlighting the need for accurate **strain control**.
  - Although the printability of PU-SMP using FDM was limited due to filament quality and thermal instability, two prototype structures were successfully fabricated and tested, both demonstrating good shape recovery and post-recovery crack closure.

The results validate the practical potential of PU-SMPs in smart, cold-programmable applications and provide a framework for assessing shape memory behavior in thermoplastic systems. However, limitations such as poor printability in FDM and handling issues at high temperatures led to a redirection toward thermoset-based SLA 3D printing in the following stages of the research.

- **Transition to thermoset SMEp (SLA)**
  - A systematic investigation was conducted on thermoset SMEp fabricated by SLA 3D printing method to evaluate **how printing orientation affects its microstructure, thermal response, mechanical properties, and shape memory behavior**.

- Two types of dog-bone specimens were printed with identical geometries but different build orientations: **SMEp1 from the side surface** and **SMEp2 from the flat surface**, resulting in different numbers of layers and surface areas per layer.
- **Microstructural analysis:** SMEp1 showed **stronger, thicker interlayer bonding** from repeated UV exposure; SMEp2 showed weaker, irregular bonding, probably due to less repeated exposure to UV.
- The **structural differences** directly affected **dimensional stability and water absorption**, with SMEp1 displaying lower swelling and more uniform absorption behavior.
- **Thermal analysis:** TGA and DSC confirmed that both specimens were chemically identical, but SMEp1 exhibited a slightly higher T_g, greater thermal stability, and reduced molecular mobility due to its stronger interlayer adhesion.
- **TMA analysis** emphasized the significance of holding force from the probe and heating rate in accurate capturing of the expansion behavior and detecting T_g. SMEp2 displayed higher thermal expansion through thickness and length, attributed to its larger area of layers and lower interfacial constraints.
- **Mechanical behavior**: SMEp1 had higher ultimate strength but lower ductility, while SMEp2 exhibited greater elongation and plastic deformation, likely due to its higher free volume and weaker interlayer bonding.
- **Microstructural observation** confirmed brittle fracture of SMEp1 and shear-induced delamination in SMEp2.
- **Shape memory behavior:** Thermomechanical shape memory characterization showed that **both SMEp1 and SMEp2** demonstrated **excellent shape fixity (~95%)**, however**, SMEp1 consistently achieved higher shape recovery (74% vs. 66%)** and **faster** recovery rates, linked to its superior interlayer cohesion and lower thermal expansion. **SMEp2**, on the other hand, exhibited **greater uniaxial thermal elongation**, which introduced stress relaxation and reduced the efficiency and speed of the shape recovery.

Overall, the results confirm that SLA printing orientation plays a crucial role in defining the performance of 4D-printed thermoset SMPs. SMEp1, with its finer layer resolution and improved interlayer bonding, offers superior mechanical performance and shape memory

behavior, making it a more suitable candidate for precision applications such as soft robotics and adaptive micro-mechanisms. This study provided essential design and fabrication insights for optimizing 4D-printed smart structures based on thermally responsive SMPs.

In the final experimental stage of this research, knowledge acquired from prior thermomechanical and microstructural investigations of SMEp was applied to the design and development of functional 4D-printed prototypes.

- **Design and fabrication of 4D-printed prototypes (SLA, SMEp)**
    - A design methodology was introduced that strategically **combined compliant joints and kinematic chains** within **monolithic** structures fabricated entirely from **SMEp**. These compliant joints (engineered as thinner, localized regions) served as internal actuators, enabling programmable shape transformation in response to thermal stimuli.
    - The prototypes were fabricated using SLA 3D printing, and two types of active joints were explored: **S-shaped linear actuators** and **torsional compliant springs**.
    - **Layer orientation was aligned with force direction** to improve durability.
    - All devices were fabricated in a **single printing step**, **without post-processing or assembly**, demonstrating the synergy between geometry-based design and high-resolution additive manufacturing.
    - **Localized thermomechanical cycles** showed that deformation and recovery could be achieved by **stimulating only the actuator region**, reducing actuation time. The SMEp material demonstrated fast and effective response under localized heating, and due to its water-resistant properties, the entire shape memory cycle could also be executed via hot and cold-water immersion.
    - **Thermal imaging confirmed localized heating**, further validating the efficiency of the design.
    - Quantitative analysis showed **near-perfect fixity (~100%) and high recovery (~93–96%)** across prototypes, even in complex geometries.
    - The **torsional spring actuator achieved the highest deformation (~97%)** while maintaining excellent recovery.

- **Overall significance**

This study demonstrated that by coupling appropriate material selection, smart structural design, and printing strategy, it is possible to produce non-assembled, stimulus-responsive, shape-morphing systems suitable for real-world use in soft robotics, biomedical devices, deployable mechanisms, and adaptive microstructures. This work establishes a strong foundation for future developments in single-material 4D-printed devices, particularly those requiring localized actuation and precise shape control.

REFERENCES

1. Kang, D.; Jeong, J.-M.; Jeong, K. Il; Kim, S.S. Improving the Deformability and Recovery Moment of Shape Memory Polymer Composites for Bending Actuators: Multiple Neutral Axis Skins and Deployable Core. *ACS Appl. Mater. Interfaces* **2023**, *15*, 33944–33956, doi:10.1021/acsami.3c02590.
2. Rodriguez, J.N.; Zhu, C.; Duoss, E.B.; Wilson, T.S.; Spadaccini, C.M.; Lewicki, J.P. Shape-morphing composites with designed micro-architectures. *Sci. Rep.* **2016**, *6*, 27933, doi:10.1038/srep27933.
3. Nabavian Kalat, M.; Staszczak, M.; Urbański, L.; Polvorinos-Fernández, C.; Aguilar Vega, C.; Cristea, M.; Ionita, D.; Díaz Lantada, A.; Pieczyska, E.A. Investigating a shape memory epoxy resin and its application to engineering shape-morphing devices empowered through kinematic chains and compliant joints. *Mater. Des.* **2023**, *233*, 112263, doi:10.1016/j.matdes.2023.112263.
4. Sofla, A.Y.N.; Meguid, S.A.; Tan, K.T.; Yeo, W.K. Shape morphing of aircraft wing: Status and challenges. *Mater. Des.* **2010**, *31*, 1284–1292, doi:10.1016/j.matdes.2009.09.011.
5. Daynes, S.; Weaver, P.M. Review of shape-morphing automobile structures: concepts and outlook. *Proc. Inst. Mech. Eng. Part D J. Automob. Eng.* **2013**, *227*, 1603–1622, doi:10.1177/0954407013496557.
6. Kim, H.; Ahn, S.; Mackie, D.M.; Kwon, J.; Kim, S.H.; Choi, C.; Moon, Y.H.; Lee, H.B.; Ko, S.H. Shape morphing smart 3D actuator materials for micro soft robot. *Mater. Today* **2020**, *41*, 243–269, doi:10.1016/j.mattod.2020.06.005.
7. Chen, Q.; Lv, P.; Huang, J.; Huang, T.-Y.; Duan, H. Intelligent Shape-Morphing Micromachines. *Research* **2021**, *2021*, doi:10.34133/2021/9806463.
8. Rathinasuriyan, C.; Chandar, J.B.; Lenin, N.; Puviyarasan, M. Exploring materials, technologies, applications, and future outlooks in 4D printing: a comprehensive survey. *Prog. Addit. Manuf.* **2025**, doi:10.1007/s40964-025-01034-3.
9. Bethan Davies Multifunctional Shape-Morphing Material for Soft Robots Available online: https://www.azorobotics.com/Article.aspx?ArticleID=514.
10. Baines, R.; Fish, F.; Bongard, J.; Kramer-Bottiglio, R. Robots that evolve on demand. *Nat. Rev. Mater.* **2024**, *9*, 822–835, doi:10.1038/s41578-024-00711-z.

11. Jennifer Chu Magnetic 3-D-printed structures crawl, roll, jump, and play catch Available online: https://meche.mit.edu/news-media/magnetic-3-d-printed-structures-crawl-roll-jump-and-play-catch.
12. Santo, L.; Quadrini, F.; Bellisario, D.; Iorio, L. Applications of Shape-Memory Polymers, and Their Blends and Composites. In; 2020; pp. 311–329.
13. Kotikian, A.; McMahan, C.; Davidson, E.C.; Muhammad, J.M.; Weeks, R.D.; Daraio, C.; Lewis, J.A. Untethered soft robotic matter with passive control of shape morphing and propulsion. *Sci. Robot.* **2019**, *4*, doi:10.1126/scirobotics.aax7044.
14. Huang, T.; Sakar, M.S.; Mao, A.; Petruska, A.J.; Qiu, F.; Chen, X.; Kennedy, S.; Mooney, D.; Nelson, B.J. 3D Printed Microtransporters: Compound Micromachines for Spatiotemporally Controlled Delivery of Therapeutic Agents. *Adv. Mater.* **2015**, *27*, 6644–6650, doi:10.1002/adma.201503095.
15. Chen, K.; Thompson, A.J.; Ahmad, B. Multi-DoF Optothermal Microgripper for Micromanipulation Applications. *IEEE Robot. Autom. Lett.* **2025**, *10*, 4061–4068, doi:10.1109/LRA.2025.3549240.
16. Lantada, A.D.; de Blas Romero, A.; Tanarro, E.C. Micro-vascular shape-memory polymer actuators with complex geometries obtained by laser stereolithography. *Smart Mater. Struct.* **2016**, *25*, 065018, doi:10.1088/0964-1726/25/6/065018.
17. Liu, M.; Jin, L.; Yang, S.; Wang, Y.; Murray, C.B.; Yang, S. Shape Morphing Directed by Spatially Encoded, Dually Responsive Liquid Crystalline Elastomer Micro-Actuators. *Adv. Mater.* **2023**, *35*, doi:10.1002/adma.202208613.
18. Li, T.; Tsui, G.C.-P.; Wong, C.-H.; Tang, C.-Y.; Tang, K.; Tan, Y. Stimulus-responsive gradient hydrogel micro-actuators fabricated by two-photon polymerization-based 4D printing. *Nanotechnol. Rev.* **2025**, *14*, doi:10.1515/ntrev-2025-0145.
19. Ashuri, T.; Armani, A.; Jalilzadeh Hamidi, R.; Reasnor, T.; Ahmadi, S.; Iqbal, K. Biomedical soft robots: current status and perspective. *Biomed. Eng. Lett.* **2020**, *10*, 369–385, doi:10.1007/s13534-020-00157-6.
20. Zapata Martínez, R.; Aguilar, C.; Solórzano-Requejo, W.; Contreras-Almengor, O.; Polvorinos Fernández, C.; Molina-Aldareguia, J.; Díaz Lantada, A. 4D Printed Surgical Devices: Current Capabilities and Challenges. In Proceedings of the Proceedings of the 16th International Joint Conference on Biomedical Engineering Systems and Technologies;

SCITEPRESS - Science and Technology Publications, 2023; pp. 157–163.

21. Lendlein, A.; Kelch, S. Shape-Memory Polymers. *Angew. Chemie Int. Ed.* **2002**, *41*, 2034, doi:10.1002/1521-3773(20020617)41:12<2034::AID-ANIE2034>3.0.CO;2-M.
22. Sajjad, R.; Chauhdary, S.T.; Anwar, M.T.; Zahid, A.; Khosa, A.A.; Imran, M.; Sajjad, M.H. A review of 4D printing – Technologies, shape shifting, smart polymer based materials, and biomedical applications. *Adv. Ind. Eng. Polym. Res.* **2024**, *7*, 20–36, doi:10.1016/j.aiepr.2023.08.002.
23. Holman, H.; Kavarana, M.N.; Rajab, T.K. Smart materials in cardiovascular implants: Shape memory alloys and shape memory polymers. *Artif. Organs* **2021**, *45*, 454–463, doi:10.1111/aor.13851.
24. Yuliang Xia, Yang He, Fenghua Zhang, Yanju Liu, J.L. A Review of Shape Memory Polymers and Composites: Mechanisms, Materials, and Applications. *Adv. Mater.* **2020**, *33*, doi:https://doi.org/10.1002/adma.202000713.
25. Anju Singhwane, Ayushi Jaiswal, Kamana Chaturvedi, Medha Mili, Kunal Pal, Ranjan K. Mohapatra, Mohd. Akram Khan, H. N. Bhargaw, A. K. Srivastava, S.V. Smart shape memory polymers and their significance in biomedical applications: A review. *Polym. Adv. Technol.* **2023**, *34*, 3552–3568, doi:https://doi.org/10.1002/pat.6138.
26. Liu, Y.; Du, H.; Liu, L.; Leng, J. Shape memory polymers and their composites in aerospace applications: a review. *Smart Mater. Struct.* **2014**, *23*, 023001, doi:10.1088/0964-1726/23/2/023001.
27. Hu, J.; Chen, S. A review of actively moving polymers in textile applications. *J. Mater. Chem.* **2010**, *20*, 3346, doi:10.1039/b922872a.
28. Lvov, V.A.; Senatov, F.S.; Veveris, A.A.; Skrybykina, V.A.; Díaz Lantada, A. Auxetic Metamaterials for Biomedical Devices: Current Situation, Main Challenges, and Research Trends. *Materials (Basel).* **2022**, *15*, 1439, doi:10.3390/ma15041439.
29. Xia, Y.; He, Y.; Zhang, F.; Liu, Y.; Leng, J. A Review of Shape Memory Polymers and Composites: Mechanisms, Materials, and Applications. *Adv. Mater.* **2021**, *33*, doi:10.1002/adma.202000713.
30. Liu, C.; Qin, H.; Mather, P.T. Review of progress in shape-memory polymers. *J. Mater. Chem.* **2007**, *17*, 1543, doi:10.1039/b615954k.
31. Leng, J.; Lan, X.; Liu, Y.; Du, S. Shape-memory polymers and their composites: Stimulus

methods and applications. *Prog. Mater. Sci.* **2011**, *56*, 1077–1135, doi:10.1016/j.pmatsci.2011.03.001.

32. Hu, J.; Zhu, Y.; Huang, H.; Lu, J. Recent advances in shape–memory polymers: Structure, mechanism, functionality, modeling and applications. *Prog. Polym. Sci.* **2012**, *37*, 1720–1763, doi:10.1016/j.progpolymsci.2012.06.001.
33. Staszczak, M.; Nabavian Kalat, M.; Golasiński, K.M.; Urbański, L.; Takeda, K.; Matsui, R.; Pieczyska, E.A. Characterization of Polyurethane Shape Memory Polymer and Determination of Shape Fixity and Shape Recovery in Subsequent Thermomechanical Cycles. *Polymers (Basel).* **2022**, *14*, 4775, doi:10.3390/polym14214775.
34. Hornat, C.C.; Urban, M.W. Shape memory effects in self-healing polymers. *Prog. Polym. Sci.* **2020**, *102*, 101208, doi:10.1016/j.progpolymsci.2020.101208.
35. Small, IV, W.; Singhal, P.; Wilson, T.S.; Maitland, D.J. Biomedical applications of thermally activated shape memory polymers. *J. Mater. Chem.* **2010**, *20*, 3356, doi:10.1039/b923717h.
36. Wong, Y.; Kong, J.; Widjaja, L.K.; Venkatraman, S.S. Biomedical applications of shape-memory polymers: how practically useful are they? *Sci. China Chem.* **2014**, *57*, 476–489, doi:10.1007/s11426-013-5061-z.
37. Wan, L.; Yan, M.; Wang, J.; Liu, X.; Huang, J.; Yang, H.; Kong, X. Thermal programming of triple-shape-memory epoxy with flexible segments and Diels–Alder networks. *Iran. Polym. J.* **2024**, *33*, 93–103, doi:10.1007/s13726-023-01235-z.
38. Lee, B.S.; Chun, B.C.; Chung, Y.-C.; Sul, K. Il; Cho, J.W. Structure and Thermomechanical Properties of Polyurethane Block Copolymers with Shape Memory Effect. *Macromolecules* **2001**, *34*, 6431–6437, doi:10.1021/ma0018421.
39. Tobushi, H.; Hashimoto, T.; Ito, N.; Hayashi, S.; Yamada, E. Shape Fixity and Shape Recovery in a Film of Shape Memory Polymer of Polyurethane Series. *J. Intell. Mater. Syst. Struct.* **1998**, *9*, 127–136, doi:10.1177/1045389X9800900206.
40. Sava, Ștefan-D.; Lohan, N.-M.; Pricop, B.; Popa, M.; Cimpoeșu, N.; Comăneci, R.-I.; Bujoreanu, L.-G. On the Thermomechanical Behavior of 3D-Printed Specimens of Shape Memory R-PETG. *Polymers (Basel).* **2023**, *15*, 2378, doi:10.3390/polym15102378.
41. Saadoun Al Azzawi, W. Analytical and Experimental Analysis of the Shape Recovery Behavior of Continuous Fiber Reinforced Shape Memory Polymer. *Diyala J. Eng. Sci.*

2023, 49–58, doi:10.24237/djes.2023.160404.

42. Yin, F.; Liu, Q.; Hu, J.; Ju, Y. Natural Oleanolic Acid-Tailored Eutectogels Featuring Multienvironment Shape Memory Performance. *ACS Appl. Mater. Interfaces* **2024**, *16*, 6424–6432, doi:10.1021/acsami.3c17517.
43. Wang, X.; Li, Z. Role of heating rate on the triple-shape memory effect of amorphous polymers: A cooperative thermodynamic model. *Polymer (Guildf).* **2023**, *274*, 125931, doi:10.1016/j.polymer.2023.125931.
44. Thakur, V.; Singh, R.; Kumar, R.; Gehlot, A. 4D printing of thermoresponsive materials: a state-of-the-art review and prospective applications. *Int. J. Interact. Des. Manuf.* **2023**, *17*, 2075–2094, doi:10.1007/s12008-022-01018-5.
45. Kjar, A.; Huang, Y. Application of Micro-Scale 3D Printing in Pharmaceutics. *Pharmaceutics* **2019**, *11*, 390, doi:10.3390/pharmaceutics11080390.
46. Pereira, T.; Kennedy, J. V; Potgieter, J. A comparison of traditional manufacturing vs additive manufacturing, the best method for the job. *Procedia Manuf.* **2019**, *30*, 11–18, doi:10.1016/j.promfg.2019.02.003.
47. Attaran, M. The rise of 3-D printing: The advantages of additive manufacturing over traditional manufacturing. *Bus. Horiz.* **2017**, *60*, 677–688, doi:10.1016/j.bushor.2017.05.011.
48. Saleh Alghamdi, S.; John, S.; Roy Choudhury, N.; Dutta, N.K. Additive Manufacturing of Polymer Materials: Progress, Promise and Challenges. *Polymers (Basel).* **2021**, *13*, 753, doi:10.3390/polym13050753.
49. A Comprehensive Guide to Understanding and Mastering SLA 3D Printing Available online: https://rapidmade.com/3d-printing/a-comprehensive-guide-to-understanding-and-mastering-sla-3d-printing/.
50. Latika Vishnu Dhawade; Tonchar, D.S. A Review on 3D Printing Technology Used in Pharmaceutical Industry. *Int. J. Adv. Res. Sci. Commun. Technol.* **2024**, 409–419, doi:10.48175/IJARSCT-22747.
51. Rafiee, M.; Farahani, R.D.; Therriault, D. Multi-Material 3D and 4D Printing: A Survey. *Adv. Sci.* **2020**, *7*, doi:10.1002/advs.201902307.
52. Alsaadi, M.; Hinchy, E.P.; McCarthy, C.T.; Moritz, V.F.; Zhuo, S.; Fuenmayor, E.; Devine, D.M. Liquid-Based 4D Printing of Shape Memory Nanocomposites: A Review. *J. Manuf.*

Mater. Process. **2023**, *7*, 35, doi:10.3390/jmmp7010035.

53. Cerbe, F.; Sinapius, M.; Böl, M. Methodology for FDM 4D printing with thermo-responsive SMPs. *Mater. Today Proc.* **2024**, *101*, 1–6, doi:10.1016/j.matpr.2022.11.440.
54. Mei, S.; Wang, J.; Li, Z.; Ding, B.; Li, S.; Chen, X.; Zhao, W.; Zhang, Y.; Zhang, X.; Cui, Z.; et al. 4D printing of polyamide 1212 based shape memory thermoplastic polyamide elastomers by selective laser sintering. *J. Manuf. Process.* **2023**, *92*, 157–164, doi:10.1016/j.jmapro.2023.02.033.
55. Sandanamsamy, L.; Harun, W.S.W.; Ishak, I.; Romlay, F.R.M.; Kadirgama, K.; Ramasamy, D.; Idris, S.R.A.; Tsumori, F. A comprehensive review on fused deposition modelling of polylactic acid. *Prog. Addit. Manuf.* **2023**, *8*, 775–799, doi:10.1007/s40964-022-00356-w.
56. Kristiawan, R.B.; Imaduddin, F.; Ariawan, D.; Ubaidillah; Arifin, Z. A review on the fused deposition modeling (FDM) 3D printing: Filament processing, materials, and printing parameters. *Open Eng.* **2021**, *11*, 639–649, doi:10.1515/eng-2021-0063.
57. Jain, P.; Kuthe, A.M. Feasibility Study of Manufacturing Using Rapid Prototyping: FDM Approach. *Procedia Eng.* **2013**, *63*, 4–11, doi:10.1016/j.proeng.2013.08.275.
58. Rabbaje, F.; Ait Taleb, A.; Lasri, L. Emerging Trends and Future Directions in Fused Deposition Modeling: A Bibliometric Analysis (2013-2023). *E3S Web Conf.* **2025**, *601*, 00030, doi:10.1051/e3sconf/202560100030.
59. Choudhari, C.M.; Patil, V.D. Product Development and its Comparative Analysis by SLA, SLS and FDM Rapid Prototyping Processes. *IOP Conf. Ser. Mater. Sci. Eng.* **2016**, *149*, 012009, doi:10.1088/1757-899X/149/1/012009.
60. Przekop, R.E.; Gabriel, E.; Pakuła, D.; Sztorch, B. Liquid for Fused Deposition Modeling Technique (L-FDM)—A Revolution in Application Chemicals to 3D Printing Technology: Color and Elements. *Appl. Sci.* **2023**, *13*, 7393, doi:10.3390/app13137393.
61. Two-Photon Polymerization Available online: https://www.nanoscribe.com/en/microfabrication-technologies/2pp-two-photon-polymerization/.
62. Tasos Polygenis The Ultimate Guide to 3D Printing Post-Processing Techniques Available online: https://www.wevolver.com/article/the-ultimate-guide-to-3d-printing-post-processing-techniques.
63. Kantaros, A.; Petrescu, F.I.T.; Brachos, K.; Ganetsos, T.; Petrescu, N. Evaluating Benchtop

Additive Manufacturing Processes Considering Latest Enhancements in Operational Factors. *Processes* **2024**, *12*, 2334, doi:10.3390/pr12112334.

64. Authors, V. Abstracts of poster presentations - XXVII Congresso Nazionale CDUO. *J. Osseointegration* **2020**, *12*, 241–665, doi:10.23805/JO.2020.12.03.6.
65. Kim, T.; Lee, S.; Kim, G.B.; Hong, D.; Kwon, J.; Park, J.-W.; Kim, N. Accuracy of a simplified 3D-printed implant surgical guide. *J. Prosthet. Dent.* **2020**, *124*, 195-201.e2, doi:10.1016/j.prosdent.2019.06.006.
66. Puspaputra, P.; Risdiyono; Riza, R. The analysis of the acrylic, CNC, and SLA 3Dprint results as the basis of the jewelry master production.; 2023; p. 080003.
67. Zhu, W.; Huo, F.-Y.; Cao, L.-M.; Li, Z.-Z.; Zhu, Q.; He, R.; Chen, B.; Liang, Y.; Cai, B.; He, H.; et al. Two-photon polymerization 3D printing of biomimetic microstructures for functionalizing surfaces to inhibit bacterial growth. *Chem. Eng. J.* **2025**, *511*, 161907, doi:10.1016/j.cej.2025.161907.
68. Grigorianaitė, G.; Borodinas, S.; Zigmantaitė, V.; Limanovskaja, K.; Andrijec, D.; Kilikevičius, A.; Vainorius, D.; Pautienius, A.; Jonušauskas, L. 3D printing of stents via two-photon polymerization. *Sci. Rep.* **2025**, *15*, 22736, doi:10.1038/s41598-025-07190-4.
69. Taormina, G.; Sciancalepore, C.; Messori, M.; Bondioli, F. 3D printing processes for photocurable polymeric materials: technologies, materials, and future trends. *J. Appl. Biomater. Funct. Mater.* **2018**, *16*, 151–160, doi:10.1177/2280800018764770.
70. Martín-Montal, J.; Pernas-Sánchez, J.; Varas, D. Experimental Characterization Framework for SLA Additive Manufacturing Materials. *Polymers (Basel).* **2021**, *13*, 1147, doi:10.3390/polym13071147.
71. Calignano, F.; Lorusso, M.; Roppolo, I.; Minetola, P. Investigation of the Mechanical Properties of a Carbon Fibre-Reinforced Nylon Filament for 3D Printing. *Machines* **2020**, *8*, 52, doi:10.3390/machines8030052.
72. GUIDE TO SLA 3D PRINTING AND ITS 10 BEST PRINTING SERVICES Available online: https://makenica.com/guide-to-sla-3d-printing-and-its-10-best-printing-services/.
73. DLP 3D Printing Materials Available online: https://www.dic-global.com/en/products/trindy/.
74. Paul Hanaphy Sinterit's SLS 3D printing technology opens new applications for TPUs Available online: https://3dprintingindustry.com/news/sinterits-sls-3d-printing-

technology-opens-new-applications-for-tpus-176313/.

75. Morano, C.; Pagnotta, L. Additive manufactured parts produced by selective laser sintering technology: porosity formation mechanisms. *J. Polym. Eng.* **2023**, *43*, 537–555, doi:10.1515/polyeng-2023-0028.
76. Iftekar, S.F.; Aabid, A.; Amir, A.; Baig, M. Advancements and Limitations in 3D Printing Materials and Technologies: A Critical Review. *Polymers (Basel).* **2023**, *15*, 2519, doi:10.3390/polym15112519.
77. Farhadi Machekposhti, D.; Tolou, N.; Herder, J.L. A Review on Compliant Joints and Rigid-Body Constant Velocity Universal Joints Toward the Design of Compliant Homokinetic Couplings. *J. Mech. Des.* **2015**, *137*, doi:10.1115/1.4029318.
78. Rami Alfattani Design of Shape-Morphing Structures Consisting of Bistable Design of Shape-Morphing Structures Consisting of Bistable Compliant Mechanisms Compliant Mechanisms. *USF Tampa Grad. Theses Diss.* **2019**.
79. Lu, K.-J.; Kota, S. Design of Compliant Mechanisms for Morphing Structural Shapes. *J. Intell. Mater. Syst. Struct.* **2003**, *14*, 379–391, doi:10.1177/1045389X03035563.
80. Kumar, P.; Sauer, R.A.; Saxena, A. On topology optimization of large deformation contact-aided shape morphing compliant mechanisms. *Mech. Mach. Theory* **2021**, *156*, 104135, doi:10.1016/j.mechmachtheory.2020.104135.
81. Milojević, A.P.; Pavlović, N.D. Development of a new adaptive shape morphing compliant structure with embedded actuators. *J. Intell. Mater. Syst. Struct.* **2016**, *27*, 1306–1328, doi:10.1177/1045389X15590270.
82. Conlan-Smith, C.; Bhattacharyya, A.; James, K.A. Optimal design of compliant mechanisms using functionally graded materials. *Struct. Multidiscip. Optim.* **2018**, *57*, 197–212, doi:10.1007/s00158-017-1744-y.
83. Ling, M.; Howell, L.L.; Cao, J.; Chen, G. Kinetostatic and Dynamic Modeling of Flexure-Based Compliant Mechanisms: A Survey. *Appl. Mech. Rev.* **2020**, *72*, doi:10.1115/1.4045679.
84. Kota, S.; Lu, K.-J.; Kreiner, Z.; Trease, B.; Arenas, J.; Geiger, J. Design and Application of Compliant Mechanisms for Surgical Tools. *J. Biomech. Eng.* **2005**, *127*, 981–989, doi:10.1115/1.2056561.
85. Naficy, S.; Gately, R.; Gorkin, R.; Xin, H.; Spinks, G.M. 4D Printing of Reversible Shape

Morphing Hydrogel Structures. *Macromol. Mater. Eng.* **2017**, *302*, 1600212, doi:10.1002/mame.201600212.

86. Yue, L.; Sun, X.; Yu, L.; Li, M.; Montgomery, S.M.; Song, Y.; Nomura, T.; Tanaka, M.; Qi, H.J. Cold-programmed shape-morphing structures based on grayscale digital light processing 4D printing. *Nat. Commun.* **2023**, *14*, 5519, doi:10.1038/s41467-023-41170-4.
87. Bodaghi, M.; Noroozi, R.; Zolfagharian, A.; Fotouhi, M.; Norouzi, S. 4D Printing Self-Morphing Structures. *Materials (Basel).* **2019**, *12*, 1353, doi:10.3390/ma12081353.
88. Piedade, A.P. 4D Printing: The Shape-Morphing in Additive Manufacturing. *J. Funct. Biomater.* **2019**, *10*, 9, doi:10.3390/jfb10010009.
89. Waidi, Y.O. Recent Advances in 4D-Printed Shape Memory Actuators. *Macromol. Rapid Commun.* **2025**, doi:10.1002/marc.202401141.
90. Khalid, M.Y.; Arif, Z.U.; Ahmed, W.; Umer, R.; Zolfagharian, A.; Bodaghi, M. 4D printing: Technological developments in robotics applications. *Sensors Actuators A Phys.* **2022**, *343*, 113670, doi:10.1016/j.sna.2022.113670.
91. Jeong, H.Y.; An, S.-C.; Lim, Y.; Jeong, M.J.; Kim, N.; Jun, Y.C. 3D and 4D Printing of Multistable Structures. *Appl. Sci.* **2020**, *10*, 7254, doi:10.3390/app10207254.
92. Zolfagharian, A.; Kaynak, A.; Bodaghi, M.; Kouzani, A.Z.; Gharaie, S.; Nahavandi, S. Control-Based 4D Printing: Adaptive 4D-Printed Systems. *Appl. Sci.* **2020**, *10*, 3020, doi:10.3390/app10093020.
93. Ali, M.H.; Abilgaziyev, A.; Adair, D. 4D printing: a critical review of current developments, and future prospects. *Int. J. Adv. Manuf. Technol.* **2019**, *105*, 701–717, doi:10.1007/s00170-019-04258-0.
94. Choong, Y.Y.C.; Maleksaeedi, S.; Eng, H.; Wei, J.; Su, P.-C. 4D printing of high performance shape memory polymer using stereolithography. *Mater. Des.* **2017**, *126*, 219–225, doi:10.1016/j.matdes.2017.04.049.
95. Ge, Q.; Sakhaei, A.H.; Lee, H.; Dunn, C.K.; Fang, N.X.; Dunn, M.L. Multimaterial 4D Printing with Tailorable Shape Memory Polymers. *Sci. Rep.* **2016**, *6*, 31110, doi:10.1038/srep31110.
96. Andrés Díaz Lantada Metodología Para el Desarrollo de Dispositivos Médicos Basados en el Empleo de Polímeros Activos Como Sensores y Actuadores, Universidad Politécnica de Madrid, 2009.

97. Zeng, C.; Liu, L.; Zhao, W.; Liu, Z.; Xin, X.; Liu, Y.; Leng, J. Mechanical properties and shape memory behavior of 4D printed functionally graded cellular structures. *Sci. China Technol. Sci.* **2023**, *66*, 3522–3533, doi:10.1007/s11431-023-2475-3.
98. Akbar, I.; El Hadrouz, M.; El Mansori, M.; Tarfaoui, M. Investigation of thermo-mechanical shape memory signatures of 3D printed and Injection molded polymers. *CIRP J. Manuf. Sci. Technol.* **2023**, *41*, 277–291, doi:10.1016/j.cirpj.2022.12.011.
99. Yu, B.; Zheng, J.; Wu, J.; Ma, H.; Zhou, X.; Hui, Y.; Liu, F.; He, J. Preparation of isotropic tensile photosensitive resins for digital light processing 3D printing using orthogonal thiol-ene and thiol-epoxy dual-cured strategies. *Polym. Test.* **2022**, *116*, 107767, doi:10.1016/j.polymertesting.2022.107767.
100. Cosmi, F.; Dal Maso, A. A mechanical characterization of SLA 3D-printed specimens for low-budget applications. *Mater. Today Proc.* **2020**, *32*, 194–201, doi:10.1016/j.matpr.2020.04.602.
101. Kafle, A.; Luis, E.; Silwal, R.; Pan, H.M.; Shrestha, P.L.; Bastola, A.K. 3D/4D Printing of Polymers: Fused Deposition Modelling (FDM), Selective Laser Sintering (SLS), and Stereolithography (SLA). *Polymers (Basel).* **2021**, *13*, 3101, doi:10.3390/polym13183101.
102. Wikło, M.; Byczuk, B.H.; Skrzek, K. Mechanical Characterization of FDM 3D-Printed Components Using Advanced Measurement and Modeling Techniques. *Materials (Basel).* **2025**, *18*, 1086, doi:10.3390/ma18051086.
103. Somireddy, M.; Czekanski, A. Anisotropic material behavior of 3D printed composite structures – Material extrusion additive manufacturing. *Mater. Des.* **2020**, *195*, 108953, doi:10.1016/j.matdes.2020.108953.
104. Zohdi, N.; Yang, R. (Chunhui) Material Anisotropy in Additively Manufactured Polymers and Polymer Composites: A Review. *Polymers (Basel).* **2021**, *13*, 3368, doi:10.3390/polym13193368.
105. Balderrama-Armendariz, C.O.; MacDonald, E.; Espalin, D.; Cortes-Saenz, D.; Wicker, R.; Maldonado-Macias, A. Torsion analysis of the anisotropic behavior of FDM technology. *Int. J. Adv. Manuf. Technol.* **2018**, *96*, 307–317, doi:10.1007/s00170-018-1602-0.
106. Shardakov, I.N.; Trufanov, A.N. Identification of the Temperature Dependence of the Thermal Expansion Coefficient of Polymers. *Polymers (Basel).* **2021**, *13*, 3035, doi:10.3390/polym13183035.

107. Al Azzawi, W.; Islam, M.M.; Leng, J.; Li, F.; Epaarachchi, J.A. Quantitative and qualitative analyses of mechanical behavior and dimensional stability of styrene-based shape memory composites. *J. Intell. Mater. Syst. Struct.* **2017**, *28*, 3115–3126, doi:10.1177/1045389X17705210.
108. Staszczak, M.; Urbański, L.; Cristea, M.; Ionita, D.; Pieczyska, E.A. Investigation of Shape Memory Polyurethane Properties in Cold Programming Process Towards Its Applications. *Polymers (Basel).* **2024**, *16*, 219, doi:10.3390/polym16020219.
109. Gunes, I.S.; Cao, F.; Jana, S.C. Effect of thermal expansion on shape memory behavior of polyurethane and its nanocomposites. *J. Polym. Sci. Part B Polym. Phys.* **2008**, *46*, 1437–1449, doi:10.1002/polb.21480.
110. Rath, B.B.; Gallo, G.; Dinnebier, R.E.; Vittal, J.J. Reversible Thermosalience in a One-Dimensional Coordination Polymer Preceded by Anisotropic Thermal Expansion and the Shape Memory Effect. *J. Am. Chem. Soc.* **2021**, *143*, 2088–2096, doi:10.1021/jacs.0c12363.
111. Issabayeva, Z.; Shishkovsky, I. Prediction of The Mechanical Behavior of Polylactic Acid Parts with Shape Memory Effect Fabricated by FDM. *Polymers (Basel).* **2023**, *15*, 1162, doi:10.3390/polym15051162.
112. da Silva, M.M.; Proença, M.P.; Covas, J.A.; Paiva, M.C. Shape-Memory Polymers Based on Carbon Nanotube Composites. *Micromachines* **2024**, *15*, 748, doi:10.3390/mi15060748.
113. Salas, A.; Zanatta, M.; Sans, V.; Roppolo, I. Chemistry in light-induced 3D printing. *ChemTexts* **2023**, *9*, 4, doi:10.1007/s40828-022-00176-z.
114. Pagac, M.; Hajnys, J.; Ma, Q.-P.; Jancar, L.; Jansa, J.; Stefek, P.; Mesicek, J. A Review of Vat Photopolymerization Technology: Materials, Applications, Challenges, and Future Trends of 3D Printing. *Polymers (Basel).* **2021**, *13*, 598, doi:10.3390/polym13040598.
115. Nabavian Kalat, M.; Ziai, Y.; Dziedzic, K.; Gradys, A.; Urbański, L.; Zaszczyńska, A.; Díaz Lantada, A.; Kowalewski, Z. Experimental evaluation of build orientation effects on the microstructure, thermal, mechanical, and shape memory properties of SLA 3D-printed epoxy resin. *Eur. Polym. J.* **2025**, *228*, 113829, doi:10.1016/j.eurpolymj.2025.113829.
116. Chacón, J.M.; Caminero, M.A.; García-Plaza, E.; Núñez, P.J. Additive manufacturing of PLA structures using fused deposition modelling: Effect of process parameters on mechanical properties and their optimal selection. *Mater. Des.* **2017**, *124*, 143–157,

doi:10.1016/j.matdes.2017.03.065.

117. Behl, M.; Lendlein, A. Shape-memory polymers. *Mater. Today* **2007**, *10*, 20–28, doi:10.1016/S1369-7021(07)70047-0.
118. Shahi, K.; Boomurugan, R.; Velmurugan, R. Cold programming of epoxy-based shape memory polymer. *Structures* **2021**, *29*, 2082–2093, doi:10.1016/j.istruc.2020.05.023.
119. Li, G.; Wang, A. Cold, warm, and hot programming of shape memory polymers. *J. Polym. Sci. Part B Polym. Phys.* **2016**, *54*, 1319–1339, doi:10.1002/polb.24041.
120. Li, G.; Xu, W. Thermomechanical behavior of thermoset shape memory polymer programmed by cold-compression: Testing and constitutive modeling. *J. Mech. Phys. Solids* **2011**, *59*, 1231–1250, doi:10.1016/j.jmps.2011.03.001.
121. Cai, S.; Sun, Y.-C.; Ren, J.; Naguib, H.E. Toward the low actuation temperature of flexible shape memory polymer composites with room temperature deformability via induced plasticizing effect. *J. Mater. Chem. B* **2017**, *5*, 8845–8853, doi:10.1039/C7TB02068F.
122. Shahi, K.; Ramachandran, V. Theoretical and Experimental Investigation of Shape Memory Polymers Programmed below Glass Transition Temperature. *Polymers (Basel).* **2022**, *14*, 2753, doi:10.3390/polym14132753.
123. Kramer, E.J. Microscopic and molecular fundamentals of crazing. In *Crazing in Polymers*; Springer-Verlag: Berlin/Heidelberg; pp. 1–56.
124. Passaglia, E. Crazes and fracture in polymers. *J. Phys. Chem. Solids* **1987**, *48*, 1075–1100, doi:10.1016/0022-3697(87)90119-3.
125. Jonathan Cailloux Modified Poly (Lactic Acid) Sheets Manufactured by One-Step Reactive Extrusion-Calendering: Thermal, Rheological, Mechanical and Fracture Behaviours. Ph.D Thesis, Universitat Politècnica de Catalunya, Barcelona, Spain, 2016.
126. Li, G.; Ajisafe, O.; Meng, H. Effect of strain hardening of shape memory polymer fibers on healing efficiency of thermosetting polymer composites. *Polymer (Guildf).* **2013**, *54*, 920–928, doi:10.1016/j.polymer.2012.12.046.
127. Staszczak, M.; Urbański, L.; Gradys, A.; Cristea, M.; Pieczyska, E.A. Nucleation, Development and Healing of Micro-Cracks in Shape Memory Polyurethane Subjected to Subsequent Tension Cycles. *Polymers (Basel).* **2024**, *16*, 1930, doi:10.3390/polym16131930.
128. Wang, X.; Xu, J.; Zhang, Y.; Wang, T.; Wang, Q.; Li, S.; Yang, Z.; Zhang, X. A stretchable,

mechanically robust polymer exhibiting shape-memory-assisted self-healing and clustering-triggered emission. *Nat. Commun.* **2023**, *14*, 4712, doi:10.1038/s41467-023-40340-8.

129. C. Mirchel Skinner Membrane Hinges for Deployable Systems, Brigham Young University, 2024.
130. Soares, J.S.; Moore, J.E. Biomechanical Challenges to Polymeric Biodegradable Stents. *Ann. Biomed. Eng.* **2016**, *44*, 560–579, doi:10.1007/s10439-015-1477-2.
131. Wiggins, M.J.; Anderson, J.M.; Hiltner, A. Effect of strain and strain rate on fatigue-accelerated biodegradation of polyurethane. *J. Biomed. Mater. Res. Part A* **2003**, *66A*, 463–475, doi:10.1002/jbm.a.10584.
132. Seong, M.; Sun, K.; Kim, S.; Kwon, H.; Lee, S.-W.; Veerla, S.C.; Kang, D.K.; Kim, J.; Kondaveeti, S.; Tawfik, S.M.; et al. Multifunctional Magnetic Muscles for Soft Robotics. *Nat. Commun.* **2024**, *15*, 7929, doi:10.1038/s41467-024-52347-w.
133. Song, K.; Cho, N.-K.; Lee, S.; Choi, Y.; Nam, H. Cyclic mechanical behaviours of polydimethylsiloxane / multi-walled carbon nanotube micro-composites sensor: Effects of strain range and strain rate. *Sensors Actuators A Phys.* **2025**, *382*, 116158, doi:10.1016/j.sna.2024.116158.
134. Smerdova, O.; Pecora, M.; Gigliotti, M. Cyclic indentation of polymers: Instantaneous elastic modulus from reloading, energy analysis, and cyclic creep. *J. Mater. Res.* **2019**, *34*, 3688–3698, doi:10.1557/jmr.2019.289.
135. Yu, J.; Breite, C.; Van Loock, F.; Pardoen, T.; Swolfs, Y. Experimental investigation of yield and hysteresis behaviour of an epoxy resin under cyclic compression in the large deformation regime. *Express Polym. Lett.* **2024**, *18*, 133–143, doi:10.3144/expresspolymlett.2024.11.
136. Yu, K.; Li, H.; McClung, A.J.W.; Tandon, G.P.; Baur, J.W.; Qi, H.J. Cyclic behaviors of amorphous shape memory polymers. *Soft Matter* **2016**, *12*, 3234–3245, doi:10.1039/C5SM02781K.
137. Diani, J.; Fayolle, B.; Gilormini, P. A review on the Mullins effect. *Eur. Polym. J.* **2009**, *45*, 601–612, doi:10.1016/j.eurpolymj.2008.11.017.
138. Cantournet, S.; Desmorat, R.; Besson, J. Mullins effect and cyclic stress softening of filled elastomers by internal sliding and friction thermodynamics model. *Int. J. Solids Struct.*

2009, *46*, 2255–2264, doi:10.1016/j.ijsolstr.2008.12.025.

139. Yang, T.-T.; Shui, Y.; Wei, C.-S.; Huang, L.-Z.; Yang, C.-W.; Sun, G.-A.; Han, J.-J.; Xu, J.-Z.; Li, Z.-M.; Liu, D. Effect of cyclic straining with various rates on stress softening/hysteresis and structural evolution of filled rubber: A time-resolved SANS study. *Compos. Part B Eng.* **2022**, *242*, 110100, doi:10.1016/j.compositesb.2022.110100.
140. Zhang, C.; Gou, X.; Xiao, R. Hysteresis in glass microsphere filled elastomers under cyclic loading. *Polym. Test.* **2021**, *95*, 107081, doi:10.1016/j.polymertesting.2021.107081.
141. *Advances in Shape Memory Materials*; Sun, Q., Matsui, R., Takeda, K., Pieczyska, E.A., Eds.; Advanced Structured Materials; Springer International Publishing: Cham, 2017; Vol. 73; ISBN 978-3-319-53305-6.
142. Gupta, S.; Bit, A. Rapid prototyping for polymeric gels. In *Polymeric Gels*; Elsevier, 2018; pp. 397–439.
143. Salmoria, G.V.; Gonzalez, V.J.; Ahrens, C.H.; Soldi, V.; Pires, A.T.N. Stereolithography Somos 7110 photosensitive resin: study of curing kinetic and thermal degradation. *J. Mater. Process. Technol.* **2005**, *168*, 164–171, doi:10.1016/j.jmatprotec.2004.11.012.
144. Sabu, M.; Bementa, E.; Jaya Vinse Ruban, Y.; Ginil Mon, S. A novel analysis of the dielectric properties of hybrid epoxy composites. *Adv. Compos. Hybrid Mater.* **2020**, *3*, 325–335, doi:10.1007/s42114-020-00166-0.
145. Menczel, J.D.; Judovits, L.; Prime, R.B.; Bair, H.E.; Reading, M.; Swier, S. Differential Scanning Calorimetry (DSC). In *Thermal Analysis of Polymers*; Wiley, 2009; pp. 7–239.
146. Bute, I.; Tarasovs, S.; Vidinejevs, S.; Vevere, L.; Sevcenko, J.; Aniskevich, A. Thermal properties of 3D printed products from the most common polymers. *Int. J. Adv. Manuf. Technol.* **2023**, *124*, 2739–2753, doi:10.1007/s00170-022-10657-7.
147. A.J. Hughes; T.K. Mallick; T.S. O'Donovan Investigation of the Effects of Temperature on the Microstructure of PTFE Microfiltration Membranes Under Membrane Distillation Conditions. *J. Adv. Therm. Sci. Res.* **2020**, *7*, 11–21, doi:10.15377/2409-5826.2020.07.2.
148. Yang, W.; Liu, F.; Chen, H.; Dai, X.; Liu, W.; Qiu, X.; Ji, X. Influence of Heating Rate on the Structure and Mechanical Properties of Aromatic BPDA–PDA Polyimide Fiber. *Polymers (Basel).* **2020**, *12*, 510, doi:10.3390/polym12030510.
149. Lutomski, M.; Gawdzik, B. Polymer Dimensional Changes in Optical Cables. *Ann. UMCS, Chem.* **2014**, *68*, doi:10.2478/umcschem-2013-0004.

150. Lutomski, M.; Gawdzik, B.; Podkościelna, B. Temperature-modulated thermomechanical analysis as a potential technique for irreversible stress relaxation measurement in various cables. *J. Therm. Anal. Calorim.* **2016**, *125*, 1425–1430, doi:10.1007/s10973-016-5616-2.
151. Alsewailem, F.D. On the Thermal Expansion Behavior of Polystyrene/Polyethyleneterephthalate Blend Systems: Experimental Study. *J. Thermoplast. Compos. Mater.* **2009**, *22*, 585–604, doi:10.1177/0892705709091859.
152. Li, Y.; Teng, Z. Effect of printing orientation on mechanical properties of SLA 3D-printed photopolymer. *Fatigue Fract. Eng. Mater. Struct.* **2024**, *47*, 1531–1545, doi:10.1111/ffe.14265.
153. Aberoumand, M.; Rahmatabadi, D.; Soltanmohammadi, K.; Soleyman, E.; Ghasemi, I.; Baniassadi, M.; Abrinia, K.; Bodaghi, M.; Baghani, M. Stress recovery and stress relaxation behaviors of PVC 4D printed by FDM technology for high-performance actuation applications. *Sensors Actuators A Phys.* **2023**, *361*, 114572, doi:10.1016/j.sna.2023.114572.
154. Shan, W.; Liu, P.; Quoc Bui, T.; Duan, H. Shape memory polymers structure with different printing direction: Effect of fracture toughness. *Theor. Appl. Fract. Mech.* **2023**, *127*, 104002, doi:10.1016/j.tafmec.2023.104002.
155. Piqué, A.; Auyeung, R.C.Y.; Kim, H.; Charipar, N.A.; Mathews, S.A. Laser 3D micro-manufacturing. *J. Phys. D. Appl. Phys.* **2016**, *49*, 223001, doi:10.1088/0022-3727/49/22/223001.
156. Hayes, M.D.; Edwards, D.B.; Shah, A.R. Fractography Basics. In *Fractography in Failure Analysis of Polymers*; Elsevier, 2015; pp. 48–92.
157. Zhao, J.; Han, M.; Li, L. Characterization of Anisotropic Shape Memory Behavior of Thermoresponsive Components in 4D Printing. *3D Print. Addit. Manuf.* **2024**, *11*, 1055–1063, doi:10.1089/3dp.2023.0165.
158. Liu, T.; Liu, L.; Zeng, C.; Liu, Y.; Leng, J. 4D printed anisotropic structures with tailored mechanical behaviors and shape memory effects. *Compos. Sci. Technol.* **2020**, *186*, 107935, doi:10.1016/j.compscitech.2019.107935.
159. Tobushi, H.; Shimada, D.; Hayashi, S.; Endo, M. Shape fixity and shape recovery of polyurethane shape-memory polymer foams. *Proc. Inst. Mech. Eng. Part L J. Mater. Des. Appl.* **2003**, *217*, 135–143, doi:10.1177/146442070321700205.
160. P, J.; Pionteck, J.; Hässler, R.; George, S.M.; Cvelbar, U.; Thomas, S. Studies on Stress

Relaxation and Thermomechanical Properties of Poly(acrylonitrile-butadiene-styrene) Modified Epoxy−Amine Systems. *Ind. Eng. Chem. Res.* **2011**, *50*, 4432–4440, doi:10.1021/ie1016915.

161. Chen, J.; Liu, X.; Tian, Y.; Zhu, W.; Yan, C.; Shi, Y.; Kong, L.B.; Qi, H.J.; Zhou, K. 3D-Printed Anisotropic Polymer Materials for Functional Applications. *Adv. Mater.* **2022**, *34*, doi:10.1002/adma.202102877.
162. Xin, X.; Lin, C.; Wang, X.; Liu, F.; Dong, L.; Liu, L.; Liu, Y.; Leng, J. Dynamically customizable 4D printed shape memory polymer biomedical devices: a review. *Mater. Futur.* **2025**, *4*, 012402, doi:10.1088/2752-5724/ad8898.
163. Slavkovic, V.; Palic, N.; Milenkovic, S.; Zivic, F.; Grujovic, N. Thermo-Mechanical Characterization of 4D-Printed Biodegradable Shape-Memory Scaffolds Using Four-Axis 3D-Printing System. *Materials (Basel).* **2023**, *16*, 5186, doi:10.3390/ma16145186.
164. Megdich, A.; Habibi, M.; Laperrière, L.; Li, Z.; Abdin, Y. Advanced nanocomposites for 4D printing: High-performance electroactive shape memory polymers for smart applications. *Appl. Mater. Today* **2025**, *44*, 102702, doi:10.1016/j.apmt.2025.102702.